Exploring processes and applications of metal-microbe interactions

Edited by
Eva Pakostova, Carmen Falagan and
Alfonso Mazuelos Rojas

Published in
Frontiers in Microbiology

About Frontiers

Frontiers is more than just an open access publisher of scholarly articles: it is a pioneering approach to the world of academia, radically improving the way scholarly research is managed. The grand vision of Frontiers is a world where all people have an equal opportunity to seek, share and generate knowledge. Frontiers provides immediate and permanent online open access to all its publications, but this alone is not enough to realize our grand goals.

Frontiers journal series

The Frontiers journal series is a multi-tier and interdisciplinary set of open-access, online journals, promising a paradigm shift from the current review, selection and dissemination processes in academic publishing. All Frontiers journals are driven by researchers for researchers; therefore, they constitute a service to the scholarly community. At the same time, the *Frontiers journal series* operates on a revolutionary invention, the tiered publishing system, initially addressing specific communities of scholars, and gradually climbing up to broader public understanding, thus serving the interests of the lay society, too.

Dedication to quality

Each Frontiers article is a landmark of the highest quality, thanks to genuinely collaborative interactions between authors and review editors, who include some of the world's best academicians. Research must be certified by peers before entering a stream of knowledge that may eventually reach the public - and shape society; therefore, Frontiers only applies the most rigorous and unbiased reviews. Frontiers revolutionizes research publishing by freely delivering the most outstanding research, evaluated with no bias from both the academic and social point of view. By applying the most advanced information technologies, Frontiers is catapulting scholarly publishing into a new generation.

What are Frontiers Research Topics?

Frontiers Research Topics are very popular trademarks of the *Frontiers journals series*: they are collections of at least ten articles, all centered on a particular subject. With their unique mix of varied contributions from Original Research to Review Articles, Frontiers Research Topics unify the most influential researchers, the latest key findings and historical advances in a hot research area.

Find out more on how to host your own Frontiers Research Topic or contribute to one as an author by contacting the Frontiers editorial office: frontiersin.org/about/contact

Exploring processes and applications of metal-microbe interactions

Topic editors

Eva Pakostova — Laurentian University, Canada
Carmen Falagan — University of Portsmouth, United Kingdom
Alfonso Mazuelos Rojas — University of Seville, Spain

Table of contents

Editorial: Exploring processes and applications of metal-microbe interactions

Eva Pakostova[1,2]*, Carmen Falagan[3] and
Alfonso Mazuelos Rojas[4]

[1]MIRARCO Mining Innovation, Sudbury, ON, Canada, [2]Faculty of Science, Engineering & Architecture,
School of Natural Sciences, Laurentian University, Sudbury, ON, Canada, [3]Faculty of Science and
Health, University of Portsmouth, Portsmouth, United Kingdom, [4]Department of Chemical
Engineering, University of Seville, Seville, Spain

Editorial on the Research Topic
Exploring processes and applications of metal-microbe interactions

Interactions between microorganisms and metals occur in both natural and anthropogenic environments, encompassing a wide range of processes from microbially catalyzed transformations within biogeochemical metal(loid) cycling to microbiology-based applications for metal recovery and removal. The main goal of this Research Topic is to present recent research on metal-microbe interactions and related processes, with the main focus on advances in metal recovery using microorganisms (biomining/bioleaching) and remediation of metal(loid)-contaminated environments. This Research Topic includes 10 manuscripts reporting on metal-microbe interactions, covering bioremediation and biomineralization, cell adhesion, bioleaching, electron transport, and the negative effects of microbes on the quality of industrial fluids.

Microbial processes play a crucial role in biogeochemical cycling, which encompasses mineral formation and weathering, soil and water acidification, carbon capture, nutrient availability, and many other processes. A large number of microbes and their metabolic traits can be harvested to improve industrial applications and processes. Guo et al. reported that an elevated molybdenum content increases the adhesion of *Bacillus subtilis* to the surface of low-alloy steel, and improves subsequent biomineralization that mitigates metal corrosion. The results suggest that molybdenum content can affect the chemotaxis, mobility and carbonic anhydrase secretion-related genes in the bacterium. Guberman-Pfeffer provided a perspective on the electrically conductive filaments of redox-active cytochromes ("nanowires") in *Geobacter sulfurreducens,* a bacterium that profoundly shapes Earth's biogeochemistry by discharging electrons to minerals and other microbes through the filaments. The above study summarizes our current mechanistic understanding of physiological metal-microbe interactions and thus contributes to efforts to optimize these interactions for bioremediation and energy or chemical production.

There is a growing global interest in implementing "green" biotechnologies in industrial extractive processes, and bioleaching is a cost-effective alternative to conventional pyro- and hydrometallurgical processing that has reduced negative environmental effects. Lithium is becoming increasingly important due to its use in

batteries needed for electrification and the transition to net zero. Kirk et al. investigated the bioleaching of lithium from three different minerals using the acidophile *Acidithiobacillus ferrooxidans*, including performing kinetic modeling to predict the dominant reaction pathways for lithium extraction. The study successfully demonstrated the potential for acidophilic bioleaching in jadarite processing, with implications for other lithium-bearing deposits. Antimony (Sb) is another important strategic material, mainly used as a flame retardant in electronic devices, batteries, printing industries, semiconductors, and pharmaceuticals. Zheng et al. improved the dissolution rate of stibnite (Sb_2S_3) by adding pyrite (FeS_2), which led to the formation of FeS_2-Sb_2S_3 galvanic cell and promoted the electron transfer efficiency and antimony extraction by *Sulfobacillus thermosulfidooxidans*. Importantly, the mechanism of (bio)leaching of Sb-bearing sulfides and chemical speciation was described based on the results obtained via a combination of experiments and modeling.

Metal mining generates large amounts of waste (such as waste rock and mine tailings) that are stored at or near mine sites and present serious risks to the environment due to acid mine drainage (AMD) and the mobilization of hazardous metal(loid)s that cause problems for humans and wildlife. A wide range of remediation strategies have been developed to mitigate the negative environmental impacts of mining, and many of these strategies are based on and affected by microbial activity. Sulfate-reducing bacteria (SRB) are often used in both active and passive mine water treatment to immobilize metal(loid) contaminants as insoluble sulfides. The majority of known SRBs are neutrophils, but species that are capable of sulfate reduction under acidic conditions are of particular interest for practical applications due to many mine-impacted environments being acid-generating. The metabolic activity of acid-tolerant SRBs was enhanced in the deep layer of an acidic pit lake in Spain, via sulfur and organic amendments that promoted the formation of low-solubility sulfide minerals (Liu et al.). Microbial community analysis of enrichment samples revealed the dominance of *Desulfosporosinus acididurans*. Dong et al. applied SRBs to treat synthetic AMD and real mine tailings from a zinc-lead mine, reporting on the metal tolerance and bio-cementing strength of SRBs. The mechanism by which SRBs fix pollutants in tailings was revealed via a detailed analysis of the solids.

Revegetation is an environmentally sustainable technique for *in situ* mine site remediation, and it is less costly than traditional physicochemical techniques. However, due to the elevated levels of dissolved metal(loid)s and low microbial activity in the tailings area, it is generally difficult for plants to survive. Mao et al. studied the specific microbiome associated with *Imperata cylindrica*, a dominant pioneer plant in many abandoned mines. The authors reported an increased diversity of fungi in the rhizosphere soil, which is expected to lead to enhanced nutrient availability and thus improved mine restoration efficacy. In recent years, bacterial exopolysaccharides (EPS) have been investigated as an emerging approach in the remediation of mine-impacted environments

contaminated with heavy metals. A genomic study by Najjari et al. evaluated the metal biosorption potential of EPS produced by a novel *Psychrobacillus* strain isolated from an iron ore deposit in northern Tunisia, indicating greater adsorption of iron and lead compared to copper and cadmium. Another innovative approach, electrokinetic remediation, is based on metal removal by low-potential electrodes installed into contaminated soil. Narenkumar et al. investigated the potential of biosurfactants produced by *Pseudomonas stutzeri* and *Bacillus cereus* to serve as electrolytes during the electrokinetic process, achieving the removal rate of 70–75% of chromium from contaminated soil, without negative effects on plant seed germination.

In addition to positive effects, microbial activity can negatively affect material quality, and promote deterioration and corrosion. It has been shown that microbial proliferation in metal-cutting fluid decreases its quality; organic acids secreted by anaerobic microorganisms and decomposition of some of the fluid components by aerobes lowered the pH of the cutting fluid and its corrosion resistance. In addition, the accumulation of fungal mycelium resulted in reduced lubricity and poor stability (Shen et al.).

In summary, understanding microbial processes and metal-microbe interactions can help develop effective measures to promote beneficial microbial processes (such as metal extraction during bioleaching, metal immobilization in remediation systems, and formation of protective layers on metal surfaces) and inhibit deleterious microbial activities (e.g., deterioration of industrial materials).

Author contributions

EP: Writing – original draft, Writing – review & editing. CF: Writing – review & editing. AM: Writing – review & editing.

Conflict of interest

Publisher's note

Check for updates

Study on the effectiveness of sulfate-reducing bacteria to remove Pb(II) and Zn(II) in tailings and acid mine drainage

Yanrong Dong[1,2]*, Ziqing Gao[1], Junzhen Di[1], Dong Wang[2], Zhenhua Yang[2], Xuying Guo[3] and Xiaotong Zhu[1]

[1]College of Civil Engineering, Liaoning Technical University, Fuxin, China, [2]School of Mining, Liaoning Technical University, Fuxin, China, [3]College of Science, Liaoning Technical University, Fuxin, China

In view of water and soil getting polluted by Pb(II), Zn(II), and other heavy metals in tailings and acid mine drainage (AMD), we explored the removal effect of sulfate-reducing bacteria (SRB) on Pb(II), Zn(II), and other pollutants in solution and tailings based on the microbial treatment technology. We used the scanning electron microscope-energy dispersive spectroscopy (SEM-EDS), X-ray diffraction (XRD), and X-ray fluorescence (XRF), to reveal the mechanism of SRB treatment of tailings. The results showed that SRB had a strong removal capacity for Zn(II) at 0−40 mg/L; however, Zn(II) at 60−100 mg/L inhibited the growth of SRB. Similarly, SRB exhibited a very strong ability to remove Pb(II) from the solution. At a Pb(II) concentration of 10−50 mg/L, its removal percentage by SRB was 100%. SRB treatment could effectively immobilize the pollutants leached from the tailings. With an increase in the amount of tailings added to each layer, the ability of SRB to treat the pollutants diminished. When 1 cm of tailingssand was added to each layer, SRB had the best effect on tailing sand treatment. After treatment, the immobilization rates of SO_4^{2-}, Fe(III), Mn(II), Pb(II), Zn(II), Cu(II), and total Cr in the leachate of #1 tailing sand were 95.44%, 100%, 90.88%, 100%, 96.20%, 86.23%, and 93.34%, respectively. After the tailings were treated by SRB, although the tailings solidified into a cohesive mass from loose granular particles, their mechanical strength was <0.2 MPa. *Desulfovibrio* and *Desulfohalotomaculum* played the predominant roles in treating tailings by mixing SRB. The S^{2-} and carbonate produced by mixing SRB during the treatment of tailings could metabolize sulfate by combining with the heavy metal ions released by the tailings to form FeS, MnS, ZnS, CuS, PbS, Cr_2S_3, $CaCO_3$, $MnCO_3$, and other precipitated particles. These particles were attached to the surface of the tailings, reducing the environmental pollution of the tailings in the water and soil around the mining area.

Highlights

- SRB had a strong removal capacity for Zn(II) in the concentration range of 0−40 mg/L.
- SRB had a very strong ability to remove Pb(II).
- SRB treatment can effectively reduce environmental pollution.
- SRB can facilitate precipitation through metabolic activities.

1 Introduction

Mining activities cause immense acid mine drainage (AMD) containing SO_4^{2-} and heavy metal ions (Nguyen et al., 2020). High concentrations of heavy metals and acidic pH in AMD pose major risks to surface water and groundwater, leading to the loss of biodiversity and deterioration of aquatic ecosystems (Rambabu et al., 2020). As AMD spreads further, it pollutes the surrounding water and soil and has a serious impact on the environment (Ryu et al., 2019; Watanabe et al., 2020). Consequently, heavy metal (Pb, Cd, Zn, etc.) pollution of soil and water has become a threat to human health in recent years (Kim et al., 2018; Zeng et al., 2022). For instance, according to China's soil pollution survey, 7% of agricultural soil is contaminated by Pb, which exceeds China's soil environmental quality standards (Yang et al., 2021). Pb, Zn, and other heavy metals can enter the food chain through rice, alfalfa, and other plants, causing serious harm to human health (Fang et al., 2020). These toxic metal ions are non-degradable, and their continuous presence in the ecosystem significantly pollutes the surface and groundwater resources, thus causing a serious public health challenge. Therefore, the remediation of water and soil containing Pb, Zn, and other heavy metal ions has become a research hot spot in recent years.

Bioremediation is an innovative technology for treating acidic heavy metal environmental pollution (Ayangbenro et al., 2018). Compared to traditional physical and chemical methods, bioremediation is an attractive alternative method (Razia et al., 2023). It is low-cost, maintains ecological balance, and helps rebuild the polluted environment (Martins et al., 2011). In particular, the sustainable bioremediation technology based on sulfate-reducing bacteria (SRB) is considered to be one of the best treatment schemes to alleviate environmental pollution caused by AMD (Alexandrino et al., 2011). Dissimilatory SRB is the main driving force behind AMD bioremediation (Chai et al., 2023). SRB can promote the conversion of sulfate into sulfide, which reacts with heavy metals to generate toxic metals and form a large number of metal sulfides. These metal sulfides are very stable and can be easily removed (Ayangbenro et al., 2018). The traditional chemical treatment of heavy metals often forms unstable metal hydroxide precipitation, making it difficult to recover these metals and causing secondary sludge disposal problems (Kumar et al., 2021). On the other hand, SRB can remove heavy metals and form insoluble salts (the Ksp of Zn, Cd, and Pb sulfides are 23.8, 26.1, and 28.0, respectively) even at very low pH (Su et al., 2022). This process promotes the application of SRB in the treatment of toxic heavy metal pollutants.

Nguyen et al. (2020) isolated an acid-resistant sulfate-reducing bacteria S_4 from the mud of an AMD storage tank in Vietnam, which demonstrated great potential for remediating sulfate and heavy metals (Fe, Zn, Cu) in solution. Alexandrino et al. (2011) isolated a strain of SRB from a fumarole in Iceland, which showed very high sulfate reduction capacity in a mixture solution comprising 0.75 g/L iron, 0.20 g/L zinc, and 0.080 g/L copper. Lin et al. (2023) showed that the alkaline pretreatment of peanut shells as the SRB carbon source had a good removal effect of SO_4^{2-} in solution and SO_4^{2-} biological reduction load (140.61 mg/g). Gu et al. (2020) demonstrated that SRB could effectively remove Pd (II), Cd (II), and Ca (II) in solution, and the sediments (PbS, CdS, etc.) were very stable in wastewater. Nogueira et al. (2021) showed that SRB with bagasse as an electron donor could effectively remove SO_4^{2-} and heavy metals in AMD, with removal rates of 55–91% for SO_4^{2-} and 80%, 73%, and 60% for Zn, Cu, and Mn, respectively. Kumar and Pakshirajan (2021) reported that SRB could remove and recover heavy metals from synthetic wastewater containing Cd(II), Cu(II), Fe(III), Ni(II), Pb(II), and Zn(II). They had previously reported that when the influent concentration of Cu and Zn was 50 mg/L and 10 mg/L, respectively, they could be removed by SRB by more than 90% (Kumar and Pakshirajan, 2020). Hwang and Jho (2018) showed that native SRB isolated from soil samples in

GRAPHICAL ABSTRACT
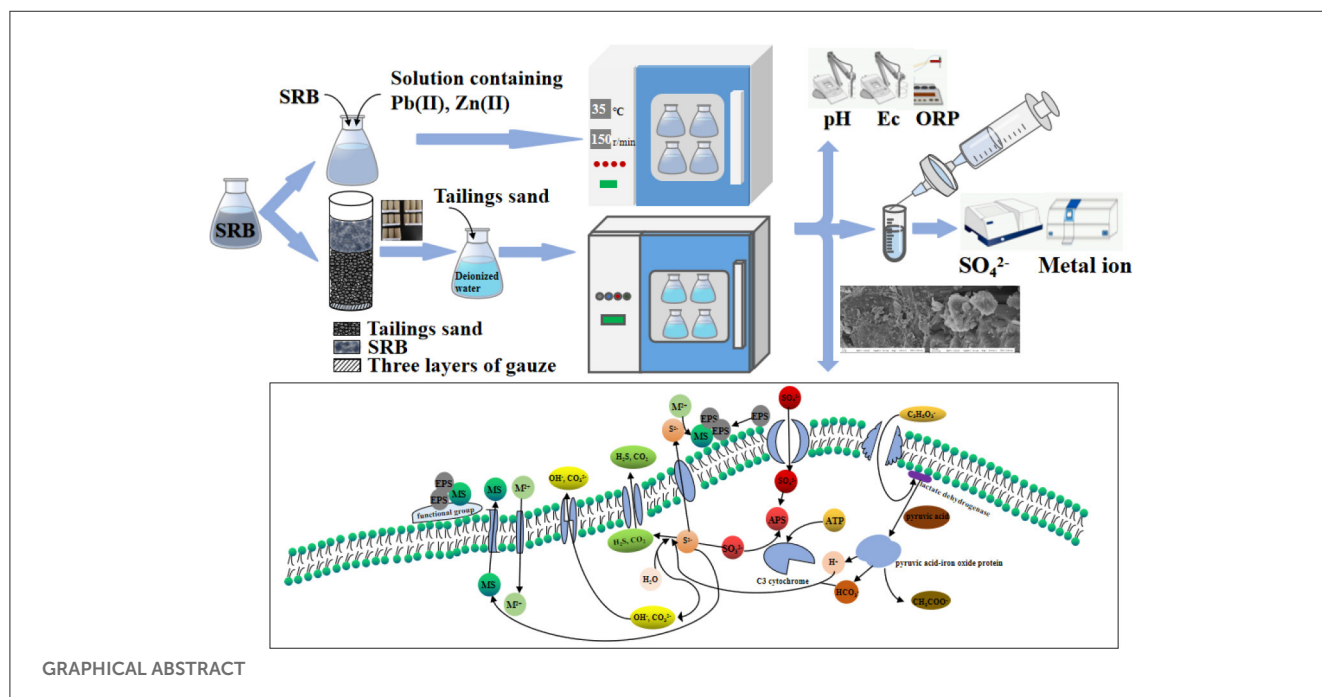
a mining area had a removal effect on the heavy metals and sulfates in the synthetic AMD prepared in the laboratory.

These studies establish that both SRB cultivated in the soil and pure SRB strains that were purchased had good removal effects on SO_4^{2-} and heavy metal ions in simulated AMD solution. However, most of the SO_4^{2-} and heavy metal ions in AMD come from the oxidation and dissolution release of minerals in the mine tailings. The acidic environment of AMD further promotes the dissolution of pollutants in tailings. The pollutants released from tailings are relatively complex, and laboratory simulations of AMD cannot fully reflect the remediation effect of SRB on pollutants. Especially, the fixation effect of SRB on pollutants in tailing sand is not clear. This limits the wide application of SRB in the field of environmental remediation in mining areas.

Therefore, this paper used soil to enrich SRB and discuss the immobilization effect SRB had on Pb(II), Zn (II), SO_4^{2-}, and other pollutants in a simulated AMD solution containing Pb(II) and Zn(II) and tailings. Using SEM-EDS, XRF, XRD, and other tests, the mechanism of SRB fixing pollutants in tailings was revealed. The results provide the technical reference for SRB effectively and sustainably repair AMD and tailings.

2 Materials and methods

2.1 Test materials

2.1.1 Chemical reagent

The chemical reagents used in the experiments were all purchased from Tianjin Zhiyuan Chemical Reagent Co., Ltd. Deionized water prepared using the YL-400BU ultrapure water system was used to prepare the required solutions.

The composition of 1 L of modified Starkey medium included the following: 0.5 g K_2HPO_4, 1.0 g NH_4Cl, 2.0 g $MgSO_4 \cdot 7H_2O$, 0.5 g Na_2SO_4, 0.1 g $CaCl_2 \cdot H_2O$, 1.0 g yeast extract, 4 mL sodium lactate, 0.5 g $(NH_4)_2Fe(SO_4)_2 \cdot 6H_2O$, and 0.1 g (Dong et al., 2020) ascorbic acid. The pH of the medium was adjusted to 7.0. Except for $(NH_4)_2Fe(SO_4)_2 \cdot 6H_2O$ and ascorbic acid, other chemicals were dissolved in deionized water and sterilized at $121°C$ for 30 min. Since $(NH_4)_2Fe(SO_4)_2 \cdot 6H_2O$ and ascorbic acid cannot be sterilized at high temperatures, they were filtered through a 0.22 μm filter membrane for sterilization.

The solution containing Zn(II) was prepared with $ZnSO_4 \cdot 7H_2O$, and its pH value was adjusted to 5 using 1 mol/L of HNO_3 and 1 mol/L of NaOH. The solution containing Pb(II) was prepared with $Pb(NO_3)_2$.

2.1.2 Bacterial culture

The SRB used in the experiment was cultivated from wet mud from Fuxin City, Liaoning Province (121° 41′ E, 41° 59′ N) (Dong et al., 2020). SRB in the logarithmic growth phase was used for the batch experiment. 5 g of seed sludge was added to 120 mL of sterilized modified Starkey medium. The solution was sealed with sterile liquid paraffin and a rubber stopper to create an anaerobic environment. The above solutions were cultured in a constant temperature oscillation incubator (HZ-9811K, Changzhou Langyue Instrument Manufacturing Co., Ltd.,

Jiangsu, China) at $35°C$ and 150 r/min. When the medium turned black, and the smell of rotten eggs emanated when the rubber plug was opened, it indicated that the mixed SRB had been cultured (Dong et al., 2020). The mixed SRB in the logarithmic growth phase was selected for the batch experiments.

The enriched mixed SRB solution was sent to Emer Biotechnology (Xiamen) Co., Ltd. for microbial community structure analysis. The results are shown in Figure 1. It can be seen from Figure 1 that both *Desulfovibrio* and *Desulfotomaculum* were at the genus level of SRB and can metabolize sulfate. Among them, *Desulfovibrio* belonged to *δ-proteobacteria,* and *Desulfotomaculum* belonged to *Clostridium*. The relative abundance of *Desulfovibrio_idahonensis* in *Desulfovibrio* was 31.04%, and the relative abundance of *Desulfotomaculum_sp.* in *Desulfohalotomaculum* was 15.51%. It showed that *Desulfovibrio* and *Desulfotomaculum* were the dominant bacteria in the enriched mixed SRB.

2.2 Test materials

2.2.1 Batch experiments

A series of batch tests were used to explore the removal of Zn(II) and Pb(II) by SRB. The test steps for removing Zn(II) by SRB included inoculating SRB into the solution with pH=5 and Zn(II) concentrations of 20 mg/L, 40 mg/L, 60 mg/L, 80 mg/L, and 100 mg/L. The volume ratio of SRB to the solution containing Zn(II) was 1:20. The solutions were sealed with sterile liquid paraffin and a rubber stopper. After placing the conical flasks in a constant temperature oscillation incubator (HZ-9811K type) at $35°C$ and 150 r/min, samples were taken for testing after incubation for a certain time. The sterile medium was used as the blank group. Three replicates were made for each test sample. The sample was filtered with a 0.22 μm filter membrane, and the filtered sample was tested for SO_4^{2-} and metal ion concentration. Finally, the percentage removal rate of SO_4^{2-} and Zn(II) was calculated. The test procedure for removing Pb(II) by SRB was similar to the above-mentioned process. Pb(II) was prepared with $Pb(NO_3)_2$, and the initial concentration of Pb(II) was 10 mg/L, 20 mg/L, 30 mg/L, 40 mg/L, and 50 mg/L.

2.2.2 Experiment of SRB treatment on tailing sand

Test method for SRB to treat tailing sand: tailing sand was taken from a lead-zinc mine enterprise in Huludao City, Liaoning Province, China (120°38′E, 40°56′N). 60–100 mesh size tailing sand was screened for testing. An acrylic tube with an inner diameter of 50 mm and height of 170 mm was used as the mold in the test. The bottom end of the mold was sealed with three layers of gauze. Every day, 1 cm of tailing sand was added into the #1 mold. In the #2 mold, 2 cm of tailing sand was added every 2 days. Similarly, 3 cm of tailing sand was into the #3 mold every 3 days and 4 cm into the #4 mold every 4 days. In the #5 mold, 10 cm of tailing sand was added once on the first day and then 2 cm on day 11. When the tailing sand in molds #1-5 reached a height of 12 cm, we stopped adding any more. 150 mL of SRB was injected into all five molds every day for 13 consecutive days,
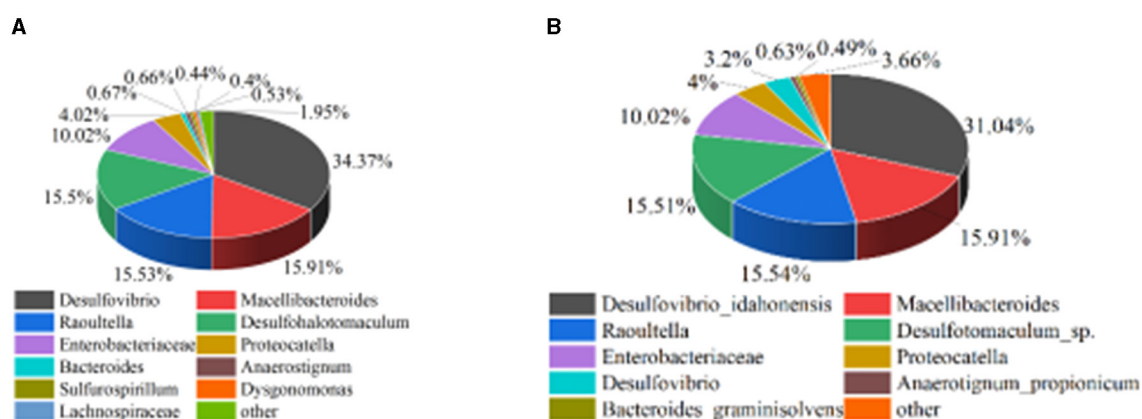
FIGURE 1
Microbial community structure analysis of mixed SRB. **(A)** Genus level. **(B)** Species level.

and three repetitions were made for each group. The schematic diagram of the experimental setup for SRB treatment of tailing sand is shown in Figure 2. Prior to drying, samples of treated #1 tailing sand (the wet tailing sand at the bottom of the cylinder) were sent to Emerson Biotech (Xiamen) Co., Ltd. for microbial community structure analysis. The tailing sand samples treated with SRB in the 15 cylinders were removed from the molds. They were forced dried in an air drying oven (model GZX-9246MBE) at 105°C. The tailing sand cylinders were then ground with sandpaper to produce specimens 5 cm in diameter and 10 cm in height. These specimens were placed on a TH-8100 universal testing machine and subjected to unconfined compressive strength (UCS) tests at a loading rate of 2 mm/min. After UCS testing, the tailing sand were ground and sieved, and the 60–100 mesh fraction of SRB-treated tailing sand was subjected to leaching tests for pollutant analysis. The tailings in molds #1-5 were respectively recorded as #1-5. They were then added to deionized water according to the solid-liquid ratio of 1 g:5 mL and subject to leaching test at 25°C and 150 r/min. Tailings without SRB treatment were used as the blank group in the test. The leachate was measured every day for its pH value and the concentration of iron, manganese, copper, zinc, lead, cadmium, chromium, and SO_4^{2-}. The tailing sand from mold #1 was selected as the experimental group, while tailing sand was used as the blank control group for SEM, EDS, and XRD testing.

2.2.3 Analytical methods

Based on the electrode method (HJ 1147-2020), a PHS-3C pH meter was used to measure pH values. The oxidation-reduction potential (ORP) was measured with a CT-8022 ORP meter. Electrical conductivity (Ec) was measured with a pen-type Ec meter. The OD_{600} value was measured with a V-1600PC visible spectrophotometer. Based on the barium chromate spectrophotometry (HJ/T 342-2007), the concentration of SO_4^{2-} was determined by a V-1600PC visible spectrophotometer. Based on the atomic absorption spectrophotometry (GB 7475-87), the concentrations of Cu, Zn, Pb, and Cd were determined by a Z-2000 flame atomic spectrophotometer. The elements of Fe and Mn were determined by flame atomic absorption spectrophotometry

(GB 11911-89). Cr was determined by flame atomic absorption spectrophotometry (HJ 757-2015).

Zeiss Sigma 500 scanning electron microscope was used to detect the tailings by SEM, and EDS scanning energy spectrometer was used to detect the chemical substances on the surface of the samples. The tailing sand samples were ground to 200 mesh, and XRD detection was conducted. The scanning step for XRD detection with Bruker D8 Advance X-ray diffractometer was 5–90°.

3 Results and discussion

3.1 Effect of SRB on zn(II) removal

From Figure 3A, we can see the change in OD_{600} when SRB metabolizes Zn(II). When the concentration of Zn(II) is 20–60 mg/L, the OD_{600} value first increases and then decreases. When the concentration of Zn(II) is 80–100 mg/L, the OD_{600} value first increases and then stabilizes. When the concentration of Zn(II) is 20 mg/L, 40 mg/L, 60 mg/L, 80 mg/L, and 100 mg/L, the OD_{600} values are 0.67, 0.92, 0.60, 0.36, and 0.31, respectively, after adding SRB for 5 days. When the concentration of Zn(II) is 20–40 mg/L, the OD_{600} value gradually increases with the increase of Zn(II) concentration, indicating that proper increase of Zn(II) concentration within this range is conducive to stimulating SRB reproduction. When the initial concentration of Zn(II) is 40 mg/L and is increased to 100 mg/L, the OD_{600} value gradually decreases with the increase of Zn(II) concentration, indicating that Zn(II) in this concentration range inhibits the growth of SRB.

It can be seen from Figures 3B–D that when the concentration of Zn(II) is 20 mg/L, 40 mg/L, 60 mg/L, 80 mg/L, and 100 mg/L, respectively, the pH, ORP, and Ec values change after SRB is added to the solution containing Zn(II). After adding SRB for 8 days, the pH values are 6.55, 6.76, 6.70, 6.17, and 5.75, respectively. The ORP values are −334 mV, −342 mV, −208 mV, −159 mV, and −133 mV, respectively. The Ec values are 2.82 mS/cm, 3.46 mS/cm, 3.48 mS/cm, 4.06 mS/cm, and 4.43 mS/cm, respectively. With the extension of time, the ORP and Ec values generally show a downward trend. When the initial concentration of Zn(II)
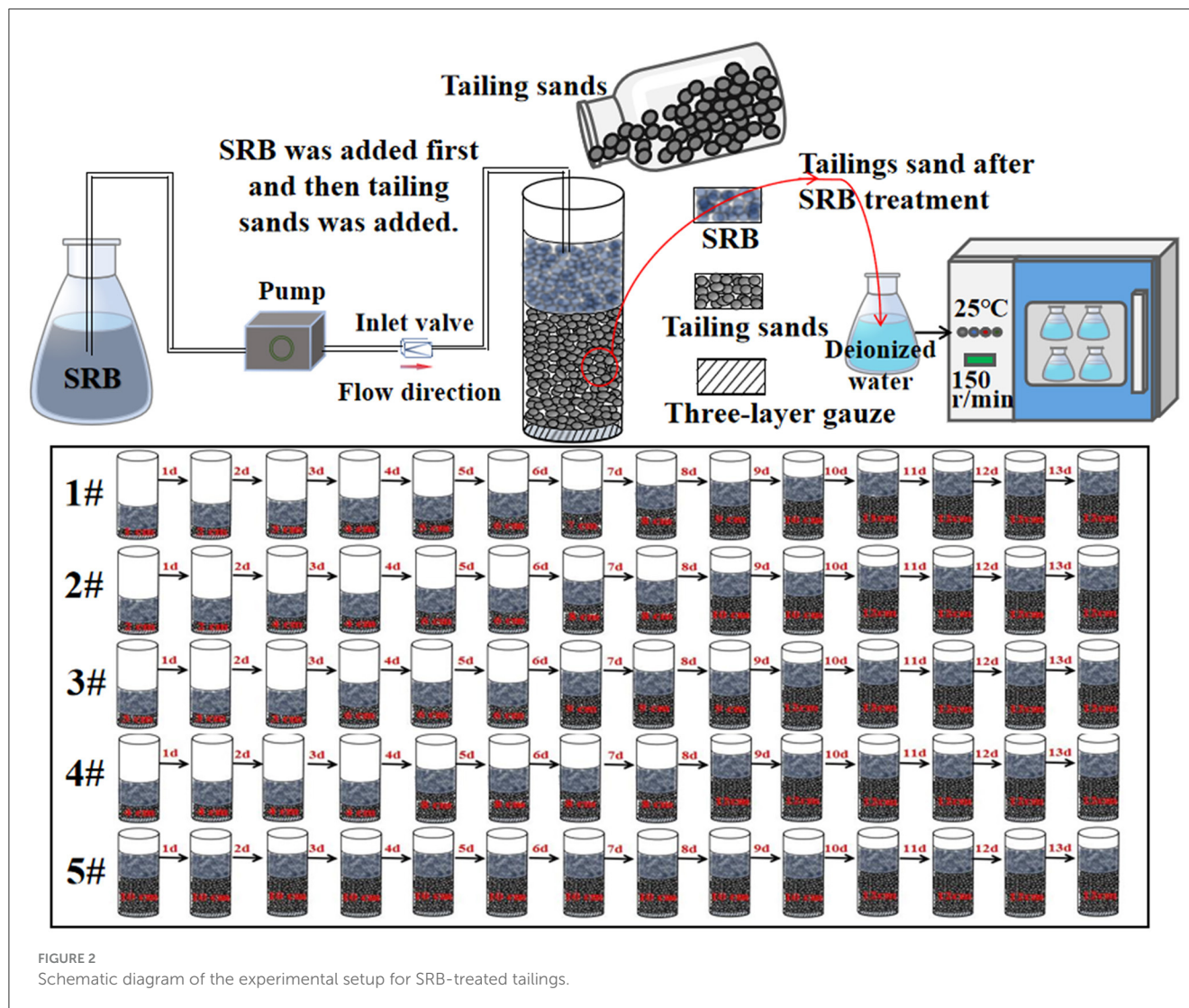
FIGURE 2
Schematic diagram of the experimental setup for SRB-treated tailings.

is 10–80 mg/L, the pH value generally shows an upward trend. When the concentration of Zn(II) is 80 mg/L and 100 mg/L, the rate of change in pH value is significantly reduced. In particular, when the concentration of Zn(II) is 100 mg/L, the pH value first increases slowly and then finally stabilizes at 5.7–5.8. When the initial concentration of Zn(II) is 80 mg/L and 100 mg/L, the rate of change in ORP and Ec values decreases significantly, indicating that a high concentration of Zn(II) inhibits SRB metabolism.

It can be seen from Figures 3E, F that when SRB metabolizes Zn(II), the removal percentage of SO_4^{2-} and Zn(II) by SRB generally increases first and then tends to be stable. At 1–6 days, SRB metabolizes vigorously and reduces more SO_4^{2-}, and the removal percentage of SO_4^{2-} and Zn(II) increases rapidly. At 6–8 days, SRB gradually enters the decay stage, and the removal percentage of SO_4^{2-} and Zn(II) tends to be stable. Properly increasing the concentration of Zn(II) in the range of 0–40 mg/L will increase the activity of SRB, while Zn(II) in the range of 40–100 mg/L will inhibit the reduction of SO_4^{2-} by SRB. When the initial concentration of Zn(II) is 20 mg/L, 40 mg/L, 60 mg/L, 80 mg/L, and 100 mg/L, the removal percentages of SO_4^{2-} and Zn(II)

are 70.71%, 75.72%, 53.21%, 38.21%, and 33.21%, and 77.61%, 76.69%, 53.89%, 38.70%, and 33.64%, respectively, after adding SRB for 8 days. It is reported that Zn(II) can precipitate in a weak acidic environment in the reactor for SRB removing heavy metals (Hedrich and Johnson, 2014). According to the change in pH values, pH value was not the main factor limiting the removal of Zn(II) by SRB. At the initial stage, Zn(II) reacts with S^{2-} produced by SRB metabolism to form ZnS, achieving the aim of removing Zn(II). With the reaction proceeding, the alkalinity produced by SRB metabolism also promoted the transformation from ZnS to $ZnCO_3$ precipitation (Dvorak et al., 1992). Jong and Parry (2003) and others used silica sand as the filler and treated light heavy metal polluted water with mixed SRB strain for 14 days, and the removal percentage of Zn(II) at 5–50 mg/L reached 97.5%. In contrast, the removal percentage of SRB for 40 mg/L Zn(II) was significantly lower than the above removal percentage, mainly because the SRB in this study was floating in solution and had no attached carrier, and the bacterial activity was easily affected by sulfide and heavy metal ions (Bijmans et al., 2009; Barbosa et al., 2014). Wang (2014) reported that when the concentration of Zn(II) was >45 mg/L, it
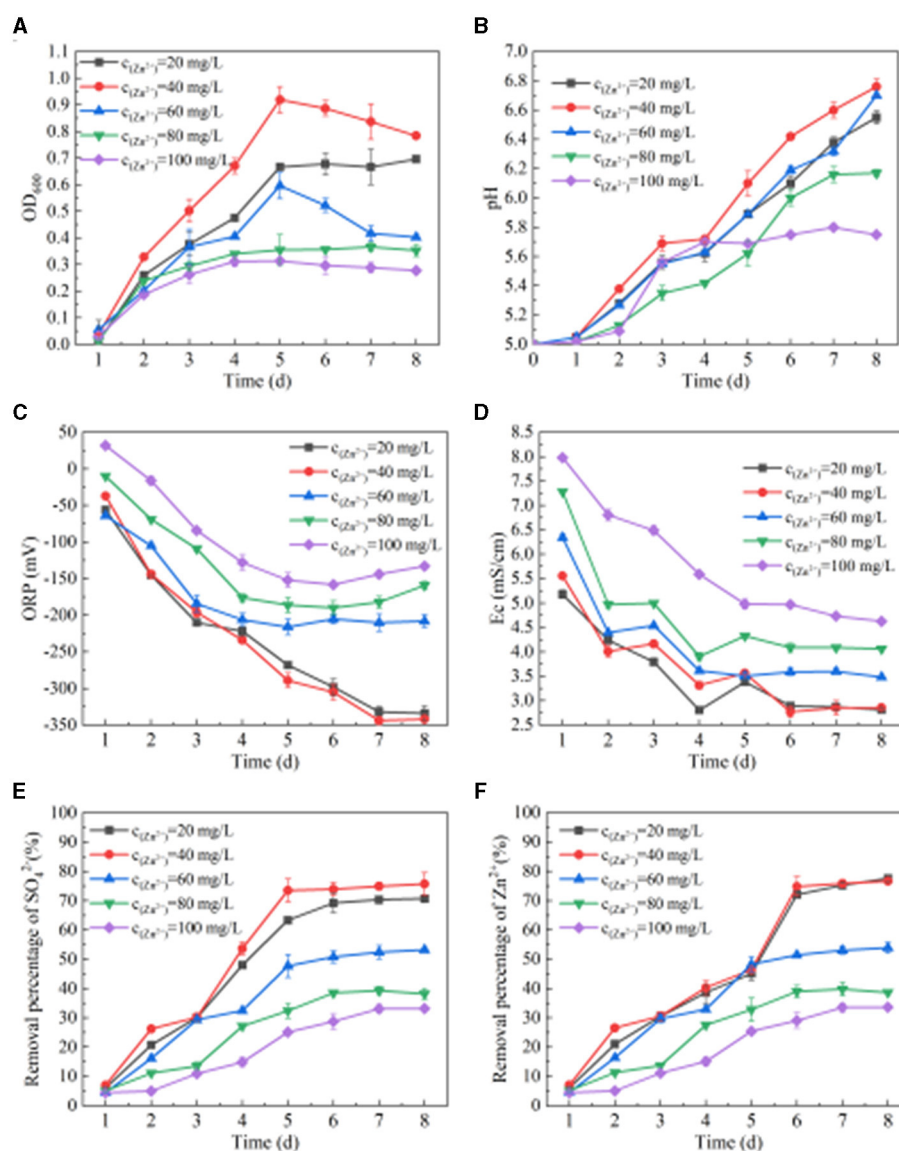
FIGURE 3
Effect of SRB on removing Zn(II). **(A)** Change of OD_{600} value. **(B)** Change of pH value. **(C)** Change of ORP value. **(D)** Change of Ec value. **(E)** SO_4^{2-} removal percentage. **(F)** Zn(II) removed by SRB.

inhibits SRB. The results of this study were similar to those of the above studies.

To sum up, SRB has a strong Zn(II) removal capacity when it is in the concentration range of 0–40 mg/L. If the initial concentration of Zn(II) is 60–100 mg/L, then the growth of SRB would be inhibited. The tolerance concentration of SRB to Zn(II) was found to be 40 mg/L. At this concentration, the maximum values of OD_{600}, pH value, SO_4^{2-} fixation rate, and Zn(II) fixation rate were 0.92, 6.76, 75.72%, and 76.69% respectively, and the minimum values of ORP and Ec were −344 mV and 2.77 mS/cm respectively.

3.2 Effect of SRB on Pb(II) removal

From Figure 4A, we can see the change in OD_{600} when SRB metabolizes Pb(II). When the concentration of Pb(II) is 10 mg/L,

the OD_{600} value shows an upward trend. When the concentration of Pb(II) is 20 mg/L, the OD_{600} value first increases and then stabilizes. When the concentration of Pb(II) is 30–50 mg/L, the OD_{600} value shows a trend of increasing first and then decreasing slightly. When the Pb(II) concentration is 10 mg/L, 20 mg/L, 30 mg/L, 40 mg/L, and 50 mg/L, respectively, the OD_{600} values are 0.92, 0.87, 0.87, 0.87, and 0.83 after SRB addition for 6 days. It can be seen from Figures 4B–D that when the concentration of Pb(II) is 10 mg/L, 20 mg/L, 30 mg/L, 40 mg/L, and 50 mg/L, respectively, the pH, ORP, and Ec values change after SRB is added to the solution containing Pb(II). After adding SRB for 8 days, the pH values are 6.78, 6.79, 6.77, 6.72, and 6.62, respectively. The ORP values are −330 mV, −356 mV, −359 mV, −347 mV, and −341 mV, respectively. The ORP values all dropped below −330 mV, while the Ec values were 2.96 mS/cm, 2.91 mS/cm, 2.71 mS/cm, 2.91 mS/cm, and 3.10 mS/cm, respectively. With the

extension of time, the pH value generally shows an upward trend, while the ORP and Ec values generally show a downward trend. With the change of initial Pb(II) concentration, the changes in pH, ORP, and Ec values are similar, indicating that a change in Pb(II) concentration has little impact on SRB metabolism at this time. It can be seen from Figures 4E, F that when SRB metabolizes Pb(II), the removal percentage of SO_4^{2-} and Pb(II) by SRB generally increases first and then tends to be stable. When the initial Pb(II) concentration is 10 mg/L, 20 mg/L, 30 mg/L, 40 mg/L, and 50 mg/L, respectively, the removal percentage of SO_4^{2-} is 77.95%, 76.04%, 76.33%, 69.81%, and 66.45% after adding SRB for 8 days. The final removal percentage of Pb(II) reached 100%, indicating that SRB has a very strong ability to remove Pb(II).

3.3 Effect and mechanism of SRB treatment of tailings

The specimens in molds #1-5 formed after treating the tailing sand with SRB are shown in Figure 5A, and the UCS results are shown in Figure 5B. It can be observed from Figures 5A, B that the tailing sand, after SRB treatment, transforms from a loose granular state to a cohesive whole. The UCS values of specimens #1-5 are 0.15 MPa, 0.08 MPa, 0.15 MPa, 0.12 MPa, and 0.12 MPa, respectively. Compared to the loose tailing sand, the UCS values are enhanced after SRB treatment, but the relatively small increase in UCS results in large errors in the three parallel tests. The UCS values of #1-5 are all <0.2 MPa, indicating that the effectiveness of SRB bio-cementation in solidifying tailing sand particles is unsatisfactory.

It can be seen from Figure 5C that the pH value of the leachate of #1-5 tailing sand is stable at 7.41–7.81, which is weakly alkaline. However, the pH value of tailing leachate is stable at 6.21–6.31, showing weak acidity. It can be seen from the comparison of pH values that the pH value of tailing leachate increases after the SRB treatment of tailings. The main reason for the increase in pH value after SRB treatment is that SRB produces HCO_3^- and other metabolites during sulfate metabolism. After the pH value is raised, when the tailing sand is stacked in the outdoor environment, the pollutants, such as heavy metals dissolved by rain and other actions, are reduced. According to Figure 5D, the Ec value of #1-5 tailing sand leachate is 354–832 μS/cm, while the Ec value of tailings leachate is 1,252–2,254 μS/cm. Compared with the Ec value of tailings leachate, the Ec value of tailings leachate after SRB treatment is significantly lower, indicating that SRB treatment can effectively inhibit the dissolution of soluble substances in tailings. Therefore, SRB treatment can effectively reduce the diffusion of pollutants in tailing sand and reduce the impact of tailing sand accumulation on the environment.

It can be seen from Figure 5E that the concentration of SO_4^{2-} in tailing sand leachate increases with the leaching time. The concentration of SO_4^{2-} is 1,528 mg/L after leaching tailings for 5 days. After #1-5 tailings leaching for 5 days, the concentrations of SO_4^{2-} are 70 mg/L, 111 mg/L, 139 mg/L, 167 mg/L, 449 mg/L. Compared with the concentration of SO_4^{2-} in the tailings leachate, the concentration of SO_4^{2-} in the leachate after SRB treatment of tailings decreased by 95.44%, 92.73%, 90.87%, 89.07%, and

70.62% at day 5, respectively, indicating that SRB can effectively fix the SO_4^{2-} in tailings. Comparing the SO_4^{2-} concentration in the leachate of #1-5 tailing sand, it can be seen that with the increase of each layer's thickness of tailing sand, the ability of SRB to fix SO_4^{2-} gradually decreases. This is because when the amount of tailings addition is small (#1-4), SRB has sufficient contact with tailings, and SRB can convert SO_4^{2-} released by dissolution of tailings into sulfide precipitation. However, when the amount of tailings addition is large (#5), the contact of SRB with the tailings at the bottom layer is limited, resulting in an increase in the overall SO_4^{2-} leaching amount.

It can be seen from Figures 5F, G that the concentration of Zn(II) and Pb(II) in tailing leaching first increases and then tends to stabilize with the prolongation of leaching time. After 5 days of leaching, the concentrations of Zn(II) and Pb(II) in the leachate are 1.15 mg/L and 0.06 mg/L, respectively. However, after 5 days of leaching of #1-5 tailings, the concentration of Pb(II) in the leachate is 0 mg/L, and the concentration of Zn(II) is 0.044 mg/L, 0.083 mg/L, 0.097 mg/L, 0.11 mg/L, 0.15 mg/L respectively. Comparing the concentration of Pb(II) in the leachate, it can be seen that after SRB treatment of tailings, Pb(II) is completely fixed, and there is no secondary release of Pb(II). Compared with tailings, the concentration of Zn(II) in the leachate of #1-5 tailings after SRB treatment decreased by 96.20%, 92.76%, 91.58%, 90.34%, and 87.05%, respectively, on day 5, indicating that SRB can effectively repair the Zn(II) and Pb(II) pollution in tailings. Compared with #1-5, the ability of SRB to fix Zn(II) gradually decreases with the increase of the thickness of each layer of tailings.

It can be seen from Figures 5H, I that the concentration of Fe(III) and Mn(II) in tailings leaching firstly increases and then tends to stabilize with the leaching time. After 5 days of leaching, the concentrations of Fe(III) and Mn(II) in the leachate of tailing sand are 0.12 mg/L and 20.61 mg/L, respectively. However, after 5 days of leaching #1-5 tailing sand, the concentration of Fe(III) in the leachate is 0 mg/L, and the concentrations of Mn(II) are 1.88 mg/L, 2.35 mg/L, 2.76 mg/L, 3.40 mg/L and 6.20 mg/L respectively. By comparing the concentration of Fe(III) in the leachate, it can be seen that after SRB treatment of tailings, Fe(III) in the tailing sand is completely immobilized, and there is no dissolution released. Compared with tailings, the concentration of Mn(II) in the leachate of #1-5 tailings after SRB treatment decreased by 90.88%, 88.60%, 86.62%, 83.50%, and 69.91%, respectively, on day 5, indicating that the use of SRB can effectively repair Fe(III) and Mn(II) pollution in tailings. With the increase of the thickness of each layer of tailings, the ability of SRB to fix Mn(II) gradually decreases, which is related to the ability of SRB to fix SO_4^{2-} in tailings. When SRB metabolizes more SO_4^{2-}, it produces more S^{2-} and CO_3^{2-}, and a large amount of S^{2-} and CO_3^{2-} precipitates the Mn(II) in the solution. The fixation effect of SRB on Mn(II) in tailing sand is significantly lower than that of Fe(III), mainly due to the high concentration of Mn(II) released from tailing sand and the high solubility product of MnS and other precipitates.

It can be seen from Figures 5J, K that the concentration of Cu(II) and total Cr leached from tailing sand increases with the leaching time. After 5 days of leaching, the concentrations of Cu(II) and total Cr in the leachate of tailing sand are 1.12 mg/L and 1.84 mg/L, respectively. However, after #1-5 tailing sand leaching for 5 days, the concentrations of Cu(II) in the leachate are 0.15
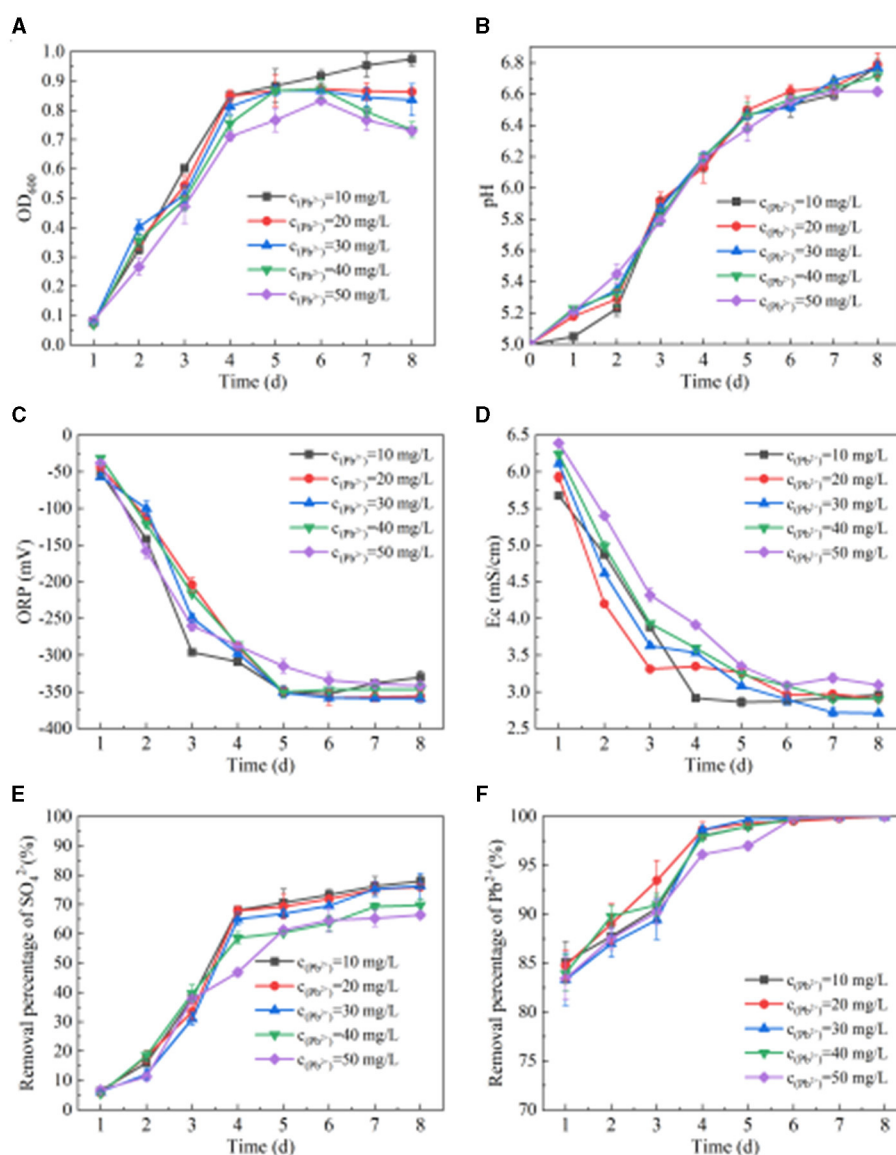
FIGURE 4
Effect of SRB on Pb(II) removal. **(A)** Change of OD_{600} value. **(B)** Change of pH value. **(C)** Change of ORP value. **(D)** Change of Ec value. **(E)** SO_4^{2-} removal percentage. **(F)** Pb(II) removed by SRB.

mg/L, 0.16 mg/L, 0.16 mg/L, 0.18 mg/L and 0.19 mg/L respectively, and the concentrations of total Cr are 0.12 mg/L, 0.14 mg/L, 0.16 mg/L, 0.16 mg/L, and 0.24 mg/L, respectively. Compared with the tailings, the concentrations of Cu(II) in the leachate of #1-5 tailings after SRB treatment decreased by 86.23%, 85.74%, 85.74%, 84.27%, and 82.81% respectively on day 5, and the total Cr concentration decreased by 93.34%, 92.22%, 91.11%, 91.11%, and 86.67% respectively, indicating that SRB can effectively immobilize Cu(II) and total Cr in tailings. According to the comparison of #1-5, the ability of SRB to immobilize Cu(II) and total Cr gradually decreases with the increase of the thickness of each layer of tailings.

To sum up, compared with the tailings, the concentration of pollutants leached from #1-5 tailings after SRB treatment is significantly lower, indicating that SRB has a good fixation effect on soluble SO_4^{2-}, Fe(III), Mn(II), Pb(II), Zn(II), Cu(II), total Cr and other pollution ions in tailings. SRB can effectively reduce the

impact of dissolved pollutants and the release of tailing sand to the environment. At the same time, when comparing the different concentrations of pollutants in the leachate of #1-5 tailing sand, the amount of tailing sand added in each layer had a great impact on the pollutants in the tailing sand immobilized by the SRB. As a whole, the ability of SRB to immobilize the pollutants in the tailings decreased with the increase in the amount of tailings added in each layer. When 1 cm of tailings (#1) was added to each layer, the immobilization percentage of SO_4^{2-}, Fe(III), Mn(II), Pb(II), Zn(II), Cu(II) and total Cr in the leachate after SRB treatment of tailings were 95.44%, 100%, 90.88%, 100%, 96.20%, 86.23%, and 93.34%, respectively.

Tailing sand from #1 was taken for SEM-EDS, XRD, and XRF detection. The results are shown in Figures 6, 7, Table 1. The community structure analysis of the mixed SRB before and after the tailings treatment is shown in Figure 8.

FIGURE 5
The UCS after SRB treatment of tailings and leaching of pollutants from tailing sand. **(A)** The specimen formed after SRB treatment of tailings sand and the UCS test diagram of the specimen. **(B)** UCS of the specimen. **(C)** Leachate pH value. **(D)** Leachate Ec value. **(E)** Leaching concentration of SO_4^{2-}. **(F)** Leaching concentration of Zn(II). **(G)** Leaching concentration of Pb(II). **(H)** Leaching concentration of Fe(III). **(I)** Leaching concentration of Mn(II). **(J)** Leaching concentration of Cu(II). **(K)** Leaching concentration of total chromium.

FIGURE 6
SEM-EDS diagram of #1 tailing sand.
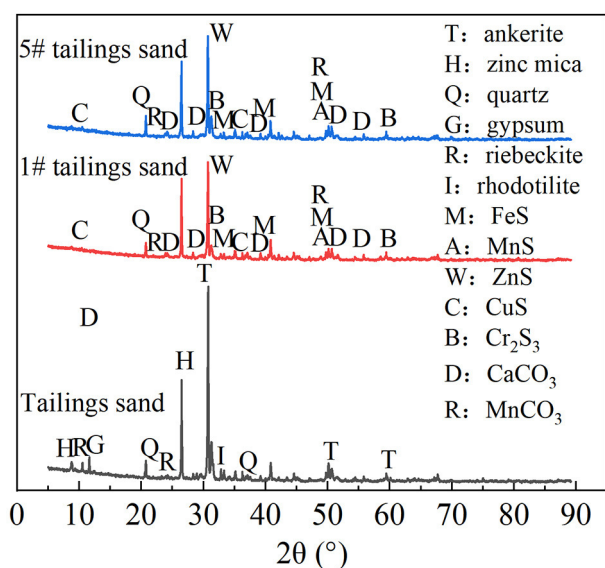
FIGURE 7
XRD diagram of tailings.

It can be seen from Figure 6 that a large number of small particles appear on the surface of #1 tailing sand particles. An EDS analysis of these small particles shows that the contents of S, Ca, Cr, Mn, Fe, Cu, Zn, Cd, and Pb in the particles are 3.35%, 18.28%, 0%, 19.31%, 35.77%, 9.77%, 4.75%, 0%, and 8.78%, respectively. It shows that after SRB treatment, the soluble ionic substances in the tailings were converted into precipitates and attached to the surface of the tailings. These precipitates formed by SRB mainly contained S, Ca, Mn, Fe, Cu, Zn, Pb, and other elements. It can be seen from Figure 7 that the tailing sand is mainly composed of quartz, ankerite, zinc-mica, sodium amphibole, gypsum, rhodochrosite, and other minerals. Among them, iron dolomite, zinc mica,

sodium amphibole, gypsum, rhodochrosite, and other minerals easily dissolve and produce pollutants such as sulfate and heavy metal ions. FeS, MnS, ZnS, CuS, Cr_2S_3, $CaCO_3$, $MnCO_3$, and other new substances appeared in #1 and #5 tailing sand. It shows that SRB can metabolize sulfate to produce S^{2-} and carbonate and other metabolites when processing tailings. These metabolites combine with heavy metal ions released from tailings to form precipitated particles, which then get attached to the surface of the tailings. It can be seen from the XRF test results in Table 1 that the main chemical components in the tailings change before and after the SRB treatment. The content of Na_2O, MgO, SO_3, Cr_2O_3, and CuO in the tailings treated by SRB is significantly reduced, which is related to the dissolution of minerals in the solidification process. In particular, the reduction of S content is related to the release of large amounts of sulfate from tailings leaching. The content of MnO, Fe_2O_3, ZnO, and PbO in #1 tailing sand formed after SRB treatment is significantly increased, which is related to the deposition of Mn, Fe, Zn, and Pb in the tailing sand after plasma dissolution and reaction with SRB's metabolic products S^{2-}, CO_3^{2-}, and other reactions to adhere to the surface of tailing sand.

To sum up, the iron dolomite, zinc mica, sodium amphibole, gypsum, and red silicon calcium manganese ore in the tailing sand are easily dissolvable and produce pollutants such as sulfate and heavy metal ions. SRB can metabolize sulfate to produce S^{2-} and carbonate and other metabolites when processing tailings. These metabolites combine with heavy metal ions released from the tailings to form FeS, MnS, ZnS, CuS, PbS, Cr_2S_3, $CaCO_3$, $MnCO_3$, and other precipitated particles, which are attached to the surface of tailings.

According to Figure 8, prior to treating the tailings, the mixed SRB community at the genus level is primarily composed of *Desulfovibrio*, *Macellibacteroides*, *Raoultella*, *Desulfohalotomaculum*, *Enterobacteriaceae*, *Proteocatella*, *Bacteroides*, *Anaerostignum*, *Sulfurospirillum*, *Dysgonomonas*, *Lachnospiraceae*, and *Enterobacter*, with relative abundances of

TABLE 1 Main chemical composition of tailings before and after solidification (%).

Component	Na$_2$O	MgO	Al$_2$O$_3$	SiO$_2$	SO$_3$	K$_2$O	CaO	Cr$_2$O$_3$	MnO	Fe$_2$O$_3$	CuO	ZnO	PbO
Tailing sands	0.13	10.03	2.92	24.48	7.25	0.77	18.43	0.12	19.23	15.22	0.23	0.40	0.38
1# tailing sands	0.01	9.44	3.07	23.87	6.50	0.76	16.69	0.02	19.45	17.18	0.06	0.41	0.39

FIGURE 8
Analysis of microbial community structure of mixed SRB (before and after tailings treatment) at the genus level.
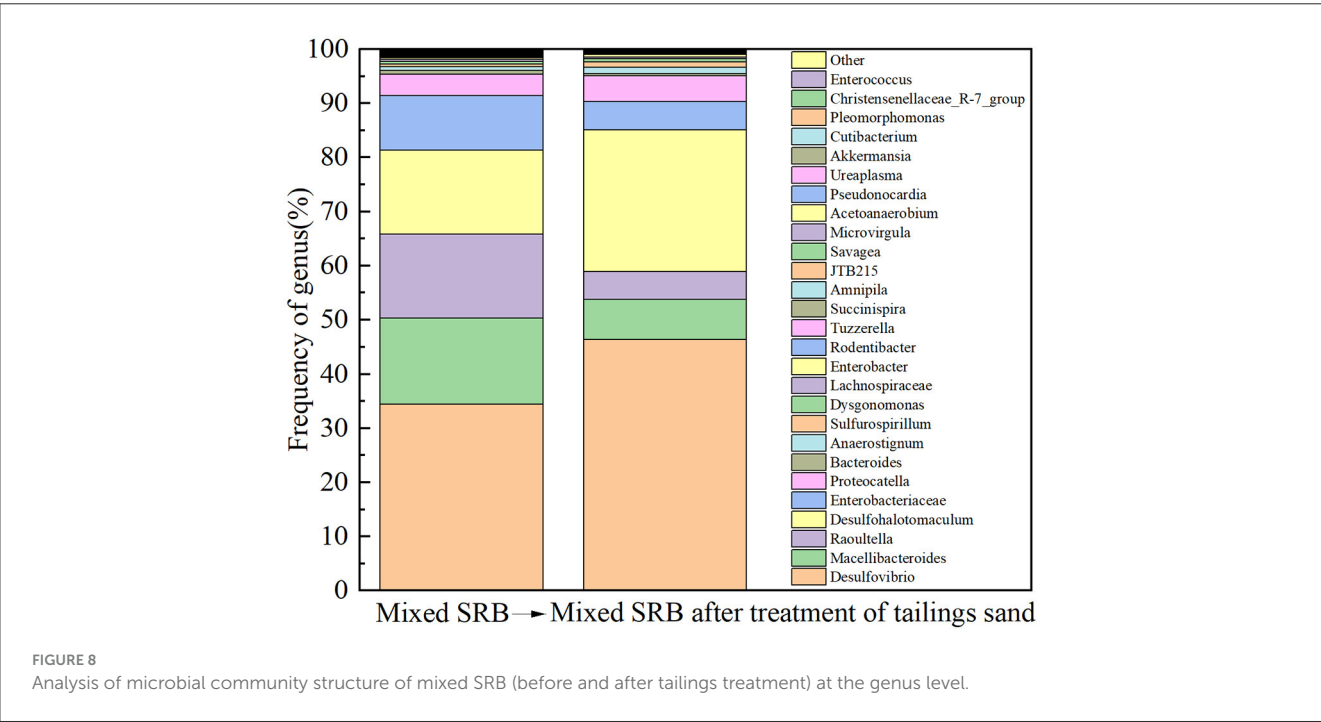
34.38%, 15.92%, 15.54%, 15.51%, 10.02%, 4.02%, 0.67%, 0.66%, 0.53%, 0.44%, 0.4%, and 0.3%, respectively. After treating the tailings, the mixed SRB community at the genus level is primarily composed of *Desulfovibrio*, *Macellibacteroides*, *Raoultella*, *Desulfohalotomaculum*, *Enterobacteriaceae*, *Proteocatella*, *Bacteroides*, *Anaerostignum*, and *Sulfurospirillum*, with relative abundances of 46.42%, 7.34%, 5.11%, 26.18%, 5.31%, 4.72%, 0.42%, 1.15%, and 0.98%, respectively. Comparing the relative abundances of the organisms before and after treating the tailings, it can be observed that *Desulfovibrio*, *Desulfohalotomaculum*, *Proteocatella*, *Anaerostignum*, *Sulfurospirillum*, *Enterobacter*, and *Dysgonomonas* increased by 12.04%, 10.67%, 0.70%, 0.49%, 0.45%, 0.15%, and 0.13%, respectively. *Desulfovibrio* and *Desulfohalotomaculum*, belonging to SRB, and *Sulfurospirillum*, associated with sulfur metabolism, are the primary bacteria involved in the sulfate reduction of lead-zinc tailings. The increase in their relative abundances indicates that the high concentration of sulfate released from lead-zinc tailings promotes the growth and proliferation of sulfur-metabolizing bacteria. Additionally, this suggests that the concentration of heavy metals released from the tailings is not sufficient to suppress the growth of sulfur-metabolizing bacteria. Considering the metabolic products after treating the tailings, it can be inferred that FeS, MnS, ZnS, CuS, PbS, Cr$_2$S$_3$, CaCO$_3$, and MnCO$_3$ formed after the mixed SRB treatment of tailings are primarily metabolized by *Desulfovibrio* and *Desulfohalotomaculum*.

3.4 Discussion

In this study, SRB had a strong ability to remove Zn(II) and Pb(II) in the solution state. The maximum value of pH, removal percentage of SO$_4^{2-}$, and percentage removal of Zn(II) were 6.76, 75.72, and 76.69%, respectively, and the minimum value of ORP was −344 mV when Zn(II) solution of 40 mg/L was treated with SRB. The pH value and Pb(II) removal percent were 6.62 and 100%, and the minimum value of ORP was −341 mV. It has been reported that the ORP value is an important indicator in SRB reaction activity; when the ORP value was below −100 mV, it was favorable to maintain the SRB activity, and when the ORP value was higher than −100 mV, it would inhibit SRB activity (Xu and Chen, 2020). The ORP values of SRB in Zn(II) and Pb(II) solutions were much lower than −100 mV, indicating that SRB could maintain higher activity in Zn(II) and Pb(II) solutions.

The main mechanism of Zn(II) and Pb(II) removal by SRB is that SRB metabolizes organics and SO$_4^{2-}$ to produce S^{2-} and CO$_3^{2-}$. Meanwhile, S^{2-} together with CO$_3^{2-}$ reacts with the Zn(II) and Pb(II) in the solution to form precipitation to remove Zn(II) and Pb(II). Besides, it produces large amounts of extracellular polymeric substances (EPS) when SRB activity is high. It has been reported that EPS had the ability to adsorb heavy metal cations, which subsequently combined with S^{2-}, and it was a key step in the microbial synthesis of metal sulfide crystals (Su et al., 2022). It has also been reported that a concentration of 45 mg/L of Zn(II) in AMD was a high concentration in wastewater (Gandy et al., 2023).

As for the biological treatment of high concentrations of Zn(II)-containing AMD, Gandy et al. (2023) found that the addition of a liquid carbon source (propionic acid) could help to increase the SRB activity, resulting in the removal percent of Zn(II) reaching 99% after treating for 193 days. The removal of Zn(II) by SRB in this study (76.69%) was relatively low compared to the study above, but the removal period in this study was only 8 days, which was much shorter than the study period above.

The long cycle of SRB growth consumed large amounts of organics, increasing the cost of SRB treating Zn(II). Nielsen et al. (2018) established a bioreactor with waste rock and SRB using polyethylene drums on the floor of the Silver King mine. The initial concentrations of Zn(II) and Cd(II) flowing into the reactor were 640.4 μg/L and 10.5 μg/L, with a hydraulic retention time (HRT) of 2 weeks, and the removal rates of Zn(II) and Cd(II) reached 80.6% and 90.5% after treating. Compared with the studies above, the removal rate of Zn(II) by SRB in this study was relatively high, and the removal period was relatively short, which greatly saved the cost of SRB treating heavy metal-containing wastewater.

Miao et al. (2018) evaluated the ability of a natural strain of SRB called *Desulfuromonas alkenivorans S-7* to remove acidic water (pH=6.0) containing different Pb(II) concentrations (1.0–11.6 mg/L) and showed that strain *S-7* could remove 90.0% of Pb(II) after 7 days of cultivation. Gopi Kiran et al. (2018) used sodium alginate to immobilize SRB for batch heavy metal removal experiments and found that insoluble metal sulfides were formed outside the surface of sodium alginate immobilized SRB particles, and the removal percentage in 25 mg/L Zn(II) and 25 mg/L Pb(II) was higher than 95%. Compared to the studies above, the removal percentage of Pb(II) by SRB in this study was relatively high at 100% for 50 mg/L Pb(II).

Zhang et al. (2019) protected SRB by wrapping it with a complex of polyvinyl alcohol and sodium alginate and used this SRB to treat the solution with Pb(II). They found that the adsorption of Pb(II) increased with the addition of initial Pb(II) concentration. When the 50 mg/L of Pb(II) in the reaction system was at 35°C and pH=8.0, the removal efficiency reached the highest, with a maximum adsorption capacity of 707.3 mg/g. Their study showed that the complex containing polyvinyl alcohol and sodium alginate could protect SRB from slightly acidic and heavy metal ions. On the other hand, in this study, the SRB without any protection from other materials could still reach a similar removal capacity to 50 mg/L Pb(II). It indicated that the SRB enriched from this study had a strong tolerance to Pb(II). Above all, the SRB used in this study was more tolerant to Zn(II) and Pb(II) and could reach relatively high efficiency in removing Zn(II) and Pb(II) in a short time cycle. It was more suitable for removing tailing sand loaded with heavy metals.

Achal et al. (2013) found that the compressive strength of the chrome slag brick after being immobilized with *Bacillus sp. CS*8 was approximately at 0.36 Mpa, which prevented Cr(VI) contamination in the surrounding environment. Hataf and Baharifard (2019) treated landfill soil with *Bacillus sphericalus*. The results showed that *Bacillus sphaericus* could successfully reduce the permeability of landfill soils and form an effective protective barrier. However, solid waste such as chromium slag and landfill soil can release large amounts of contaminant ions. The studies above analyzed the stabilization effect of solid waste by bacteria only from the perspective of mechanical analysis, such as compressive strength and permeability, and ignored the diffusion of polluting ions. In this study, the fixed percentage of SO_4^{2-}, Fe(III), Mn(II), Pb(II), Zn(II), Cu(II), and total Cr in tailing sand leachate by SRB reached 95.44%, 100%, 90.88%, 100%, 96.20%, 86.23%, and 93.34%, respectively.

Following SRB treatment of tailings, although the tailings could solidify from loose granular particles into a cohesive mass, the UCS of the specimens remained below 0.2 MPa. Research has indicated that after using *Bacillus subtilis* to cement and solidify artificially simulated lead-contaminated soil, the UCS of the soil increased from 0.065 MPa to 0.525–0.539 MPa (Hadiz et al., 2022). Achal et al. (2013) utilized *Bacillus sp*. CS8 to cement and solidify chromium-contaminated soil, resulting in a UCS increase of 0.36 MPa. Some scholars have also used *T. tumescens* to cement and solidify sand soil, resulting in a UCS of 0.67 MPa (Meng et al., 2016). Preliminary experimental studies have shown that a mixed culture of *Sporosarcina pasteurii* can cement and solidify lead-zinc tailings, with UCS reaching 0.9 MPa after treatment (Dong, 2023a,b). Compared with these, in this study, the UCS after SRB treatment of tailings was significantly lower than that achieved with Bacillus. This indicates that although SRB can undergo microbially induced calcium carbonate precipitation (MICP), the cementation and solidification effect of MICP is not as ideal as that of Bacillus.

The mineralized products formed after SRB treatment of tailings are primarily sulfides, with a small amount of CaCO₃. The main factors determining the effectiveness of MICP cementation and solidification are the production and adhesive properties of biogenic CaCO₃. The CaCO₃ formed after SRB treatment of tailing sand exhibits a binding effect capable of cementing the tailing sand. However, due to the limited amount of CaCO₃ generated, the lead-zinc tailing sand treated with SRB could only transition from a loose granular state to a solidified mass, resulting in relatively low UCS values. Compared to untreated lead-zinc tailings, the heavy metal ions in the tailings were effectively immobilized after the SRB treatment. Additionally, although the amount of biogenic CaCO₃ produced through MICP by SRB was relatively low, it still contributed to the cementation and solidification of some tailings particles. This helps alleviate the potential for landslides and debris flows during tailings deposition.

Zhu et al. (2016) found that the urease-producing bacteria *Bacillus cereus NS*4 had the ability to reduce the soluble changeable part of Ni to 38 mg/kg. Govarthanan et al. (2013) used *Bacillus sp*. *KK*1 to stabilize the Pb²⁺ in soil and found that the content of PbCO₃ in the soil after treatment increased by 38%. Zhao et al. (2017) used carbonate biomineralizing microorganisms *GZ-22* enriched from the mining soils. The bacteria had the strongest ability to remove Cd of 10 mg/L at 48 h, in the way of turning Cd into CdCO₃, and the removal percentage was 60.72%. The studies above showed that the bacteria had a good fixation effect on Ni and Pb in the soil or solution. However, most studies focused on a particular heavy metal ion. In this study, the tailing sand was the sample soil enriched from the mine site, which contained a more complicated composition of heavy metals. In the study of solidifying soil, many kinds of heavy metal pollutants may exist in the soil at the same site. Therefore, many researchers have attempted to precipitate mixtures of heavy metal ions using multiple types of bacteria or in the composite method of combining bacteria with other materials (Chen and Tian, 2021). Hu et al.

(2021) found that with a continuous biofiltration treatment using biochar as the medium, nearly 100% removal percentage of As, Cd, Mn, and Ni can be obtained in the conditions of co-treatment of shale oil and gas-produced water (PW) with synthetic domestic wastewater (SDW) (PW:SDW=1:1) and urea concentration of 4 g/L. Compared to the combination of microorganisms, biochar, PW, and SDW in the above studies, this study achieved higher fixation efficiency for all heavy metals using only the combination of microorganisms and tailings, which was simpler and less costly.

In this study, SRB not only immobilized heavy metal ions in the tailing sand but also raised the pH of the tailing sand leachate from 6.21–6.31 to 7.41–7.81. It indicated that the metabolites of SRB could raise the pH and that a higher pH value was conducive to the immobilization of metal ions. A few studies also obtained the same conclusions (Nguyen et al., 2020; Nogueira et al., 2021; Chai et al., 2023). Nguyen et al. (2020) isolated an acid-tolerant sulfate-reducing bacterium, strain S4, which could reduce sulfate in a low pH environment and was resistant to very high concentrations of heavy metals (Fe of 3,000 mg/L, Zn of 100 mg/L, and Cu of 100 mg/L). Chai et al. (2023) found that SRB had the ability to raise the pH value when cultivating SRB using organic waste. The removal percentage of sulfate in the solution could reach 95.6%, and the highest removal percentage of Al and Mn were 99.0% and 96%, respectively. Nogueira et al. (2021) treated artificial synthesis of AMD using SRB as the fillers of underflow structured bed bioreactors and found that SRB could increase the pH from moderately acidic to 6.7–7.5; the removal percentage of sulfate was 55%-91%, and the removal percentage of Fe, Zn, Cu, and Mn were 70%, 80%, 73%, and 60%, respectively. Most of these studies aimed to raise the pH when removing sulfate and heavy metal ions from the solution using SRB. Compared to the studies above, this study showed that SRB could raise the pH value not only in solutions but also in solid soil leachate and effectively reduce the release of contaminants from tailing soils.

Liu et al. (2021) found that soluble Pb, Zn, and Cd were reduced by 33.3–85.9%, 21.4–66.0%, and 13.6–29.9%, respectively, with Pb, Zn, and Cd mostly forming carbonate precipitates after bioremediation while using the urease-producing bacteria *sporosarcina pasteurii* to remedy the contaminated soils polluted by Pb, Zn, and Cd; the pH value of the soil was 7.41. Chen and Achal (2019) proved that the ureolytic bacteria in the soil mainly turned Cu(II) into $CuCO_3$ to immobilize Cu(II), and the soluble, exchangeable part of Cu decreased from 45.54 mg/kg to 1.55 mg/kg, with an initial soil pH value of 7.11. Peng et al. (2020) isolated a type of ureolytic bacteria *Enterobacter sp.* which had a maximum immobilization percentage of 56.10% for Cd(II) in the soil, and the pH of the leachate was at ∼8. The mechanism of removing Cd was mainly through the absorption of Cd(II) by biominerals, including calcite and sphalerite. Similarly, Xu et al. (2019) found that *S. pasteurii* (CGMCC1.3687) could effectively reduce the leachability of heavy metals in municipal solid waste incineration fly ash with a pH value of 10.8. The leaching concentrations of Zn, Cu, Pb, Cr, and Cd after treatment were 0.048, 1.16, 0.005, 0.065, and 0.001 mg/L, respectively. And the unconfined compressive strength could reach approximately 0.16 MPa. Above all, bacteria, such as *sporosarcina pasteurii*, had a good immobilization effect on heavy metals in soil; the mechanism of immobilizing heavy metals by these bacteria is mostly related to the formation of carbonate

precipitates. Meanwhile, the pH background of the soil in the studies above mostly appeared as neutral and alkaline (ranging between 7.11 and 10.8). In this study, the pH of the tailing sand leachate was 6.21–6.31, which was weakly acidic. Compared to the alkaline environment, weakly acidic environments could intensify the release of heavy metal contaminants from tailing sand and were less conducive to the remediation of heavy metals by bacteria.

High concentrations of metal cations may even have toxic or inhibitory effects on bacterial communities (Ayangbenro et al., 2018). Meanwhile, the pH value may have an effect on the form of carbonate precipitation. Usually, at the same pH value conditions, from the solubility product, we know that sulfide precipitation of heavy metals was more stable than hydroxide precipitation or carbonate precipitation (Kumar et al., 2021; Su et al., 2022). Therefore, compared to carbonate-producing bacteria such as *sporosarcina pasteurii* in this study, the heavy metal ions in the tailing sand immobilized by SRB were more stable.

Yan et al. (2020) found that mixed SRB, including *Desulfovibrio*, *Desulfomicrobium*, and *Desulfococcus*, were effective in removing sulfate from AMD. Hái and Hǎng (2016) enriched mixed SRB from wastewater generated in aquaculture processing. This mixed SRB mainly consisted of *Desulfovibrio*, *Desulfomicrobium*, and *Desulfobulbus spp*. These mixed SRB exhibited a fixation rate of 85–88% for Fe^{2+} in AMD (with an initial Fe^{2+} concentration of 200 mg/L) (Hái and Hǎng, 2016). Walters et al. (2013) conducted six field-scale AMD remediation column experiments at the Tab-Simco site. The results indicated that SRBs such as *Desulfotomaculum* and *Desulfococcus* in the microbial community exhibited strong remediation capabilities for sulfate and heavy metals in AMD. Dev et al. (2021) reported that SRB, including *Desulfosporosinus* and *Desulfotomaculum*, play a significant role in the effective biological treatment of AMD in cold regions.

In summary, *Desulfovibrio*, *Desulfomicrobium*, *Desulfococcus*, *Desulfobulbus spp.*, *Desulfotomaculum*, *Desulfosporosinus*, and similar SRB species all belong to sulfate-reducing bacteria and are capable of driving sulfate reduction, thus facilitating the bioremediation of AMD. Considering the findings from the aforementioned studies and the biodiversity of mixed SRB in this study, it is evident that *Desulfovibrio* and *Desulfohalotomaculum* play a predominant role in treating tailings. These bacteria metabolize the sulfate and heavy metals released from the tailings, forming precipitate products such as FeS, MnS, ZnS, CuS, PbS, Cr_2S_3, $CaCO_3$, and $MnCO_3$. This process mitigates pollution by tailings while cementing and solidifying tailings particles, thereby improving the mechanical properties of the tailings. Above all, this study demonstrated that SRB is more suitable for environmental remediation of tailing sand in the mining environment, and it is a technique for *in situ* remediation of multiple contaminants in tailing sand.

4 Conclusion

To address heavy metal pollution in tailings and AMD, soil-enriched SRB was employed using microbial treatment technology. By analyzing the treatment effects of SRB on simulated solutions containing different concentrations of Pb(II) and Zn(II), the tolerance of SRB to Pb(II) and Zn(II) concentrations was

investigated. The pollutants released from lead-zinc tailings are more complex than those from AMD. By analyzing the fixation effect of SRB on heavy metal pollutants in tailings, the generation of heavy metal-containing wastewater can be reduced from the source, thereby lowering the cost of environmental management in mining areas. Combined with UCS, the cementing strength of SRB on tailings particles was analyzed from a mechanical perspective. Although the UCS strength is relatively low, in the future, the strength of SRB cemented tailings can be enhanced from the perspectives of fiber reinforcement and reinforced solidification, providing technical references for bio-cementation reinforcement technology of tailings particles in mining areas and mitigating the impact of geological disasters such as tailing slides and debris flows. Additionally, combining SEM-EDS, XRF, and XRD with other detection methods revealed the mechanism of SRB fixation of pollutants in the tailings. This method provides technical references for the effective and sustainable remediation of AMD and tailings by SRB, promoting the implementation of green mining construction.

(1) SRB had a strong removal capacity for Zn(II) in the concentration range of 0-40 mg/L. If the initial concentration of Zn(II) is increased to 60-100 mg/L, then the growth of SRB would be inhibited. The tolerance concentration of SRB to Zn(II) is 40 mg/L. At this concentration, the maximum values of OD_{600}, pH value, and immobilization percentages of SO_4^{2-} and Zn(II) were 0.92, 6.76, 75.72%, and 76.69% respectively, and the minimum values of ORP and Ec were -344 mV and 2.77 mS/cm respectively.

(2) SRB had a very strong ability to remove Pb(II). When the initial Pb(II) concentration was 10 mg/L, 20 mg/L, 30 mg/L, 40 mg/L, and 50 mg/L, respectively, the removal percentages of SO_4^{2-} were 77.95%, 76.04%, 76.33%, 69.81%, and 66.45% after adding SRB for 8 days. The final removal percentage of Pb(II) reached 100%.

(3) SRB treatment can effectively fix SO_4^{2-}, Fe(III), Mn(II), Pb(II), Zn(II), Cu(II), total Cr, and other pollutants leached from tailings, and reduce environmental pollution of tailings to water and soil around the mining area. At the same time, with an increase in the amount of tailings added to each layer, the ability of SRB to treat the pollutants in the tailings decreased. After SRB treatment, although the tailings can be solidified from loose granular particles into a cohesive mass, the UCS of the specimens remains below 0.2 MPa. The enhancement of strength in SRB-treated tailings awaits further research in directions such as fiber reinforcement and reinforced curing. When 1 cm of tailing sand was added to each layer (#1 tailing sand), SRB had the best effect on treating tailing sand. The removal percentages of SO_4^{2-}, Fe(III), Mn(II), Pb(II), Zn(II), Cu(II), and total Cr in the leachate of #1 tailing sand after SRB treatment were 95.44%, 100%, 90.88%, 100%, 96.20%, 86.23%, and 93.34%, respectively.

(4) The iron dolomite, zinc mica, sodium amphibole, gypsum, and red silicon calcium manganese ore in the tailing sand were easy to dissolve and produce pollutants such as sulfate and heavy metal ions. *Desulfovibrio* and *Desulfohalotomaculum* play a predominant role in treating tailings within the mixed SRB. Mixed

SRB can metabolize sulfate to produce S^{2-} and carbonate and other metabolites when metabolizing tailings. These metabolites combine with heavy metal ions released from tailings to form FeS, MnS, ZnS, CuS, PbS, Cr_2S_3, $CaCO_3$, $MnCO_3$, and other precipitated particles, which were attached to the surface of tailings.

Data availability statement

The original contributions presented in the study are included in the article/supplementary material, further inquiries can be directed to the corresponding author.

Author contributions

YD: Writing – original draft. ZG: Writing – review & editing. JD: Writing – review & editing. DW: Writing – review & editing. ZY: Writing – review & editing. XG: Writing – review & editing. XZ: Writing – review & editing.

Funding

Conflict of interest

The authors declare that the research was conducted in the absence of any commercial or financial relationships that could be construed as a potential conflict of interest.

Publisher's note

References

Achal, V., Pan, X., Lee, D. J., Kumari, D., and Zhang, D. (2013). Remediation of Cr(VI) from chromium slag by biocementation. *Chemosphere* 93, 1352–1358. doi: 10.1016/j.chemosphere.2013.08.008

Alexandrino, M., Macias, F., Costa, R., Gomes, N. C., Canario, A. V., and Costa, M. C. (2011). A bacterial consortium isolated from an Icelandic fumarole displays exceptionally high levels of sulfate reduction and metals resistance. *J. Hazard. Mater.* 187, 362–370. doi: 10.1016/j.jhazmat.2011.01.035

Ayangbenro, A. S., Olanrewaju, O. S., and Babalola, O. O. (2018). Sulfate-reducing bacteria as an effective tool for sustainable acid mine bioremediation. *Front. Microbiol.* 9, 1986. doi: 10.3389/fmicb.2018.01986

Barbosa, L. P., Costa, P. F., Bertolino, S. M., Silva, J. C., Guerra-Sa, R., Leao, V. A., et al. (2014). Nickel, manganese and copper removal by a mixed consortium of sulfate reducing bacteria at a high COD/sulfate ratio. *World J. Microbiol. Biotechnol.* 30, 2171–2180. doi: 10.1007/s11274-013-1592-x

Bijmans, M. F. M., Dopson, M., Peeters, T., Lens, P., and Buisman, C. (2009). Sulfate reduction at pH 5 in a high-rate membrane bioreactor: reactor performance and microbial community analyses. *J. Microbiol. Biotechnol.* 19, 7.

Chai, G., Wang, D., Zhang, Y., Wang, H., Li, J., Jing, X., et al. (2023). Effects of organic substrates on sulfate-reducing microcosms treating acid mine drainage: performance dynamics and microbial community comparison. *J. Environ. Manage.* 330, 117148. doi: 10.1016/j.jenvman.2022.117148

Chen, J., and Tian, Y. (2021). Hexavalent chromium reducing bacteria: mechanism of reduction and characteristics. *Environ. Sci. Pollut. Res. Int.* 28, 20981–20997. doi: 10.1007/s11356-021-13325-7

Chen, X., and Achal, V. (2019). Biostimulation of carbonate precipitation process in soil for copper immobilization. *J. Hazard. Mater.* 368, 705–713. doi: 10.1016/j.jhazmat.2019.01.108

Dev, S., Galey, M., Chun, C. L., Novotny, C., Ghosh, T., and Aggarwal, S. (2021). Enrichment of psychrophilic and acidophilic sulfate-reducing bacterial consortia-a solution toward acid mine drainage treatment in cold regions. *Environ. Sci.: Proc. Impacts* 23, 2007–2020. doi: 10.1039/D1EM00256B

Dong, Y., Di, J., Yang, Z., Zhang, Y., Wang, X., Guo, X., et al. (2020). Study on the effectiveness of sulfate-reducing bacteria combined with coal gangue in repairing acid mine drainage containing Fe and Mn. *Energies* 13, 995. doi: 10.3390/en13040995

Dong, Y., Gao, Z., Di, J., Wang, D., Yang, Z., Wang, Y., et al. (2023a), Experimental study on solidification and remediation of lead–zinc tailings based on microbially induced calcium carbonate precipitation (MICP). *Construct. Build. Mater.* 369, 130611. doi: 10.1016/j.conbuildmat.2023.130611

Dong, Y., Gao, Z., Wang, D., Di, J., Guo, X., Yang, Z., et al. (2023b), Optimization of growth conditions and biological cementation effect of Sporosarcina pasteurii. *Construct. Build. Mater.* 395, 132288. doi: 10.1016/j.conbuildmat.2023.132288

Dvorak, D. H., Hedin, R. S., Edenborn, H. M., and Mclntiret, P. E. (1992) Treatment of metal-contaminated water using bacterial sulfate reduction: results from pilot-scale reactors. *Biotech. Bioeng.* 40, 609–616. doi: 10.1002/bit.260400508

Fang, L., Ju, W., Yang, C., Jin, X., Liu, D., Li, M., et al. (2020). Exogenous application of signaling molecules to enhance the resistance of legume-rhizobium symbiosis in Pb/Cd-contaminated soils. *Environ. Pollut* 265, 114744. doi: 10.1016/j.envpol.2020.114744

Gandy, C. J., Gray, N. D., Mejeha, O. K., Sherry, A., and Jarvis, A. P. (2023). Use of propionic acid additions to enhance zinc removal from mine drainage in short residence time, flow-through sulfate-reducing bioreactors. *J. Environ. Manage.* 327, 116862. doi: 10.1016/j.jenvman.2022.116862

Gopi Kiran, M., Pakshirajan, K., and Das, G. (2018). Heavy metal removal from aqueous solution using sodium alginate immobilized sulfate reducing bacteria: mechanism and process optimization. *J. Environ. Manage.* 218, 486–496. doi: 10.1016/j.jenvman.2018.03.020

Govarthanan, M., Lee, K. J., Cho, M., Kim, J. S., Kamala-Kannan, S., and Oh, B. T. (2013). Significance of autochthonous Bacillus sp. KK1 on biomineralization of lead in mine tailings. *Chemosphere* 90, 2267–2272. doi: 10.1016/j.chemosphere.2012.10.038

Gu, S., Fu, B., and Ahn, J. W. (2020). Simultaneous removal of residual sulfate and heavy metals from spent electrolyte of lead-acid battery after precipitation and carbonation. *Sustainability* 12, 1263. doi: 10.3390/su12031263

Hái, N. T., and Hǎng, D. T. (2016). Elimination of iron from acidic mine drainage (AMD) in the co-treatment with poultry wastewater through a sulfate-reducing bioreactor. *Viet. J. Biotechnol.* 14, 369–375. doi: 10.15625/1811-4989/14/2/9363

Hadiz., S., and Saeed, K A. (2022). Effect of microbial-induced calcite precipitation (MICP) on the strength of soil contaminated with lead nitrate. *J. Mechan. Behav. Mater.* 31, 143–149. doi: 10.1515/jmbm-2022-0016

Hataf, N., and Baharifard, A. (2019). Reducing soil permeability using microbial induced carbonate precipitation (MICP) method: a case study of shiraz landfill soil. *Geomicrobiol. J.* 37, 147–158. doi: 10.1080/01490451.2019.1678703

Hedrich, S., and Johnson, D. B. (2014). Remediation and selective recovery of metals from acidic mine waters using novel modular bioreactors. *Environ. Sci. Technol.* 48, 12206–12212. doi: 10.1021/es5030367

Hu, L., Wang, H., Xu, P., and Zhang, Y. (2021). Biomineralization of hypersaline produced water using microbially induced calcite precipitation. *Water Res.* 190, 116753. doi: 10.1016/j.watres.2020.116753

Hwang, S. K., and Jho, E. H. (2018). Heavy metal and sulfate removal from sulfate-rich synthetic mine drainages using sulfate reducing bacteria. *Sci. Total Environ.* 635, 1308–1316. doi: 10.1016/j.scitotenv.2018.04.231

Jong, T., and Parry, D. L. (2003). Removal of sulfate and heavy metals by sulfate reducing bacteria in short-term bench scale upflow anaerobic packed bed reactor runs. *Water Res.* 37, 3379–3389. doi: 10.1016/S0043-1354(03)00165-9

Kim, H. S., Seo, B. H., Kuppusamy, S., Lee, Y. B., Lee, J. H., Yang, J. E., et al. (2018). A DOC coagulant, gypsum treatment can simultaneously reduce As, Cd and Pb uptake by medicinal plants grown in contaminated soil. *Ecotoxicol. Environ. Saf.* 148, 615–619. doi: 10.1016/j.ecoenv.2017.10.067

Kumar, M., Nandi, M., and Pakshirajan, K. (2021). Recent advances in heavy metal recovery from wastewater by biogenic sulfide precipitation. *J. Environ. Manage.* 278, 111555. doi: 10.1016/j.jenvman.2020.111555

Kumar, M., and Pakshirajan, K. (2020). Novel insights into mechanism of biometal recovery from wastewater by sulfate reduction and its application in pollutant removal. *Environm. Technol. Innovat.* 17, 100542. doi: 10.1016/j.eti.2019.100542

Kumar, M., and Pakshirajan, K. (2021). Continuous removal and recovery of metals from wastewater using inverse fluidized bed sulfidogenic bioreactor. *J. Clean. Prod.* 284, 124769. doi: 10.1016/j.jclepro.2020.124769

Lin, H., Zhi, T., Zhang, L., Liu, C., and Dong, Y. (2023). Effects of acid/alkali-pretreated peanut shells as a cheap carbon source for the bio-reduction of sulfate. *J. Clean. Prod.* 385. doi: 10.1016/j.jclepro.2022.135753

Liu, P., Zhang, Y., Tang, Q., and Shi, S. (2021). Bioremediation of metal-contaminated soils by microbially-induced carbonate precipitation and its effects on ecotoxicity and long-term stability. *Biochem. Eng. J.* 166, 107856. doi: 10.1016/j.bej.2020.107856

Martins, M., Santos, E. S., Faleiro, M. L., Chaves, S., Tenreiro, R., Barros, R. J., et al. (2011). Performance and bacterial community shifts during bioremediation of acid mine drainage from two Portuguese mines. *Int. Biodeterior. Biodegradation* 65, 972–981. doi: 10.1016/j.ibiod.2011.07.006

Meng, L., Xiaohui, C., Hongxian, G., and Zuan, Y. (2016), Biomineralization of carbonate by terrabacter tumescens for heavy metal removal and biogrouting applications. *J. Environm. Eng.* 142, C4015005. doi: 10.1061/(ASCE)EE.1943-7870.0000970

Miao, Z., He, H., Tan, T., Zhang, T., Tang, J., Yang, Y., et al. (2018). Biotreatment of Mn^{2+} and Pb^{2+} with Sulfate-Reducing Bacterium Desulfuromonas alkenivorans S-7. *J. Environm. Eng.* 144, 1330. doi: 10.1061/(ASCE)EE.1943-7870.0001330

Nguyen, H. T., Nguyen, H. L., Nguyen, M. H., Nguyen, T. K. N., and Dinh, H. T. (2020). Sulfate reduction for bioremediation of AMD facilitated by an indigenous acidand metal-tolerant sulfate-reducer. *J. Microbiol. Biotechnol.* 30, 1005–1012. doi: 10.4014/jmb.2001.01012

Nielsen, G., Hatam, I., Abuan, K. A., Janin, A., Coudert, L., Blais, J. F., et al. (2018). Semi-passive in-situ pilot scale bioreactor successfully removed sulfate and metals from mine impacted water under subarctic climatic conditions. *Water Res.* 140, 268–279. doi: 10.1016/j.watres.2018.04.035

Nogueira, E. W., Gouvea de Godoi, L. A., Marques Yabuki, L. N., Brucha, G., and Zamariolli Damianovic, M. H. R. (2021). Sulfate and metal removal from acid mine drainage using sugarcane vinasse as electron donor: performance and microbial community of the down-flow structured-bed bioreactor. *Bioresour. Technol.* 330, 124968. doi: 10.1016/j.biortech.2021.124968

Peng, D., Qiao, S., Luo, Y., Ma, H., Zhang, L., Hou, S., et al. (2020). Performance of microbial induced carbonate precipitation for immobilizing Cd in water and soil. *J. Hazard. Mater.* 400, 123116. doi: 10.1016/j.jhazmat.2020.123116

Rambabu, K., Banat, F., Pham, Q. M., Ho, S. H., Ren, N. Q., and Show, P. L. (2020). Biological remediation of acid mine drainage: review of past trends and current outlook. *Environ. Sci. Ecotechnol.* 2, 100024. doi: 10.1016/j.ese.2020.100024

Razia, S., Hadibarata, T., and Lau, S. Y. (2023). Acidophilic microorganisms in remediation of contaminants present in extremely acidic conditions. *Bioprocess Biosyst. Eng.* 46, 341–358. doi: 10.1007/s00449-022-02844-3

Ryu, S., Naidu, G., Hasan Johir, M. A., Choi, Y., Jeong, S., and Vigneswaran, S. (2019). Acid mine drainage treatment by integrated submerged membrane distillation-sorption system. *Chemosphere* 218, 955–965. doi: 10.1016/j.chemosphere.2018.11.153

Su, Z., Li, X., Xi, Y., Xie, T., Liu, Y., Liu, B., et al. (2022). Microbe-mediated transformation of metal sulfides: mechanisms and environmental significance. *Sci. Total Environ.* 825, 153767. doi: 10.1016/j.scitotenv.2022.153767

Walters, E. R., Pugh, C. W., Bender, K. S., and Liliana, L. (2013). Use of sulfur isotopes to quantify biological and abiotic processes contributing to sulfur cycling in an AMD treatment system. *Mineral. Mag.* 77, 2443. doi: 10.1180/minmag.2013.077.5.23

Wang, B. (2014). *The Experimental Study on the Growth and Reproduction Characters of SRB Domesticated with New Carbon Sources and Treatment of Acid Mine Drainage (Masters)*. Fuxin: Liaoning Technical University.

Watanabe, M., Higashioka, Y., Kojima, H., and Fukui, M. (2020). Proposal of Desulfosarcina ovata subsp. sediminis subsp. nov., a novel toluene-degrading sulfate-reducing bacterium isolated from tidal flat sediment of Tokyo Bay. *Syst Appl Microbiol* 43, 126109. doi: 10.1016/j.syapm.2020.126109

Xu, H., Zheng, H., Wang, J. N., Ding, X. Q., and Chen, P. (2019). Laboratory method of microbial induced solidification/stabilization for municipal solid waste incineration fly ash. *MethodsX* 6, 1036–1043. doi: 10.1016/j.mex.2019.05.006

Xu, Y. N., and Chen, Y. (2020). Advances in heavy metal removal by sulfate-reducing bacteria. *Water Sci. Technol.* 81, 1797–1827. doi: 10.2166/wst.2020.227

Yan, S., Cheng, K. Y., Morris, C., Douglas, G., Ginige, M. P., Zheng, G, et al. (2020). Sequential hydrotalcite precipitation and biological sulfate reduction for acid mine drainage treatment. *Chemosphere* 252, 126570. doi: 10.1016/j.chemosphere.2020.126570

Yang, F., Zhai, W., Li, Z., Huang, Y., Manzoor, M., Yang, B., et al. (2021). Immobilization of lead and cadmium in agricultural soil by bioelectrochemical reduction of sulfate in underground water. *Chem. Eng. J.* 422. doi: 10.1016/j.cej.2021.130010

Zeng, T., Guo, J., Li, Y., and Wang, G. (2022). Oyster shell amendment reduces cadmium and lead availability and uptake by rice in contaminated paddy soil. *Environ. Sci. Pollut. Res. Int.* 29, 44582–44596. doi: 10.1007/s11356-022-18727-9

Zhang, H., Su, M., Li, M., Yan, J., Tang, J., Gong, C., et al. (2019). Efficient removal of Pb(II) ions from aqueous solution by novel PVA-sodium alginate immobilized sulfate reducing bacteria. *Desalination Water Treat.* 138, 280–290. doi: 10.5004/dwt.2019.23256

Zhao, Y., Yao, J., Yuan, Z., Wang, T., Zhang, Y., and Wang, F. (2017). Bioremediation of Cd by strain GZ-22 isolated from mine soil based on biosorption and microbially induced carbonate precipitation. *Environ. Sci. Pollut. Res. Int.* 24, 372–380. doi: 10.1007/s11356-016-7810-y

Zhu, X., Li, W., Zhan, L., Huang, M., Zhang, Q., and Achal, V. (2016). The large-scale process of microbial carbonate precipitation for nickel remediation from an industrial soil. *Environ. Pollut.* 219, 149–155. doi: 10.1016/j.envpol.2016.10.047

To be or not to be a cytochrome: electrical characterizations are inconsistent with *Geobacter* cytochrome 'nanowires'

Matthew J. Guberman-Pfeffer*

Department of Chemistry and Biochemistry, Baylor University, Waco, TX, United States

Geobacter sulfurreducens profoundly shapes Earth's biogeochemistry by discharging respiratory electrons to minerals and other microbes through filaments of a two-decades-long debated identity. Cryogenic electron microscopy has revealed filaments of redox-active cytochromes, but the same filaments have exhibited hallmarks of organic metal-like conductivity under cytochrome denaturing/inhibiting conditions. Prior structure-based calculations and kinetic analyses on multi-heme proteins are synthesized herein to propose that a minimum of ~7 cytochrome 'nanowires' can carry the respiratory flux of a *Geobacter* cell, which is known to express somewhat more (≥20) filaments to increase the likelihood of productive contacts. By contrast, prior electrical and spectroscopic structural characterizations are argued to be physiologically irrelevant or physically implausible for the known cytochrome filaments because of experimental artifacts and sample impurities. This perspective clarifies our mechanistic understanding of physiological metal-microbe interactions and advances synthetic biology efforts to optimize those interactions for bioremediation and energy or chemical production.

KEYWORDS

Geobacter, nanowire, pili, cytochrome, multi-heme, OmcS, OmcZ, conductivity

Introduction

Filaments from *Geobacter sulfurreducens* were reported nearly 20 years ago to be electrically conductive (Reguera et al., 2005), and yet, an intense debate persists over their identity, structure, and *in vivo* mechanism (Lovley and Walker, 2019; Reguera and Kashefi, 2019; Wang et al., 2019; Yalcin and Malvankar, 2020). Two hypotheses have divided the field (Figure 1) (Boesen and Nielsen, 2013): (1) The filament is a supramolecular assembly of cytochromes that transfers electrons through a "bucket-brigade" succession of reduction–oxidation (redox) reactions (Strycharz-Glaven et al., 2011; Boyd et al., 2015) or (2) the filament is a supramolecular assembly of PilA-N (formerly known as PilA) proteins that delocalizes electrons through a crystalloid array of stacked aromatic residues to realize metallic-like conductivity (Malvankar et al., 2011; Malvankar and Lovley, 2012).

The redox-conduction-through-cytochrome (RCTC) hypothesis is consistent with the long-established theory and function of redox cofactor chains in biology that connect catalytic centers (Page et al., 1999; Moser et al., 2000); some of these chains are even known as "molecular wire[s]" (Taylor et al., 1999; Leys et al., 2002; Pokkuluri et al., 2011). The "original hypothesis" (Tran, 2009) is supported by a wealth of spectroscopic and electrochemical data consistent with the redox chemistry of biofilms (Boyd et al., 2015), the prevalence of

extracellular cytochromes expressed by *G. sulfurreducens*, and the cryogenic electron microscopy (CryoEM) determination of five filamentous cytochrome polymers from *G. sulfurreducens* (Figure 1A) (Filman et al., 2019; Wang et al., 2019, 2022a,b; Gu et al., 2023) and other prokaryotes (Baquero et al., 2023). It has also been considered implausible for crystalline-like order to be maintained among rotatable aromatic sidechains throughout a non-covalent protein assembly under ambient conditions (Strycharz-Glaven et al., 2011; Yan et al., 2015; Ru et al., 2019). The CryoEM structure of the *G. sulfurreducens* heterodimeric PilA-N/PilA-C pilus (Gu et al., 2021), in fact, shows no continuous chain of aromatic residues that can support electrical conductivity (Figure 1A).

However, heterologous expression of the *G. sulfurreducens* PilA-N protein in bacteria that do not produce outer-surface cytochromes yields (Liu et al., 2019; Ueki et al., 2020) 3-nn thinner pili with a similar diameter and conductance as 90% of the filaments emanating from *G. sulfurreducens* (Liu et al., 2021). The spectrophotometrically-detected low density of cytochromes in biofilms, as well as the immunogold-labeling and AFM-measured large spacing between (presumed) cytochrome globules on pili filaments make the RTCT hypothesis "physically impossible" (Malvankar et al., 2012b). The invariance of electrical conductivity of pili preparations to cytochrome denaturing or inhibiting conditions "definitively rule[] out" the role of *c*-type cytochromes (Malvankar et al., 2012a). A suite of experiments
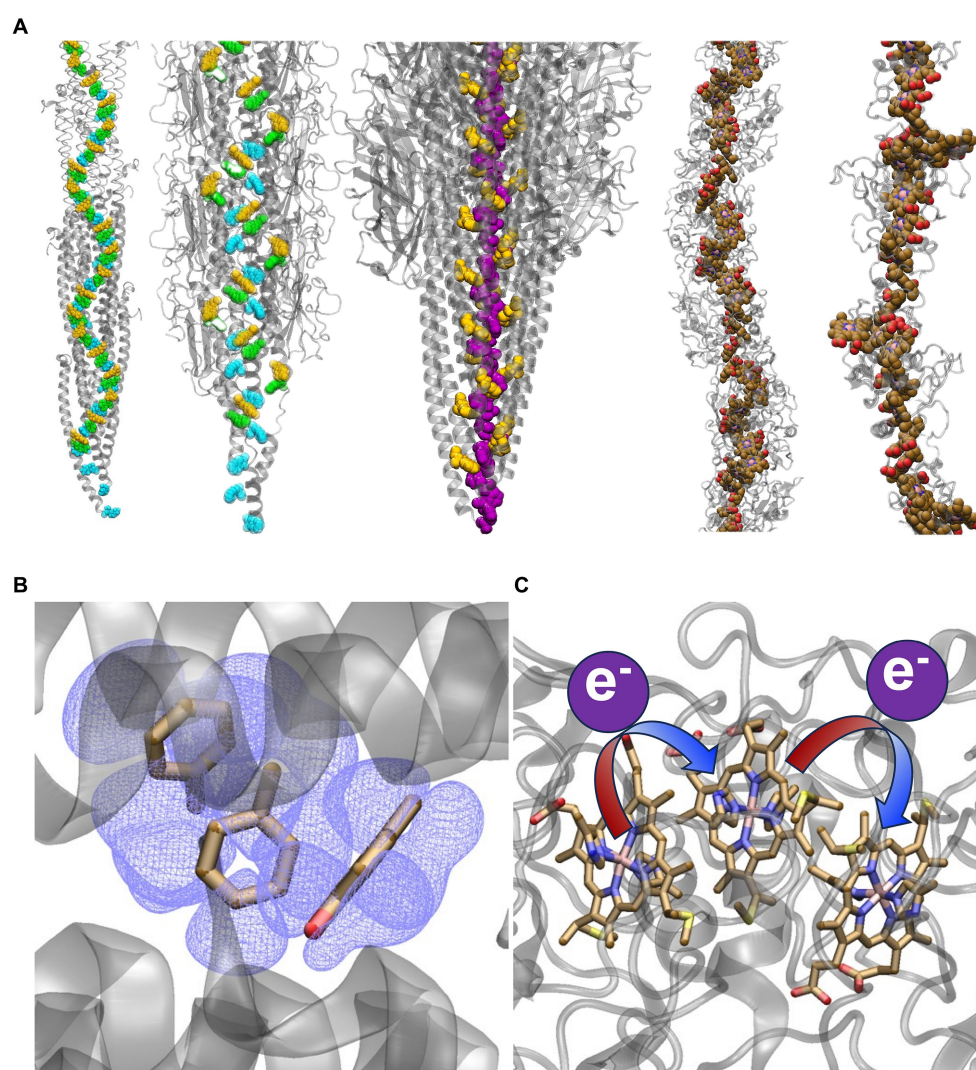
FIGURE 1
Competing structural and electrical conduction models for extracellular electron transfer. **(A)** Models of stacked Phe and Tyr residues or heme cofactors providing a conductive pathway for electrons. From left-to-right the structures are: the Arc-1 homology model of the *G. sulfurreducens* PilA-N pilus (Xiao et al., 2016) and the CryoEM resolved structure of the *G. sulfurreducens* PilA-N/PilA-C pilus (Gu et al., 2021), both with Phe-1, Phe-24, and Tyr-27 in PilA-N colored cyan, green, and yellow, respectively; CryoEM-resolved structure of the archaellum from *Methanospirillum hungatei* (Walker et al., 2019) with Phe-1 and Phe-13 colored purple and yellow respectively; and CryoEM-resolved structures of the *G. sulfurreducens* outer-membrane cytochrome types S (Wang et al., 2019) and Z (Gu et al., 2023) filaments with the hemes colored in brown. The archaellum is included to show that a continuous chain of aromatics has been observed in an experimentally-resolved structure of a natural protein assembly, which may lend some plausibility to the homology-modeled *G. sulfurreducens* PilA-N pilus. Representations of conduction via **(B)** electronic delocalization over aromatic residues or **(C)** a succession of redox reactions from one heme to the next.

have shown temperature (Malvankar et al., 2011, 2014), pH (Malvankar et al., 2011, 2014; Tan et al., 2016a), voltage (Malvankar et al., 2011, 2012b), crystallinity (Malvankar et al., 2015; Xiao et al., 2016), charge propagation (Malvankar et al., 2014; Lovley and Malvankar, 2015), and aromatic density-related (Vargas et al., 2013; Adhikari et al., 2016; Tan et al., 2016a,b) dependencies of pili or biofilm conductivity—sometimes under cytochrome denaturing or inhibiting conditions—similar to synthetic organic metals (Malvankar and Lovley, 2012).

Strikingly, for example, expression of pili from other *Geobacter* spp. and point mutations in the *G. sulfurreducens* pilus caused cells to produce filaments that had a ~10^7-fold range in conductivity (3.8×10^{-5} to 2.8×10^2 S/cm) that correlated with aromatic residue density in the pilus (Adhikari et al., 2016; Tan et al., 2016a,b; Tan et al., 2017). For cytochromes to account for this phenomenon, a series of independent pleotropic effects would have to yield no less than five different cytochrome filaments, almost all with the same diameter (Adhikari et al., 2016; Tan et al., 2016a,b; Tan et al., 2017), that had electrical conductivities varied in precisely the way expected for the introduced pili variants.

These observations have been rationalized in terms of the metallic-like pilus (MLP) hypothesis, with the homology-modeled prediction of a seamlessly stacked array of aromatic residues (Figure 1A) (Malvankar et al., 2015; Xiao et al., 2016; Shu et al., 2017, 2019, 2020). Inspired by this picture, experiments on modified or *de novo* designed proteins lacking redox active cofactors have demonstrated, in some cases, electrical conductivities that are surprisingly high and due to mechanisms under active investigation (Creasey et al., 2015; Kalyoncu et al., 2017; Ing et al., 2018b; Shapiro et al., 2022; Krishnan et al., 2023).

But in the case of *G. sulfurreducens* biofilms and filaments, some of the experimental hallmarks of metallic-like conductivity have come to be debated on grounds of inappropriate experimental design (Bond et al., 2012; Strycharz-Glaven and Tender, 2012; Malvankar et al., 2012a, 2016; Yates et al., 2016), unreproduced by others in magnitude (Ing et al., 2017) or sign (Ing et al., 2018a), shown to depend heavily on experimental conditions (Phan et al., 2016), and found to be inconsistent with further modeling efforts (Strycharz-Glaven et al., 2011; Feliciano et al., 2012; Boesen and Nielsen, 2013; Bonanni et al., 2013; Reardon and Mueller, 2013; Lebedev et al., 2015; Yan et al., 2015; Yates et al., 2015; Ru et al., 2019). In light of the CryoEM-resolved cytochrome filament structures (Figure 1A), some (but not all) advocates of the MLP hypothesis as a "new paradigm for biological electron transfer and bioelectronics" (Malvankar and Lovley, 2012) have abandoned it in favor of the more traditional RTCT perspective.

Only a few years after reports entitled, for example, *Conductivity of Individual Geobacter Pili*, (Adhikari et al., 2016) some of the same investigators have claimed "conduction along the length of a single *bona fide* PilA filament has not been demonstrated" (Wang et al., 2019) because "[t]here has never been any direct evidence that conductive *Geobacter* extracellular filaments are composed of PilA" (Wang et al., 2019). Instead, it is now argued that filamentous outer-membrane cytochromes are "the same filaments previously thought to be TYPE IV pili" (Wang et al., 2019; Yalcin et al., 2020).

If this debated (Lovley and Walker, 2019) contention is granted, then (1) the prior cytochrome denaturation/inhibition studies that showed no change in conductivity must have been flawed, as previously charged (Strycharz-Glaven and Tender, 2012); (2)

cytochromes must be capable of a 10^7-fold variation in conductivity that coincidentally correlates with the number of aromatic residues in the *Geobacter* pilus; and (3) observations of metallic-like conductivity inconsistent with cytochromes must now either be deemed erroneous, as alleged earlier (Bond et al., 2012; Strycharz-Glaven and Tender, 2012; Yates et al., 2016), or somehow ascribed to cytochromes.

Herein, I consider if the magnitude, variation, and dependencies of the reported filament conductivities for *Geobacter* 'nanowires' are consistent with the CryoEM-resolved cytochrome filaments (Filman et al., 2019; Wang et al., 2019, 2022a,b; Baquero et al., 2023; Gu et al., 2023), structure-based state-of-the-art computations, (Eshel et al., 2020; Jiang et al., 2020; Livernois and Anantram, 2021; Dahl et al., 2022; Guberman-Pfeffer, 2022, 2023; Livernois and Anantram, 2023), electron transfer kinetics in multi-heme proteins (van Wonderen et al., 2019, 2021), and biological considerations (Moser et al., 2000; Page et al., 2003; Noy et al., 2006). Note that whether or not electrically conductive pili (*e*-pili) exist, and whether or not they have metallic-like conductivity are not the issues at hand. By failing to find some structural and electrical characterizations consistent with cytochromes, however, lends circumstantial support to the *e*-pilus hypothesis.

Heme-to-heme electron transfer rates are independent of filament identity

Thousands of successive redox reactions are thought to move electrons through micron-scale filamentous cytochromes under physiological conditions (Blumberger, 2018). In each reaction, electrons 'hop' between weakly (<0.02 eV) coupled hemes (Blumberger, 2018; Jiang et al., 2020; Dahl et al., 2022; Guberman-Pfeffer, 2022; Guberman-Pfeffer, 2023) packed in highly conserved T- and slip-stacked geometries (Supplementary Tables S1, S2; Supplementary Figure S1) (Baquero et al., 2023). The van der Waals-packing permits the surrounding protein/water media to impose only a small (<|0.3| eV) free energy difference on the heme-to-heme self-exchange reaction (Supplementary Tables S3, S4) (O'Brien, 2020; Dahl et al., 2022; Shipps, 2022; Guberman-Pfeffer, 2023). A > 0.4 eV cost is also imposed for the reorganization of the environment to the altered charge distribution in the reaction (Supplementary Table S5) (Jiang et al., 2020; Dahl et al., 2022; Guberman-Pfeffer, 2023). The lowering of this penalty by active site polarizability is found to be minimal (~0.04 eV; Supplementary Tables S6–S8). This picture is derived from spectroelectrochemical experiments (O'Brien, 2020; Shipps, 2022) and structure-based calculations (Jiang et al., 2020; Dahl et al., 2022; Guberman-Pfeffer, 2022; Guberman-Pfeffer, 2023) on the CryoEM-resolved cytochrome filaments.

The energetic constraints ensure the applicability of non-adiabatic Marcus theory (Blumberger, 2018) and encode ground-state inter-heme electron transfers on the hundreds of ns to μs timescales (Figure 2; Supplementary Table S9). For all computations to date (Jiang et al., 2020; Dahl et al., 2022; Guberman-Pfeffer, 2023) reaction rates between T- and slip-stacked heme pairs in the filaments are on average 5.3×10^7 to 2.0×10^9 s^{-1} and 3.0×10^9 to 2.0×10^{10} s^{-1}, respectively (Supplementary Table S10). These rates are in excellent agreement with the average rates derived from kinetic analyses of ultrafast transient absorption measurements on photosensitized variants of the small tetraheme cytochrome (STC) (van Wonderen et al., 2019) and the metal reducing cytochrome type C (MtrC) (van Wonderen et al., 2021) from *Shewanella oneidensis*. As anticipated
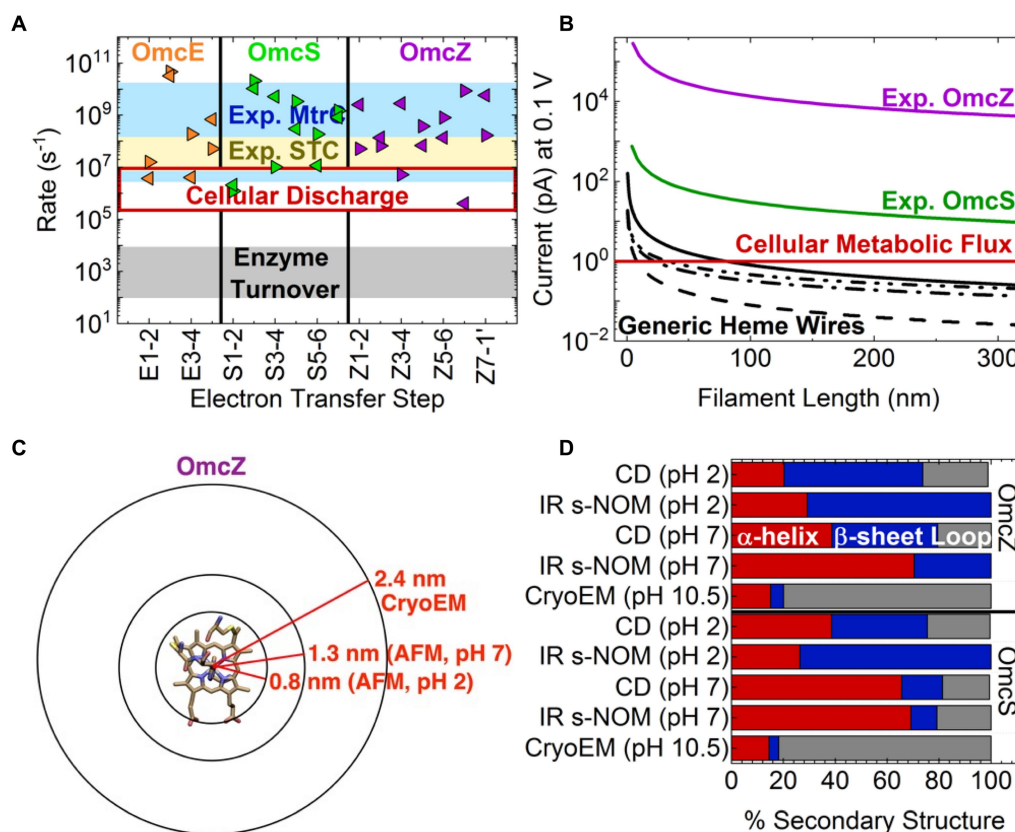
FIGURE 2
Inconsistencies in the electrical and structural characterizations of cytochrome filaments. *Top*: Heme-to-heme electron transfer rates are independent of protein identity and meet or exceed cellular metabolic flux but are cannot account for than reported conductivities. **(A)** Comparison of computed structure-based Marcus theory rates for the outer-membrane cytochrome (Omc) types E, S, and Z from *Geobacter sulfurreducens* (Guberman-Pfeffer, 2023) to experimentally measured rates for the same highly conserved heme packing geometries in the small tetraheme cytochrome (STC; van Wonderen et al., 2019) and metal reducing cytochrome type C (MtrC; van Wonderen et al., 2021) from *Shewanella oneidensis*. **(B)** The length dependence of the protein-limited current at 0.1V through generic heme wires compared to the currents through Omc- S and Z based on the reported conductivities (Yalcin et al., 2020; Dahl et al., 2022). The solid, dashed, dashed-dot, and dashed-dot-dot curves, respectively, correspond to heme chains with all slip-stacked, all T-stacked, strictly alternating slipped and T-stacked, and a T→S→S→S→T→S→T→S (T=T-stacked; S=slip-stacked) pattern as found in OmcZ. Computational details accompany Supplementary Table S11. *Bottom*: Infrared nanospectroscopy using scattering-type scanning near-field optical microscopy (IR s-NOM), circular dichroism (CD) and atomic force microscopy (AFM) structural characterizations are inconsistent with the cryogenic electron microscopy (CryoEM)-resolved filaments. **(C)** Comparison of filament radii for OmcZ measured by CryoEM and AFM at different pHs. **(D)** Secondary structure compositions reported by CryoEM, IR s-NOM, and CD at different pHs. The data is reproduced from Yalcin et al. (2020).

by Blumberger and co-workers (van Wonderen et al., 2021) and Page, Moser, and Dutton two decades earlier (Page et al., 1999), inter-heme electron transfer rates within highly conserved packing geometries are also highly conserved.

Evolution favors robustness over tunability

Independence from the surrounding protein affords evolutionary robustness at the expense of tunability, which seems tolerable because the rates already exceed typical timescales for enzymatic turnover ($\geq \mu$s vs. ms; Figure 2A) (Noy et al., 2006), and do not therefore pose the rate-limiting step for cellular respiration (Page et al., 2003). Indeed, if the cytochrome filaments are optimized for electrical conductivity, why do nearly half (Filman et al., 2019; Wang et al., 2019, 2022a,b; Baquero et al., 2023; Gu et al., 2023) of all heme pairs adopt a T-stacked geometry that enforces 10-fold slower electron transfers than a slip-stacked geometry? It is important not to fall into the Panglossian paradigm (Page et al., 2003).

Functional robustness permits adaptation of the environment-filament interface formed by the surrounding protein without having to re-invent the mechanism for long-range electron transfer. This "design"-strategy is analogous to how the conserved photosystems of photosynthesis are interfaced to distinct spectral niches by highly adapted light harvesting antenna (Guberman-Pfeffer, 2023). Finding modular solutions to decoupled problems is a meta-strategy of evolution. An implication is that *de novo* design seems to be a more promising avenue for application-tailored cytochrome 'nanowires' than mutagenesis.

A minimum of seven cytochrome filaments/cell can carry the total metabolic current

Theory and experiment both suggest that 1×10^8 and 1×10^9 s^{-1} are protein-independent, order-of-magnitude estimates for ground-state heme-to-heme electron transfer in T- and slip-stacked geometries,

respectively. Using these generic rates, the experimentally characterized 300 nm-long filaments are predicted to support protein-limited currents of ~0.14 pA (Figure 2B; Supplementary Table S11), a result somewhat underestimated by structure-based calculations (Supplementary Figure S2). A *G. sulfurreducens* cell discharging ~1 pA (i.e., oxidizing $\sim 8 \times 10^5$ acetate molecules/s) would require a minimum of ~7 cytochrome filaments; somewhat more (≥ 20 filaments/cell) are likely expressed to increase the chance of productive contacts with (microbial or mineral) electron sinks (Reguera et al., 2005; Summers et al., 2010; Reguera and Kashefi, 2019).

Chemical, not electrical gradients drive electrons through cytochrome filaments

An open question with the conventional picture of redox conduction is what provides the needed driving force for a succession of thousands of reactions to transfer electrons on the micrometer scale. Each one-electron heme-to-heme step incurs a reorganization penalty at least quadruple the ~0.1 V drop between the intra-cellular acetate oxidation and extracellular iron oxide reduction half reactions connected by the filament. This penalty accumulates along the filament length, while heme-to-heme reaction free energies are nearly net-zero through a filament subunit (Supplementary Table S4). The external bias is energetically smaller than thermal noise between any two adjacent hemes (if linearly interpolated along the filament) and furthermore screened by mobile ions. The exodus of $3 \times 10^5 - 9 \times 10^6$ electrons/s/cell (Lampa-Pastirk et al., 2016; Karamash et al., 2022) must, it seems, provide the needed driving force in the form of a concentration gradient.

Current electrical characterizations reflect abiological artifacts

But heme-Fe redox activity (Amdursky et al., 2013; Blumberger, 2018; Agam et al., 2020; Futera et al., 2020) and concentration gradients (Strycharz-Glaven et al., 2011; Bostick et al., 2018) are not relevant under the electron transport (as opposed to transfer) conditions of the performed conducting probe atomic force microsocpy (CP-AFM) experiments; namely electrode adsorbed, air-dried, and mechanically compressed filaments exposed to electric fields unscreened by mobile ions. Some other mechanism may be operative. In support of this hypothesis, the measured currents are $10^2 - 10^5$-fold larger than the computed and biologically reasonable maximum redox current of 0.14 pA/filament (Figure 2B), even at a voltage well-below the protein-limited threshold (Wang et al., 2019; Yalcin et al., 2020; Dahl et al., 2022). Contrary to some (Dahl et al., 2022) but not all (Eshel et al., 2020; Guberman-Pfeffer, 2022; Guberman-Pfeffer, 2023) prior claims, a physiologically relevant succession of redox reactions (multi-step hopping) cannot even come close to account for the reported conductivities.

Moreover, the 30 nA current reported at 0.1 V for OmcZ (Yalcin et al., 2020) requires an effective electron transfer rate of 3×10^{12} s^{-1}. This rate is nearly at the non-adiabatic electronic coupling-maximum 'speed limit' of 10^{13} s^{-1} for metal ions in van der Waals contact (Gray and Winkler, 2010), even though the Fe centers are separated by at least triple that distance. Only if active-site polarizability reduces the

computed reorganization energies by 45% (Kontkanen et al., 2023), every heme-to-heme electron transfer is activationless, and all electronic couplings are 20-fold larger than computed from the CryoEM structure can the measured conductivity be explained by the redox process. There is no basis for the hypothesis that increased electronic couplings due to some hemes being ~1.0 Å closer can account for the 10^3-fold greater conductivity of Omc- Z versus S (Guberman-Pfeffer, 2023).

Of note, there was also no basis for the reported conductivities when Omc- Z and S were argued to be the F51W-F57W and wild-type pili, respectively (Tan et al., 2016a). An increase in aromatic density was then claimed to explain the higher conductivity of the F51W-F57W pilus by erroneously counting the substitution of one aromatic residue (Trp) for a different aromatic residue (Phe) as introducing an additional aromatic residue.

In addition to the abiological electron transport conditions used experimentally, the reported conductivities may be artificially large because the 40–60 nm-wide tip used in CP-AFM can contact ~10 filament subunits, or ~10^2 hemes along its diameter. The observed current scales linearly with the number of electrode-protein contacts (Polizzi et al., 2012). Also, a force of 10–50 nN was applied to the filaments in CP-AFM experiments (Yalcin et al., 2020; Dahl et al., 2022), which is known to mechanically deform much more structured proteins (e.g., azurin, plastocyanin, and cytochrome *c*) (Zhao and Davis, 2003; Zhao et al., 2004; Andolfi and Cannistraro, 2005; Bonanni et al., 2005; Axford et al., 2007; Li et al., 2012), and change the electron transport mechanism; for example, by changing the packing density. More force can increase the packing density, which in turn promotes transmission of electrons. In this context, the experimental procedure of measuring the length dependence of the resistance by passing the current through previously crushed segments of the filament (Yalcin et al., 2020; Dahl et al., 2022) is problematical. The cytochrome filaments are potentially more responsive to compressional force than previously studied proteins because $\geq 50\%$ of the secondary structure consists of flexible turns and loops (Filman et al., 2019; Wang et al., 2019, 2022a,b; Baquero et al., 2023; Gu et al., 2023).

Cytochromes cannot logically have properties inconsistent with cytochromes

Several other characterizations of *Geobacter* 'nanowires' may also be experimental artifacts if the contention is granted that the filaments have always been cytochromes.

Carbon nanotube-like charge delocalization supported by crystalline π-π stacking

Electrostatic force microscopy (EFM) experiments showed holes delocalize rapidly for microns along individual filaments and accumulate in what were described as cytochrome-like globules on the filament surface (Malvankar et al., 2014). Extensive delocalization was attributed to the crystalline order of π-π stacking interactions that control the conjugation length or mean free path of electrons (Malvankar et al., 2011, 2015; Yalcin et al., 2020).

Electrons in cytochromes, however, propagate through spatially confined and weakly coupled heme-centered molecular orbitals that participate in discrete redox transitions under physiological conditions. The reported conductivities are much too small to justify

a band-theory electronic description (Polizzi et al., 2012). Instead, the EFM results may be an artifact of the ±10 V bias used to inject charges into the filaments (Malvankar et al., 2014),which accessed electronic excited states completely forbidden to biology.

Synthetic metal-like voltage dependent conductivity

Electrochemical gating showed an organic metal-like sigmoidal voltage dependence with no peak in conductivity at the formal potential and an increase at highly oxidizing potentials (Malvankar et al., 2012b). Cytochromes, as redox conductors, have a strongly peaked conductivity at the formal potential that falls to zero at the extremes where populations of both charge donating and accepting hemes are unavailable (Strycharz-Glaven et al., 2011). By contrast, highly oxidizing potentials were suggested to be necessary for conductivity in the homology-modeled *G. sulfurreducens* pilus (Ru et al., 2019).

More recently, a 6-fold higher conductivity of fully reduced versus fully oxidized OmcS was rationalized by invoking a 0.3–0.6 V electrochemical hysteresis for each heme (Supplementary Table S3) (Dahl et al., 2022). This hysteresis was not observed in two independent sets of spectroelectrochemical experiments (O'Brien, 2020; Shipps, 2022) performed in the investigators' laboratory years before publishing this explanation. Anantram and co-workers (Livernois and Anantram, 2023) have instead proposed that the redox-state-dependent conductivity is because of improved alignment and coupling of the heme orbitals with the Fermi level of the electrodes upon reduction, an effect with no biological relevance.

Synthetic metal-like temperature dependent conductivity

The conductivity of biofilms (Malvankar et al., 2011), films of filaments (Malvankar et al., 2011), and individual filaments (Dahl et al., 2022) exponentially increased upon cooling down to a cross-over temperature, below which the conductivity exponentially decreased upon further cooling. This behavior, which has not been reproduced by others (Ing et al., 2018a) and may strongly depend on uncontrolled humidity in the experiments (Phan et al., 2016) was ascribed to delocalized electrons that move freely without thermal activation and experience reduced phonon scattering upon cooling, but encounter disorder, or localizing traps at temperatures below the crossover point, as in synthetic organic metals (Kaiser, 2001).

Redox conduction in cytochromes, by contrast, is expected to show Arrhenius-type kinetics, as computationally demonstrated by the present author for the OmcS filament (Guberman-Pfeffer, 2022). Other computational work (Dahl et al., 2022) found that if unphysically negative redox potentials in contradiction to spectroelectrochemical analyses (O'Brien, 2020; Shipps, 2022) are considered, the conductivity at 310 versus 270 K can be severely underestimated, and thereby give the impression of validating the experimental temperature dependence.

Increased conductivity at cytochrome denaturing pHs

Filaments from *G. sulfurreducens* became more conductive upon acidification from pH 7 to 2 (Malvankar et al., 2011; Tan et al., 2016a). Redox conduction in cytochromes may become more favorable with an increased H^+ concentration if the electron and proton transfers are coupled. The reported kinetic isotope effect (KIE) on conductivity in OmcS was similar to other proton-coupled-electron-transfer (PCET) systems, and the present author found 26–42% charge compensation from coupled protonation and redox state changes (Guberman-Pfeffer, 2022). Dynamical solvent control may also contribute to the KIE (Mostajabi Sarhangi and Matyushov, 2023).

Cytochromes, however, are expected to denature at pH 2. Furthermore, circular dichroism (CD) spectra of OmcS in pH 7 potassium phosphate and pH 2 sodium citrate buffers were more similar to one another than to CD spectra under solid-state conditions (Yalcin et al., 2020). The pH-dependence, which is already physiologically irrelevant at pH 2, may be an artifact of surface adsorption and dehydration.

These artifacts may manifest as the observed structural changes (Figures 2C,D); namely (1) a ~ 1.0 nm shrinkage in filament diameter from pH 7 to 2 that left OmcZ no wider than a single heme group, as if the protein had been hydrolyzed away, and (2) an α-helical-to-β-sheet transition quantified with techniques that disagreed on the magnitude of the effect (50% versus ≤21% conversion) (Yalcin et al., 2020). How, and energetically why such a large structural change of the polypeptide backbone can be accommodated by the geometrical constraints of covalent thioether linkages and coordinative His-Fe bonds to each heme is difficult to comprehend.

Electrical measurements have not been performed on known cytochrome filament structures

Some unknown and abiological mechanism in cytochromes may be operative under experimental conditions to account for these observations. However, it is also true that spectroscopic characterizations of protein structure in the same study (Yalcin et al., 2020) that reported electrical measurements disagree with the CryoEM analyses (Figure 2B) (Filman et al., 2019; Wang et al., 2019, 2022a,b; Baquero et al., 2023; Gu et al., 2023). Infrared nanospectroscopy using scattering-type scanning near-field optical microscopy (IR s-SNOM) and CD measurements on purportedly OmcS filaments indicated 66–69% (instead of 14%) α-helical content, 10–16% (instead of 4%) β-sheet content, and 18–21% (instead of 82%) loops/turns. For purportedly OmcZ filaments, α-helical content was 70% by IR s-NOM and 39% by CD in the same study, instead of 15% by CryoEM; β-sheet content was 30% by IR-SNOM and 41% by CD, instead of 5% by CryoEM; and neither IR s-NOM nor CD found any of the 80% loops/turns witnessed by CryoEM.

The discrepancies of IR s-NOM (but not CD) were attributed to a particular sensitivity of the technique to C=O versus N-H stretching (Yalcin et al., 2020), but this explanation is both technically inaccurate and inapplicable. IR s-NOM "primarily probes molecular vibrations that oscillate perpendicular to the sample surface" (Amenabar et al., 2013), which only translates to a particular sensitivity to C=O versus N-H stretching in the case of an oriented protein, such as membrane-embedded bacteriorhodopsin in the original publication for the technique. The orientation of the putative cytochrome filaments, by contrast, was not controlled for the experiments in any way.

It was furthermore claimed that secondary structure percentages from IR s-NOM are only quantitative in a comparative sense because of the alleged particular sensitivity of the technique (Yalcin et al., 2020). If true, why did IR s-NOM and CD find 19 and 10% more β-sheet content in Omc- Z versus S, respectively, whereas CryoEM found the same amount of β-sheet content in the two proteins (Wang et al., 2022a; Gu et al., 2023)? Of note, a false impression was given that there is no discrepancy by stating (Yalcin et al., 2020)—at odds with the accompanying structure (PDB 7LQ5)—that the CryoEM model of OmcZ has 21 instead of 5% β-strands and by wrongly counting β-turns as regular secondary structure.

Discussion

The structural discrepancies relative to CryoEM, on top of the physiological irrelevance or physical implausibility of electrical characterizations for a multi-heme architecture beg of the filaments the title question: To be or not to be a cytochrome?

The foregoing evidence suggests answering in the affirmative: A handful of cytochrome filaments resolved by CryoEM can carry the entire metabolic flux of electrons from a *Geobacter* cell at rates that are both consistent with kinetic analyses on other multi-heme proteins and do not pose the rate-limiting step to cellular respiration. Cytochrome filaments are proposed to be physiologically relevant. Meanwhile, the reported 10^2–10^5-fold larger conductivities, the 10^7-fold variation in conductivity with PilA-N aromatic density, the hallmarks of metallic-like charge propagation, voltage, temperature, and pH dependences, and the spectroscopically-deduced secondary structure compositions are all irreconcilable with the known cytochrome filaments.

The conclusion follows that earlier claims of inappropriate experimental design are true (Boyd et al., 2015), biologically irrelevant phenomena have been measured, and/or the conformation or composition of the characterized proteins is something other than the known cytochrome filaments. Experiments designed to assess the redox-based electrical conductivity of well-characterized (e.g., composition, purity, structure) filament samples under physiologically relevant conditions are urgently needed. Just as urgently needed are efforts to independently reproduce the electrical characterizations that have been the claims of only a few laboratories.

Data availability statement

The original contributions presented in the study are included in the article/Supplementary material, further inquiries can be directed to the corresponding author.

Author contributions

MJG-P: Conceptualization, Data curation, Formal analysis, Investigation, Methodology, Visualization, Writing – original draft, Writing – review & editing.

Funding

Conflict of interest

The author declares that the research was conducted in the absence of any commercial or financial relationships that could be construed as a potential conflict of interest.

Publisher's note

All claims expressed in this article are solely those of the authors and do not necessarily represent those of their affiliated organizations, or those of the publisher, the editors and the reviewers. Any product that may be evaluated in this article, or claim that may be made by its manufacturer, is not guaranteed or endorsed by the publisher.

Supplementary material

The Supplementary material for this article can be found online at: https://www.frontiersin.org/articles/10.3389/fmicb.2024.1397124/full#supplementary-material

References

Adhikari, R. Y., Malvankar, N. S., Tuominen, M. T., and Lovley, D. R. (2016). Conductivity of individual Geobacter pili. *RSC Adv.* 6, 8354–8357. doi: 10.1039/C5RA28092C

Agam, Y., Nandi, R., Kaushansky, A., Peskin, U., and Amdursky, N. (2020). The porphyrin ring rather than the metal ion dictates long-range electron transport across proteins suggesting coherence-assisted mechanism. *PNAS* 117, 32260–32266. doi: 10.1073/pnas.2008741117

Amdursky, N., Ferber, D., Pecht, I., Sheves, M., and Cahen, D. (2013). Redox activity distinguishes solid-state electron transport from solution-based electron transfer in a natural and artificial protein: cytochrome C and hemin-doped human serum albumin. *Phys. Chem. Chem. Phys.* 15, 17142–17149. doi: 10.1039/c3cp52885e

Amenabar, I., Poly, S., Nuansing, W., Hubrich, E. H., Govyadinov, A. A., Huth, F., et al. (2013). Structural analysis and mapping of individual protein complexes by infrared nanospectroscopy. *Nat. Commun.* 4:2890. doi: 10.1038/ncomms3890

Andolfi, L., and Cannistraro, S. (2005). Conductive atomic force microscopy study of plastocyanin molecules adsorbed on gold electrode. *Surf. Sci.* 598, 68–77. doi: 10.1016/j.susc.2005.08.027

Axford, D., Davis, J. J., Wang, N., Wang, D., Zhang, T., Zhao, J., et al. (2007). Molecularly resolved protein electromechanical properties. *J. Phys. Chem. B* 111, 9062–9068. doi: 10.1021/jp070262o

Baquero, D. P., Cvirkaite-Krupovic, V., Hu, S. S., Fields, J. L., Liu, X., Rensing, C., et al. (2023). Extracellular cytochrome nanowires appear to be ubiquitous in prokaryotes. *Cell* 186, 2853–2864.e8. doi: 10.1016/j.cell.2023.05.012

Blumberger, J. (2018). Electron transfer and transport through multi-heme proteins: recent progress and future directions. *Curr. Opin. Chem. Bio. l* 47, 24–31. doi: 10.1016/j.cbpa.2018.06.021

Boesen, T., and Nielsen, L. P. (2013). Molecular dissection of bacterial nanowires. *MBio* 4:e00270-13. doi: 10.1128/mbio.00270-13

Bonanni, B., Alliata, D., Andolfi, L., Bizzarri, A., and Cannistraro, S. (2005). "Redox metalloproteins on metal surfaces as hybrid systems for bionanodevices: An extensive characterization at the single molecule level" in *Surface science research developments*. ed. C. P. Norris (Hauppauge, HY: Nova Science Publishers, Inc)

Bonanni, P. S., Massazza, D., and Busalmen, J. P. (2013). Stepping stones in the electron transport from cells to electrodes in *Geobacter sulfurreducens* biofilms. *Phys. Chem. Chem. Phys.* 15, 10300–10306. doi: 10.1039/c3cp50411e

Bond, D. R., Strycharz-Glaven, S. M., Tender, L. M., and Torres, C. I. (2012). On electron transport through Geobacter biofilms. *ChemSusChem* 5, 1099–1105. doi: 10.1002/cssc.201100748

Bostick, C. D., Mukhopadhyay, S., Pecht, I., Sheves, M., Cahen, D., and Lederman, D. (2018). Protein bioelectronics: A review of what we do and do not know. *Rep. Prog. Phys.* 81:026601. doi: 10.1088/1361-6633/aa85f2

Boyd, D. A., Snider, R. M., Erickson, J. S., Roy, J. N., Strycharz-Glaven, S. M., and Tender, L. M. (2015). "Theory of redox conduction and the measurement of electron transport rates through electrochemically active biofilms" in *Biofilms in bioelectrochemical systems*. eds. H. Beyenal and J. Babauta (Hoboken, NJ: J. Wiley), 177–209.

Creasey, R. C., Shingaya, Y., and Nakayama, T. (2015). Improved electrical conductance through self-assembly of bioinspired peptides into nanoscale fibers. *Mater. Chem. Phys.* 158, 52–59. doi: 10.1016/j.matchemphys.2015.03.034

Dahl, P. J., Yi, S. M., Gu, Y., Acharya, A., Shipps, C., Neu, J., et al. (2022). A 300-fold conductivity increase in microbial cytochrome nanowires due to temperature-induced restructuring of hydrogen bonding networks. *Sci. Adv.* 8:eabm7193. doi: 10.1126/sciadv.abm7193

Eshel, Y., Peskin, U., and Amdursky, N. (2020). Coherence-assisted electron diffusion across the multi-heme protein-based bacterial nanowire. *Nanotechnology* 31:314002. doi: 10.1088/1361-6528/ab8767

Feliciano, G. T., Da Silva, A. J., Reguera, G., and Artacho, E. (2012). Molecular and electronic structure of the peptide subunit of *Geobacter sulfurreducens* conductive pili from first principles. *J. Phys. Chem. A* 116, 8023–8030. doi: 10.1021/jp302232p

Filman, D. J., Marino, S. F., Ward, J. E., Yang, L., Mester, Z., Bullitt, E., et al. (2019). Cryo-EM reveals the structural basis of long-range electron transport in a cytochrome-based bacterial nanowire. *Commun. Biol.* 2:219. doi: 10.1038/s42003-019-0448-9

Futera, Z., Ide, I., Kayser, B., Garg, K., Jiang, X., Van Wonderen, J. H., et al. (2020). Coherent Electron transport across a 3 nm bioelectronic junction made of multi-Heme proteins. *J. Phys. Chem. Lett.* 11, 9766–9774. doi: 10.1021/acs.jpclett.0c02686

Gray, H. B., and Winkler, J. R. (2010). Electron flow through metalloproteins. *Biochim. Biophys. Acta* 1797, 1563–1572. doi: 10.1016/j.bbabio.2010.05.001

Gu, Y., Guberman-Pfeffer, M. J., Srikanth, V., Shen, C., Giska, F., Gupta, K., et al. (2023). Structure of Geobacter cytochrome OmcZ identifies mechanism of nanowire assembly and conductivity. *Nat. Microbiol.* 8, 284–298. doi: 10.1038/s41564-022-01315-5

Gu, Y., Srikanth, V., Salazar-Morales, A. I., Jain, R., O'Brien, J. P., Yi, S. M., et al. (2021). Structure of Geobacter pili reveals secretory rather than nanowire behaviour. *Nature* 597, 430–434. doi: 10.1038/s41586-021-03857-w

Guberman-Pfeffer, M. J. (2022). Assessing thermal response of redox conduction for anti-Arrhenius kinetics in a microbial cytochrome nanowire. *J. Phys. Chem. B* 126, 10083–10097. doi: 10.1021/acs.jpcb.2c06822

Guberman-Pfeffer, M. J. (2023). Structural determinants of redox conduction favor robustness over Tunability in microbial cytochrome nanowires. *J. Phys. Chem. B* 127, 7148–7161. doi: 10.1021/acs.jpcb.3c02912

Ing, N. L., El-Naggar, M. Y., and Hochbaum, A. I. (2018a). Going the distance: long-range conductivity in protein and peptide bioelectronic materials. *J. Phys. Chem. B* 122, 10403–10423. doi: 10.1021/acs.jpcb.8b07431

Ing, N. L., Nusca, T. D., and Hochbaum, A. I. (2017). *Geobacter sulfurreducens* pili support ohmic electronic conduction in aqueous solution. *Phys. Chem. Chem. Phys.* 19, 21791–21799. doi: 10.1039/C7CP03651E

Ing, N. L., Spencer, R. K., Luong, S. H., Nguyen, H. D., and Hochbaum, A. I. (2018b). Electronic conductivity in biomimetic α-helical peptide nanofibers and gels. *ACS Nano* 12, 2652–2661. doi: 10.1021/acsnano.7b08756

Jiang, X., van Wonderen, J. H., Butt, J. N., Edwards, M. J., Clarke, T. A., and Blumberger, J. (2020). Which multi-Heme protein complex transfers electrons more efficiently? Comparing MtrCAB from Shewanella with OmcS from Geobacter. *J. Phys. Chem. Lett.* 11, 9421–9425. doi: 10.1021/acs.jpclett.0c02842

Kaiser, A. B. (2001). Systematic conductivity behavior in conducting polymers: effects of heterogeneous disorder. *Adv. Mater.* 13, 927–941. doi: 10.1002/1521-4095(200107)13:12/13<927::AID-ADMA927>3.0.CO;2-B

Kalyoncu, E., Ahan, R. E., Olmez, T. T., and Seker, U. O. S. (2017). Genetically encoded conductive protein nanofibers secreted by engineered cells. *RSC Adv.* 7, 32543–32551. doi: 10.1039/C7RA06289C

Karamash, M., Stumpe, M., Dengjel, J., Salgueiro, C. A., Giese, B., and Fromm, K. M. (2022). Reduction kinetic of water soluble metal salts by *Geobacter sulfurreducens*: Fe2+/Hemes stabilize and regulate Electron flux rates. *Front. Microbiol.* 13:909109. doi: 10.3389/fmicb.2022.909109

Kontkanen, O. V., Biriukov, D., and Futera, Z. (2023). Applicability of perturbed matrix method for charge transfer studies at bio/metallic interfaces: a case of conductive azurin. *Phys. Chem. Chem. Phys.* 25, 12479–12489. doi: 10.1039/D3CP00197K

Krishnan, S., Aksimentiev, A., Lindsay, S., and Matyushov, D. (2023). Long-range conductivity in proteins mediated by aromatic residues. *ACS Phys. Chem. Au.* 3, 444–455. doi: 10.1021/acsphyschemau.3c00017

Lampa-Pastirk, S., Veazey, J. P., Walsh, K. A., Feliciano, G. T., Steidl, R. J., Tessmer, S. H., et al. (2016). Thermally activated charge transport in microbial protein nanowires. *Sci. Rep.* 6:23517. doi: 10.1038/srep23517

Lebedev, N., Mahmud, S., Griva, I., Blom, A., and Tender, L. M. (2015). On the electron transfer through *Geobacter sulfurreducens* P il A protein. *J. Polym. Sci. B Polym. Phys.* 53, 1706–1717. doi: 10.1002/polb.23809

Leys, D., Meyer, T. E., Tsapin, A. S., Nealson, K. H., Cusanovich, M. A., and Van Beeumen, J. J. (2002). Crystal structures at atomic resolution reveal the novel concept of "electron-harvesting" as a role for the small tetraheme cytochrome c. *J. Biol. Chem.* 277, 35703–35711. doi: 10.1074/jbc.M203866200

Li, W., Sepunaru, L., Amdursky, N., Cohen, S. R., Pecht, I., Sheves, M., et al. (2012). Temperature and force dependence of nanoscale electron transport via the cu protein azurin. *ACS Nano* 6, 10816–10824. doi: 10.1021/nn3041705

Liu, X., Walker, D. J., Nonnenmann, S. S., Sun, D., and Lovley, D. R. (2021). Direct observation of electrically conductive pili emanating from *Geobacter sulfurreducens*. *MBio* 12:e0220921. doi: 10.1128/mbio.02209-21

Liu, X., Wang, S., Xu, A., Zhang, L., Liu, H., and Ma, L. Z. (2019). Biological synthesis of high-conductive pili in aerobic bacterium *Pseudomonas aeruginosa*. *Appl. Microbiol. Biotechnol.* 103, 1535–1544. doi: 10.1007/s00253-018-9484-5

Livernois, W., and Anantram, M. (2021). Quantum transport in conductive bacterial nanowires. IEEE 16th nanotechnology materials and devices conference (NMDC), 2021. IEEE.

Livernois, W., and Anantram, M. P. (2023). A spin-dependent model for multi-Heme bacterial nanowires. *ACS Nano* 17, 9059–9068. doi: 10.1021/acsnano.2c12027

Lovley, D. R., and Malvankar, N. S. (2015). Seeing is believing: novel imaging techniques help clarify microbial nanowire structure and function. *Environ. Microbiol.* 17, 2209–2215. doi: 10.1111/1462-2920.12708

Lovley, D. R., and Walker, D. J. (2019). Geobacter protein nanowires. *Front. Microbiol.* 10:2078. doi: 10.3389/fmicb.2019.02078

Malvankar, N. S., and Lovley, D. R. (2012). Microbial nanowires: a new paradigm for biological electron transfer and bioelectronics. *ChemSusChem* 5, 1039–1046. doi: 10.1002/cssc.201100733

Malvankar, N. S., Rotello, V. M., Tuominen, M. T., and Lovley, D. R. (2016). Reply to'Measuring conductivity of living *Geobacter sulfurreducens* biofilms'. *Nat. Nanotechnol.* 11, 913–914. doi: 10.1038/nnano.2016.191

Malvankar, N. S., Tuominen, M. T., and Lovley, D. R. (2012a). "Comment on 'On Electrical Conductivity of Microbial Nanowires and Biofilms" by N. S. Malvankar, M. T. Tuominen, and D. R. Lovley, Energy Environ. Sci. 2012, 5. *Energy Environ. Sci.* 5, 6250–6255. doi: 10.1039/c2ee02613a

Malvankar, N. S., Tuominen, M. T., and Lovley, D. R. (2012b). Lack of cytochrome involvement in long-range electron transport through conductive biofilms and nanowires of *Geobacter sulfurreducens*. *Energy Environ. Sci.* 5:8651. doi: 10.1039/c2ee22330a

Malvankar, N. S., Vargas, M., Nevin, K. P., Franks, A. E., Leang, C., Kim, B. C., et al. (2011). Tunable metallic-like conductivity in microbial nanowire networks. *Nat. Nanotechnol.* 6, 573–579. doi: 10.1038/nnano.2011.119

Malvankar, N. S., Vargas, M., Nevin, K., Tremblay, P. L., Evans-Lutterodt, K., Nykypanchuk, D., et al. (2015). Structural basis for metallic-like conductivity in microbial nanowires. *MBio* 6:e00084. doi: 10.1128/mBio.00084-15

Malvankar, N. S., Yalcin, S. E., Tuominen, M. T., and Lovley, D. R. (2014). Visualization of charge propagation along individual pili proteins using ambient electrostatic force microscopy. *Nat. Nanotechnol.* 9, 1012–1017. doi: 10.1038/nnano.2014.236

Moser, C. C., Page, C. C., Chen, X., and Dutton, P. L. (2000). "Electron transfer in natural proteins theory and design" in *Enzyme-catalyzed Electron and radical transfer: Subcellular biochemistry*. eds. A. Holzenberg and N. S. Scutton (New York, NY: Springer), 1–28.

Mostajabi Sarhangi, S., and Matyushov, D. V. (2023). Effect of water Deuteration on protein Electron transfer. *J. Phys. Chem. Lett.* 14, 723–729. doi: 10.1021/acs.jpclett.2c03690

Noy, D., Moser, C. C., and Dutton, P. L. (2006). Design and engineering of photosynthetic light-harvesting and electron transfer using length, time, and energy scales. *Biochim. Biophys. Acta Rev. Cancer* 1757, 90–105. doi: 10.1016/j.bbabio.2005.11.010

O'Brien, J. P. (2020). *A tale of two nanowires: The biochemical and spectroscopic characterization of the conductive cytochrome OmcS and OmcZ filaments of Geobacter Sulfurreducens*. [New Haven, CT]: Yale University.

Page, C. C., Moser, C. C., Chen, X., and Dutton, P. L. (1999). Natural engineering principles of electron tunnelling in biological oxidation–reduction. *Nature* 402, 47–52. doi: 10.1038/46972

Page, C. C., Moser, C. C., and Dutton, P. L. (2003). Mechanism for electron transfer within and between proteins. *Curr. Opin. Chem. Biol.* 7, 551–556. doi: 10.1016/j.cbpa.2003.08.005

Phan, H., Yates, M. D., Kirchhofer, N. D., Bazan, G. C., Tender, L. M., and Nguyen, T. Q. (2016). Biofilm as a redox conductor: a systematic study of the moisture and temperature dependence of its electrical properties. *Phys. Chem. Chem. Phys.* 18, 17815–17821. doi: 10.1039/C6CP03583C

Pokkuluri, P., Londer, Y., Duke, N., Pessanha, M., Yang, X., Orshonsky, V., et al. (2011). Structure of a novel dodecaheme cytochrome c from *Geobacter sulfurreducens* reveals an extended 12 nm protein with interacting hemes. *J. Struct. Biol.* 174, 223–233. doi: 10.1016/j.jsb.2010.11.022

Polizzi, N. F., Skourtis, S. S., and Beratan, D. N. (2012). Physical constraints on charge transport through bacterial nanowires. *Faraday Discuss.* 155, 43–61. doi: 10.1039/C1FD00098E

Reardon, P. N., and Mueller, K. T. (2013). Structure of the type IVa major pilin from the electrically conductive bacterial nanowires of *Geobacter sulfurreducens*. *J. Biol. Chem.* 288, 29260–29266. doi: 10.1074/jbc.M113.498527

Reguera, G., and Kashefi, K. (2019). The electrifying physiology of Geobacter bacteria, 30 years on. *Adv. Microb. Physiol.* 74, 1–96. doi: 10.1016/bs.ampbs.2019.02.007

Reguera, G., McCarthy, K. D., Mehta, T., Nicoll, J. S., Tuominen, M. T., and Lovley, D. R. (2005). Extracellular electron transfer via microbial nanowires. *Nature* 435, 1098–1101. doi: 10.1038/nature03661

Ru, X., Zhang, P., and Beratan, D. N. (2019). Assessing possible mechanisms of micrometer-scale electron transfer in heme-free *Geobacter sulfurreducens* pili. *J. Phys. Chem. B* 123, 5035–5047. doi: 10.1021/acs.jpcb.9b01086

Shapiro, D. M., Mandava, G., Yalcin, S. E., Arranz-Gibert, P., Dahl, P. J., Shipps, C., et al. (2022). Protein nanowires with tunable functionality and programmable self-assembly using sequence-controlled synthesis. *Nat. Commun.* 13:829. doi: 10.1038/s41467-022-28206-x

Shipps, C. (2022). *Electrons on the move in proteins: Microbial cytochrome nanowires in extracellular Electron transfer and as functional materials*. [New Haven (CT)]: Yale University.

Shu, C., Xiao, K., and Sun, X. (2017). Structural basis for the influence of A1, 5A, and W51W57 mutations on the conductivity of the *Geobacter sulfurreducens* pili. *Crystals* 8:10. doi: 10.3390/cryst8010010

Shu, C., Xiao, K., and Sun, X. (2020). Structural basis for the high conductivity of microbial pili as potential nanowires. *J. Nanosci. Nanotechnol.* 20, 64–80. doi: 10.1166/jnn.2020.16883

Shu, C., Zhu, Q., Xiao, K., Hou, Y., Ma, H., Ma, J., et al. (2019). Direct extracellular electron transfer of the *Geobacter sulfurreducens* pili relevant to interaromatic distances. *BioMed. Res. Int.* 2019:6151587. doi: 10.1155/2019/6151587

Strycharz-Glaven, S. M., Snider, R. M., Guiseppi-Elie, A., and Tender, L. M. (2011). On the electrical conductivity of microbial nanowires and biofilms. *Energy Environ. Sci.* 4:4366. doi: 10.1039/c1ee01753e

Strycharz-Glaven, S. M., and Tender, L. M. (2012). Reply to the 'comment on "on electrical conductivity of microbial nanowires and biofilms"' by S. M. Strycharz-Glaven, R. M. Snider, A. Guiseppi-Elie and L. M. Tender, Energy Environ. Sci., 2011, 4, 4366. *Energy Environ. Sci.*, 5, 6250–6255. doi: 10.1039/C2EE03056J

Summers, Z. M., Fogarty, H. E., Leang, C., Franks, A. E., Malvankar, N. S., and Lovley, D. R. (2010). Direct exchange of electrons within aggregates of an evolved syntrophic coculture of anaerobic bacteria. *Science* 330, 1413–1415. doi: 10.1126/science.1196526

Tan, Y., Adhikari, R. Y., Malvankar, N. S., Pi, S., Ward, J. E., Woodard, T. L., et al. (2016a). Synthetic biological protein nanowires with high conductivity. *Small* 12, 4481–4485. doi: 10.1002/smll.201601112

Tan, Y., Adhikari, R. Y., Malvankar, N. S., Ward, J. E., Nevin, K. P., Woodard, T. L., et al. (2016b). The low conductivity of *Geobacter uraniireducens* pili suggests a diversity of extracellular electron transfer mechanisms in the genus Geobacter. *Front. Microbiol.* 7:980. doi: 10.3389/fmicb.2016.00980

Tan, Y., Adhikari, R. Y., Malvankar, N. S., Ward, J. E., Woodard, T. L., Nevin, K. P., et al. (2017). Expressing the *Geobacter metallireducens* PilA in *Geobacter sulfurreducens* yields pili with exceptional conductivity. *MBio* 8:e02203-16. doi: 10.1128/mbio.02203-16

Taylor, P., Pealing, S. L., Reid, G. A., Chapman, S. K., and Walkinshaw, M. D. (1999). Structural and mechanistic mapping of a unique fumarate reductase. *Nat. Struct. Biol.* 6, 1108–1112.

Tran, H. T. (2009) *Investigation of chemotaxis genes and their functions in Geobacter species*, Amherst, MA University of Massachusetts.

Ueki, T., Walker, D. J., Woodard, T. L., Nevin, K. P., Nonnenmann, S. S., and Lovley, D. R. (2020). An *Escherichia coli* chassis for production of electrically conductive protein nanowires. *ACS Synth. Biol.* 9, 647–654. doi: 10.1021/acssynbio.9b00506

van Wonderen, J. H., Adamczyk, K., Wu, X., Jiang, X., Piper, S. E. H., Hall, C. R., et al. (2021). Nanosecond heme-to-heme electron transfer rates in a multiheme cytochrome nanowire reported by a spectrally unique his/met-ligated heme. *Proc. Natl. Acad. Sci. U. S. A.* 118:e2107939118. doi: 10.1073/pnas.2107939118

van Wonderen, J. H., Hall, C. R., Jiang, X., Adamczyk, K., Carof, A., Heisler, I., et al. (2019). Ultrafast light-driven Electron transfer in a Ru(II)tris(bipyridine)-labeled Multiheme cytochrome. *J. Am. Chem. Soc.* 141, 15190–15200. doi: 10.1021/jacs.9b06858

Vargas, M., Malvankar, N. S., Tremblay, P.-L., Leang, C., Smith, J. A., Patel, P., et al. (2013). Aromatic amino acids required for pili conductivity and long-range extracellular electron transport in *Geobacter sulfurreducens*. *MBio* 4:e00105-13. doi: 10.1128/mbio.00105-13

Walker, D. J., Martz, E., Holmes, D. E., Zhou, Z., Nonnenmann, S. S., and Lovley, D. R. (2019). The archaellum of *Methanospirillum hungatei* is electrically conductive. *MBio* 10:e00579-19. doi: 10.1128/mbio.00579-19

Wang, F., Chan, C. H., Suciu, V., Mustafa, K., Ammend, M., Hochbaum, A. I., et al. (2022a). Structure of Geobacter OmcZ filaments suggests extracellular cytochrome polymers evolved independently multiple times. *eLife* 11:e81551. doi: 10.7554/eLife.81551

Wang, F., Gu, Y., O'Brien, J. P., Sophia, M. Y., Yalcin, S. E., Srikanth, V., et al. (2019). Structure of microbial nanowires reveals stacked hemes that transport electrons over micrometers. *Cell* 177:e10, 361–369.e10. doi: 10.1016/j.cell.2019.03.029

Wang, F., Mustafa, K., Suciu, V., Joshi, K., Chan, C. H., Choi, S., et al. (2022b). Cryo-EM structure of an extracellular Geobacter OmcE cytochrome filament reveals tetrahaem packing. *Nat. Microbiol.* 7, 1291–1300. doi: 10.1038/s41564-022-01159-z

Xiao, K., Malvankar, N. S., Shu, C., Martz, E., Lovley, D. R., and Sun, X. (2016). Low energy atomic models suggesting a pilus structure that could account for electrical conductivity of *Geobacter sulfurreducens* pili. *Sci. Rep.* 6:23385. doi: 10.1038/srep23385

Yalcin, S. E., and Malvankar, N. S. (2020). The blind men and the filament: understanding structures and functions of microbial nanowires. *Curr. Opin. Chem. Biol.* 59, 193–201. doi: 10.1016/j.cbpa.2020.08.004

Yalcin, S. E., O'Brien, J. P., Gu, Y., Reiss, K., Yi, S. M., Jain, R., et al. (2020). Electric field stimulates production of highly conductive microbial OmcZ nanowires. *Nat. Chem. Biol.* 16, 1136–1142. doi: 10.1038/s41589-020-0623-9

Yan, H., Chuang, C., Zhugayevych, A., Tretiak, S., Dahlquist, F. W., and Bazan, G. C. (2015). Inter-aromatic distances in *Geobacter Sulfurreducens* pili relevant to biofilm charge transport. *Adv. Mat.* 27, 1908–1911. doi: 10.1002/adma.201404167

Yates, M. D., Golden, J. P., Roy, J., Strycharz-Glaven, S. M., Tsoi, S., Erickson, J. S., et al. (2015). Thermally activated long range electron transport in living biofilms. *Phys. Chem. Chem. Phys.* 17, 32564–32570. doi: 10.1039/C5CP05152E

Yates, M. D., Strycharz-Glaven, S. M., Golden, J. P., Roy, J., Tsoi, S., Erickson, J. S., et al. (2016). Measuring conductivity of living *Geobacter sulfurreducens* biofilms. *Nat. Nanotechnol.* 11, 910–913. doi: 10.1038/nnano.2016.186

Zhao, J., and Davis, J. J. (2003). Force dependent metalloprotein conductance by conducting atomic force microscopy. *Nanotechnology* 14, 1023–1028. doi: 10.1088/0957-4484/14/9/317

Zhao, J., Davis, J. J., Sansom, M. S., and Hung, A. (2004). Exploring the electronic and mechanical properties of protein using conducting atomic force microscopy. *J. Am. Chem. Soc.* 126, 5601–5609. doi: 10.1021/ja039392a

Check for updates

Seed endophytes and rhizosphere microbiome of *Imperata cylindrica*, a pioneer plant of abandoned mine lands

Wenqin Mao[1†], Ying Wu[2†], Qiaohong Li[2], Yingying Xiang[3], Wenting Tang[1], Haiyan Hu[4], Xiuling Ji[1] and Haiyan Li[1*]

[1]Life Science and Technology and Medical Faculty, Kunming University of Science and Technology, Kunming, China, [2]The First People's Hospital of Yunnan Province, Kunming, China, [3]The Affiliated Yanan Hospital of Kunming Medical University, Kunming, China, [4]State Key Laboratory of Environmental Geochemistry, Institute of Geochemistry, Chinese Academy of Sciences, Guiyang, China

Some plant-associated microorganisms could improve host plants biotic and abiotic stress tolerance. *Imperata cylindrica* is a dominant pioneer plant in some abandoned mine lands with higher concentrations of heavy metal (HM). To discover the specific microbiome of *I. cylindrica* in this extreme environment and evaluate its role, the microbiome of *I. cylindrica*'s seeds and rhizosphere soils from HM heavily contaminated (H) and lightly contaminated (L) sites were studied. It was found that HM-contamination significantly reduced the richness of endophytic bacteria in seeds, but increased the abundance of resistant species, such as *Massilia* sp. and *Duganella* sp. Spearman's rank correlation coefficient analysis showed that both *Massilia* sp. and *Duganella* sp. showed a significant positive correlation with Zn concentration, indicating that it may have a strong tolerance to Zn. A comparison of the microbiome of rhizosphere soils (RS) and adjacent bare soils (BS) of site H showed that *I. cylindrica* colonization significantly increased the diversity of fungi in rhizosphere soil and the abundance of Ascomycota associated with soil nutrient cycling. Spearman's rank correlation coefficient analysis showed that Ascomycota was positively correlated with the total nitrogen. Combined with the fact that the total nitrogen content of RS was significantly higher than that of BS, we suppose that Ascomycota may enhance the nitrogen fixation of *I. cylindrica*, thereby promoting its growth in such an extreme environment. In conclusion, the concentration of HM and nutrient contents in the soil significantly affected the microbial community of rhizosphere soils and seeds of *I. cylindrica*, in turn, the different microbiomes further affected soil HM concentration and nutrient contents. The survival of *I. cylindrica* in HM severely contaminated environment may mainly be through recruiting more microorganisms that can enhance its nutrition supply.

1 Introduction

In the past 100 years, with the continuous progress and development of human society, the scale and intensity of mineral resources have increased (Gutierrez, 2020). However, during resource extraction, a large quantity of mineral waste was produced, which contains many toxic and harmful substances and poses a potential threat to the environment (Trannum et al., 2020; Xie and van Zyl, 2020). Revegetation is a plant-based technology for *in situ* restoration (Zhou et al., 2020). Vegetation restoration is environmentally sustainable and less costly than traditional physicochemical techniques (Mendez and Maier, 2008). Due to the characteristics of high heavy metal (HM) content, barren soil, and low microbial activity in the tailing area, it is generally difficult for plants to survive (De la Iglesia et al., 2006; Ginocchio et al., 2017). A previous study found that the role of the dominant plant species (*Imperata cylindrica*) was found to be important in the restoration of the plant community in the mining district (Jia et al., 2020). *I. cylindrica*, a gramineous genus, is a common plant in the wasteland and exposed tailing areas. Its rhizomes are well-developed, which can maximize the nutrients in the soil and have strong adaptability to extreme environments (Song et al., 2019). *I. cylindrica* has been shown to grow as an HMs accumulator plant in the mining district (Shaltout et al., 2016; Mahdavian et al., 2017; Li et al., 2018; Vidal et al., 2021). Previous studies showed that microbial colonization could enhance nutrient uptake and HM resistance of *I. cylindrica*, thereby promoting its growth in HM-stress environment (Jia et al., 2019; Liang et al., 2023).

Seeds are carriers of many endophytes. Seed endophytes are mostly passed down from generation to generation by vertical transmission, so they become the basis for the establishment of the plant endophyte community (Mao et al., 2023). Seed endophytes not only improve the viability and germination rate of seeds but also promote the growth and development of plants, thus enhancing the biotic and abiotic stress resistance of the host plant (Santoyo et al., 2016; Shahzad et al., 2016). For example, Parmar et al. (2022) found that seed endophyte *Epicoccum nigrum* (FZT214) can directly affect the reclaimed plants by utilizing hormone regulation and antioxidant stress, to alleviate HM stress in the mine environment and promote plant growth and "site fitness." In addition, when the pioneer plant seeds migrated to the exposed tailing area, the endophytic bacteria could provide some nutrients for the pioneer plant by producing plant hormones, phosphorus solubilizing, potassium solubilizing, and nitrogen-fixing (Islam et al., 2021). Wang et al. (2020) and Mahmud et al. (2021) found that *Epichloë* can give plants stronger environmental tolerance by adjusting soil physical and chemical properties and changing the soil microbiome. Therefore, in the process of vegetation reclamation in the exposed tailing area, seed endophytes can significantly promote seed colonization, germination, and seedling growth of pioneer plants, enhance their heavy metal resistance, and facilitate vegetation reclamation in the tailing area (Ultra and Manyiwa, 2021).

Soil microorganisms can change the soil pH value, the physical, and chemical properties, and soil respiration rate, etc. by producing various active ingredients and play an extremely important role in soil nutrient cycling, organic matter content, biogeochemical cycling, and plant biomass (Zhao et al., 2021; Naz et al., 2022). Zhao et al. (2021) found that different vegetation reclamation modes in mining areas have different soil microbial communities, which in turn feed on the development of the plant community. Gazitúa et al. (2021) confirmed

the important role of the soil microbiome in mining adaptability, early colonization, and pioneer plant growth. Therefore, soil biomes play a key role in the restoration of degraded terrestrial ecosystems (Dangi et al., 2012; Cheng et al., 2022).

However, the role of microorganisms on pioneer plants' survival in the tailing area with higher concentrations of HM is still unknown. It was supposed that the pioneer plant growing in HM heavily contaminated sites may contain some special seed endophytes, which benefited them to grow in these extreme environments. And the colonization of these pioneer plants may further change the rhizosphere microbial community, which benefit the other plants growth by colonization of these special endophytes in heavy metals contaminated areas. Therefore, in the present study, culture-independent technology was used to analyze the microbial communities of seeds and rhizosphere soils of *I. cylindrica*, a pioneer plant of an abandoned Pb-Zn tailing area.

2 Methods

2.1 Study sites, seed and soil sampling

The study site located in Puxiong town, Jianshui county, Yunnan province, Southwest China. One sampling site is the Pb-Zn tailing area (site H-HM heavily contaminated) (23°30′26″ N, 103°1′13″ E), with an altitude of 1924.9 m, and the vegetation was sparse, *I. cylindrica* was a dominant pioneer plant there. The other sampling site L (site L-HM lightly contaminated) is 5 km away from site H (23°30′21″ N, 103°2′18″ E), with an altitude of 1896.5 m. Soil contents of total potassium (TK) and total phosphorus (TP) were significantly lower at L site than at H site. And the concentrations of Pb, Zn, and Cd at L site were significantly lower than those at H site ($p < 0.05$, t-test) (Table 1). The sample was collected on November 25, 2020.

The S-type sampling method was used to randomly select 15 healthy plants from sites H and L respectively, about 40 m² area of each site were chosen for sampling and the rhizosphere soil was collected by shaking root method (Teixeira et al., 2010). Simultaneously, the background soil (without plants growing) at a depth of 5–10 cm adjacent to the sampling plants was collected. Each sample was placed separately into a sterile plastic bag, labeled, and transported to the laboratory, and the seeds were surface sterilized within 24 h. *I. cylindrica* seeds from site H and L were mixed, respectively, and evenly divided into three portions, and 0.25 ± 0.023 g was taken from each portion. Then, the seeds were surface sterilized by immersing in 75% (v/v) ethanol for 2.5 min, and were extensively rinsed with sterile distilled water five times, followed by repeating the above procedures one time (Li et al., 2012). The efficacy of the surface sterilization was checked by following the imprint method. Meanwhile, 20 ± 0.75 g soils were taken from BS and RS of site H. Thereafter, the samples were homogenized in liquid nitrogen. The seeds and soil samplings were then stored to −80°C, respectively.

2.2 Soil properties

The soils were ground using a high-speed blender, and the content of Pb, Zn, total nitrogen, total phosphorus, and total potassium were determined by Inductively Coupled Plasma-Atomic Emission

TABLE 1 The chemical properties of soils from two sites (mean ± SD).

Sample	TN (mg/kg)	TP (mg/kg)	TK (mg/kg)	Pb (mg/kg)	Zn (mg/kg)	Cd (mg/kg)	pH
H (BS)	381 ± 19.67	545.33 ± 6.69	11521.33 ± 718.14	3119.33 ± 201	1360.67 ± 40.08	2.89 ± 0.06	6.65 ± 0.11
RS	523 ± 18.23*	432 ± 18.58*	5266.67 ± 693.15*	1869.67 ± 167.49*	1083 ± 41.9*	2.83 ± 0.28	7.12 ± 0.02*
L	974.67 ± 34.28*	408.33 ± 3.38*	17341 ± 457.2*	123 ± 6.24*	161 ± 4.04*	0.66 ± 0.26*	6.86 ± 0.04

"*" indicates that the value is significantly different from the mean of site H (BS) (*$p < 0.05$, t-test), means ± SD ($n = 3$).
TN, Total Nitrogen; TP, Total Phosphorus; TK, Total Potassium. H, Heavy metal heavily contaminated site; L, Heavy metal lightly contaminated site; BS, Bare soils of site H; RS, Rhizosphere soils of site H.

Spectrometry (ICP-AES) (Li et al., 2016), and the concentration of Cd was analyzed by Inductively Coupled Plasma-Mass Spectrometry (ICP-MS) (Chen et al., 2022).

2.3 The microbiome of seed endophytes and soils

2.3.1 DNA extraction and PCR amplification

The total genomic DNA was extracted taking approximately 0.2 mg of homogenized powdered samples using the MoBio PowerSoil® DNA Isolation Kit (MO BIO Laboratories, Inc., Carlsbad, CA, United States) following the manufacturer's protocol. Extracted DNA was verified by electrophoresis on a 1.5% (w/v) agarose gel. The qualified DNA samples were stored at −20°C for subsequent analyses.

Amplification of the seed endophytic bacterial 16S rRNA V3-V4 region was performed using primer 799F (5'-AACMGGATTA GATACCCKG-3') and 1193R (5'-ACGTCATCCCCACCTTCC-3') resulting in amplicons of approximately 394 bp. And amplification of the soil bacterial 16S rRNA V3-V4 region was performed using primer 338F (5'-ACTCCTACGGGAGGCAGCAG-3') and 806R (5'-GGACTACH VGGGTWTCTAAT-3') resulting in amplicons of approximately 468 bp. In addition, amplification of the fungal 18S ITS1 (internal transcribed spacer 1) region was performed using primer ITS1-F (5'-CTTGGTCA TTTAGAGGAAGTAA-3') and ITS2-R (5'-GCTGCGTTCTTCAT CGATGC-3') resulting in amplicons of approximately 350 bp. PCR reactions were performed in a 25 μL volume and contained: 2.5 μL 10× PCR buffer, 1.5 μL Mg²⁺ (25 mM MgCl₂), 2.5 μL dNTP mixture (4 mM each), 0.5 μL KOD-PlusNeo (1 units μL⁻¹; TOYOBO), 1 μL Template DNA (0.4 ng), 2.5 μL primer (10 μM each) and 14.5 μL sterilized double-distilled H₂O. The PCR program consisted of an initial denaturation step at 94°C for 5 min, followed by 30 cycles of denaturation at 94°C for 20 s, annealing at 50°C for 30 s, elongation at 72°C for 30 s, with a final extension of 5 min at 72°C. The PCR products were purified with an OMEGA Gel Extraction Kit (Omega Bio-Tek, United States) according to the manufacturer's protocol. The resulting amplicons were subsequently subjected to high-throughput sequencing using the Illumina MiSeq platform (Illumina, 2013). All steps were implemented at Shanghai Majorbio Bio-pharm Technology Company (Shanghai, China). The Illumina sequencing data are available in the NCBI Sequence Read Archive (SRA) repository with the BioProject accession number PRJNA1037316.

2.3.2 Analysis of sequence data

The raw Illumina MiSeq sequencing data were obtained in FASTA files along with sequencing quality files. Paired-end reads from the original DNA fragments theoretically were merged using FLASH v.1.2.11, and files were accessed using MOTHUR v.1.30.2 bioinformatics software for further processing and analyses. All sequences were denoised before barcodes, and primers were removed. The cleaned-up sequences were aligned and classified along known sequences in the SILVA v.138 rRNA database. Next, chimeric sequences were detected using the UCHIME algorithm, and the remaining sequences were assigned to OTUs based on a 97% similarity criterion. Rarefaction curves were performed to check the sample adequacy using a 50 sequence increment. Finally, taxonomic information for each OTU was used the RDP Classifier v.2.13 at 0.5 confidence threshold (Wang et al., 2007). To indicate the microbial diversity in seeds, the α-diversity indices (including Shannon's H′ and Ace indices) were quantified in terms of OTU richness.

2.3.3 Statistical analysis

Relative abundance differences among different groups were detected by Kruskal-Wallis (KW) sum-rank test. A t-test was used to estimate the difference of α-diversity indices of seed endophytes between sites H and L and soil microbiome between RS and BS. All statistical analyses were performed with SPSS 27.

3 Results

3.1 The effect of soil HM-contamination on seed endophyte diversity and community structure

3.1.1 Seed bacterial endophytes

The OTUs of endophytic bacterial in seeds were more abundant at site L (537) than at site H (313), and 208 OTUs were shared by both two sites (Figure 1A). Rank-Abundance curve showed that the richness of seed endophytic bacteria at site L was relatively higher than that at site H (Figure 1B).

The results of 16S rRNA sequencing of seed endophytic bacterial were assigned to 19 phyla, 37 classes, 111 orders, 191 families, and 358 genera. Proteobacteria displayed the most relative abundance with sites H and L accounting for 77.01 and 60.41%, respectively (Figure 1C). At genus level, *Sphinomonas* sp. was the most dominant genus at both sites, and its relative abundance consists 36.08% at site L and 15.74% at site H. *Erwinia* sp. (13.51%) ($p = 0.0495$, Kruskal-Wallis sum-rank test) and *Massilia* sp. (13.16%) ($p = 0.0495$, Kruskal-Wallis sum-rank test) were also dominant genera at site H (Figure 1D), and their relative abundance at site H was significantly higher than that at site L (Figure 1E). Meanwhile, *Erwinia* sp. and *Massilia* sp. are also the indicator species of seed endophytic bacterial at site H at genus level (Figure 1E). It was found that the soil HM-contamination significantly decreased the richness of seed endophytic bacterial ($p = 0.0398$, t-test; Ace index; Table 2).

FIGURE 1
The diversity of seed bacterial endophytes of *I. cylindrica* from different heavy metal–contaminated environments. **(A)** The Venn diagram analysis of OTUs. **(B)** The rank curve based on OTU abundance. **(C,D)** Relative abundance of seed endophytic bacterial at phylum and genus level. **(E)** The indicator species of seed endophytic bacterial at genus level. H, Heavy metal heavily contaminated site; L, Heavy metal lightly contaminated site.

3.1.2 Seed fungal endophytes

The OTUs of endophytic fungal in seeds were more abundant at site H (402) than at site L (343), and 240 OTUs were shared by both two sites (Figure 2A). Rank-Abundance curve indicated that the richness of seed endophytic fungi at site H was relatively higher than that at site L (Figure 2B).

The results of ITS sequencing of seed endophytic fungal were assigned to 6 phyla, 323 classes, 56 orders, 123 families, and 222 genera. Ascomycota was the most dominant fungal phylum (Figure 2C). At genus level, *Epicoccum* sp. displayed the most relative abundance in both sites H and L, with 44.78 and 55.91%, respectively. Other dominant genera in site H followed by *Cladosporium* sp.

Seed endophytes	Sample	Shannon's H′	Ace
Bacteria	H	3.07 ± 0.07	247.14 ± 14.24
	L	2.71 ± 0.14	323.95 ± 17.81*
Fungi	H	2.3 ± 0.19	299.6 ± 49.29
	L	1.96 ± 0.14	263.01 ± 13.66

"*" Indicates that the value is significantly different from the mean of site H (*$p < 0.05$, *t*-test). H, Heavy metal heavily contaminated site; L, Heavy metal lightly contaminated site.

(17.87%) and unclassified Phaeosphaeriaceae (7.57%), with higher relative abundance than site L (Figure 2D), but neither of them was a indicator species at site H at genus level (Figure 2E). According to α-diversity analysis, it was found that *I. cylindrica* seed endophytic fungal diversity and richness of site H were higher than site L, but the difference was not significant (Table 2).

3.1.3 The effect of environmental factors on seed endophyte community

The contents of HMs (Cd, Pb, Zn) at site H were significantly higher than those at site L, while the contents of nutrients (TN and TK) at site L were significantly higher than those at site H (Table 1). *Massilia* sp. had the highest relative abundance of seed endophytic bacteria of *I. cylindrica* in site H. Spearman's rank correlation coefficient analysis showed a significant positive correlation between *Massilia* sp. and Zn (Figure 3A). In addition, the result showed that *Cladosporium* sp. was negatively correlated with pH. Similarly, *Microdochium* sp. was a relatively dominant fungus at site H, and its abundance was significantly different from that at site L. Spearman's rank correlation coefficient analysis indicated that *Microdochium* sp. was significantly positively correlated with TP and Pb (Figure 3B).

3.2 The effect of HM-contamination on soil microbial diversity and community structure

3.2.1 Microbial diversity of bare soils and rhizosphere soils of *Imperata cylindrica* in HM heavily contaminated site

A total of 263,311 and 355,189 sequences high-quality of bacteria and fungi were obtained after demultiplexing and filtration steps. The mean number of valid bacterial sequences was 31,563, whereas the mean number of valid fungal sequences was 32,254. These sequences were divided into 2,434 and 1,933 different OTUs, respectively, with 97% similarity.

The results of 16S rRNA sequencing of soil bacterial were assigned to 32 phyla, 91 classes, 312 orders, 316 families, and 570 genera. Actinobacteriota displayed the most relative abundance in both soil samples (Figure 4A). At genus level, *Rhodococcus* sp. was the most dominant genus in BS (Bare soil) (9.90%). Contrary to this, the most dominant genus of RS (Rhizosphere soil) was *Antrobacter* sp. (8.99%). Many OTUs were unclassified at genus level in both soil samples (Figure 4B). The results of α-diversity (Shannon's H′ and Ace indexes)

analysis indicated that BS and RS was not significantly different (Figures 4C,D).

The results of ITS sequencing of soil fungal were assigned to 9 phyla, 37 classes, 98 orders, 233 families, and 497 genera. Ascomycota displayed the most relative abundance in both soil samples (Figure 5A), and the relative abundance of RS was significantly higher than that of BS ($p = 0.0495$, Kruskal-Wallis sum-rank test) (Figure 5B). At the same time, Ascomycota is also the indicator species of soil fungal at phylum level of RS (Figure 5B). At genus level, unclassified Ascomycota and unclassified Didymellaceae were the most dominant fungi in BS (15.03%) and in RS (10.28%) (Figure 5C). The results of Ace index indicating that the species richness of RS was significantly higher than that of BS ($p = 0.0237$, *t*-test) (Figure 5D), while the results of Shannon index showed that the diversity of the two soil samples was not significantly different (Figure 5E).

3.2.2 The effect of environmental factors on bare soils and rhizosphere soils microbiome of *Imperata cylindrica* in HM heavily contaminated site

The contents of HMs (Pb and Zn) and nutrients (TP and TK) of BS were significantly higher than that of RS (Table 1). Mantel-test Network heatmap showed that at the phylum level, bacterial communities in BS were negatively correlated with Pb, while bacterial communities in RS were only positively correlated with TP and Cd, but the differences were not significant (Figure 6A). For fungi, at phylum level, Mantel-test Network heatmap shown that fungal communities in BS were positively correlated with TN, Cd, and pH, while fungal communities in RS were positively correlated with TN, Cd, Zn, and pH, but the differences were not significant (Figure 6B). Spearman's rank correlation coefficient analysis showed that *Rhodococcus* sp. was significantly positively correlated with Pb, Zn, and TK, and *Arthrobacter* sp. was significantly negatively correlated with TP at genus level (Figure 6C). For fungi, Spearman's rank correlation coefficient analysis indicated that Ascomycota was significantly positively correlated with TN, but significantly negatively correlated with TP (Figure 6D).

4 Discussion

Previous researches has demonstrated that *I. cylindrica* plays an important role in plant community restoration in the mining district (Zheng et al., 2019; Jia et al., 2020). Meanwhile, various research indicated that plant-associated microorganisms can enhance host plants' stress tolerance (Trivedi et al., 2020). However, the microbiome of pioneer plants growing in the bare mine tailing with higher concentrations of HMs as well as its role are still unknown. The present study indicated that HM contamination reduced the endophytic bacterial richness of *I. cylindrica* seeds. Proteobacteria was the most dominant of *I. cylindrica* seeds in site H. Some studies have established that Proteobacteria is relatively more abundant in plants growing in HM-contamination environments, as it is composed of many facultative anaerobic members that can survive in extreme pH environments, proving to be taxa most tolerant to HMs (Sun et al., 2010; Sánchez-López et al., 2018; Kasemodel et al., 2019). Simultaneously, some Proteobacteria are plant growth-promoting bacteria that have been proven to fix nitrogen symbiotically with host
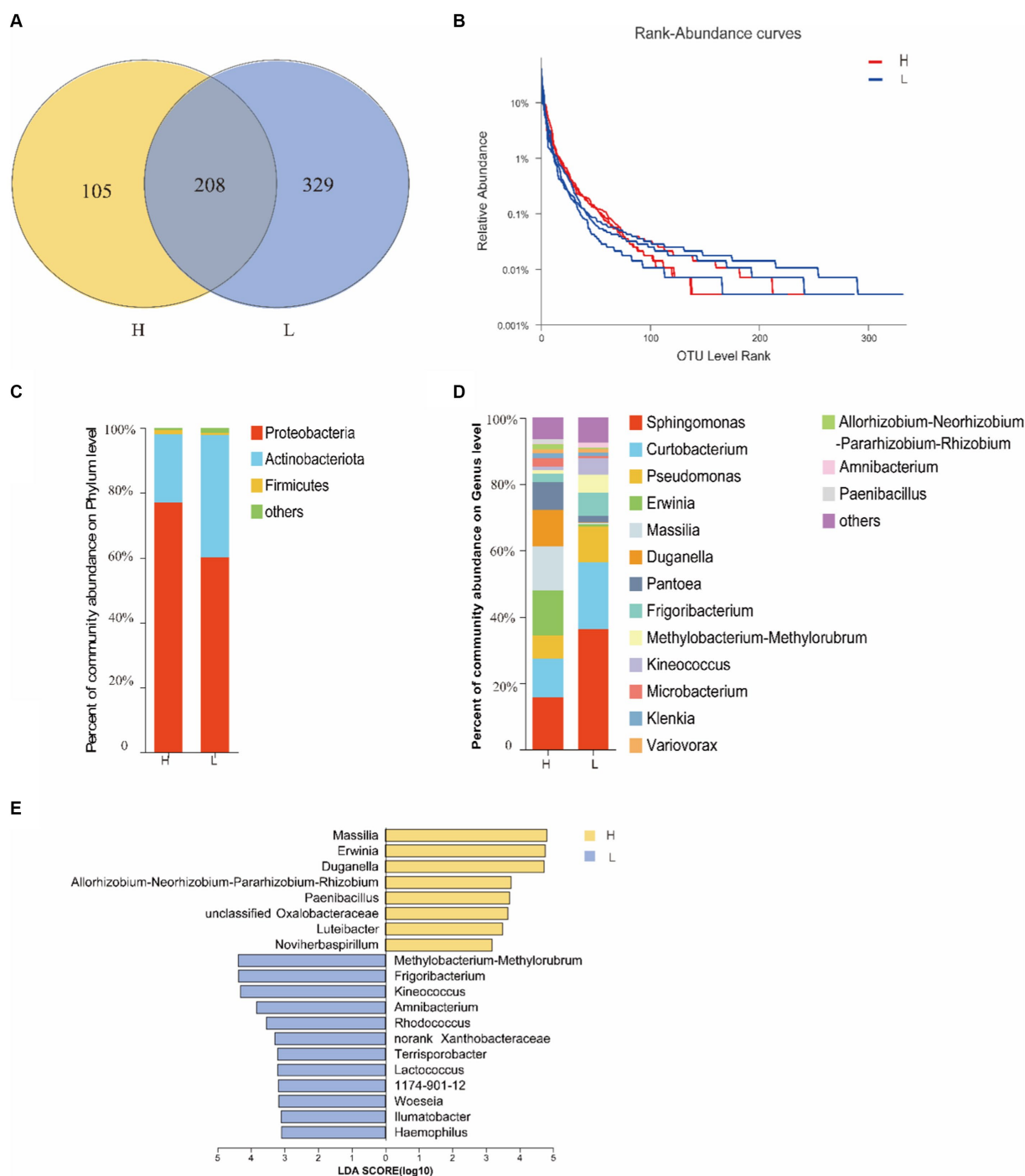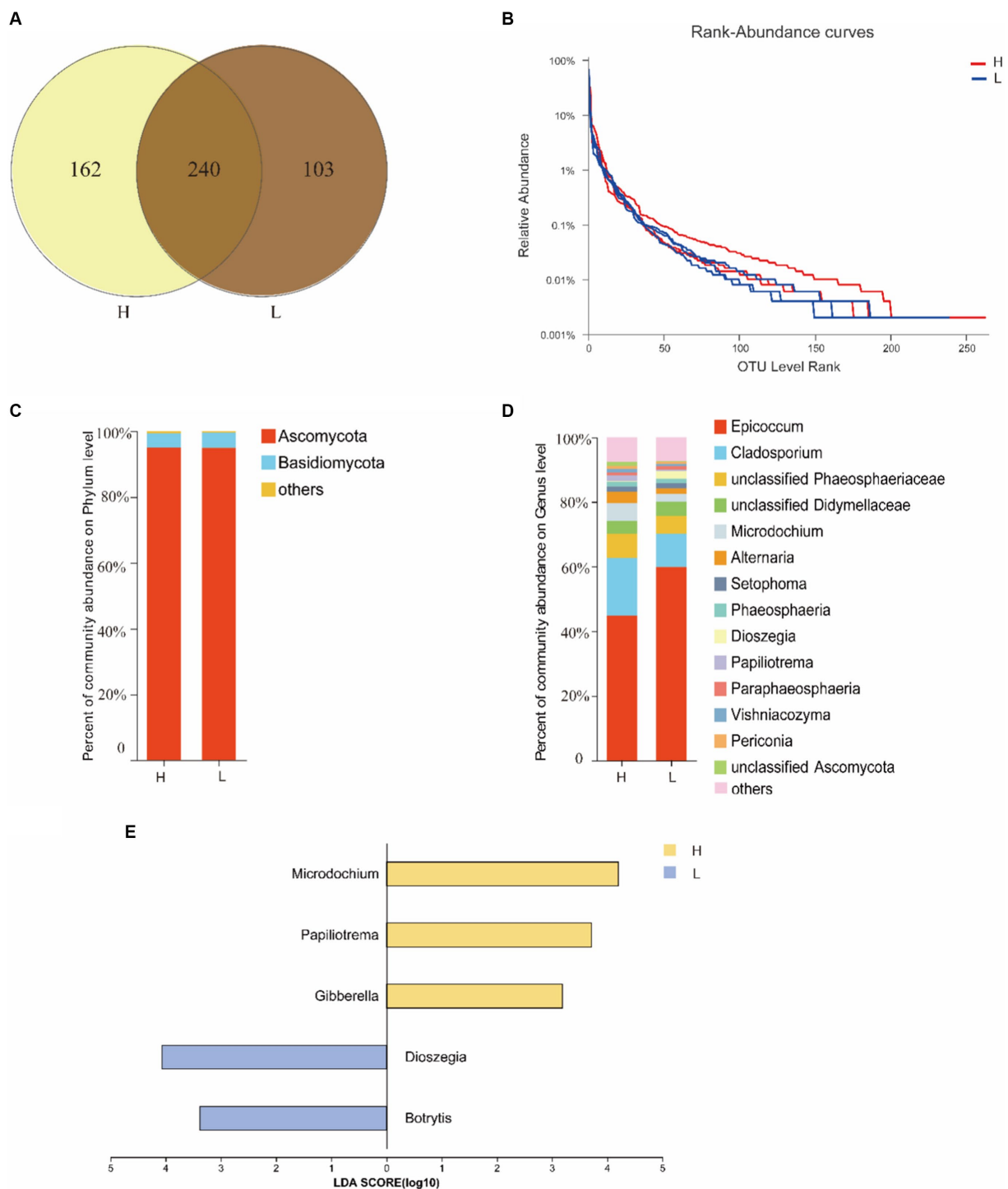
FIGURE 2

The diversity of seed fungal endophytes of *I. cylindrica* from different heavy metal-contaminated environments. **(A)** The Venn diagram analysis of OTUs. **(B)** The rank curve based on OTU abundance. **(C,D)** Relative abundance of seed endophytic fungal at phylum and genus level. **(E)** The indicator species of seed endophytic fungal at genus level. H, Heavy metal heavily contaminated site; L, Heavy metal lightly contaminated site.

plants (Wu et al., 2022). *Massilia* sp. is a genus of Proteobacteria. It was found to be a dominant genus in site H, and its relative abundance was significantly higher than that in site L. At the same time, it is an indicator species for seed endophytic bacterial in site H. Moreover, Spearman's rank correlation coefficient analysis demonstrated that *Massilia* sp. had a significant positive correlation with Zn

concentration in soils. Wang et al. (2021) found that *Massilia* was a potential Zinc-mobilizing species in soil and that it was significantly positively correlated with Zn concentration in wheat grains. Analogously, Wang et al. (2022) found that *Massilia* sp. had a significant positive relationship with DTPA-Pb (diethylene-triamine-pentaacetic-acid-Pb) in soils and Pb accumulation in roots. *Massilia*
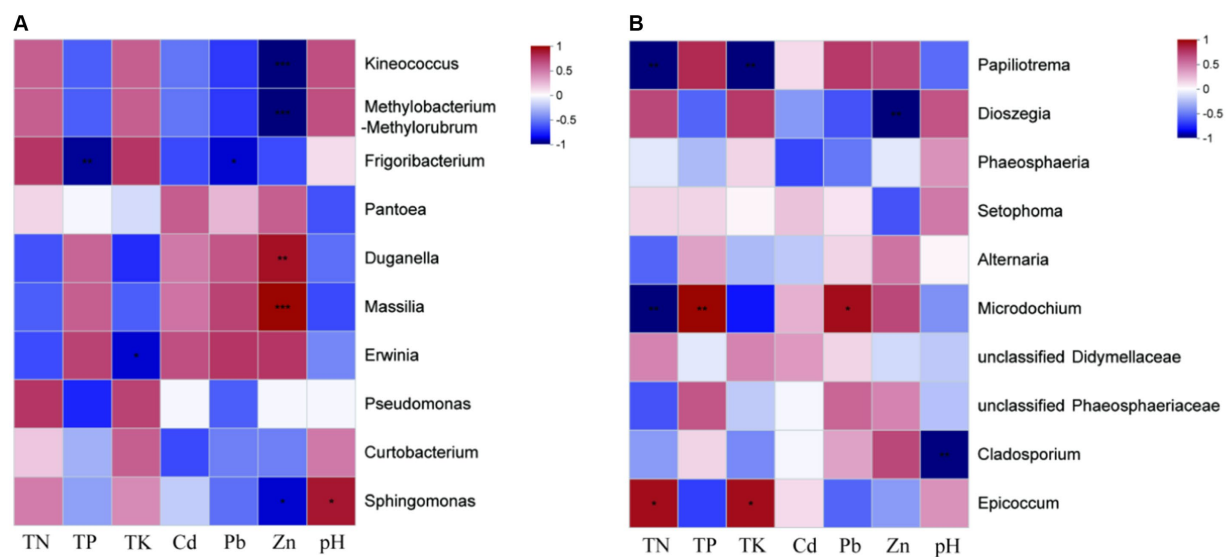
FIGURE 3

Spearman correlation heatmap of *I. cylindrica* seed endophytes at genus level. **(A)** Seed endophytic bacteria. **(B)** Seed endophytic fungi. "*" indicates statistically significant difference (*$p < 0.05$; **$p < 0.01$; ***$p < 0.001$).
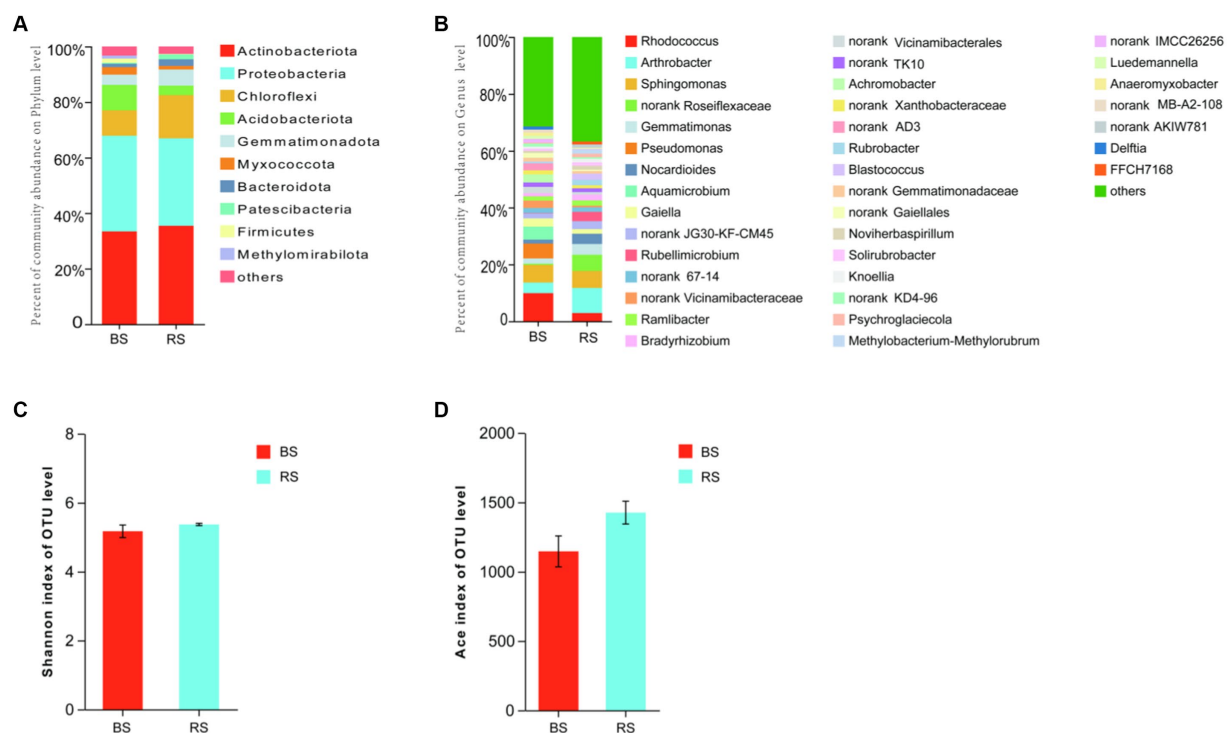
FIGURE 4

Bacterial diversity in bare soils and rhizosphere soils in HM heavily contaminated site. **(A,B)** Relative abundance of soil bacterial composition at the level of phylum and genus. **(C)** Shannon's H'. **(D)** Ace index. BS, Bare soils of site H; RS, Rhizosphere soils of site H.

sp. was isolated from sludge, farmland, and mining soils contaminated by heavy metals, suggesting that *Massilia* sp. is an important microorganism in HM-contaminated soils (Bensidhoum and Nabti, 2019). In addition, it has also been reported as *Massilia* sp. with strong phosphate solubilizing ability (Zheng et al., 2017). In terms of fungi, the diversity and richness of seed endophytes of *I. cylindrica* in site H were higher than those in site L, but the difference was not significant. The results indicated that HM contamination had no significant effect
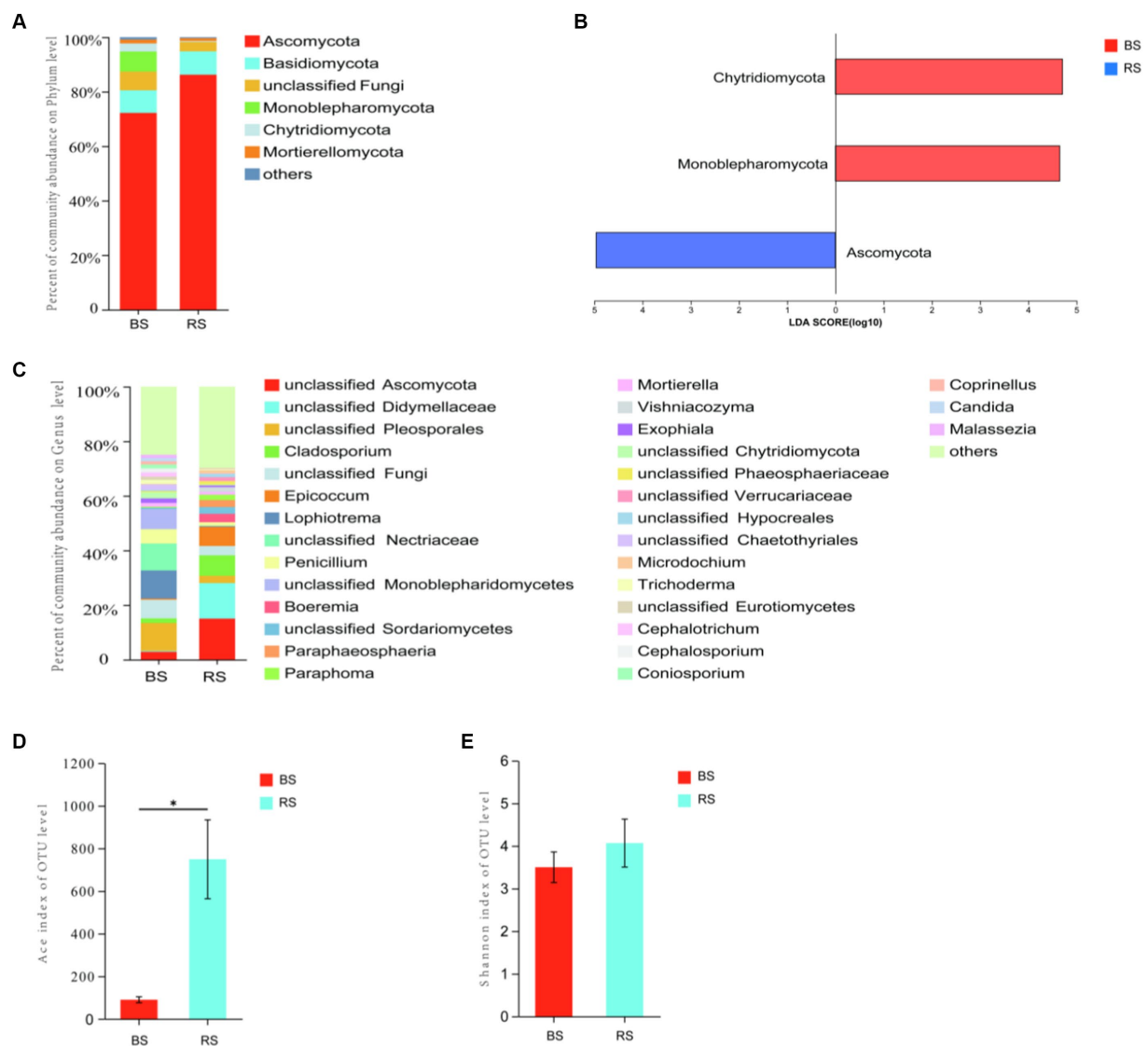
FIGURE 5
Fungal diversity in bare soils and rhizosphere soils in HM heavily contaminated site. **(A)** Relative abundance of soil fungal composition at the level of phylum. **(B)** The indicator species of soil fungal at phylum level. **(C)** Relative abundance of soil fungal composition at the level of genus. **(D)** Ace index. **(E)** Shannon's H'. "*" indicates statistically significant difference (*$p < 0.05$, t-test). BS, Bare soils of site H; RS, Rhizosphere soils of site H.

on seed endophytic fungal diversity and richness. However, relative abundance of *Microdochium* sp. in site H was significantly higher than that in site L. At the same time, it is an indicator species for endophytic fungi in seeds in site H. It was found that *Microdochium* sp. could promote the growth of *Hordeum vulgare* L. under Cd stress, and significantly increase Cd accumulation in barley roots (Shadmani et al., 2021). In addition, it has been reported that *Microdochium* sp. is well tolerant to Pb and it has also been found that the accumulation of Pb in *Microdochium* sp. increases with the concentration of Pb in the growth media (Parada et al., 2022). Similarly, our earlier study found that *Microdochium* sp. was tolerant to 2000 mg/L Pb. This was consistent with the results of correlation analysis of soil environmental factors, which showed a significant positive correlation between *Microdochium* sp. and Pb, indicating that its large presence in the seeds of *I. cylindrica* in the tailing area may improve the host's Pb-tolerance. At the same time, a previous study found that

Microdochium sp. is capable of synthesizing IAA *in vitro* (Rothen et al., 2018). Based on the above results, we supposed that *Massilia* sp. and *Microdochium* sp. may play an important role in the tailing area plant community restoration. For this reason, a series of pot experiments used to investigate the effects of *Massilia* sp. and *Microdochium* sp. on seed germination, plant growth, and rhizosphere microbiome reshaping of *I. cylindrica* is already in progress.

It is well known that in addition to endophytes, rhizosphere microorganisms also play an important role in the process of vegetation community restoration in the tailing area (Wang et al., 2023). Plant growth has been reported to alter the abundance of specific functional microorganisms (Sun et al., 2018; Zhu et al., 2023). In the present study, it was found that the microbial diversity and richness in rhizosphere soils of *I. cylindrica* were higher than those in bare soils, and there was a significant difference in fungal richness between the two soil samples. Ascomycota displayed the most relative
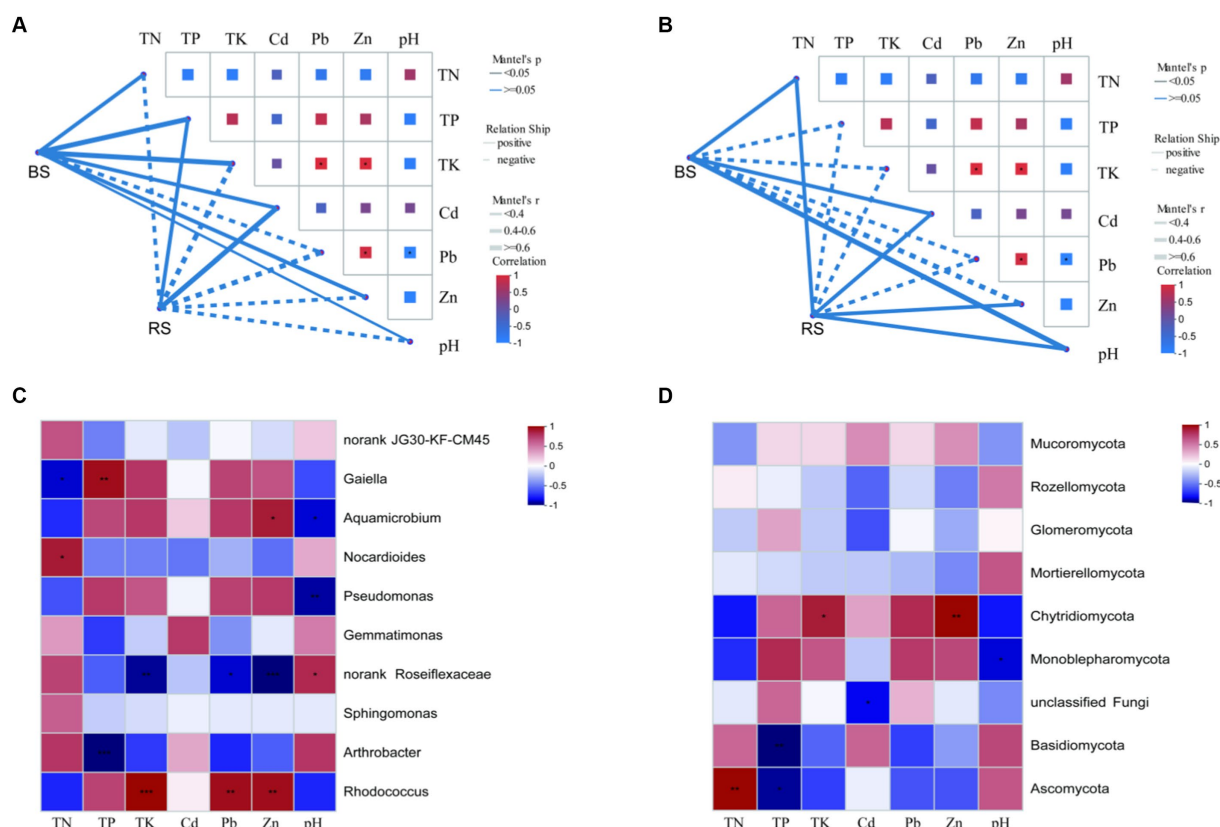
FIGURE 6
Heat map of bacterial and fungal correlation with environmental factors in bare soils and rhizosphere soils of HM heavily contaminated site. **(A,B)** Mantel-test Network heatmap of bacteria and fungi at phylum level. **(C)** Spearman's rank correlation coefficient heatmap of bacteria at genus level. **(D)** Spearman's rank correlation coefficient heatmap of fungi at phylum level. "*" indicates statistically significant difference (*$p < 0.05$; **$p < 0.01$). BS, Bare soils of site H; RS, Rhizosphere soils of site H.

abundance in rhizosphere soils, and it was significantly higher than that in bare soils. The same phenomenon was observed in other studies (Bourceret et al., 2016; Rosatto et al., 2019). We suggested that one of the reason for the higher relative abundance of Ascomycota in rhizosphere soils of *I. cylindrica* may be its ability to efflux complex spores providing extra-resistant against the toxicities of HMs (López-González et al., 2015; Liu et al., 2022). Simultaneously, Spearman correlation analysis showed that Ascomycota was positively correlated with total nitrogen content. Regarding bacteria, *Arthrobacter* sp. is the most dominant genus in rhizosphere soils, and its relative abundance in rhizosphere soils was significantly higher than that in bare soils. It has been demonstrated that *Arthrobacter* sp. not only contained HM-resistance genes but also strongly correlated with higher siderophore and IAA production (Rosatto et al., 2019; Senthil Kumar et al., 2023). Meanwhile, Wan et al. (2020) found that *Arthrobacter* sp. could utilize multiple phosphorus sources. Therefore, we suggested that to adapt HM-contamination environment, *I. cylindrica* recruits many beneficial microorganisms to colonize in the rhizosphere, which helps it enhance HM resistance and nutrient uptake.

Some studies have shown that endophytes can help host plants resist stressful environments by regulating root exudates and remodeling rhizosphere microbiome structure (Li et al., 2019; Wang et al., 2023). Jin et al. (2022) found that under Cd stress, inoculation of *Epichloe gansuensis* could increase the contents of organic acids and

amino acids in root exudates of *Achnatherum inebrians*, thereby recruiting different rhizosphere microbe and enhancing the host plant resistance to Cd stress. We suggested that the endophytic consortium in the seeds of *I. cylindrica* in the HM heavily contaminated site might increase the relative abundance of microorganisms in rhizosphere soils related to HM-fixation and soil nutrient cycling by regulating root exudates during plant growth, which would help plants adapt to HM stress (Liu et al., 2022). However, the functional mechanisms by which the interactions among plants, endophytes, and soils enhance the "site fitness" of host plants remain unclear. Studying the combined effects of endophytes and rhizosphere soil microorganisms can better reveal the reasons for the restoration of natural vegetation in the tailing area.

5 Conclusion

HM-contamination significantly reduced the richness of endophytic bacteria in seeds, but increased the abundance of resistant species. The colonization of *I. cylindrica* significantly increased the richness of fungi in rhizosphere soils. Ascomycota was positively correlated with the total nitrogen, and it may enhance the nitrogen fixation of *I. cylindrica*, thus promoting its growth in extreme environment. The survival of *I. cylindrica* in HM severely

contaminated environment may mainly be through recruiting more microorganisms that can enhance its nutrition supply. The study indicated that the seed endophytic community of *I. cylindrica* from HM heavily contaminated site differed from that of uncontaminated site, therefore, the future work will focus on discovering the function and mechanism of the special endophytes of pioneer plants from HM-contaminated site, and further exploring them in the tailing area restoration.

Data availability statement

The datasets presented in this study can be found in online repositories. The names of the repository/repositories and accession number(s) can be found at: https://www.ncbi.nlm.nih.gov/, PRJNA1037316.

Author contributions

WM: Conceptualization, Methodology, Writing – original draft, Writing – review & editing. YW: Conceptualization, Methodology, Writing – original draft, Writing – review & editing. QL: Formal analysis, Investigation, Writing – review & editing. YX: Formal analysis, Investigation, Writing – review & editing. WT: Formal analysis, Investigation, Supervision, Writing – review & editing. HH: Supervision, Writing – review & editing. XJ: Supervision, Writing – review & editing. HL: Conceptualization, Funding acquisition, Methodology, Writing – review & editing, Project administration, Resources.

Funding

Conflict of interest

The authors declare that the research was conducted in the absence of any commercial or financial relationships that could be construed as a potential conflict of interest.

Publisher's note

All claims expressed in this article are solely those of the authors and do not necessarily represent those of their affiliated organizations, or those of the publisher, the editors and the reviewers. Any product that may be evaluated in this article, or claim that may be made by its manufacturer, is not guaranteed or endorsed by the publisher.

References

Bensidhoum, L., and Nabti, E. (2019). "Plant growth-promoting bacteria for improving crops under saline conditions" in Microorganisms in saline environments: strategies and functions. eds. B. Giri and A. Varma (Cham: Springer International Publishing), 329–352.

Bourceret, A., Cébron, A., Tisserant, E., Poupin, P., Bauda, P., Beguiristain, T., et al. (2016). The bacterial and fungal diversity of an aged PAH- and heavy metal-contaminated soil is affected by plant cover and edaphic parameters. *Microb. Ecol.* 71, 711–724. doi: 10.1007/s00248-015-0682-8

Chen, W., Yang, Y., Fu, K., Zhang, D., and Wang, Z. (2022). Progress in ICP-MS analysis of minerals and heavy metals in traditional medicine. *Front. Pharmacol.* 13:891273. doi: 10.3389/fphar.2022.891273

Cheng, C., Li, Y., Long, M., Gao, M., Zhang, Y., Lin, J., et al. (2022). Moss biocrusts buffer the negative effects of karst rocky desertification on soil properties and soil microbial richness. *Plant Soil* 475, 153–168. doi: 10.1007/s11104-020-04602-4

Dangi, S. R., Stahl, P. D., Wick, A. F., Ingram, L. J., and Buyer, J. S. (2012). Soil microbial community recovery in reclaimed soils on a surface coal mine site. *Soil Sci. Soc. Am. J.* 76, 915–924. doi: 10.2136/sssaj2011.0288

De la Iglesia, R., Castro, D., Ginocchio, R., van der Lelie, D., and González, B. (2006). Factors influencing the composition of bacterial communities found at abandoned copper-tailings dumps. *J. Appl. Microbiol.* 100, 537–544. doi: 10.1111/j.1365-2672.2005.02793.x

Gazitúa, M. C., Morgante, V., Poupin, M. J., Ledger, T., Rodríguez-Valdecantos, G., Herrera, C., et al. (2021). The microbial community from the early-plant colonizer (Baccharis linearis) is required for plant establishment on copper mine tailings. *Sci. Rep.* 11:10448. doi: 10.1038/s41598-021-89769-1

Ginocchio, R., León-Lobos, P., Arellano, E. C., Anic, A., Ovalle, J. F., and Baker, A. J. M. (2017). Soil physicochemical factors as environmental filters for spontaneous plant colonization of abandoned tailing dumps. *Environ. Sci. Pollut. Res. Int.* 24, 13484–13496. doi: 10.1007/s11356-017-8894-8

Gutierrez, M. (2020). Editorial for special issue "Sustainable use of abandoned mines.". *Fortschr. Mineral.* 10:1015. doi: 10.3390/min10111015

Illumina. (2013). *16S metagenomic sequencing library preparation.* Available at: http://support.illumina.com/downloads/16s_metagenomic_sequencing_library_preparation.html

Islam, M. S., Kormoker, T., Idris, A. M., Proshad, R., Kabir, M. H., and Ustaoğlu, F. (2021). Plant–microbe–metal interactions for heavy metal bioremediation: a review. *Crop Pasture Sci.* 73, 181–201. doi: 10.1071/CP21322

Jia, T., Guo, T., and Chai, B. (2020). Bacterial community characteristics and enzyme activities in Imperata cylindrica litter as phytoremediation progresses in a copper tailings dam. *PeerJ* 8:e9612. doi: 10.7717/peerj.9612

Jia, T., Wang, R., and Chai, B. (2019). Effects of heavy metal pollution on soil physicochemical properties and microbial diversity over different reclamation years in a copper tailings dam. *J. Soil Water Conserv.* 74, 439–448. doi: 10.2489/jswc.74.5.439

Jin, J., Huang, R., Wang, J., Wang, C., Liu, R., Zhang, H., et al. (2022). Increase in Cd tolerance through seed-borne endophytic fungus Epichloë gansuensis affected root exudates and rhizosphere bacterial community of Achnatherum inebrians. *Int. J. Mol. Sci.* 23:13094. doi: 10.3390/ijms232113094

Kasemodel, M. C., Sakamoto, I. K., Varesche, M. B. A., and Rodrigues, V. G. S. (2019). Potentially toxic metal contamination and microbial community analysis in an abandoned Pb and Zn mining waste deposit. *Sci. Total Environ.* 675, 367–379. doi: 10.1016/j.scitotenv.2019.04.223

Li, B., Li, Y., Jiang, M., Chen, J., Wang, J., Li, T., et al. (2018). Accumulation and distribution of heavy metals in Imperata cylindrica at lead-zinc mining area. *IOP Conf. Ser. Earth Environ. Sci.* 199:042050. doi: 10.1088/1755-1315/199/4/042050

Li, X., Ma, L., Li, Y., Wang, L., and Zhang, L. (2019). Endophyte infection enhances accumulation of organic acids and minerals in rice under Pb^{2+} stress conditions. *Ecotoxicol. Environ. Saf.* 174, 255–262. doi: 10.1016/j.ecoenv.2019.02.072

Li, H.-Y., Shen, M., Zhou, Z.-P., Li, T., Wei, Y., and Lin, L. (2012). Diversity and cold adaptation of endophytic fungi from five dominant plant species collected from the Baima Snow Mountain, Southwest China. *Fungal Divers.* 54, 79–86. doi: 10.1007/s13225-012-0153-1

Li, L., Zheng, S., Yang, Q., Chen, S., and Huang, L. (2016). Distinguishing astragalus mongholicus and its planting soil samples from different regions by ICP-AES. *Molecules* 21:482. doi: 10.3390/molecules21040482

Liang, X., Liang, X., Liao, M., and Jia, T. (2023). Effects of Arbuscular Mycorrhizal fungi on the growth of Imperata cylindrica and soil enzyme activies under copper pollution. *J. Shanxi Univ. Nat. Sci. Ed.* 46, 951–960. doi: 10.13451/j.sxu.ns.2022081

Liu, B., Yao, J., Ma, B., Li, S., and Duran, R. (2022). Disentangling biogeographic and underlying assembly patterns of fungal communities in metalliferous mining and smelting soils. *Sci. Total Environ.* 845:157151. doi: 10.1016/j.scitotenv.2022.157151

López-González, J. A., Vargas-García, M. D. C., López, M. J., Suárez-Estrella, F., Jurado, M. D. M., and Moreno, J. (2015). Biodiversity and succession of mycobiota associated to agricultural lignocellulosic waste-based composting. *Bioresour. Technol.* 187, 305–313. doi: 10.1016/j.biortech.2015.03.124

Mahdavian, K., Ghaderian, S. M., and Torkzadeh-Mahani, M. (2017). Accumulation and phytoremediation of Pb, Zn, and Ag by plants growing on Koshk lead–zinc mining area, Iran. *J. Soils Sediments* 17, 1310–1320. doi: 10.1007/s11368-015-1260-x

Mahmud, K., Lee, K., Hill, N. S., Mergoum, A., and Missaoui, A. (2021). Influence of Tall fescue Epichloë endophytes on rhizosphere soil microbiome. *Microorganisms* 9:1843. doi: 10.3390/microorganisms9091843

Mao, W., Wu, Y., Li, F., Tang, W., Gong, W., Han, X., et al. (2023). Seed endophytes and their roles in host plant stress resistance. *J. Soil Sci. Plant Nutr.* 23, 2927–2937. doi: 10.1007/s42729-023-01279-3

Mendez, M. O., and Maier, R. M. (2008). Phytostabilization of mine tailings in arid and semiarid environments--an emerging remediation technology. *Environ. Health Perspect.* 116, 278–283. doi: 10.1289/ehp.10608

Naz, M., Dai, Z., Hussain, S., Tariq, M., Danish, S., Khan, I. U., et al. (2022). The soil pH and heavy metals revealed their impact on soil microbial community. *J. Environ. Manag.* 321:115770. doi: 10.1016/j.jenvman.2022.115770

Parada, R., Mendoza, L., Cotoras, M., and Ortiz, C. (2022). Endophytic fungi isolated from plants present in a mine tailing facility show a differential growth response to lead. *Lett. Appl. Microbiol.* 75, 345–354. doi: 10.1111/lam.13730

Parmar, S., Sharma, V. K., Li, T., Tang, W., and Li, H. (2022). Fungal seed endophyte FZT214 improves *Dysphania ambrosioides* Cd tolerance throughout different developmental stages. *Front. Microbiol.* 12:783475. doi: 10.3389/fmicb.2021.783475

Rosatto, S., Roccotiello, E., Di Piazza, S., Cecchi, G., Greco, G., Zotti, M., et al. (2019). Rhizosphere response to nickel in a facultative hyperaccumulator. *Chemosphere* 232, 243–253. doi: 10.1016/j.chemosphere.2019.05.193

Rothen, C., Miranda, V., Fracchia, S., Godeas, A., and Rodríguez, A. (2018). *Microdochium bolleyi* (Ascomycota: Xylariales): Physiological characterization and structural features of its association with wheat. *Bol. Soc. Argent. Bot.* 53, 169–182. doi: 10.31055/1851.2372.v53.n2.20574

Sánchez-López, A. S., Thijs, S., Beckers, B., González-Chávez, M. C., Weyens, N., Carrillo-González, R., et al. (2018). Community structure and diversity of endophytic bacteria in seeds of three consecutive generations of *Crotalaria pumila* growing on metal mine residues. *Plant Soil* 422, 51–66. doi: 10.1007/s11104-017-3176-2

Santoyo, G., Moreno-Hagelsieb, G., Orozco-Mosqueda M del, C., and Glick, B. R. (2016). Plant growth-promoting bacterial endophytes. *Microbiol. Res.* 183, 92–99. doi: 10.1016/j.micres.2015.11.008

Senthil Kumar, R., Koner, S., Tsai, H., Chen, J., Huang, S., and Hsu, B. (2023). Deciphering endemic rhizosphere microbiome community's structure towards the host-derived heavy metals tolerance and plant growth promotion functions in serpentine geo-ecosystem. *J. Hazard. Mater.* 452:131359. doi: 10.1016/j.jhazmat.2023.131359

Shadmani, L., Jamali, S., and Fatemi, A. (2021). Effects of root endophytic fungus, *Microdochium bolleyi* on cadmium uptake, translocation and tolerance by *Hordeum vulgare* L. *Biologia* 76, 711–719. doi: 10.2478/s11756-020-00598-5

Shahzad, R., Waqas, M., Khan, A. L., Asaf, S., Khan, M. A., Kang, S., et al. (2016). Seed-borne endophytic *Bacillus amyloliquefaciens* RWL-1 produces gibberellins and regulates endogenous phytohormones of *Oryza sativa*. *Plant Physiol. Biochem.* 106, 236–243. doi: 10.1016/j.plaphy.2016.05.006

Shaltout, K. H., Galal, T. M., and El-Komi, T. M. (2016). Phenology, biomass and nutrients of *Imperata cylindrica* and *Desmostachya bipinnata* along the water courses in Nile Delta, Egypt. *Rendiconti Lincei* 27, 215–228. doi: 10.1007/s12210-015-0459-5

Song, F., Zhang, X., Liu, J., Pu, D., Zhao, Y., and Qiao, Q. (2019). Absorption and accumulation of heavy metals by Imperata cylindrical in iron tailings. *J. Northwest A F Univ.* 47, 83–90+100. doi: 10.13207/j.cnki.jnwafu.2019.04.011

Sun, L., Zhang, Y., He, L., Chen, Z., Wang, Q., Qian, M., et al. (2010). Genetic diversity and characterization of heavy metal-resistant-endophytic bacteria from two copper-tolerant plant species on copper mine wasteland. *Bioresour. Technol.* 101, 501–509. doi: 10.1016/j.biortech.2009.08.011

Sun, X., Zhou, Y., Tan, Y., Wu, Z., Lu, P., Zhang, G., et al. (2018). Restoration with pioneer plants changes soil properties and remodels the diversity and structure of bacterial communities in rhizosphere and bulk soil of copper mine tailings in Jiangxi Province, China. *Environ. Sci. Pollut. Res. Int.* 25, 22106–22119. doi: 10.1007/s11356-018-2244-3

Teixeira, L. C. R. S., Peixoto, R. S., Cury, J. C., Sul, W. J., Pellizari, V. H., Tiedje, J., et al. (2010). Bacterial diversity in rhizosphere soil from Antarctic vascular plants of Admiralty Bay, maritima Antarctica. *ISME J.* 4, 989–1001. doi: 10.1038/ismej.2010.35

Trannum, H. C., Næss, R., and Gundersen, H. (2020). Macrofaunal colonization of mine tailings impacted sediments. *Sci. Total Environ.* 708:134866. doi: 10.1016/j.scitotenv.2019.134866

Trivedi, P., Leach, J. E., Tringe, S. G., Sa, T., and Singh, B. K. (2020). Plant-microbiome interactions: from community assembly to plant health. *Nat. Rev. Microbiol.* 18, 607–621. doi: 10.1038/s41579-020-0412-1

Ultra, V. U., and Manyiwa, T. (2021). Influence of mycorrhiza and fly ash on the survival, growth and heavy metal accumulation in three Acacia species grown in Cu–Ni mine soil. *Environ. Geochem. Health* 43, 1337–1353. doi: 10.1007/s10653-020-00627-x

Vidal, C., Larama, G., Riveros, A., Meneses, C., and Cornejo, P. (2021). Main molecular pathways associated with copper tolerance response in *Imperata cylindrica* by de novo transcriptome assembly. *Plants (Basel)* 10:357. doi: 10.3390/plants10020357

Wan, W., Qin, Y., Wu, H., Zuo, W., He, H., Tan, J., et al. (2020). Isolation and characterization of phosphorus solubilizing bacteria with multiple phosphorus sources utilizing capability and their potential for lead immobilization in soil. *Front. Microbiol.* 11:752. doi: 10.3389/fmicb.2020.00752

Wang, Q., Garrity, G. M., Tiedje, J. M., and Cole, J. R. (2007). Naive Bayesian Classifier for rapid assignment of rRNA sequences into the new bacterial taxonomy. *Appl. Environ. Microbiol.* 73, 5261–5267. doi: 10.1128/AEM.00062-07

Wang, L., Gong, L., Gan, D., Li, X., Yao, J., Wang, L., et al. (2022). Diversity, function and assembly of the *Trifolium repens* L. root-associated microbiome under lead stress. *J. Hazard. Mater.* 438:129510. doi: 10.1016/j.jhazmat.2022.129510

Wang, S., Guo, Z., Wang, L., Zhang, Y., Jiang, F., Wang, X., et al. (2021). Wheat rhizosphere metagenome reveals newfound potential soil Zn-mobilizing bacteria contributing to cultivars' variation in grain Zn concentration. *Front. Microbiol.* 12:689855. doi: 10.3389/fmicb.2021.689855

Wang, J., Hou, W., Christensen, M. J., Li, X., Xia, C., Li, C., et al. (2020). Role of Epichloë endophytes in improving host grass resistance ability and soil properties. *J. Agric. Food Chem.* 68, 6944–6955. doi: 10.1021/acs.jafc.0c01396

Wang, H., Liu, H., Yang, T., Lv, G., Li, W., Chen, Y., et al. (2023). Mechanisms underlying the succession of plant rhizosphere microbial community structure and function in an alpine open-pit coal mining disturbance zone. *J. Environ. Manag.* 325:116571. doi: 10.1016/j.jenvman.2022.116571

Wu, B., Luo, S., Luo, H., Huang, H., Xu, F., Feng, S., et al. (2022). Improved phytoremediation of heavy metal contaminated soils by *Miscanthus floridulus* under a varied rhizosphere ecological characteristic. *Sci. Total Environ.* 808:151995. doi: 10.1016/j.scitotenv.2021.151995

Xie, L., and van Zyl, D. (2020). Distinguishing reclamation, revegetation and phytoremediation, and the importance of geochemical processes in the reclamation of sulfidic mine tailings: A review. *Chemosphere* 252:126446. doi: 10.1016/j.chemosphere.2020.126446

Zhao, J., Ma, J., Yang, Y., Yu, H., Zhang, S., and Chen, F. (2021). Response of soil microbial community to vegetation reconstruction modes in mining areas of the loess plateau, China. *Front. Microbiol.* 12:714967. doi: 10.3389/fmicb.2021.714967

Zheng, B., Bi, Q., Hao, X., Zhou, G., and Yang, X. (2017). *Massilia phosphatilytica* sp. nov., a phosphate solubilizing bacteria isolated from a long-term fertilized soil. *Int. J. Syst. Evol. Microbiol.* 67, 2514–2519. doi: 10.1099/ijsem.0.001916

Zheng, H., Zhang, Z., Xing, X., Hu, T., Qu, C., Chen, W., et al. (2019). Potentially toxic metals in soil and dominant plants from tonglushan Cu–Fe deposit, central China. *Bull. Environ. Contam. Toxicol.* 102, 92–97. doi: 10.1007/s00128-018-2501-7

Zhou, W., Wang, Y., Lian, Z., Yang, T., Zeng, Q., Feng, S., et al. (2020). Revegetation approach and plant identity unequally affect structure, ecological network and function of soil microbial community in a highly acidified mine tailings pond. *Sci. Total Environ.* 744:140793. doi: 10.1016/j.scitotenv.2020.140793

Zhu, F., Zhang, X., Guo, X., Yang, X., and Xue, S. (2023). Root architectures differentiate the composition of organic carbon in bauxite residue during natural vegetation. *Sci. Total Environ.* 883:163588. doi: 10.1016/j.scitotenv.2023.163588

Genome and pan-genome analysis of a new exopolysaccharide-producing bacterium *Pyschrobacillus* sp. isolated from iron ores deposit and insights into iron uptake

Afef Najjari[1], Marwa Jabberi[2,3,4], Saïda Fatma Chérif[5,6], Ameur Cherif[3], Hadda Imene Ouzari[1], Javier A. Linares-Pastén[7]* and Haitham Sghaier[2,3]

[1]Laboratoire de Microbiologie et Biomolécules Actives (LR03ES03), Faculté des Sciences de Tunis, Université Tunis El Manar, Tunis, Tunisia, [2]Laboratory "Energy and Matter for Development of Nuclear Sciences" (LR16CNSTN02), National Center for Nuclear Sciences and Technology (CNSTN), Sidi Thabet Technopark, Ariana, Tunisia, [3]ISBST, LR11-ES31 BVBGR, University of Manouba, Biotechpole Sidi Thabet, Ariana, Tunisia, [4]Biochemistry and Molecular Biology Lab of Faculty of Sciences of Bizerte, Risks Related to Environmental Stress, Struggle and Prevention (UR17ES20), University of Carthage, Bizerte, Tunisia, [5]Laboratoire de Matériaux, Cristallochimie et Thermodynamique Appliquée, Faculté des Sciences de Tunis, Université de Tunis El Manar, Tunis, Tunisia, [6]Institut Préparatoire aux Etudes d'Ingénieurs—El Manar, Université de Tunis El Manar, El Manar II, Tunis, Tunisia, [7]Department of Biotechnology, Faculty of Engineering, Lunds Tekniska Högskola (LTH), Lund University, Lund, Sweden

Bacterial exopolysaccharides (EPS) have emerged as one of the key players in the field of heavy metal-contaminated environmental bioremediation. This study aimed to characterize and evaluate the metal biosorption potential of EPS produced by a novel *Psychrobacillus* strain, NEAU-3TGS, isolated from an iron ore deposit at Tamra iron mine, northern Tunisia. Genomic and pan-genomic analysis of NEAU-3TGS bacterium with nine validated published *Psychrobacillus* species was also performed. The results showed that the NEAU-3TGS genome (4.48 Mb) had a mean GC content of 36%, 4,243 coding sequences and 14 RNA genes. Phylogenomic analysis and calculation of nucleotide identity (ANI) values (less than 95% for new species with all strains) confirmed that NEAU-3TGS represents a potential new species. Pangenomic analysis revealed that *Psychrobacillus* genomic diversity represents an "open" pangenome model with 33,091 homologous genes, including 65 core, 3,738 shell, and 29,288 cloud genes. Structural EPS characterization by attenuated total reflectance-Fourier transform infrared (ATR-FTIR) spectroscopy showed uronic acid and α-1,4-glycosidic bonds as dominant components of the EPS. X-ray diffraction (XRD) analysis revealed the presence of chitin, chitosan, and calcite $CaCO_3$ and confirmed the amorphous nature of the EPS. Heavy metal bioabsorption assessment showed that iron and lead were more adsorbed than copper and cadmium. Notably, the optimum activity was observed at 37°C, pH=7 and after 3 h contact of EPS with each metal. Genomic insights on iron acquisition and metabolism in *Psychrobacillus* sp. NEAU-3TGS suggested that no genes involved in siderophore biosynthesis were found, and only the gene cluster *Feu*ABCD and trilactone hydrolase genes involved in the uptake of siderophores, iron transporter and exporter are present. Molecular modelling and docking of *Feu*A (protein peptidoglycan siderophore-binding protein) and siderophores ferrienterobactine $[Fe^{+3} (ENT)]^{-3}$ and ferribacillibactine $[Fe^{+3} (BB)]^{-3}$ ligand revealed that $[Fe^{+3} (ENT)]^{-3}$ binds to Phe122, Lys127, Ile100, Gln314, Arg215, Arg217, and Gln252. Almost the same for $[Fe^{+3} (ENT)]^{-3}$ in addition to Cys222 and

Tyr229, but not Ile100.To the best of our knowledge, this is the first report on the characterization of EPS and the adsorption of heavy metals by *Psychrobacillus* species. The heavy metal removal capabilities may be advantageous for using these organisms in metal remediation.

1 Introduction

The genus *Psychrobacillus* belongs to the *Bacillaceae* family within the Firmicutes phylum. It was proposed by Krishnamurthi in 2010 after reclassification of three *Bacillus* strains under the genus *Psychrobacillus* based on polyphasic approaches (Krishnamurthi et al., 2010), including *Bacillus insolitus* DSM 5 T 55, *Bacillus psychrotolerans* DSM 11706 T and *Bacillus psychrodurans* DSM 11713 T; these species were transferred to the new genus *Psychrobacillus* and reclassified. *Psychrobacillus* species are considered psychrophiles, which can grow at 0–20°C, and psychrotolerants (or psychrotrophic), which can grow up to ~30°C (DasSarma and DasSarma, 2018). *Psychrobacillus* harbors Gram-positive, endospore-forming motile rods and aerobic bacteria. At the time of writing, nine validly described species: *Psychrobacillus insolitus* isolated from soil (Krishnamurthi et al., 2010), *Psychrobacillus psychrodurans and Psychrobacillus psychrotolerans* isolated from garden soil (Abd El-Rahman et al., 2002), *Psychrobacillus soli* isolated from oil-contaminated soil (Pham et al., 2015), *Psychrobacillus vulpis* isolated from faeces of a red fox (Rodríguez et al., 2020), *Psychrobacillus lasiicapitis* isolated from the head of an ant (Shen et al., 2017), *Psychrobacillus* isolated from an iceberg in Antarctica (Choi and Lee, 2020), *Psychrobacillus faecigallinarum* isolated from faeces of hen (Gilroy et al., 2021) and *Psychrobacillus antarcticus* isolated from soil sampled at Vale Ulman, King George Island (Antarctica) (Da Silva et al., 2023). Such species may tend to evolve several genes in their genome to cope with various habitats, leading to genome-wide diversity.

Using the pangenome strategy represents an appropriate method to reveal genetic variation, species diversity and evolution that could explain the adaptation of *Psychrobacillus* species to different ecological niches (Hollensteiner et al., 2023). Bacterial pangenomes represent the gene set of all species strains (Medini et al., 2005; Vernikos et al., 2015; Chaudhari et al., 2018). It includes a group of core genes that are common to all strains. The accessory genes include dispensable genes shared by two or more strains. They are crucial for environmental adaptation, genome evolution, and unique genes specific to a single strain (Zakham et al., 2021). In recent years, whole-genome sequencing analysis has provided comprehensive information on inter- and intra-species genome variation through pan-genome analysis (Naithani et al., 2023). Such genetic variation may also be responsible for the open or closed structure of the pangenome (Tettelin et al., 2005), depending on the capacity of the species for the uptake of exogenous DNA, the availability of the machinery for its utilisation and the abundance of ribosomal RNA (Diene et al., 2013). In the first part of this study, we report the in-depth genomic and pan-genomic analysis of a new bacterium, *Psychrobacillus*, isolated from an ores deposit sampled from the Tamra iron mine (Nefza mining district, N. Tunisia).

As reported in previous studies, most *Psychrobacillus* species were isolated from extreme environments, and to cope with those conditions, they may employ several strategies, one of which is to produce extracellular polymeric substances (EPSs), which act as a barrier to protect the cell from radiation (Guesmi et al., 2019), desiccation, freezing environments (Corsaro et al., 2004; Carrión et al., 2015), heavy metals (Guibaud et al., 2003; Gupta and Diwan, 2017; Cao et al., 2023), etc. Microbial EPSs are a group of high molecular weight biopolymers produced during the metabolic process that can be attached to the cell surface or released into the environment (Nwodo et al., 2012). They are reported to play an important role in bioremediation processes due to their structural and functional properties (Ates, 2015), especially for removing heavy metals, as well as emulsifying, bio-flocculating, and antioxidant agents (Ahmad et al., 2015; Chouchane et al., 2020; Da Silva et al., 2022). Several studies have been carried out on EPSs produced by different bacterial species; however, no studies have been conducted on EPS from *Psychrobacillus* species. In the second part of our study, we focused on the production, structural characterisation, and determination of metal bioabsorption by the EPS produced by the isolated *Pyschrobacillus* bacteria.

Given the origin of isolation (iron ores deposit), the third part of our study focuses on analysing the iron uptake and metabolism systems of the *Pyschrobacillus* bacterium based on whole genome mining. Iron is a crucial element for most living organisms. It is essential for many biological functions such as DNA synthesis and repair, genomic stability, respiration, and photosynthesis, and as a cofactor in many biochemical reactions (Andrews et al., 2003; Liu et al., 2022). Although it is abundant on Earth, the bioavailability of iron is minimal. To remedy this, microorganisms have developed siderophore-dependent iron uptake strategies designed to solubilise and capture iron in aerobic environments (Hoegy et al., 2005). Siderophores are low-molecular-weight (less than 10 kDa) molecules with a high affinity for ferric iron (Fe^{3+}) (Khan et al., 2018). They are generally classified based on the coordination groups that chelate the Fe^{3+}. The most common groups are catecholates (phenolates), hydroxamate siderophores and carboxylate siderophores (Saha et al., 2016). The import of siderophore-Fe^{3+} complexes is internalised by siderophore-binding proteins located on the bacterial surface. In Gram-positive bacteria, these proteins include ABC transporters with an ATP cassette located on the cytoplasmic membrane (Braun and Hantke, 2011), the case of *B. subtilis*, which employs bacillibactin as an endogenous siderophore and may subsequently import exogenous siderophores like enterobactin, petrobactin or hydroxamate siderophores like ferrichrome (Miethke et al., 2013). It is worth noting that various known siderophores can present significant structural homologies, enabling bacteria to use other siderophores produced by different bacteria (xenosiderophores) (Will et al., 2023). Several studies have reported the iron acquisition system within Gram-positive bacteria; however, no studies have been conducted on *Psychrobacillus* species. Here, we sought to analyse the insights into iron uptake and metabolism of the new *Psychrobacillus* sp. bacterium NEAU-3TGS isolated from an iron ores deposit from the Tamra iron mine (Nefza mining district, Northern Tunisia).

2 Materials and methods

2.1 Strain isolation and molecular identification

The bacterial strain NEAU-3TGS was isolated from an iron ores deposit collected from northern Tunisia's Tamra iron mine (Nefza mining district) (Longitude: 9°06.7226′E, Latitude: 37°02.7413′N). The mine has been exploited for about a century and belongs to the Nappe Zone of northern Tunisia. At the time of sampling, the temperature was 8°C, a pH of 6.85. The mineralogical characterisation of the iron ores deposit is shown in Supplementary Table S1.

Isolation was performed on tryptic soy agar (TSA) medium (Sigma Aldrich) using the serial dilution technique. The iron ore sample was first ground, and then 1 g was added to 9 mL of physiological saline water (0.9% NaCl), and then a serial dilution was performed on tryptic soy agar (TSA) medium (Sigma Aldrich). Plates were incubated at 28°C for 48 h. Identification of the NEAU-3TGS strain was based on partial 16S rRNA gene sequencing. DNA extraction was performed using sodium dodecyl sulphate proteinase K treatment (Cherif et al., 2003). 16S rRNA gene amplification was performed using the universal bacterial primers 27F (5'-TCC GGT TGA TCC TGC RG-3′) and 1492R (5′-GGT TAC CTT GTT ACG ACT T3-') (El Hidri et al., 2013). The PCR reaction mixture, containing PCR buffer (1X), MgCl2 (1.5 mM), 0.25 mM of each dNTP, 0.5 μM of each primer, 0.1 μg of chromosomal DNA, and 1 U of Taq DNA polymerase (Fermentas), was used to in 50 μL to perform PCR reactions programmed as follows: 95°C for 5 min; 35 cycles of [94°C 45 s, 55°C 45 s and 72°C 1 min], and a final extension step at 72°C for 10 min. PCR products were Sanger sequenced with an automated capillary ABI Biosystem 3,130 (MrDNA). The 16S rRNA gene sequence obtained was compared to sequences deposited on the EzBioCloud server (Yoon et al., 2017). The sequence for the 16S rRNA gene was deposited in GenBank under the accession number OR577132.

2.2 Genome assembly, annotation, and phylogenomic analysis of NEAU-3TGS strain

Genome sequencing and assembly were performed using Ion Torrent sequencing technology. Sequencing quality control of raw sequence data was performed using the FastQC algorithm (version 0.11.8),[1] and poor-quality reads were trimmed using the Trimmomatic tool (Bolger et al., 2014). *De novo* assembly using the SPAdes tool (version 3.13.1) (Bankevich et al., 2012). Then, the quality of the assembled genome was assessed using QUAST software (Meier-Kolthoff Gurevich et al., 2013). To determine the relationship of NEAU-3TGS with *Psychrobacillus* species, we first perform the whole-genome-based taxonomic analysis through the Type Strain Genome Server (Meier-Kolthoff and Göker, 2019). Pairwise genomic comparisons were calculated, and intergenomic distances were inferred using the algorithm "trimming" and distance formula d5 using 100 distance replicates in FastME 2.0 (Lefort et al., 2015). The genome of strain NEAU-3TGS was annotated using several tools. The first was the rapid

annotation subsystem technology (RAST) server (Aziz et al., 2008). Then, the predicted gene sequences were translated and searched in the National Center for Biotechnology Information (NCBI) non-redundant database and the Kyoto Encyclopedia of Genes and Genomes (KEGG) database with a cutoff value of 0.01 (Kanehisa and Goto, 2000). Indeed, ortholog prediction and functional genes annotation, including clusters of orthologous genes (COGs), were identified using EGGNOG 5.0 database and OrthoFinder software (Huerta-Cepas et al., 2019). We used FastTree with the maximum likelihood (Felsenstein, 1981) method to construct phylogenetic trees based on conserved single-copy gene sequences. The whole Genome Shotgun project has been deposited at DDBJ/ENA/GenBank under the accession JAPNOZ000000000. The version described in this paper is version JAPNOZ010000000.

2.3 Comparative genome analysis and pangenome inference of *Psychrobacillus* strains

Here, we used one of the representative genome sequences of nine *Psychrobacillus* species that have been validated in the LPSN database (Parte et al., 2020) and whose genome sequences are available in GenBank[2] (as of May 2024). We first checked the similarity of the NEAU-3TGS genome sequence with all species by comparing values of average nucleotide identity analysis (ANI), calculated using an OrthoANI in OAT (the Orthologous Average Nucleotide Identity Tool) (Lee et al., 2016). The species includes *Psychrobacillus faecigallinarum* (NZ_JACSQO000000000.1), *Psychrobacillus glaciei* (NZ_CP031223.1), *Psychrobacillus insolitus* (NZ_QKZI00000000.1), *Psychrobacillus lasiicapitis* VDGH01 (NZ_VDGH00000000.1), *Psychrobacillus psychrodurans* DSM30747 (NZ_JAMKBI000000000.1), *Psychrobacillus psychrotolerans* (NZ_FOXU00000000.1), *Psychrobacillus soli* (NZ_VDGG00000000.1), *Psychrobacillus vulpis* (NZ_VDGI00000000.1) and *Psychrobacillus antarcticus* (JAIZDB000000000.1). To assess the genetic and phylogenetic diversities of *Psychrobacillus* species, we performed a pangenome analysis using the Roary version 3.13.0 pipeline (Page et al., 2015) with an identity threshold of 90% BLASTp percentage. Roary output files were used to analyse and visualise the primary and accessory genomes of *Psychrobacillus* strains using R.[3]

2.4 Extraction of EPS

A qualitative assessment of EPS production was performed on a TSA medium supplemented with 2% glucose, and mucoid colonies characterised the EPS phenotype. The extraction of EPS was performed according to the protocol described by Guesmi et al. (2022). Briefly, pre-grown strains were inoculated into 200 mL of tryptic soy broth (TSB) medium (Sigma Aldrich) supplemented with 2% glucose and incubated at 30°C for 72 h. The culture was then centrifuged at 16,000 g for 20 min, and the supernatant was added with 3 volumes of absolute ethanol and incubated at 4°C for 24 h. Precipitated EPS were collected by centrifugation at 16,000 g for

---

1 http://www.bioinformatics.babraham.ac.uk/projects/fastqc/

2 https://www.ncbi.nlm.nih.gov

3 https://www.r-project.org/

20 min, and the pellet was dried at room temperature for 24 h. The dried pellet was dissolved in distilled water to remove proteins from crude EPS, treated with 4% (w/v) trichloroacetic acid (TCA) for 6 h and centrifuged. The supernatant EPS fraction was again purified with ethanol and left overnight at 4°C, and after centrifugation, the EPS was dried at room temperature until it reached constant weight (Shameer, 2016).

The protein content was analysed using the Bradford method (Bradford, 1976) with bovine serum albumin (BSA) as a standard. The absorbance was read at 595 nm. The content of polynucleotides (DNA and RNA) was estimated by measurement of optical density (OD) at 260 and 280 nm using a NanoDrop 2000c spectrophotometer (Thermo Fisher Scientific Inc., United States).

2.5 EPS analysis

Dried EPS samples were analysed by attenuated total reflectance-Fourier transform infrared spectroscopy (ATR-FTIR) and X-ray diffraction. ATRS-FTIR spectra of EPS were recorded in the transmission mode, using a Mattson FTIR spectrophotometer in the range of 400 to 4,000 cm^{-1}, where the functional groups of EPS were identified. The X-ray study was conducted using a D8 ADVANCE Bruker diffractometer with CuK$_\alpha$ radiation ($\lambda = 1.5418$ Å) in the 2θ range of 5–80°. The 2θ values of diffraction peaks were plotted, and the distances (d) between two lattice planes were determined using Bragg's law (Eq. 1):

$$d = \frac{\lambda}{2\sin(\theta)} \qquad (1)$$

Where λ represents the wavelength of the incident X-rays, d is the spacing between crystal lattice planes, and θ is the X-ray beam's incidence angle.

The Crystallinity Index (CI) was computed with the formula (Eq. 2):

$$CI = \frac{\text{Peak areas of crystals}}{\text{Peak areas of crystals + Peak area of amorphous peak}} \times 100 \quad (2)$$

2.6 Metal bioabsorption assessment of EPS

The evaluation of the metal biosorption potential of EPS (1.0 mg/100 mL) against the heavy metals, iron (FeCl$_3$), lead (PbCl$_2$), copper (CuSO$_4$) and cadmium (CdCl$_2$) at 1000 ppm for each metal salt based on the method of Shameer (2016) with some modifications including the contact time (1, 2, 3, 6, and 24 h) at pH 7 and 37°C, the pH (5, 6, 7, and 8) at 37°C for 24 h and the temperature (20, 28, 37, and 45°C) at pH 7 for 24 h. After the adsorption process, the solution was centrifuged at 24,000 g for 10 min to separate the EPS. All assays were performed in triplicate. The metal biosorption was measured by atomic absorption spectroscopy based on the following calculation (Shameer, 2016):

Metal removal (q) from solution expressed as mg metal removed/g dry weight $^{(-1)}$ (Volesky and Holan, 1995):

$$q\left(\text{mg g}^{-1}\right) = V\left(\text{Ci} - \text{Cf}\right)\text{m}^{-1}.$$

Where V: sample volume (l); Ci: initial concentration, Cf: final concentration; m: the amount of dry biomass (g).

2.7 Molecular modelling

The molecular structure of the protein FeuA was obtained through the deep learning program RoseTTAFold (Baek et al., 2021). FeuA was subjected to docking with the ligands [Fe+3(ENT)]$^{-3}$ and [Fe^{+3}(BB)]$^{-3}$. The atomic coordinates of the ligands were obtained from the crystal structures available in the Protein Data Bank (PDB) 2XUZ and 2WHY, respectively. Dockings were performed with AutoDock Vina (Trott and Olson, 2010), considering the total flexibility of the ligands.

3 Results and discussions

3.1 Isolation and comparative genomic analysis of the NEAU-3TGS strain
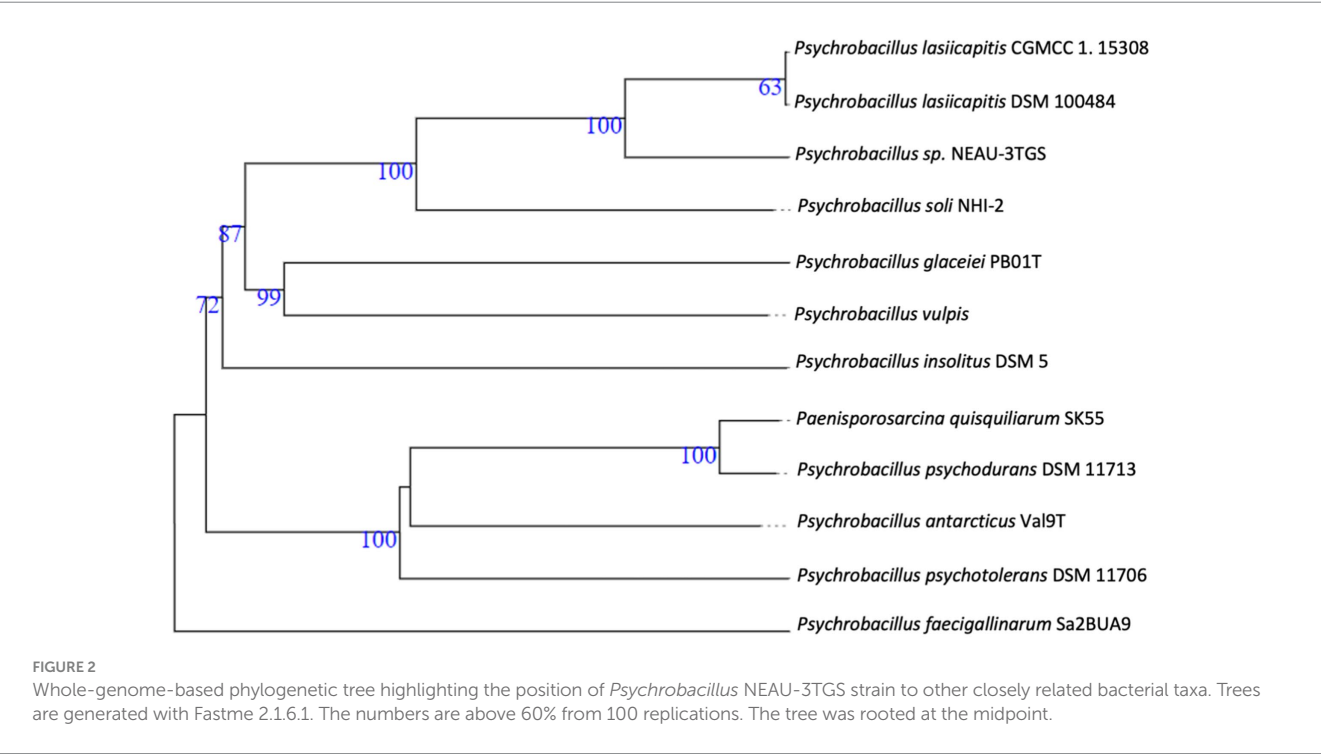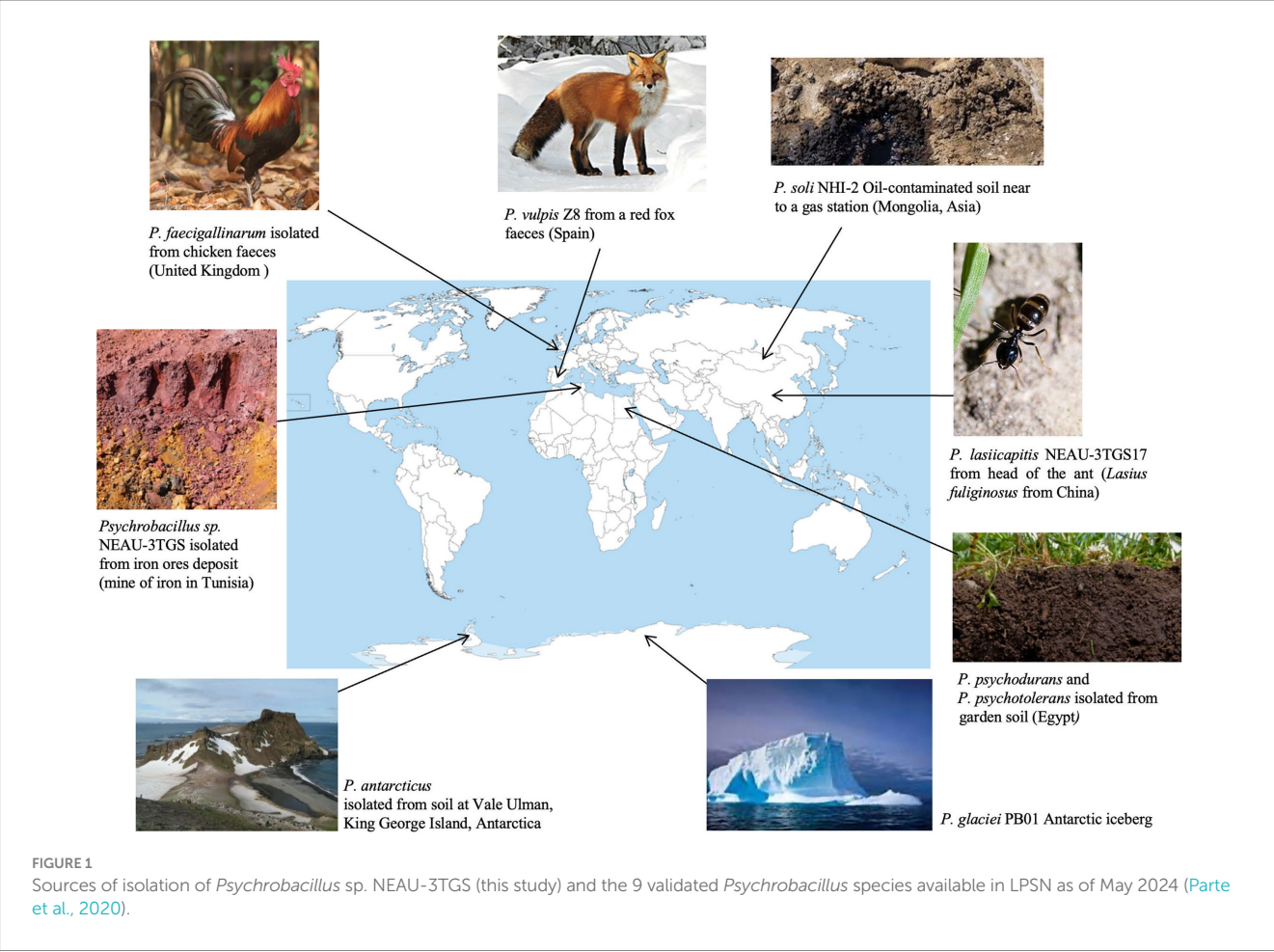
NEAU-3TGS bacteria showed white colonies of rod-shaped Gram-positive cells (Supplementary Figure S1). The NEAU-3TGS isolate identification based on partial 16S rDNA gene sequencing (570 bp) (GeneBank: OR577132) gave 99.65% of identity to the species *P. lasiicapitis* (GeneBank: KP219721). *Psychrobacillus* is a member of the *Bacillaceae* family within the Firmicutes phylum. This genus was proposed by Krishnamurthi in 2010 after re-examining certain *Bacillus* species, whereby *Bacillus insolitus*, *Bacillus psychrotolerant* and *Bacillus psychrodurans* were reclassified within the new genus *Psychrobacillus* (Krishnamurthi et al., 2010), which encompasses *P. lasiicapitis*, *P. psychrodurans*, *P. psychrotolerans*, *P. soli*, *P. insolitus*, *P. glaciei*, *P. faecigallinarum*, *P. vulpis* and *P. antarcticus* (Parte et al., 2020) (Table 1). *Psychrobacillus* are renowned for their ability to thrive at cold temperatures. They have been identified and isolated from cold environments, such as polar icebergs, and other habitats like garden soils, petroleum-contaminated soils, and red fox faeces (Choi et al., 2020) (Figure 1).

The whole assembled genome of the NEAU-3TGS strain contains 4.418 Mb in length, consisting of 16 scaffolds, with an N50 of 666.8 kb and a G + C content of 37.0% (Table 1). Phylogenomic analysis and genome-based taxonomical classification of the NEAU-3TGS strain showed that the NEAU-3TGS strain is identified as a potential new species and was placed with the same clade of *P. lasiicapitis* species represented by the two strains CGMCC 1.15308 and DSM 100484 (Shen et al., 2017) (Figure 2). To confirm whether *Psychrobacillus* sp. NEAU-3TGS is a novel species. ANI analysis was carried out with the genome sequences of representative strains belonging to the eight LPSN-validated *Psychrobacillus* species (Table 1), including *P. lasiicapitis* NEAU-3TGS17 (VDGH01000000) isolated from ant head (Shen et al., 2017), *P. glaciei* PB01 (NZ_CP031223.1) isolated from an Antarctic iceberg (Choi and Lee, 2020), *P. soli* NHI-2 (NZ_VDGG00000000.1) isolated from contaminated soil (Pham et al., 2015), *P. psychrodurans* (NZ_JAMKBI000000000.1) and *P. insolitus* DSM 5 (QKZI00000000) isolated from garden soil (Abd El-Rahman et al., 2002; Krishnamurthi et al., 2010), *P. psychrotolerans* DSM 11706 (FOXU00000000) isolated from soil (Abd El-Rahman et al., 2002),

TABLE 1 Genomic features of *Psychrobacillus* species.

Species	Accession number	No of scaffolds	Length (MB)	GC%	Proteins	rRNA operon copy number	Completeness (%)	ANI *vs* NEAU-3TGS strain (%)	Origin of isolation
Psychrobacillus sp. NEAU-3TGS	JAPNOZ000000000	16	4.41	37.00	4,243	14	99.34	–	Iron (This study)
P. lasiicapitis NEAU-3TGS17	VDGH01000000	28	4.48	37.06	4,294	19	100	93.47	Head of the ant (*Lasius fuliginosus*, China) (Shen et al., 2017)
P. soli NHI-2	VDGG00000000	101	4.22	37.12	3,993	22	100	85.01	Oil-contaminated soil near a gas station in Mongolia, Asia (Pham et al., 2015)
P. vulpis Z8	VDGI00000000	76	4.02	35.89	3,807	23	99.34	78.78	Faeces of a red fox from Spain (Rodríguez et al., 2020)
P. glaciei PB01	CP031223	2	4.35	35.97	3,952	33	99.34	77.91	Antarctic iceberg (Choi and Lee, 2020)
P. psychrotolerans DSM 11706	FOXU00000000	20	3.60	36.36	3,549	23	99.34	75.89	Soil from Egypt (Abd El-Rahman et al., 2002; Krishnamurthi et al., 2010)
P. insolitus DSM 5	QKZI00000000	33	3.28	36.02	3,200	26	99.68	76.63	NA
P. faecigallinarum Sa2BUA9	JACSQO000000000	5	4.00	36.48	3,855	32	100	74.22	Faeces from *Gallus gallus* from United Kingdom (Gilroy et al., 2021)
P. psychrodurans DSM 11713	JAMKBK000000000	48	4.02	36.00	3,844	45	99.34	76.17	Soil from Egypt (Abd El-Rahman et al., 2002; Krishnamurthi et al., 2010) (Egypt)
P. antarcticus val9	JAIZDB000000000.1	87	3.98	36.60	3,799	18	99.14	76.97	Isolated from the soil at Vale Ulman, King George Island, Antarctica (Da Silva et al., 2023)

The average nucleotide identity (ANI) was measured versus the chromosome of *Psychrobacillus* sp. NEAU-3TGS strain.

FIGURE 1

Sources of isolation of *Psychrobacillus* sp. NEAU-3TGS (this study) and the 9 validated *Psychrobacillus* species available in LPSN as of May 2024 (Parte et al., 2020).

FIGURE 2

Whole-genome-based phylogenetic tree highlighting the position of *Psychrobacillus* NEAU-3TGS strain to other closely related bacterial taxa. Trees are generated with Fastme 2.1.6.1. The numbers are above 60% from 100 replications. The tree was rooted at the midpoint.

P. faecigallinarum (NZ_JACSQO000000000.1) isolated from chicken feed (Gilroy et al., 2021), *P. vulpis* Z8 (NZ_VDGI00000000.1) isolated from red fox feed (Rodríguez et al., 2020) and *P. antarcticus* Val9 (JAIZDB000000000.1) isolated from soil (Da Silva et al., 2023). Results revealed that ANI values ranged between 74.22 and 93.47% for *P. faecigallinarum* (JACSQO000000000.1) and *P. lasiicapitis* NEAU-3TGS17 respectively, which were below the threshold value (95%) for distinguishing the different species (Goris et al., 2007) (Table 1). Accordingly, the ANI indicates that strain NEAU-3TGS represents a novel species in the *Psychrobacillus* genus.

Comparison of general genomic characteristics of *Psychrobacillus* species showed similar profiles except for chromosome size, varying from 3.28 Mb to 4.48 Mb for *P. insolitus* and *P. lasiicapitis* NEAU-3TGS17, respectively, and for rRNA operon copy numbers which range from 14 in *Psychrobacillus* sp. NEAU-3TGS to 45 in *P. psychrodurans* DSM 11713 (Table 1). This may reflect the environmental adaptation of *Psychrobacillus* species. In general, the ribosomal RNA operon represents a fundamental genetic structure in protein synthesis and, thus, a functional trait linked to the bacterial life cycle (Klappenbach et al., 2000; Stevenson and Schmidt, 2004), while bacteria with a higher number of rRNA copies can better withstand nutrient fluctuations and tend to inhabit nutrient-poor environments (Klappenbach, 2001; Jeyasingh and Weider, 2007).

Genome annotation of *Psychrobacillus* sp. NEAU-3TGS based on the RAST server revealed 4,746 DNA coding sequences (CDS) distributed in 417 subsystems with uneven distribution (Supplementary Table S2). The subsystems with the highest presence of CDS were (i) amino acids and their derivatives (535 CDS); (ii) carbohydrates (370 CDS); (iii) protein metabolism (233 CDS); (iv) cofactors, vitamins and prosthetic groups (201 CDS); (v)RNA metabolism (186); (vi) membrane transport (180 CDS); (vii) fatty acids, lipids and isoprenoids (173 CDS); (viii) DNA Metabolism (124 CDS); and (ix) cell wall and capsule (124) (Supplementary Table S2). In addition, the genome of this strain presented CDS potentially resistant toxic compounds (46 CDS), including genes implicated in copper homeostasis ($n = 4$), cobalt-zinc-cadmium resistance ($n = 10$), zinc resistance ($n = 3$), arsenic resistance ($n = 8$), cadmium resistance ($n = 1$) and resistance to chromium compounds ($n = 1$) (Supplementary Table S3). These gene fears could be correlated to the origin of strain, the contamination of iron mines with heavy metals (Decrée et al., 2008). RAST annotation was conducted for the other species, and results showed almost the same distribution of subsystem feature counts except for phages and prophages, which were absent for *P. psychotolerans* and *P. psychrodurans* (Supplementary Table S2). In addition, COG annotation of the CDSs of *Psychrobacillus* sp. NEAU-3TGS genome sequence revealed 23 COGs where the majority were assigned to unknown function (S, 22.97%), followed by amino acid transport and metabolism (E, 9.54%), translation, ribosomal structure, and biogenesis (J, 4.94%), inorganic ion transport and metabolism (P, 4.77%), and energy production and conversion (C, 4.31%). The remaining clusters are below 4%. Compared to other species, almost the same profile has been observed (Supplementary Table S4).

3.2 Pan-genome analysis of *Psychrobacillus* species

The genomic diversity of *Psychrobacillus* species undertaken in this study was performed based on pangenome analysis using the

Roary (version 3.13.0) pipeline with a 90% identity threshold of BLASTp percentage. The results showed that the pangenomic structure of the ten *Psychrobacillus* strains comprises a total of 33,091 homologous genes where (i) 65 are core genes (99% <= strains <= 100%), (ii) 33,026 are accessory genes present in <95% genomes composed of 3,738 shell genes (15% <= strains <95%) and 29,288 cloud genes (0% <= strains <15%). No soft genes (95% <= strains <99%) were identified (Figure 3A). The heatmaps (Figure 3B) generated based on the matrix of the presence or absence of genes (Supplementary Table S5) in *Psychrobacillus* species pangenomes display the variation in the distribution of accessory genes (Figure 3B). In general, pangenome gene families harbour the genetic determinants of species; core genome genes are typically involved in bacterial replication, translation, and maintenance of cellular homeostasis (Carlos Guimaraes et al., 2015; Brockhurst et al., 2019), and accessory genes are involved in responding to environmental changes during adaptive evolution (Brockhurst et al., 2019). Notably, we identified a high degree of heterogeneity among *Psychrobacillus* species, with many cloud genes (single genes) versus core genes (conserved genes). These single genes were unevenly distributed among species, with the lowest numbers in *P. lasiicapitis* ($n = 1,546$) versus *Psychrobacillus* sp. NEAU-3TGS ($n = 1,654$), *P. psychotolerans* ($n = 2,622$), *P. antarcticus* ($n = 2,915$), *P. soli* ($n = 3,082$), *P. soli* ($n = 3,082$), *P. insolutis* ($n = 3,096$), *P. psychodurans* ($n = 3,270$), *P. vilpus* (3,480) and *P. faecigallinarum* ($n = 3,789$) (Figure 2B and Supplementary Table S5). This analysis is consistent with a previous study on five *Psychrobacillus* species (Choi et al., 2020).

On the other hand, to determine whether the pangenome of *Psychrobacillus* strains is open or closed, the number of core and pangenome genes was plotted as a function of the number of cumulative genomes (V1–V10). The results showed that the size of the pangenome and the number of new genes increase steadily with the addition of each further genome (V1–V10), unlike the conserved genes, where they remain stable with low numbers (Figure 4). Accordingly, *Psychrobacillus species* had a large open pan-genome. Generally, members of species with open pan-genomes have relatively small core genomes with a more significant percentage of accessory genes within each genome, which is consistent with our results (Donati et al., 2010; Whitworth et al., 2021). Open pan-genomes profile of *Psychrobacillus* species may be correlated to the source of isolation and its geographical location, which always adds up new genes by horizontal gene transfer (HGT); typically, species living in different habitats benefit from various microbes a genetic material exchange and therefore continue to expand their total number of genes (Brockhurst et al., 2019; Chhotaray et al., 2020). *Psychrobacillus* species investigated in this analysis have been isolated from various ecological habitats, citing soils from Egypt, Gallus faeces from the UK, red fox faeces from Spain, an iceberg and soil from Antarctica, and head from China, oil-saturated soil and ferrous metal (Figure 1).

3.3 Production and structural property studies of exopolysaccharide and heavy metal bioabsorption evaluation

Psychrobacillus sp. NEAU-3TGS colonies exhibited a mucoid morphology on TSA medium supplemented with 2% glucose
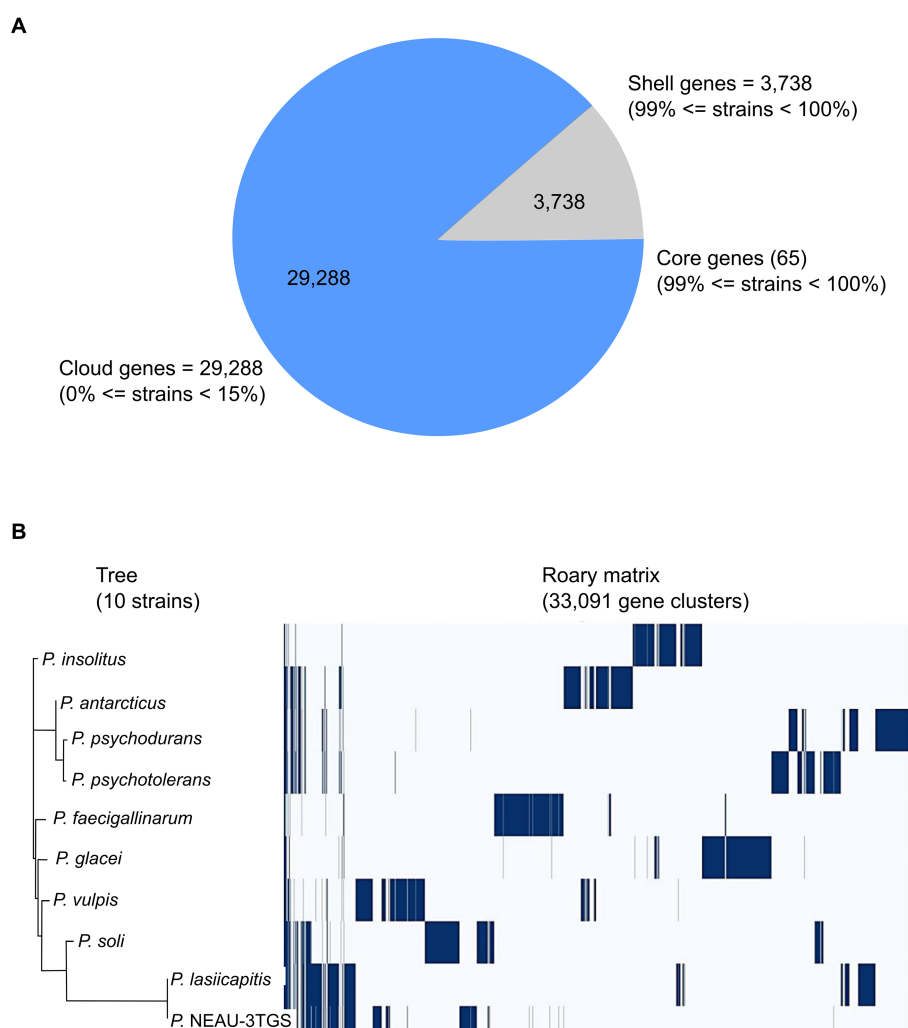
FIGURE 3
Pangenome analysis of ten strains of *Psychrobacillus* species by Roary. **(A)** Pie chart representation of pangenome of *Psychrobacillus* strains. The chart shows the gene distribution in the pangenome [Core genes (99% < strains <= 100%), shell genes (15% <= strains <= 95%) and cloud genes (0% <= strains <= 95%)]. **(B)** Phylogenetic tree of gene presence/absence matrix from pangenome analysis. Blue: the presence of the gene. White: the absence of the gene.

(Supplementary Figure S1), indicating extracellular sucrase activity (Malik et al., 2009). Genome mining for genes implicated in EPS production based on RAST annotation showed that *Psychrobacillus* sp. NEAU-3TGS contains 4 genes, including *eps*B (Manganese-dependent protein-tyrosine phosphatase), gene involved in the regulation of EPS biosynthesis (ii) *eps*C (Tyrosine-protein kinase transmembrane modulator) and *eps*D (Tyrosine-protein kinase), genes implicated on chain length determination of EPS (iii) *eps*E (Undecaprenyl-phosphate galactosephosphotransferase, gene involved on the biosynthesis of the repeating sugar units), followed by GT1 (glycosyltransferase de group 1) GT2 (glycosyltransferase de group 2) genes implicated in the process of adding glycosyl groups to the growing EPS chain. Glycosyltransferases (GTs) play a critical role in the biosynthesis of exopolysaccharides. They catalyse the formation of glycosidic linkages between sugar residues (Wang et al., 2020). EPS gene clusters vary among bacteria and are often called the *eps*ABCDE stretch. They are typically conserved and present in a specific order and play critical roles in the biosynthesis of exopolysaccharides (Deo et al., 2019).

NEAU-3TGS EPS was isolated and purified to a total dry weight of 20.5 mg per 100 mL and used for structural characterisation by ATR-FTIR and DRX analysis.

3.3.1 Powder X-ray diffraction analysis

Figure 5 displays the X-ray powder pattern of EPS, revealing three peaks around 15–40° (2θ). These peaks suggest the semi-crystalline and amorphous nature of EPS (Dogan et al., 2015; Mosharaf et al., 2018; Solmaz et al., 2018; Krishnamurthy et al., 2020; Mathivanan et al., 2021; Nwaiwu et al., 2021; Vinothkanna et al., 2022). For all the peaks observed in the XRD powder pattern, we have calculated the distance (*d*) and the Crystallinity Index (CI), as listed in Table 2.

Nicolaus et al. (2002) reported that EPS produced by thermophiles marine strains contains 81% carbohydrate, 3% protein, and 2% nucleic acid. The same study determined that the EPS was composed of glucose, mannose, galactose, and mannose-amine monomers by GC–MS analysis. Additionally, Dogan et al. (2015) reported that EPS produced by thermal *Bacillus* contains 80% of amorphous phases, including the presence of chitin, chitosan, protein, and calcite. EPS's
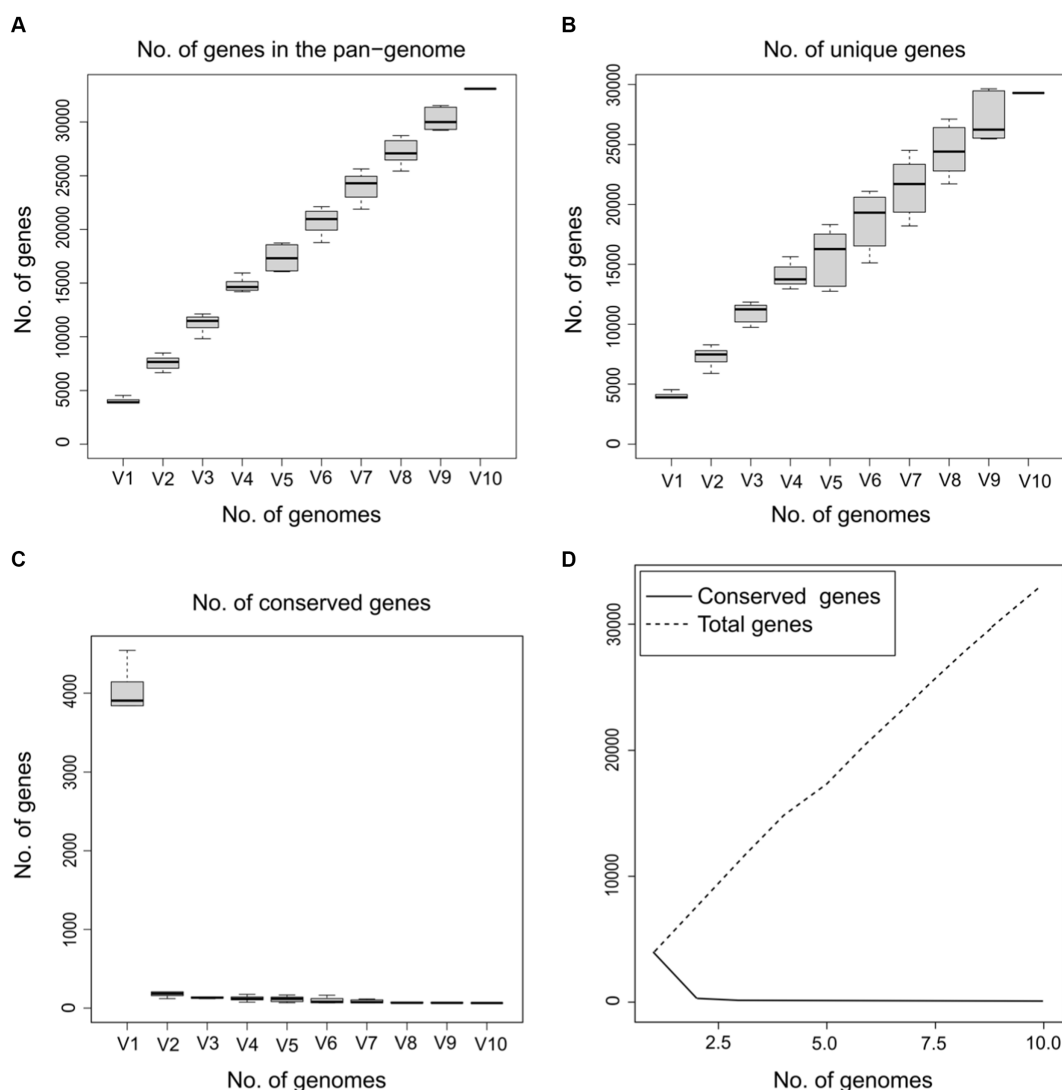
FIGURE 4
Gene discovery graphs for the ten *Psychrobacillus* strains demonstrating that as the total number of genes increases (V1–V10), the number of total (**A**) and unique genes increase (**B**) and the number of core genes gradually decreases (**C,D**).

Crystallinity Index (CI) value was determined to be 20%, indicating a semi-crystalline nature and the predominance of the amorphous phase. Based on Figure 5 and Table 2 and Dogan et al.'s findings (Dogan et al., 2015), the presence of chitin and chitosan is inferred, both observed at 4.47 Å with a CI of 13.69%. The presence of calcite (CaCO₃) is suggested at a distance of 3.08 Å, with a CI of 16.70%. An amorphous phase is indicated at 2.56 Å, with a dominant CI of 69.61%. Solmaz et al. (2018) also observed the presence of chitin and/or chitosan.

Several studies have shown that some composites of EPS, such as chitin and chitosan, have a potential for bioremediation (Samoila et al., 2019). For instance, they can be used to discolour textile dyes and remove ionic metals from wastewater (Fatima, 2021).

3.3.2 Attenuated total reflectance-Fourier transform infrared spectroscopy studies

ATR-FTIR analysis spectrum is depicted in Figure 6. The assignment of peaks to specific functional groups was based on
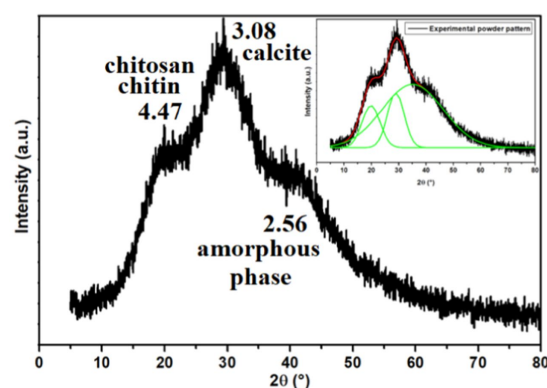

FIGURE 5
X-ray powder pattern of the exopolysaccharide. The inset illustrates the Gaussian fit result.

TABLE 2 The distance (*d*) and the crystallinity index (CI) of all peaks observed in the XRD powder pattern.

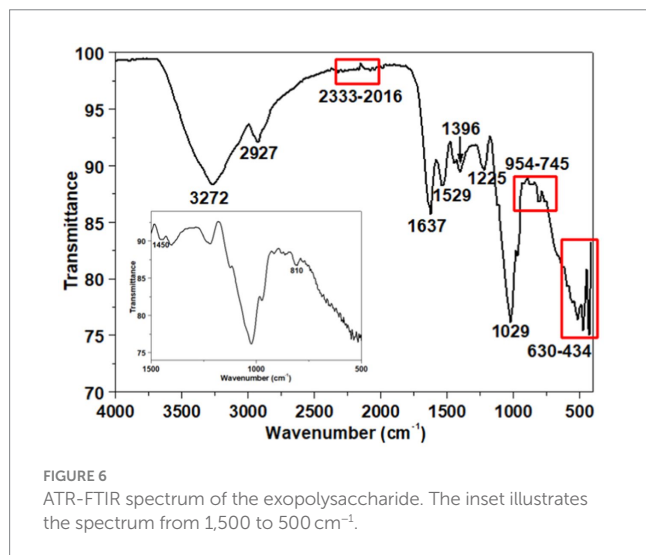| Peaks	Distance *d* (Å)	Crystallinity index CI (%)
Peak 1	4.47	13.69
Peak 2	3.08	16.70
Peak 3	2.56	69.61

FIGURE 6
ATR-FTIR spectrum of the exopolysaccharide. The inset illustrates the spectrum from 1,500 to 500 cm^{-1}.

previous studies (Badireddy et al., 2010; Jiao et al., 2010; Brian-Jaisson et al., 2016; Wang et al., 2016; Maddela et al., 2018; Hong et al., 2021; Wang et al., 2022). The peak at 3272 cm^{-1} is indicative of the stretching vibration associated with both hydroxyl groups ($-OH$) of carbohydrates in polysaccharides and amino groups ($-NH_2$ or $-NH$) of proteins (Braissant et al., 2007; Tapia et al., 2009; Liang et al., 2010; Deng et al., 2022; Wang et al., 2022). The absorption peak at 2927 cm^{-1} (Braissant et al., 2007) corresponds to the C–H stretching vibration of aliphatic $-CH_2$ or $-CH_3$ groups, revealing the carbohydrate structure of EPS (Parikh and Madamwar, 2006) and indicating the presence of sugar content (Iyer et al., 2005). The IR peaks observed in the range of 2,333–2016 cm^{-1} may be attributed to CO_2 adsorption or the asymmetric stretching of $-N=C=O-$ groups (Mishra and Jha, 2009).

Furthermore, the ATR-FTIR spectrum shows two peaks at 1637 cm^{-1} and 1,529 cm^{-1}, attributed to amides I and II of the secondary protein structure within the EPS (Maruyama, 2001; Badireddy et al., 2008, 2010; Sheng et al., 2013). The symmetric stretching of C=O in the $-COO^-$ is represented by a peak at 1396 cm^{-1} (Nara et al., 1994; Omoike and Chorover, 2004; Pongjanyakul and Puttipipatkhachorn, 2007; Badireddy et al., 2008; Freitas et al., 2009; Sheng et al., 2013). A minor peak at 1225 cm^{-1}, associated with $N-H$ bending and $C-N$ stretching vibrations (Coates, 2000), was also observed. A peak at 1029 cm^{-1} indicates the presence of uronic acid's o-acetyl ester linkage bonds (Bramhachari and Dubey, 2006). Additionally, the 954–745 cm^{-1} range confirms the presence of an α-1,4-glycosidic bond (Maddela et al., 2018). Firm absorption peaks in the 630–434 cm^{-1} range are attributed to the deformation of $-COO^-$ groups in polysaccharides (Wiercigroch et al., 2017).

Based on DRX analysis, chitin, chitosan, calcite ($CaCO_3$) and an amorphous phase were identified. The IR spectrum analysis supports

these findings, revealing characteristics peaks indicative of chitosan and chitin (notably at 3272, 1637, 1,529, 1,396, and 1,225 cm^{-1}), corresponding to N-H stretching of amine groups, C=O stretching related to the amide I band, and N-H bending associated with the amide II band (Dahmane et al., 2014; Negrea et al., 2015). For the calcite phase, characteristic peaks at 1450 and 810 cm^{-1} were observed (inset Figure 6), corresponding to the asymmetric stretching and bending vibrations of the carbonate ion (CO_3^{2-}) present in calcium carbonate (Singh and Sawant, 2022).

Overall, the FTIR spectra decipher the functional groups of the carbohydrate polymer, which are reported to play an essential role in the functional and biological activities of the EPS. For example, the presence of hydroxyl (OH) and aliphatic (CH_2) groups makes the EPS either hydrophilic or hydrophobic, making it an appropriate emulsifying agent (Sathiyanarayanan et al., 2016). Indeed, the presence of carboxylate (COO^-) functional groups allows these polymers to bind to other oppositely charged molecules, such as heavy metals (Donot et al., 2012).

Based on the structural properties of *Psychrobacillus* sp. NEAU-3TGS EPS', we have assessed its ability to remove iron, copper, lead and cadmium ions, with high toxicity and among the priority metals of public health significance (Tchounwou et al., 2012). The adsorption rate of each metal (cadmium, lead, iron, and copper) was determined as a function of contact time, pH, and temperature at 1000 ppm of metal and 1 mg/100 mL of EPS (Figure 7).

The effect of pH was tested at 37°C for 24 h. Results showed that adsorption is moderately affected by pH for all metals (Figure 7A). The maximum activities are observed at pH = 7 with 95, 88, 70, and 70% for iron, lead, cadmium and copper, respectively (*p*-value >0.05 for three replicates per test). These results are consistent with those reported on the EPS of *Bacillus*-related members conducted under the same conditions for three isolates, citing *Bacillus licheniformis*, *Bacillus cereus* and *Bacillus subtilis*, where lead was the most adsorbed compared to copper and cadmium (Shameer, 2016; Biswas et al., 2020; Krishnamurthy et al., 2020; Zainab et al., 2020). The different removal efficiency observed for iron (Fe^{3+}) compared to lead (Pb^{2+}), copper (Cu^{2+}), and cadmium (Cd^{2+}) could be attributed to the different charge density of the ions, which depends on the ionic size of the cations (Salehizadeh and Shojaosadati, 2003). Other studies have reported that the rate of adsorption of metal ions by the EPS of some *Bacillus*-related members varies depending on bacteria species, metal and pH of the solution. For instance, for *Bacillus mucilaginosus*, the iron adsorption was optimal at pH 5.0 (Yang et al., 2017). For *Bacillus firmus*, the optimal pH for lead, copper, and zinc was 4.5, 4, and 6, respectively (Salehizadeh and Shojaosadati, 2003). Differences in removal efficiency could also be attributed to the different charge densities of the ions, which depend on the cations' ionic size and the solution's pH (Salehizadeh and Shojaosadati, 2003). The pH of the solution significantly affects the adsorption process of metal ions. At low pH values, the high concentration of H^+ ions competes with metal ions for adsorption sites and at high pH values, the negative charge density on the EPS surface may increase due to deprotonation of metal binding sites, thus decreasing metal adsorption (Kim et al., 1996; Can and Jianlong, 2007; Wei et al., 2016).

The influence of temperature on the adsorption rate was tested at pH = 7 for 24 h. The results showed that the values are almost similar, and the best were observed at 37°C with 95, 88, 70 and 69.6% for iron,
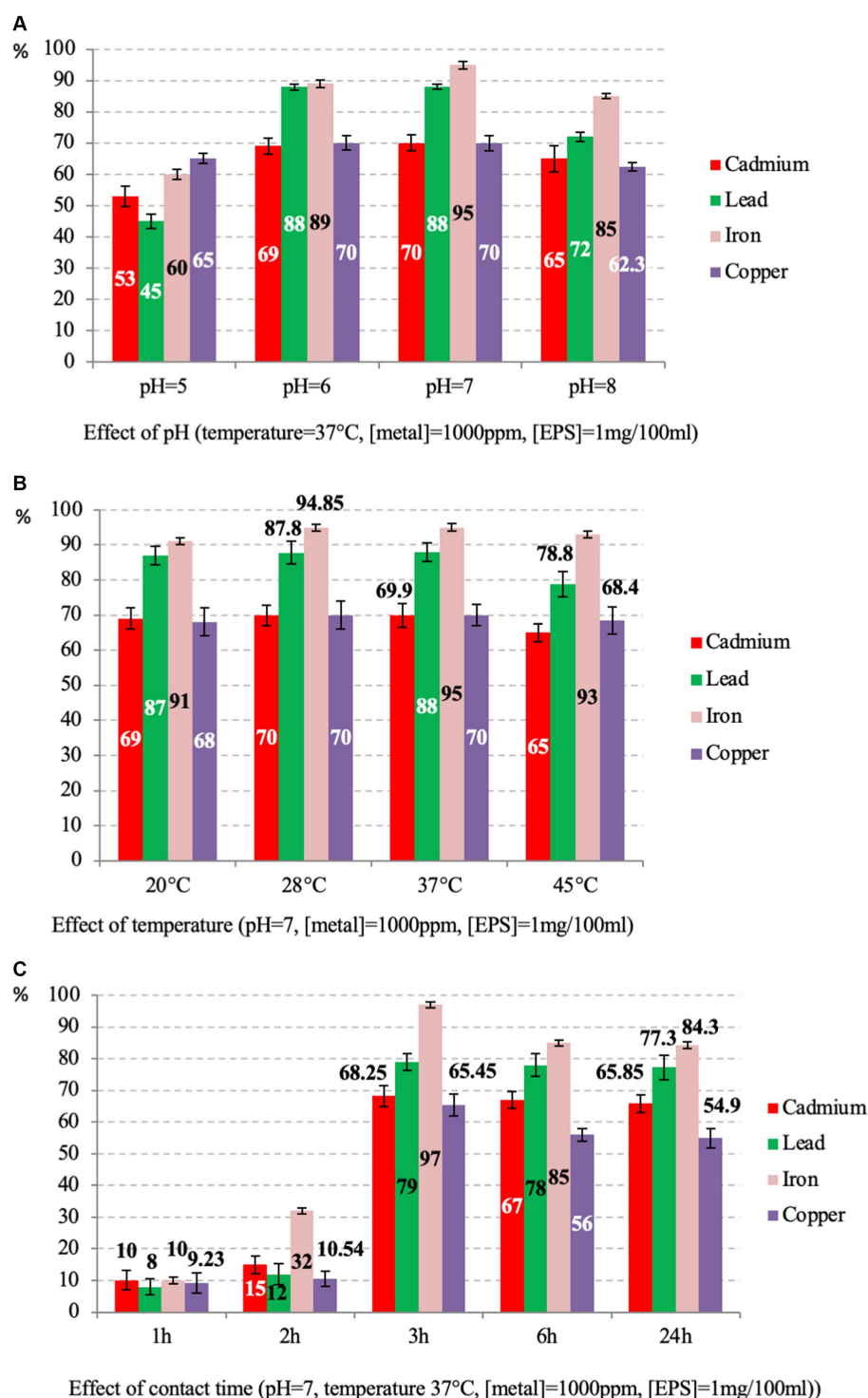
FIGURE 7

Percentage of EPS adsorption rates of caddmium, lead, iron and copper at various parameters, including pH **(A)**, temperature **(B)** and contact time **(C)**.

lead, cadmium and copper, respectively (*p*-value <0.05 for three replicates per test) (Figure 7B). Generally, the effect of temperature on metal adsorption depends on the tested metal and biomolecules, citing the example of *B. cereus*, where the optimal temperature for manganese biosorption was 35°C (Zhenggang et al., 2018).

The contact time was tested at 37°C and pH=7. The results showed that the uptake rate increased with the time of incubation. The

best rate was observed at 3 h for all metals with 97, 79, 68.25, and 65.45% (*p*-value >0.05 for three replicates per test) for iron, lead, cadmium and copper respectively, and a slightly decreasing was observed up to 24 h (Figure 7C). As the contact time increases, the adsorption rate decreases because the metal ions gradually occupy the binding sites, thus reducing the concentration of lead and cadmium ions in the solution (El-Sayed, 2013).

It is worth noting that iron was the most adsorbed in all conditions. These results agree with those reported on the EPS of *Bacillus*-related members (Krishnamurthy et al., 2020; Zainab et al., 2020). In general, EPSs are implicated in treating metal-contaminated environments (Zheng et al., 2008; Chouchane et al., 2020; Siddharth et al., 2021). It is well known that EPSs have a large surface area for interaction, especially with metals, which is helpful for survival in various contaminated areas (Pal and Paul, 2008).

3.4 Genomic insights on iron acquisition and metabolism in *Psychrobacillus* sp. NEAU-3TGS

Given its origin of isolation, we were interested in identifying the mechanisms of iron metabolism and uptake used by *Psychrobacillus* sp. NEAU-3TGS, based on RAST annotation. Results revealed that genes encoding for membrane proteins are involved in the uptake of siderophores, iron transporter, and exporter proteins, although no genes involved in siderophore biosynthesis were found. The genes are as follows: iron ABC transporter permease ($n = 9$), iron export ABC transporter permease subunit FetB ($n = 1$), iron-hydroxamate ABC transporter substrate-binding protein ($n = 1$), iron chelate uptake ABC transporter family permease subunit ($n = 1$) and iron-siderophore ABC transporter substrate-binding protein ($n = 2$) (Supplementary Table S6 and Supplementary Figure S2A). Analysis of the iron-siderophore uptake systems revealed that the NEAU-3TGS strain imports both bacillibactin and petrobactin ferric complexes. Siderophore bacillibactin (or corynebactin) is a catechol trilactone secreted by various types of bacilli, notably *Bacillus anthracis* and *Bacillus subtilis* (May et al., 2001; Cendrowski et al., 2004). The compound is mainly utilised to chelate Fe^{3+} present outside the cell and transfer them into the cytoplasm via an ABC2 transporter (Hotta et al., 2010). Ferri-bacillibactin uptake is mediated by the FeuABC transporter and tri-lactone hydrolase (YuiI). FeuA is a periplasmic binding protein component acting as a peptidoglycan siderophore-binding protein. FeuB is a membrane permease component which forms a channel through the bacteria's inner membrane where iron ions can pass. FeuC is the inner membrane's ATP-binding cassette (ABC) protein component. It is responsible for binding and hydrolysing ATP, providing the energy necessary to transport iron ions through the membrane. FeuB interacts with FeuC and works in concert with the uptake of iron ions into the bacterial cell. FeuD is an ATPase component of an ABC-type iron-compound transporter. Iron is liberated from the Fe-bacillibactin complex upon transport through hydrolysis mediated via the trilactone hydrolase (YuiI), which can cleave the siderophore. The gene cluster is organized in an apparent single operon under Fur family transcriptional regulator (Fur) containing FeuABCD and Fur regulation gene (Supplementary Figure S2B).The gene cluster FeuABCD and trilactone hydrolase (BesA) was identified in *Bacillus*-related members such as *B. anthracis, B. subtilis, B. cereus, B. thuringiensis* and *B. subtilis* groups (Miethke et al., 2006; Abergel et al., 2008; Hayrapetyan et al., 2016). Furthermore, other studies reported that the FeuABC-YusV transporter of *B. subtilis* was shown to import ferric complexes of both bacillibactin and enterobactin siderophores (Miethke et al., 2006).

Concerning the siderophore petrobactin (anthrachelin), the uptake within NEAU-3TGS strain is mediated by Fe-ABC1 (Iron compound ABC uptake transporter substrate-binding protein), the Fe-ABC2 (Iron compound ABC uptake transporter permease protein) and Fe-ABC3 (Iron compound ABC uptake transporter ATP-binding protein) (Supplementary Figure S2C). Siderophores petrobactin is a highly specific iron (III) transport ligand (Rue and Bruland, 1995; Manck et al., 2022). The iron-chelated petrobactin complex is easily subjected to photolytic oxidative decarboxylation due to its α-hydroxy carboxylate group, converting iron (III) to the more biologically useful iron (II) (Barbeau et al., 2002). Previous studies have elucidated the petrobactin-iron complex receptor (FhuA), import permeases (FpuB/FatC/FatD), ATPases (FpuC/FatE), and the petrobactin exporter (ApeX) (Hagan et al., 2018). Genome mining for iron metabolism was also assessed for the nine *Psychrobacillus* species, and the results showed that it is like the NEAU-3TGS strain, with no genes implicated in the biosynthesis of siderophore. Indeed, the siderophores petrobactin uptake system was present in all species. However, the bacillibactin uptake system (FeuABCD/YuiI) was present only within the *P. facigallinarum* genome sequence (Supplementary Table S6).

3.5 Structural analysis

The molecular model of FeuA was obtained through deep learning modelling and was used for docking siderophores ferrienterobactine $[Fe^{+3}(ENT)]^{-3}$ and ferribacillibactine $[Fe^{+3}(BB)]^{-3}$. Gram-negative bacteria, such as *E. coli*, mainly produce enterobactine (ENT). At the same time, becillibactine (BB) is secreted by gram-positive bacteria, such as some *Bacillus* species (*B. antrhacis*, *B. cereus*, *B. subtilis*). Both ENT and BB have binding to the siderophore binding site of FeuA from *Pyschrobacillus* sp. (Figure 8). $[Fe^{+3}(ENT)]^{-3}$ binds to Phe122, Lys127, Ile100, Gln314, Arg215, Arg217, and Gln252 (Figure 8A). Compared to the crystal structure of the complex FuA-$[Fe^{+3}(ENT)]^{-3}$ from *Bacillus subtilis* (Figure 8B), some conserved amino acids are present: Phe106, Lys84, Arg178, Arg180, and Gln215. In the complex of FeuA from *Pyschrobacillus* sp. and $[Fe^{+3}(BB)]^{-3}$ (Figure 8C), most of the same amino acids involved in the interaction with $[Fe^{+3}(ENT)]^{-3}$ participate. In addition, Cys222 and Tyr229, but not Ile100. Perhaps the amino acids in the binding site are flexible enough to accommodate slightly different siderophores.

4 Conclusion

A new *Psychrobacillus* sp. NEAU-3TGS bacterium was isolated from an iron ore deposit. Pangenome analysis of the nine valid species revealed that *Psychrobacillus* genomic diversity represents an "open" pangenome model. NEAU-3TGS strain showed the potential to produce EPS encoding by *eps*B (manganese-dependent protein-tyrosine phosphatase), *eps*C (tyrosine-protein kinase transmembrane modulator), *eps*D (tyrosine-protein kinase), *eps*E (undecaprenyl-phosphate galactose phosphotransferase) and GT1, 2 (glycosyltransferase de group 1 and 2). Structural characterisation of EPS with XRD analysis showed the presence of chitin, chitosan, and calcite $CaCO_3$ and confirmed the amorphous nature of the EPS. On the other hand, ATR-FTIR spectroscopy demonstrated that secondary proteins, uronic acid, α-1,4-glycosidic, and polysaccharides are the
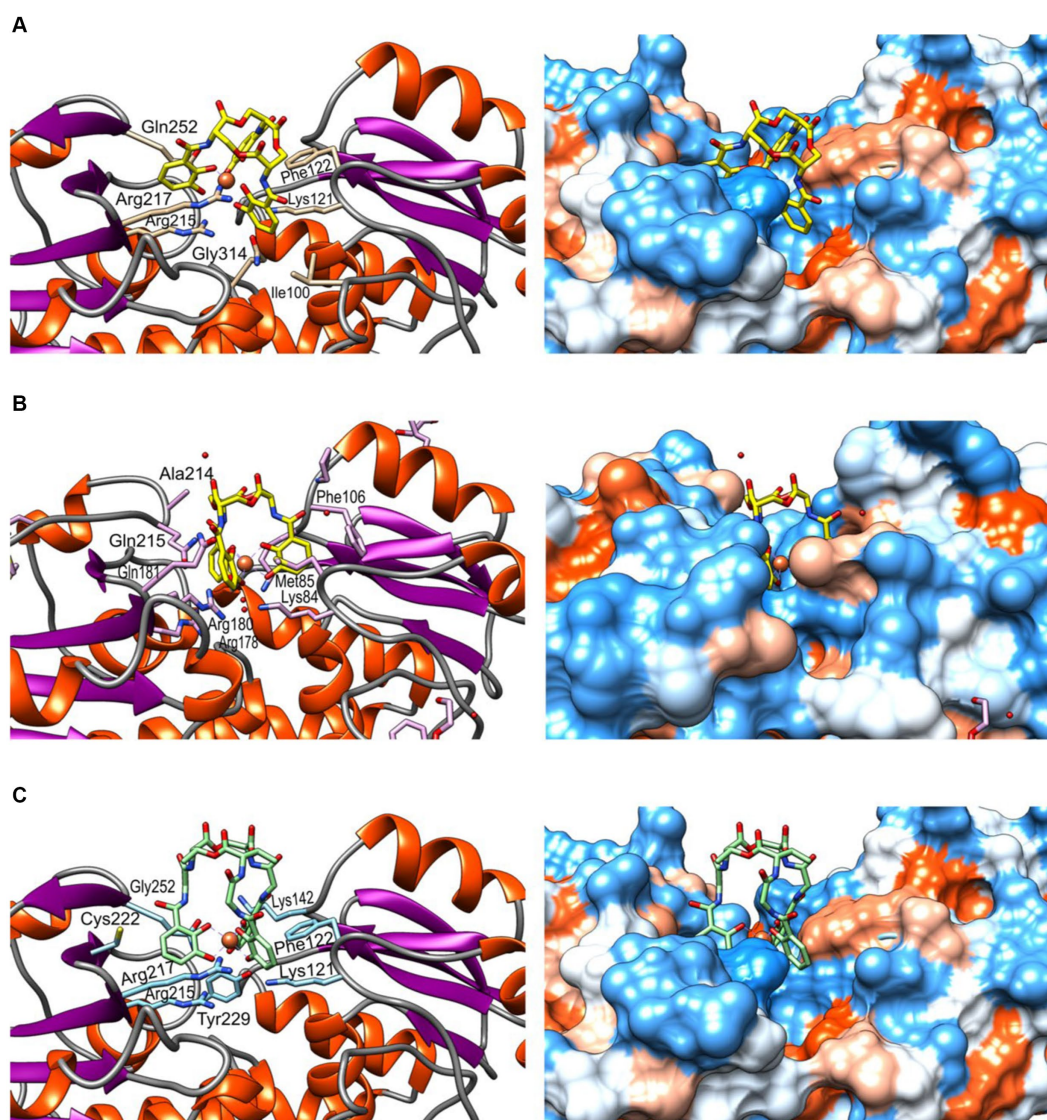
FIGURE 8
Molecular modelling and docking of FeuA. **(A)** Complex FuA-[Fe^{+3}(ENT)]$^{-3}$, **(B)** Complex FuA-[Fe^{+3}(ENT)]$^{-3}$ from *Bacillus subtilis*, crystall structure (PDB: 2XUZ) (Peuckert et al., 2011). **(C)** Complex FuA-[Fe^{+3}(BB)]$^{-3}$. According to the Kyte-Doolittle scale, the corresponding hydrophobicity surfaces are represented on the left side (Kyte and Doolittle, 1982), ranging from dodger blue for the most hydrophilic to white and orange-red for the most hydrophobic.

main components of the EPS. Heavy metal bioabsorption assessment showed that EPS adsorbs iron, lead, copper and cadmium. Based on the present results, *Psychrobacillus* sp. NEAU-3TGS may be involved in an ecological alternative for heavy metal remediation. *In silico* genomic insights into iron uptake and metabolism showed that only gene cluster *Feu*BCD and trilactone hydrolase gene involved in the uptake of siderophores, iron transporter, and exporter are present in the genome. Molecular modelling and docking of FeuA (protein peptidoglycan siderophore-binding protein) and siderophores ferrienterobactine [Fe^{+3}(ENT)]$^{-3}$ and ferribacillibactine [Fe^{+3}(BB)]$^{-3}$ ligand revealed that [Fe^{+3}(ENT)]$^{-3}$ binds to Phe122, Lys127, Ile100, Gln314, Arg215, Arg217, and Gln252. Almost the same for [Fe^{+3}(ENT)]$^{-3}$ in addition to Cys222 and Tyr229, but not Ile100. Further studies could be undertaken to understand the iron metabolism pathway via transcriptomic or proteomic analyses.

Data availability statement

The datasets presented in this study can be found in online repositories. The names of the repository/repositories and accession number(s) can be found in the article/Supplementary material.

Author contributions

AN: Conceptualization, Data curation, Investigation, Visualization, Writing – original draft, Writing – review & editing. MJ: Investigation, Methodology, Writing – review & editing. SC: Conceptualization, Data curation, Investigation, Methodology, Writing – original draft, Writing – review & editing. AC: Formal analysis, Resources, Supervision, Writing – review & editing. HO:

Formal analysis, Resources, Supervision, Validation, Writing – review & editing. JAL-P: Conceptualization, Formal analysis, Investigation, Methodology, Resources, Software, Supervision, Visualization, Writing – review & editing. HS: Conceptualization, Formal analysis, Resources, Supervision, Validation, Writing – review & editing.

Funding

Conflict of interest

The authors declare that the research was conducted in the absence of any commercial or financial relationships that could be construed as a potential conflict of interest.

The author(s) declared that they were an editorial board member of Frontiers, at the time of submission. This had no impact on the peer review process and the final decision.

Publisher's note

Supplementary material

The Supplementary material for this article can be found online at: https://www.frontiersin.org/articles/10.3389/fmicb.2024.1440081/full#supplementary-material

References

Abd El-Rahman, H. A., Fritze, D., Spröer, C., and Claus, D. (2002). Two novel psychrotolerant species, Bacillus psychrotolerans sp. nov. and Bacillus psychrodurans sp. nov., which contain ornithine in their cell walls. *Int. J. Syst. Evol. Microbiol.* 52, 2127–2133. doi: 10.1099/00207713-52-6-2127

Abergel, R. J., Zawadzka, A. M., and Raymond, K. N. (2008). Petrobactin-mediated Iron transport in pathogenic bacteria: coordination chemistry of an unusual 3,4-Catecholate/citrate Siderophore. *J. Am. Chem. Soc.* 130, 2124–2125. doi: 10.1021/ja077202g

Ahmad, N. H., Mustafa, S., and Che Man, Y. B. (2015). Microbial polysaccharides and their modification approaches: a review. *Int. J. Food Prop.* 18, 332–347. doi: 10.1080/10942912.2012.693561

Andrews, S. C., Robinson, A. K., and Rodríguez-Quiñones, F. (2003). Bacterial iron homeostasis. *FEMS Microbiol. Rev.* 27, 215–237. doi: 10.1016/S0168-6445(03)00055-X

Ates, O. (2015). Systems biology of microbial exopolysaccharides production. *Front. Bioeng. Biotechnol.* 3:e200. doi: 10.3389/fbioe.2015.00200

Aziz, R. K., Bartels, D., Best, A. A., DeJongh, M., Disz, T., Edwards, R. A., et al. (2008). The RAST server: rapid annotations using subsystems technology. *BMC Genomics* 9:75. doi: 10.1186/1471-2164-9-75

Badireddy, A. R., Chellam, S., Gassman, P. L., Engelhard, M. H., Lea, A. S., and Rosso, K. M. (2010). Role of extracellular polymeric substances in bioflocculation of activated sludge microorganisms under glucose-controlled conditions. *Water Res.* 44, 4505–4516. doi: 10.1016/j.watres.2010.06.024

Badireddy, A. R., Korpol, B. R., Chellam, S., Gassman, P. L., Engelhard, M. H., Lea, A. S., et al. (2008). Spectroscopic characterisation of extracellular polymeric substances from Escherichia coli and Serratia marcescens: suppression using sub-inhibitory concentrations of bismuth thiols. *Biomacromolecules* 9, 3079–3089. doi: 10.1021/bm800600p

Baek, M., DiMaio, F., Anishchenko, I., Dauparas, J., Ovchinnikov, S., Lee, G. R., et al. (2021). Accurate prediction of protein structures and interactions using a three-track neural network. *Science* 373, 871–876. doi: 10.1126/science.abj8754

Bankevich, A., Nurk, S., Antipov, D., Gurevich, A. A., Dvorkin, M., Kulikov, A. S., et al. (2012). SPAdes: a new genome assembly algorithm and its applications to single-cell sequencing. *J. Comput. Biol.* 19, 455–477. doi: 10.1089/cmb.2012.0021

Barbeau, K., Zhang, G., Live, D. H., and Butler, A. (2002). Petrobactin, a Photoreactive Siderophore produced by the oil-degrading marine bacterium Marinobacter hydrocarbonoclasticus. *J. Am. Chem. Soc.* 124, 378–379. doi: 10.1021/ja0119088

Biswas, J. K., Banerjee, A., Sarkar, B., Sarkar, D., Sarkar, S. K., Rai, M., et al. (2020). Exploration of an extracellular polymeric substance from earthworm gut bacterium (Bacillus licheniformis) for bioflocculation and heavy metal removal potential. *Appl. Sci.* 10:349. doi: 10.3390/app10010349

Bolger, A. M., Lohse, M., and Usadel, B. (2014). Trimmomatic: a flexible trimmer for Illumina sequence data. *Bioinformatics* 30, 2114–2120. doi: 10.1093/bioinformatics/btu170

Bradford, M. M. (1976). A rapid and sensitive method for the quantitation of microgram quantities of protein utilizing the principle of protein-dye binding. *Anal. Biochem.* 72, 248–254. doi: 10.1016/0003-2697(76)90527-3

Braissant, O., Decho, A. W., Dupraz, C., Glunk, C., Przekop, K. M., and Visscher, P. T. (2007). Exopolymeric substances of sulfate-reducing bacteria: interactions with calcium

at alkaline pH and implication for formation of carbonate minerals. *Geobiology* 5, 401–411. doi: 10.1111/j.1472-4669.2007.00117.x

Bramhachari, P. V., and Dubey, S. K. (2006). Isolation and characterisation of exopolysaccharide produced by Vibrio harveyi strain VB23. *Lett. Appl. Microbiol.* 43, 571–577. doi: 10.1111/j.1472-765X.2006.01967.x

Braun, V., and Hantke, K. (2011). Recent insights into iron import by bacteria. *Curr. Opin. Chem. Biol.* 15, 328–334. doi: 10.1016/j.cbpa.2011.01.005

Brian-Jaisson, F., Molmeret, M., Fahs, A., Guentas-Dombrowsky, L., Culioli, G., Blache, Y., et al. (2016). Characterisation and anti-biofilm activity of extracellular polymeric substances produced by the marine biofilm-forming bacterium Pseudoalteromonas ulvae strain TC14. *Biofouling* 32, 547–560. doi: 10.1080/08927014.2016.1164845

Brockhurst, M. A., Harrison, E., Hall, J. P. J., Richards, T., McNally, A., and MacLean, C. (2019). The ecology and evolution of Pangenomes. *Curr. Biol.* 29, R1094–R1103. doi: 10.1016/j.cub.2019.08.012

Can, C., and Jianlong, W. (2007). Correlating metal ionic characteristics with biosorption capacity using QSAR model. *Chemosphere* 69, 1610–1616. doi: 10.1016/j.chemosphere.2007.05.043

Cao, R., Zhang, Y., Ju, Y., Wang, W., Zhao, Y., Liu, N., et al. (2023). Exopolysaccharide-producing bacteria enhanced Pb immobilisation and influenced the microbiome composition in rhizosphere soil of pakchoi (Brassica chinensis L.). *Front. Microbiol.* 14:1117312. doi: 10.3389/fmicb.2023.1117312

Carlos Guimaraes, L., Benevides De Jesus, L., Vinicius Canario Viana, M., Silva, A., Thiago Juca Ramos, R., De Castro Soares, S., et al. (2015). Inside the Pan-genome—methods and software overview. *CG* 16, 245–252. doi: 10.2174/1389202916666150423002311

Carrión, O., Delgado, L., and Mercade, E. (2015). New emulsifying and cryoprotective exopolysaccharide from Antarctic Pseudomonas sp. ID1. *Carbohydr. Polym.* 117, 1028–1034. doi: 10.1016/j.carbpol.2014.08.060

Cendrowski, S., MacArthur, W., and Hanna, P. (2004). Bacillus anthracis requires siderophore biosynthesis for growth in macrophages and mouse virulence. *Mol. Microbiol.* 51, 407–417. doi: 10.1046/j.1365-2958.2003.03861.x

Chaudhari, N. M., Gautam, A., Gupta, V. K., Kaur, G., Dutta, C., and Paul, S. (2018). PanGFR-HM: a dynamic web resource for Pan-genomic and functional profiling of human microbiome with comparative features. *Front. Microbiol.* 9:2322. doi: 10.3389/fmicb.2018.02322

Cherif, A., Borin, S., Rizzi, A., Ouzari, H., Boudabous, A., and Daffonchio, D. (2003). Bacillus anthracis diverges from related clades of the Bacillus cereus group in 16S-23S ribosomal DNA intergenic transcribed spacers containing tRNA genes. *Appl. Environ. Microbiol.* 69, 33–40. doi: 10.1128/AEM.69.1.33-40.2003

Chhotaray, C., Wang, S., Tan, Y., Ali, A., Shehroz, M., Fang, C., et al. (2020). Comparative analysis of whole-genome and Methylome profiles of a smooth and a rough Mycobacterium abscessus clinical strain. *G3 Genes|Genomes|Genetics* 10, 13–22. doi: 10.1534/g3.119.400737

Choi, J. Y., Kim, S. C., and Lee, P. C. (2020). Comparative genome analysis of Psychrobacillus strain PB01, isolated from an iceberg. *J. Microbiol. Biotechnol.* 30, 237–243. doi: 10.4014/jmb.1909.09008

Choi, J. Y., and Lee, P. C. (2020). Psychrobacillus glaciei sp. nov., a psychrotolerant species isolated from an Antarctic iceberg. *Int. J. Syst. Evol. Microbiol.* 70, 1947–1952. doi: 10.1099/ijsem.0.003998

Chouchane, H., Najjari, A., Cherif, H., Neifar, M., Sghaier, H., Ouzari, H. I., et al. (2020). Carboxymethylated sulfated Heteroexopolysaccharide from a Haloarchaeal strain as potential biomolecule for harmless adjuvant therapy in Cancer treatment. *J. Chem.* 2020, 1–12. doi: 10.1155/2020/8907958

Coates, J. (2000). Interpretation of infrared spectra, a practical approach, R. A. Meyers (Ed.), Encyclopedia of analytical chemistry. Wiley

Corsaro, M. M., Lanzetta, R., Parrilli, E., Parrilli, M., Tutino, M. L., and Ummarino, S. (2004). Influence of growth temperature on lipid and phosphate contents of surface polysaccharides from the Antarctic bacterium Pseudoalteromonas haloplanktis TAC 125. *J. Bacteriol.* 186, 29–34. doi: 10.1128/JB.186.1.29-34.2004

Da Silva, M. B. F., Da Mota, F. F., Cypriano, J., Abreu, F., and Seldin, L. (2023). Psychrobacillus antarcticus sp. nov., a psychrotolerant bioemulsifier producer isolated from King George Island, Antarctica. *Int. J. Syst. Evol. Microbiol.* 73:e6181. doi: 10.1099/ijsem.0.006181

Da Silva, M. B. F., Da Mota, F. F., Jurelevicius, D., De Carvalho Azevedo, V. A., Da Costa, M. M., Góes-Neto, A., et al. (2022). Genomic analyses of a novel bioemulsifier-producing Psychrobacillus strain isolated from soil of King George Island, Antarctica. *Polar Biol.* 45, 691–701. doi: 10.1007/s00300-022-03028-1

Dahmane, E. M., Taourirte, M., Eladlani, N., and Rhazi, M. (2014). Extraction and characterization of chitin and chitosan from Parapenaeus longirostris from Moroccan local sources. *Int. J. Polym. Anal. Charact.* 19, 342–351. doi: 10.1080/1023666X.2014.902577

DasSarma, P., and DasSarma, S. (2018). Survival of microbes in Earth's stratosphere. *Curr. Opin. Microbiol.* 43, 24–30. doi: 10.1016/j.mib.2017.11.002

Decrée, S., De Putter, T., Yans, J., Moussi, B., Recourt, P., Jamoussi, F., et al. (2008). Iron mineralisation in Mio-Pliocene sediments of the Tamra iron mine (Nefza mining district, Tunisia): mixed influence of pedogenesis and hydrothermal alteration. *Ore Geol. Rev.* 33, 397–410. doi: 10.1016/j.oregeorev.2007.02.001

Deng, D., Meng, H., Ma, Y., Guo, Y., Wang, Z., He, H., et al. (2022). Effects of extracellular polymeric substances on the aggregation of Aphanizomenon flos-aquae under increasing temperature. *Front. Microbiol.* 13:971433. doi: 10.3389/fmicb.2022.971433

Deo, D., Davray, D., and Kulkarni, R. (2019). A diverse repertoire of exopolysaccharide biosynthesis gene clusters in Lactobacillus revealed by comparative analysis in 106 sequenced genomes. *Microorganisms* 7:444. doi: 10.3390/microorganisms7100444

Diene, S. M., Merhej, V., Henry, M., El Filali, A., Roux, V., Robert, C., et al. (2013). The rhizome of the multidrug-resistant Enterobacter aerogenes genome reveals how new killer bugs are created because of a sympatric lifestyle. *Mol. Biol. Evol.* 30, 369–383. doi: 10.1093/molbev/mss236

Dogan, N. M., Doganli, G. A., Dogan, G., and Bozkaya, O. (2015). Characterization of extracellular polysaccharides (EPS) produced by thermal Bacillus and determination of environmental conditions affecting exopolysaccharide production. *Int. J. Environ. Res.* 9:e998. doi: 10.22059/ijer.2015.998

Donati, C., Hiller, N. L., Tettelin, H., Muzzi, A., Croucher, N. J., Angiuoli, S. V., et al. (2010). Structure and dynamics of the pan-genome of Streptococcus pneumoniae and closely related species. *Genome Biol.* 11:R107. doi: 10.1186/gb-2010-11-10-r107

Donot, F., Fontana, A., Baccou, J. C., and Schorr-Galindo, S. (2012). Microbial exopolysaccharides: main examples of synthesis, excretion, genetics and extraction. *Carbohydr. Polym.* 87, 951–962. doi: 10.1016/j.carbpol.2011.08.083

El Hidri, D., Guesmi, A., Najjari, A., Cherif, H., Ettoumi, B., Hamdi, C., et al. (2013). Cultivation-Dependant assessment, diversity, and ecology of Haloalkaliphilic Bacteria in arid saline Systems of Southern Tunisia. *Biomed. Res. Int.* 2013, 1–15. doi: 10.1155/2013/648141

El-Sayed, M. T. (2013). Removal of lead(II) by Saccharomyces cerevisiae AUMC 3875. *Ann. Microbiol.* 63, 1459–1470. doi: 10.1007/s13213-013-0609-x

Fatima, B. (2021). "Sustainable treatment of heavy metals by adsorption on raw chitin/chitosan" in Trace metals in the environment - new approaches and recent advances. eds. M. Alfonso Murillo-Tovar, H. Saldarriaga-Noreña and A. Saeid (IntechOpen).

Felsenstein, J. (1981). Evolutionary trees from DNA sequences: a maximum likelihood approach. *J. Mol. Evol.* 17, 368–376. doi: 10.1007/BF01734359

Freitas, F., Alves, V. D., Pais, J., Costa, N., Oliveira, C., Mafra, L., et al. (2009). Characterization of an extracellular polysaccharide produced by a Pseudomonas strain grown on glycerol. *Bioresour. Technol.* 100, 859–865. doi: 10.1016/j.biortech.2008.07.002

Gilroy, R., Ravi, A., Getino, M., Pursley, I., Horton, D. L., Alikhan, N.-F., et al. (2021). Extensive microbial diversity within the chicken gut microbiome revealed by metagenomics and culture. *PeerJ* 9:e10941. doi: 10.7717/peerj.10941

Goris, J., Konstantinidis, K. T., Klappenbach, J. A., Coenye, T., Vandamme, P., and Tiedje, J. M. (2007). DNA–DNA hybridisation values and their relationship to whole-genome sequence similarities. *Int. J. Syst. Evol. Microbiol.* 57, 81–91. doi: 10.1099/ijs.0.64483-0

Guesmi, S., Chouchane, H., Neifar, M., Hosni, F., Cherif, A., and Sghaier, H. (2019). Radiation-inducible radioprotective exopolysaccharides of Bacillus siamensis CV5 from irradiated roots of Cistanche violacea to decrease free radical damage produced by ionising radiation. *Int. J. Radiat. Biol.* 95, 1552–1563. doi: 10.1080/09553002.2019.1649501

Guesmi, S., Mahjoubi, M., Pujic, P., Cherif, A., Normand, P., Sghaier, H., et al. (2022). Biotechnological potential of Kocuria rhizophila PT10 isolated from roots of Panicum turgidum. *Int. J. Environ. Sci. Technol.* 19, 10105–10118. doi: 10.1007/s13762-021-03824-y

Guibaud, G., Tixier, N., Bouju, A., and Baudu, M. (2003). Relation between extracellular polymers' composition and its ability to complex cd, cu and Pb. *Chemosphere* 52, 1701–1710. doi: 10.1016/S0045-6535(03)00355-2

Gupta, P., and Diwan, B. (2017). Bacterial exopolysaccharide mediated heavy metal removal: a review on biosynthesis, mechanism and remediation strategies. *Biotechnol. Rep.* 13, 58–71. doi: 10.1016/j.btre.2016.12.006

Hagan, A. K., Plotnick, Y. M., Dingle, R. E., Mendel, Z. I., Cendrowski, S. R., Sherman, D. H., et al. (2018). Petrobactin protects against oxidative stress and enhances sporulation efficiency in Bacillus anthracis Sterne. *MBio* 9:e02079. doi: 10.1128/mBio.02079-18

Hayrapetyan, H., Siezen, R., Abee, T., and Nierop Groot, M. (2016). Comparative genomics of Iron-transporting systems in Bacillus cereus strains and impact of Iron sources on growth and biofilm formation. *Front. Microbiol.* 7:842. doi: 10.3389/fmicb.2016.00842

Hoegy, F., Celia, H., Mislin, G. L., Vincent, M., Gallay, J., and Schalk, I. J. (2005). Binding of Iron-free Siderophore, a common feature of Siderophore outer membrane transporters of Escherichia coli and Pseudomonas aeruginosa. *J. Biol. Chem.* 280, 20222–20230. doi: 10.1074/jbc.M500776200

Hollensteiner, J., Schneider, D., Poehlein, A., Brinkhoff, T., and Daniel, R. (2023). Pan-genome analysis of six Paracoccus type strain genomes reveal lifestyle traits. *PLoS One* 18:e0287947. doi: 10.1371/journal.pone.0287947

Hong, T., Yin, J.-Y., Nie, S.-P., and Xie, M.-Y. (2021). Applications of infrared spectroscopy in polysaccharide structural analysis: Progress, challenge and perspective. *Food Chemistry X* 12:100168. doi: 10.1016/j.fochx.2021.100168

Hotta, K., Kim, C.-Y., Fox, D. T., and Koppisch, A. T. (2010). Siderophore-mediated iron acquisition in Bacillus anthracis and related strains. *Microbiology* 156, 1918–1925. doi: 10.1099/mic.0.039404-0

Huerta-Cepas, J., Szklarczyk, D., Heller, D., Hernández-Plaza, A., Forslund, S. K., Cook, H., et al. (2019). eggNOG 5.0: a hierarchical, functionally and phylogenetically annotated orthology resource based on 5090 organisms and 2502 viruses. *Nucleic Acids Res.* 47, D309–D314. doi: 10.1093/nar/gky1085

Iyer, A., Mody, K., and Jha, B. (2005). Characterization of an exopolysaccharide produced by a marine *Enterobacter cloacae. Indian J. Exp. Biol.* 43, 467–471.

Jeyasingh, P. D., and Weider, L. J. (2007). Fundamental links between genes and elements: evolutionary implications of ecological stoichiometry. *Mol. Ecol.* 16, 4649–4661. doi: 10.1111/j.1365-294X.2007.03558.x

Jiao, Y., Cody, G. D., Harding, A. K., Wilmes, P., Schrenk, M., Wheeler, K. E., et al. (2010). Characterisation of extracellular polymeric substances from acidophilic microbial biofilms. *Appl. Environ. Microbiol.* 76, 2916–2922. doi: 10.1128/AEM.02289-09

Kanehisa, M., and Goto, S. (2000). KEGG: Kyoto encyclopedia of genes and genomes. *Nucleic Acids Res.* 28, 27–30. doi: 10.1093/nar/28.1.27

Khan, A., Singh, P., and Srivastava, A. (2018). Synthesis, nature and utility of universal iron chelator—Siderophore: a review. *Microbiol. Res.* 212-213, 103–111. doi: 10.1016/j.micres.2017.10.012

Kim, S. Y., Kim, J. H., Kim, C. J., and Oh, D. K. (1996). Metal adsorption of the polysaccharide produced from Methylobacterium organophilum. *Biotechnol. Lett.* 18, 1161–1164. doi: 10.1007/BF00128585

Klappenbach, J. A. (2001). Rrndb: the ribosomal RNA operon copy number database. *Nucleic Acids Res.* 29, 181–184. doi: 10.1093/nar/29.1.181

Klappenbach, J. A., Dunbar, J. M., and Schmidt, T. M. (2000). rRNA operon copy number reflects ecological strategies of Bacteria. *Appl. Environ. Microbiol.* 66, 1328–1333. doi: 10.1128/AEM.66.4.1328-1333.2000

Krishnamurthi, S., Ruckmani, A., Pukall, R., and Chakrabarti, T. (2010). Psychrobacillus gen. Nov. and proposal for reclassification of Bacillus insolitus Larkin & Stokes, 1967, B. psychrotolerans Abd-El Rahman et al., 2002 and B. psychrodurans Abd-El Rahman et al., 2002 as Psychrobacillus insolitus comb. nov., Psychrobacillus psychrotolerans comb. nov. and Psychrobacillus psychrodurans comb. nov. *Syst. Appl. Microbiol.* 33, 367–373. doi: 10.1016/j.syapm.2010.06.003

Krishnamurthy, M., Jayaraman Uthaya, C., Thangavel, M., Annadurai, V., Rajendran, R., and Gurusamy, A. (2020). Optimisation, compositional analysis, and characterisation of exopolysaccharides produced by multi-metal resistant Bacillus cereus KMS3-1. *Carbohydr. Polym.* 227:115369. doi: 10.1016/j.carbpol.2019.115369

Kyte, J., and Doolittle, R. F. (1982). A simple method for displaying the hydropathic character of a protein. *J. Mol. Biol.* 157, 105–132. doi: 10.1016/0022-2836(82)90515-0

Lee, I., Ouk Kim, Y., Park, S.-C., and Chun, J. (2016). OrthoANI: an improved algorithm and software for calculating average nucleotide identity. *Int. J. Syst. Evol. Microbiol.* 66, 1100–1103. doi: 10.1099/ijsem.0.000760

Lefort, V., Desper, R., and Gascuel, O. (2015). FastME 2.0: a comprehensive, accurate, and fast distance-based phylogeny inference program. *Mol. Biol. Evol.* 32, 2798–2800. doi: 10.1093/molbev/msv150

Liang, Z., Li, W., Yang, S., and Du, P. (2010). Extraction and structural characteristics of extracellular polymeric substances (EPS), pellets in autotrophic nitrifying biofilm and activated sludge. *Chemosphere* 81, 626–632. doi: 10.1016/j.chemosphere.2010.03.043

Liu, L., Wang, W., Wu, S., and Gao, H. (2022). Recent advances in the Siderophore biology of Shewanella. *Front. Microbiol.* 13:823758. doi: 10.3389/fmicb.2022.823758

Maddela, N. R., Zhou, Z., Yu, Z., Zhao, S., and Meng, F. (2018). Functional determinants of extracellular polymeric substances in membrane biofouling: experimental evidence from pure-cultured sludge Bacteria. *Appl. Environ. Microbiol.* 84:e00756. doi: 10.1128/AEM.00756-18

Malik, A., Radji, M., Kralj, S., and Dijkhuizen, L. (2009). Screening of lactic acid bacteria from Indonesia reveals glucansucrase and fructansucrase genes in two different Weissella confusa strains from soya. *FEMS Microbiol. Lett.* 300, 131–138. doi: 10.1111/j.1574-6968.2009.01772.x

Manck, L. E., Park, J., Tully, B. J., Poire, A. M., Bundy, R. M., Dupont, C. L., et al. (2022). Petrobactin, a siderophore produced by Alteromonas, mediates community iron acquisition in the global ocean. *ISME J.* 16, 358–369. doi: 10.1038/s41396-021-01065-y

Maruyama, T. (2001). FT-IR analysis of BSA fouled on ultrafiltration and microfiltration membranes. *J. Membr. Sci.* 192, 201–207. doi: 10.1016/S0376-7388(01)00502-6

Mathivanan, K., Chandirika, J. U., Mathimani, T., Rajaram, R., Annadurai, G., and Yin, H. (2021). Production and functionality of exopolysaccharides in bacteria exposed to a toxic metal environment. *Ecotoxicol. Environ. Saf.* 208:111567. doi: 10.1016/j.ecoenv.2020.111567

May, J. J., Wendrich, T. M., and Marahiel, M. A. (2001). The dhb operon of Bacillus subtilisencodes the biosynthetic template for the Catecholic Siderophore 2,3-Dihydroxybenzoate-Glycine-threonine trimeric Ester Bacillibactin. *J. Biol. Chem.* 276, 7209–7217. doi: 10.1074/jbc.M009140200

Medini, D., Donati, C., Tettelin, H., Masignani, V., and Rappuoli, R. (2005). The microbial pan-genome. *Curr. Opin. Genet. Dev.* 15, 589–594. doi: 10.1016/j.gde.2005.09.006

Meier-Kolthoff, J. P., and Göker, M. (2019). TYGS is an automated high-throughput platform for state-of-the-art genome-based taxonomy. *Nat. Commun.* 10:2182. doi: 10.1038/s41467-019-10210-3

Meier-Kolthoff Gurevich, A., Saveliev, V., Vyahhi, N., and Tesler, G. (2013). QUAST: quality assessment tool for genome assemblies. *Bioinformatics* 29, 1072–1075. doi: 10.1093/bioinformatics/btt086

Miethke, M., Klotz, O., Linne, U., May, J. J., Beckering, C. L., and Marahiel, M. A. (2006). Ferri-bacillibactin uptake and hydrolysis in Bacillus subtilis. *Mol. Microbiol.* 61, 1413–1427. doi: 10.1111/j.1365-2958.2006.05321.x

Miethke, M., Kraushaar, T., and Marahiel, M. A. (2013). Uptake of xenosiderophores in Bacillus subtilis occurs with high affinity and enhances the folding stabilities of substrate binding proteins. *FEBS Lett.* 587, 206–213. doi: 10.1016/j.febslet.2012.11.027

Mishra, A., and Jha, B. (2009). Isolation and characterization of extracellular polymeric substances from micro-algae Dunaliella salina under salt stress. *Bioresour. Technol.* 100, 3382–3386. doi: 10.1016/j.biortech.2009.02.006

Mosharaf, M. K., Tanvir, M. Z. H., Haque, M. M., Haque, M. A., Khan, M. A. A., Molla, A. H., et al. (2018). Metal-adapted Bacteria isolated from wastewaters produce biofilms by expressing proteinaceous Curli fimbriae and cellulose nanofibers. *Front. Microbiol.* 9:1334. doi: 10.3389/fmicb.2018.01334

Naithani, S., Deng, C. H., Sahu, S. K., and Jaiswal, P. (2023). Exploring Pan-genomes: an overview of resources and tools for unraveling structure, function, and evolution of crop genes and genomes. *Biomol. Ther.* 13:1403. doi: 10.3390/biom13091403

Nara, M., Tasumi, M., Tanokura, M., Hiraoki, T., Yazawa, M., and Tsutsumi, A. (1994). Infrared studies of interaction between metal ions and ca $^{2+}$—binding proteins marker bands for identifying the types of coordination of the side-chain COO—groups to metal ions in pike parvalbumin (pI = 4.10). *FEBS Lett.* 349, 84–88. doi: 10.1016/0014-5793(94)00645-8

Negrea, P., Caunii, A., Sarac, I., and Butnariu, M. (2015). The study of infrared spectrum of chitin and chitosan extract as potential sources of biomass. *Dig. J. Nanomater. Biostruct.* 10, 1129–1138.

Nicolaus, B., Lama, L., Panico, A., Moriello, V. S., Romano, I., and Gambacorta, A. (2002). Production and characterization of exopolysaccharides excreted by thermophilic bacteria from shallow, marine hydrothermal vents of flegrean Ares (Italy). *Syst. Appl. Microbiol.* 25, 319–325. doi: 10.1078/0723-2020-00128

Nwaiwu, O., Wong, L., Lad, M., Foster, T., MacNaughtan, W., and Rees, C. (2021). Properties of the extracellular polymeric substance layer from minimally grown planktonic cells of Listeria monocytogenes. *Biomol. Ther.* 11:331. doi: 10.3390/biom11020331

Nwodo, U., Green, E., and Okoh, A. (2012). Bacterial exopolysaccharides: functionality and prospects. *IJMS* 13, 14002–14015. doi: 10.3390/ijms131114002

Omoike, A., and Chorover, J. (2004). Spectroscopic study of extracellular polymeric substances from Bacillus s ubtilis: aqueous chemistry and adsorption effects. *Biomacromolecules* 5, 1219–1230. doi: 10.1021/bm034461z

Page, A. J., Cummins, C. A., Hunt, M., Wong, V. K., Reuter, S., Holden, M. T. G., et al. (2015). Roary: rapid large-scale prokaryote pan genome analysis. *Bioinformatics* 31, 3691–3693. doi: 10.1093/bioinformatics/btv421

Pal, A., and Paul, A. K. (2008). Microbial extracellular polymeric substances: central elements in heavy metal bioremediation. *Indian J. Microbiol.* 48, 49–64. doi: 10.1007/s12088-008-0006-5

Parikh, A., and Madamwar, D. (2006). Partial characterisation of extracellular polysaccharides from cyanobacteria. *Bioresour. Technol.* 97, 1822–1827. doi: 10.1016/j.biortech.2005.09.008

Parte, A. C., Sardà Carbasse, J., Meier-Kolthoff, J. P., Reimer, L. C., and Göker, M. (2020). List of prokaryotic names with standing in nomenclature (LPSN) moves to the DSMZ. *Int. J. Syst. Evol. Microbiol.* 70, 5607–5612. doi: 10.1099/ijsem.0.004332

Peuckert, F., Ramos-Vega, A. L., Miethke, M., Schwörer, C. J., Albrecht, A. G., Oberthür, M., et al. (2011). The Siderophore binding protein FeuA shows limited promiscuity toward exogenous Triscatecholates. *Chem. Biol.* 18, 907–919. doi: 10.1016/j.chembiol.2011.05.006

Pham, V. H. T., Jeong, S.-W., and Kim, J. (2015). Psychrobacillus soli sp. nov., capable of degrading oil, isolated from oil-contaminated soil. *Int. J. Syst. Evol. Microbiol.* 65, 3046–3052. doi: 10.1099/ijs.0.000375

Pongjanyakul, T., and Puttipipatkhachorn, S. (2007). Xanthan—alginate composite gel beads: molecular interaction and in vitro characterisation. *Int. J. Pharm.* 331, 61–71. doi: 10.1016/j.ijpharm.2006.09.011

Rodríguez, M., Reina, J. C., Béjar, V., and Llamas, I. (2020). Psychrobacillus vulpis sp. nov., a new species isolated from faeces of a red fox in Spain. *Int. J. Syst. Evol. Microbiol.* 70, 882–888. doi: 10.1099/ijsem.0.003840

Rue, E. L., and Bruland, K. W. (1995). Complexation of iron (III) by natural organic ligands in the central North Pacific as determined by a new competitive ligand equilibration/adsorptive cathodic stripping voltammetric method. *Mar. Chem.* 50, 117–138. doi: 10.1016/0304-4203(95)00031-L

Saha, M., Sarkar, S., Sarkar, B., Sharma, B. K., Bhattacharjee, S., and Tribedi, P. (2016). Microbial siderophores and their potential applications: a review. *Environ. Sci. Pollut. Res.* 23, 3984–3999. doi: 10.1007/s11356-015-4294-0

Salehizadeh, H., and Shojaosadati, S. A. (2003). Removal of metal ions from aqueous solution by polysaccharide produced from Bacillus firmus. *Water Res.* 37, 4231–4235. doi: 10.1016/S0043-1354(03)00418-4

Samoila, P., Humelnicu, A. C., Ignat, M., Cojocaru, C., and Harabagiu, V. (2019). "Chitin and chitosan for water purification" in Chitin and chitosan. eds. L. A. M. Broek and C. G. Boeriu (Wiley), 429–460.

Sathiyanarayanan, G., Bhatia, S. K., Kim, H. J., Kim, J.-H., Jeon, J.-M., Kim, Y.-G., et al. (2016). Metal removal and reduction potential of an exopolysaccharide produced by Arctic psychrotrophic bacterium Pseudomonas sp. PAMC 28620. *RSC Adv.* 6, 96870–96881. doi: 10.1039/C6RA17450G

Shameer, S. (2016). Biosorption of lead, copper and cadmium using the extracellular polysaccharides (EPS) of Bacillus sp., from solar salterns. *3 Biotech* 6:194. doi: 10.1007/s13205-016-0498-3

Shen, Y., Fu, Y., Yu, Y., Zhao, J., Li, J., Li, Y., et al. (2017). Psychrobacillus lasiicapitis sp. nov., isolated from the head of an ant (Lasius fuliginosus). *Int. J. Syst. Evol. Microbiol.* 67, 4462–4467. doi: 10.1099/ijsem.0.002315

Sheng, G.-P., Xu, J., Luo, H.-W., Li, W.-W., Li, W.-H., Yu, H.-Q., et al. (2013). Thermodynamic analysis on the binding of heavy metals onto extracellular polymeric substances (EPS) of activated sludge. *Water Res.* 47, 607–614. doi: 10.1016/j.watres.2012.10.037

Siddharth, T., Sridhar, P., Vinila, V., and Tyagi, R. D. (2021). Environmental applications of microbial extracellular polymeric substance (EPS): a review. *J. Environ. Manag.* 287:112307. doi: 10.1016/j.jenvman.2021.112307

Singh, K. S., and Sawant, S. G. (2022). Identification of $CaCO_3$ polymorphs of shellfish by FTIR spectroscopy and evaluation of metals adsorption by powdered exoskeleton shell. *Ind. J. Geo Marine Sci.* 51, 304–309. doi: 10.56042/ijms.v51i04.44058

Solmaz, K. B., Ozcan, Y., Dogan, N. M., Bozkaya, O., and Ide, S. (2018). Characterization and Productio of extracellular Polysacchrides (EPS) by Bacillus Pseudomucoides U10. *Environments* 5:63. doi: 10.3390/environments5060063

Stevenson, B. S., and Schmidt, T. M. (2004). Life history implications of rRNA gene copy number in Escherichia coli. *Appl. Environ. Microbiol.* 70, 6670–6677. doi: 10.1128/AEM.70.11.6670-6677.2004

Tapia, J. M., Muñoz, J. A., González, F., Blázquez, M. L., Malki, M., and Ballester, A. (2009). Extraction of extracellular polymeric substances from the acidophilic bacterium Acidiphilium 3.2Sup(5). *Water Sci. Technol.* 59, 1959–1967. doi: 10.2166/wst.2009.192

Tchounwou, P. B., Yedjou, C. G., Patlolla, A. K., and Sutton, D. J. (2012). "Heavy metal toxicity and the environment" in Molecular, clinical and environmental toxicology. ed. A. Luch (Basel: Experientia Supplementum. Springer Basel), 133–164.

Tettelin, H., Masignani, V., Cieslewicz, M. J., Donati, C., Medini, D., Ward, N. L., et al. (2005). Genome analysis of multiple pathogenic isolates of Streptococcus agalactiae: implications for the microbial "pan-genome.". *Proc. Natl. Acad. Sci. USA* 102, 13950–13955. doi: 10.1073/pnas.0506758102

Trott, O., and Olson, A. J. (2010). 2010. AutoDock Vina: improving the speed and accuracy of docking with a new scoring function, efficient optimisation, and multithreading. *J. Comput. Chem.* 31, 455–461. doi: 10.1002/jcc.21334

Vernikos, G., Medini, D., Riley, D. R., and Tettelin, H. (2015). Ten years of pan-genome analyses. *Curr. Opin. Microbiol.* 23, 148–154. doi: 10.1016/j.mib.2014.11.016

Vinothkanna, A., Sathiyanarayanan, G., Rai, A. K., Mathivanan, K., Saravanan, K., Sudharsan, K., et al. (2022). Exopolysaccharide produced by probiotic Bacillus albus DM-15

isolated from Ayurvedic fermented Dasamoolarishta: characterization, antioxidant, and anticancer activities. *Front. Microbiol.* 13:832109. doi: 10.3389/fmicb.2022.832109

Volesky, B., and Holan, Z. R. (1995). Biosorption of heavy metals. *Biotechnol. Prog.* 11, 235–250. doi: 10.1021/bp00033a001

Wang, Z., Gao, M., Wei, J., Ma, K., Zhang, J., Yang, Y., et al. (2016). Extracellular polymeric substances, microbial activity and microbial community of biofilm and suspended sludge at different divalent cadmium concentrations. *Bioresour. Technol.* 205, 213–221. doi: 10.1016/j.biortech.2016.01.067

Wang, G., Li, J., Xie, S., Zhai, Z., and Hao, Y. (2020). The N-terminal domain of rhamnosyltransferase EpsF influences exopolysaccharide chain length determination in Streptococcus thermophilus 05-34. *PeerJ.* 8:e8524. doi: 10.7717/peerj.8524

Wang, Y.-X., Xin, Y., Yin, J.-Y., Huang, X.-J., Wang, J.-Q., Hu, J.-L., et al. (2022). Revealing the architecture and solution properties of polysaccharide fractions from Macrolepiota albuminosa (Berk.) Pegler. *Food Chem.* 368:130772. doi: 10.1016/j.foodchem.2021.13077

Wei, W., Wang, Q., Li, A., Yang, J., Ma, F., Pi, S., et al. (2016). Biosorption of Pb (II) from aqueous solution by extracellular polymeric substances extracted from Klebsiella sp. J1. *Sci. Rep.* 6:31575. doi: 10.1038/srep31575

Whitworth, D. E., Sydney, N., and Radford, E. J. (2021). Myxobacterial genomics and post-genomics: a review of genome biology, genome sequences and Related' omics studies. *Microorganisms* 9:2143. doi: 10.3390/microorganisms9102143

Wiercigroch, E., Szafraniec, E., Czamara, K., Pacia, M. Z., Majzner, K., Kochan, K., et al. (2017). Raman and infrared spectroscopy of carbohydrates: a review. *Spectrochim. Acta A Mol. Biomol. Spectrosc.* 185, 317–335. doi: 10.1016/j.saa.2017.05.045

Will, V., Gasser, V., Kuhn, L., Fritsch, S., Heinrichs, D. E., and Schalk, I. J. (2023). Siderophore specificities of the Pseudomonas aeruginosa TonB-dependent transporters ChtA and ActA. *FEBS Lett.* 597, 2963–2974. doi: 10.1002/1873-3468.14740

Yang, M., Liang, Y., Dou, Y., Lan, M., and Gao, X. (2017). Characterisation of an extracellular polysaccharide produced by Bacillus mucilaginosus MY6-2 and its application in metal biosorption. *Chem. Ecol.* 33, 625–636. doi: 10.1080/02757540.2017.1351554

Yoon, S.-H., Ha, S.-M., Kwon, S., Lim, J., Kim, Y., Seo, H., et al. (2017). Introducing EzBioCloud: a taxonomically united database of 16S rRNA gene sequences and whole-genome assemblies. *Int. J. Syst. Evol. Microbiol.* 67, 1613–1617. doi: 10.1099/ijsem.0.001755

Zainab, N., Amna Din, B. U., Javed, M. T., Afridi, M. S., Mukhtar, T., Kamran, M. A., et al. (2020). Deciphering metal toxicity responses of flax (Linum usitatissimum L.) with exopolysaccharide and ACC-deaminase producing bacteria in industrially contaminated soils. *Plant Physiol. Biochem.* 152, 90–99. doi: 10.1016/j.plaphy.2020.04.039

Zakham, F., Sironen, T., Vapalahti, O., and Kant, R. (2021). Pan and core genome analysis of 183 Mycobacterium tuberculosis strains revealed a high inter-species diversity among the human adapted strains. *Antibiotics* 10:500. doi: 10.3390/antibiotics10050500

Zheng, Y., Fang, X., Ye, Z., Li, Y., and Cai, W. (2008). Biosorption of cu(II) on extracellular polymers from Bacillus sp. F19. *J. Environ. Sci.* 20, 1288–1293. doi: 10.1016/S1001-0742(08)62223-8

Zhenggang, X., Yi, D., Huimin, H., Liang, W., Yunlin, Z., and Guiyan, Y. (2018). Biosorption characteristics of Mn (II)by Bacillus cereus strain HM-5 isolated from SoilContaminated by manganese ore. *Pol. J. Environ. Stud.* 28, 463–472. doi: 10.15244/pjoes/84838

Positive effects of molybdenum on the biomineralization process on the surface of low-alloy steel catalyzed by *Bacillus subtilis*

Zhangwei Guo[1]*, Qun Feng[1], Na Guo[1], Yansheng Yin[2] and Tao Liu[1]*

[1]College of Ocean Science and Engineering, Shanghai Maritime University, Shanghai, China, [2]Engineering Technology Research Center for Corrosion Control and Protection of Materials in Extreme Marine Environment, Guangzhou Maritime University, Guangzhou, China

The adhesion of microorganisms and the subsequent formation of mineralized layers in biofilms are of great significance in inhibiting the corrosion of metal materials. In this work, we found that the adhesion and subsequent mineralization of *Bacillus subtilis* on the surface of low-alloy steel are influenced by the molybdenum in the material. The addition of molybdenum will lead to increased adhesion of *B. subtilis* on the material surface, and the subsequent biomineralization ability has also been improved. Through transcriptome and physiological and biochemical tests, we found that molybdenum can affect the chemotaxis, mobility and carbonic anhydrase secretion related genes of *B. subtilis*, and then affect the formation and mineralization of the biofilm of *B. subtilis*.

KEYWORDS

bioprecipitation, molybdenum, corrosion, molecular mechanisms, RNAseq

1 Introduction

Bacillus subtilis, a gram-positive bacterium species of *Bacillus*, has a single cell size of $0.7–0.8 \times 2–3\,\mu m$, no capsule, and peritrichous flagella and is motile. *B. subtilis* can form endogenous spores under stress and resist various adverse environments; therefore, it has a wide survival range and has been observed in soil, freshwater, and seawater (Mohsin et al., 2021). As a gram-positive bacterium, *B. subtilis* has the functionality of biological mineralization (Yan et al., 2021; Wightman and Fein, 2005; Mudgil et al., 2018; Lin et al., 2015; Guo et al., 2019; Chalia et al., 2017), with its abundant extracellular products providing many nucleation sites for mineralization (Yin et al., 2020; Fein et al., 2002; Keren-Paz et al., 2022). More importantly, *B. subtilis* can secrete carbonic anhydrase (CA) that is a ubiquitous enzyme. It can efficiently catalyze the reversible reactions (Han et al., 2019; Mukherjee and Venkata Mohan, 2021; Barabesi et al., 2007) of CO_2 and H_2O to generate HCO_3^- and H^+, and plays a crucial role in the process of biomineralization. As a result, this property of *B. subtilis* has been widely used in the preparation of biomineralized $CaCO_3$ crystals (Song et al., 2019; Perito et al., 2018; Marvasi et al., 2010), as adsorptive materials (Arias et al., 2018), catalytic materials, ceramic materials, protective layers for sensitive materials (such as enzymes, proteins), and drug release materials, with broad application prospects in the fields of chemical, environmental protection, biological, medical, and building material industries (Kang et al., 2021). It can also be used in engineering, such as concrete micro-crack repair (Mondal and Ghosh, 2021; Huynh et al., 2019; Feng et al., 2021; Huynh et al., 2022; Mahmood et al., 2022),

building restoration and protection (Perito et al., 2014), and preparation of calcium carbonate micro- and nano-particles (Sazanova et al., 2020). Thus, its role in the protection and restoration of stone surfaces (Perito et al., 2014; Sazanova et al., 2020; Shim et al., 2011), foundation stabilization, earthquake prevention, and the capture of radionuclides and heavy metal ions (Johnson and Fein, 2019) should not be disregarded (Arias et al., 2020).

The calcium carbonate layer formed by microbial mineralization on metal surfaces can protect materials and prevent metal material corrosion. As a green, environmentally friendly, and self-healing anti-corrosion method, this approach has attracted the attention of scholars. A previous study has reported that the presence and concentration of Mo in metal materials affects the adhesion of microorganisms, thus affecting the subsequent mineralization or corrosion mediated by the microorganisms (Guo et al., 2022; Guo et al., 2019). However, although the *B. subtilis* bacterium has an excellent mineralization ability, the effect of metal alloy elements on the adhesion and mineralization performance of *B. subtilis* has not been reported. Moreover, in the CA-induced mineralization process, the CA activity will be affected by a number of factors, such as temperature, pH, and Ca^{2+} concentration. Also, whether metals affect the expression of CA remains unclear. Therefore, a study on the effects of elements present in metal materials on *B. subtilis* and its CA activity is of great significance to further clarify the mechanism of *B. subtilis* mineralization, providing an important scientific basis for the preparation of biomineralization coatings on metal surfaces. In this study, low-alloy steels containing Mo with different gradient concentrations were designed to study the influence of changes in Mo content on the adhesion and mineralization behavior of *B. subtilis*. Finally, the influence mechanism of Mo on the adhesion and mineralization behavior of *B. subtilis* was investigated through transcriptome analysis.

2 Materials and methods

2.1 Steel sample

The steel sample used in the test was low-alloy steel, and its composition is shown in Supplementary Table S1. The steel samples were processed into 10×10 mm square samples by wire cutting, and then we used 50–1,200 grit sandpaper to polish the samples in sequence. The steel samples were soaked in anhydrous ethanol and acetone, and then washed under ultrasonication for 15 min and dried with nitrogen. The samples were placed on a clean workbench for 1 h of ultraviolet sterilization before use.

2.2 Strain and culture

The *B. subtilis* used in this study was supplied by Marine Culture Collection of China (No. 1A14806), it could mineralize on the surfaces of metal materials, thereby inhibiting metal material corrosion. The strain was stored in a −80°C freezer. The medium was 2216E medium (Qingdao Hopebio), and 37.5 g of the medium was dissolved in deionized water to prepare the experimental medium. 2216E medium: 19.45 g/L NaCl, 5.98 g/L $MgCl_2$, 5.0 g/L Peptone, 3.24 g/L Na_2SO_4, 1.8 g/L $CaCl_2$, 1.0 g/L yeast extract powder, 0.55 g/L KCl, 0.16 g/L Na_2CO_3, 0.1 g/L $FeC_6H_5O_7$, 0.08 g/L KBr, 0.034 g/L $SrCl_2$, 0.022 g/L H_3BO_3, 0.008 g/L

NaH_2PO_4, 0.004 g/L Na_2SiO_3, 0.0024 g/L NaF, 0.0016 g/L NH_4NO_3. After the culture medium was sterilized at 121°C for 20 min, we cultured 100 μL of the bacterial solution overnight and inoculated the culture medium (200 mL). Then, the steel sample was placed in the culture medium and cultured in a light incubator at a temperature of 30°C and a shaker speed of 120 r/min. The growth of the bacterium was monitored by plate counting, using a series of dilutions (in a total volume of 100 μL). The concentration of viable cells was calculated based on the number of colonies grown in each well on the plate. In addition, pH and dissolved oxygen levels were measured once a day in the cultures. A pH meter (Sartorius, Germany) and a dissolved oxygen meter (Inesa JPBJ-611Y, China) were used to obtain the respective measurements. Throughout the experimental period, the changes in calcium ion concentration were measured in filtered samples (0.22 μm) using an inductively coupled plasma mass spectrometer (PerkinElmer NexION 2,200, United States).

2.3 Corrosion morphology characterization

After 14 days of cultivation, the steel samples were removed, washed with PBS, and soaked in 2.5% glutaraldehyde solution for 2 h. Afterward, the steel samples were dried with alcohol (stepwise in: 30, 50, 70, 80, 90, and 100% v/v, 15 min each) and then dried under pure nitrogen. The corrosion morphology of the steel samples was observed by scanning electron microscope (SEM, ZEISS Gemini 300, Germany), and X-ray diffractometer (XRD, Nalytical X'Pert PRO, Netherlands) was used to identify the corrosion product components on the sample surfaces (Cu-Ka radiation source at 40 kV and 10 mA with $2\theta = 20$–$90°$). The adhesion of the bacterial biofilm on the steel surface was investigated using acridine orange as staining agent, with the bacterial cells showing green fluorescence under an inverted fluorescence microscope (after 15 min staining, at 502 nm maximum excitation wavelength). Then, the specimens were washed successively with concentrated hydrochloric acid, saturated sodium bicarbonate, and deionized water to clean the product layer on the steel surface. After the samples were air-dried, pitting on the material surface was observed by an optical profiler (Bruker ContourGT, Germany).

2.4 Electrochemistry test

An electrochemistry test was conducted using a three-electrode system, where the sample served as the working electrode, the saturated calomel electrode was the reference electrode, the platinum electrode was the opposite electrode, and the test solution was 2216E medium. Before impedance testing was conducted, the sample was soaked for 60 min, and then the OCP test was performed. After a stable open-circuit potential was obtained, the EIS test was performed by an electrochemical workstation (Gamry Interface 100E, United States), using a test frequency range of 10^5–10^{-2} Hz, and the interference amplitude was ±10 mV. ZSimpWin analysis software was used.

2.5 RNA-seq test

A biofilm developed on the low-alloy steel surface, and biofilm samples were collected after 2 days of inoculation. After removal from the media, the coupons were quickly and gently washed in 0.85% NaCl

buffer at 0°C to remove the contaminated suspended cells and ultrasonically treated in 0.85% NaCl buffer at 0°C for 2 min to collect the biofilm cells from the metal surface. The buffer containing biofilm cells was centrifuged at 10000 rpm and −2°C for 3 min, then the supernatant was discarded and the precipitated biofilm cells were resuspended in 6 mL of 0.85% NaCl buffer at 0°C, transferred to a cold bead stirrer tube, and centrifuged at 10000 rpm and room temperature for 15 s. Then, the cell particles were immediately frozen in a dry ice ethanol bath, and subsequently the samples were sent to Shanghai Majorbio Bio-pharm Technology Co., Ltd., for transcriptome testing.

3 Results

3.1 Bacterial adhesion to the surface of low-alloy steel

In order to explore the effect of Mo on the adhesion of *B. subtilis* on the low-alloy steel surface and the formation of microbial film, the surfaces of the low-alloy steel samples with different Mo element contents were characterized by an inverted fluorescence microscope, after 3 days of immersion (Figure 1). The number of bacteria on the low-alloy steel surface without Mo (Figure 1A) elements was significantly lower than that of low-alloy steel containing 0.4 wt% Mo elements (Figure 1B). The number of bacteria attached to the low-alloy steel containing 1.0 wt% Mo elements (Figure 1C) was decisively the highest. Therefore, it can be seen that the adhesion number of bacteria on the low-allow steel surface increases with the increase of Mo content. According to our previous study (Guo et al., 2022; Guo et al., 2019), this was possibly due to the presence of Mo elements, which affected the chemotaxis of the bacteria and thus increased their quantity on the steel surface and affected their mineralization.

3.2 Surface morphology of low-alloy steel

Figure 2 indicates that the occurrence of triangular calcite structures raised with increasing Mo content, based on a comparison of the surface morphology of materials containing increasing Mo (Figures 2A,E,I), with the greatest number of mineralized products being observed on the low-alloy steel surface with 1.0 wt% Mo elements (Figures 2I,J). According to the mapping diagram, with blue representing the content of Ca elements on the surface, we observed that the content of Ca elements on the low-alloy steel surface rose with increasing Mo content in the low-alloy steel, which further supported the observation of elevated mineralized products on the steel surface. Green represented the content of Fe elements on the surface, and the results indicate that Fe content decreased with increasing Mo content, showing that both the amount of corrosion products and the area of uncovered steel surface decreased, while the amounts of mineralized products gradually increased.

It is apparent in Figure 3 that the thickness of the mineralized product layer on the low-alloy steel surface without Mo elements (Figure 3A) was thinner than that of low-alloy steel with Mo elements (Figures 3B,C), which also proved that the thickness of the mineralized product layer on the low-alloy steel surface increases with the increase of Mo element content.

Figure 4 shows the X-ray diffraction patterns results. As shown in the figure, compared with the low-alloy steel surface without Mo, the surface of the low-alloy steel with a higher Mo content was greater $(Mg_{.064}Ca_{.936})$ (CO_3), with a thicker mineralized product layer, as shown also in Figure 3.

3.3 Surface pitting

As shown in the Figure 5, more extensive pitting was observed on the low-alloy steel surface without Mo elements (Figure 5A), compared with the low-alloy steel containing Mo, and with an increase in Mo content, pitting essentially disappeared (1.0 wt% Mo). Supplementary Figure S1 shows the scanning electron microscope images and pitting corrosion after 14 days of immersion in a sterile solution. We observed that the addition of Mo had no effect on corrosion under sterile conditions. In previous work (Guo et al., 2022; Guo et al., 2019), we compared pitting, weight loss, and electrochemical data in sterile environments, the addition of molybdenum did not alter the corrosion resistance of low-alloy steel.

3.4 *Bacillus subtilis* growth kinetics

Figure 6 shows kinetics of the bacterial growth. As indicated by the solution pH change (Figure 6A), pH value decreased with increasing Mo content in the low-alloy steel, which was ascribed to a series of biochemical reactions. The total number of *B. subtilis* colonies (Figure 6B) was not significantly affected by the Mo content. However,
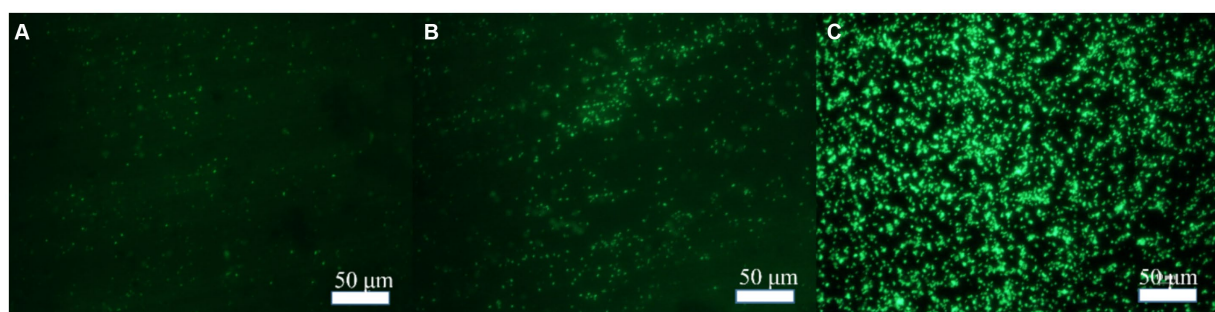

FIGURE 1
Bacterial adhesion on blank steel and steel samples containing Mo. **(A)** Blank steel, **(B)** 0.4 wt% Mo steel, and **(C)** 1.0 wt% Mo steel.
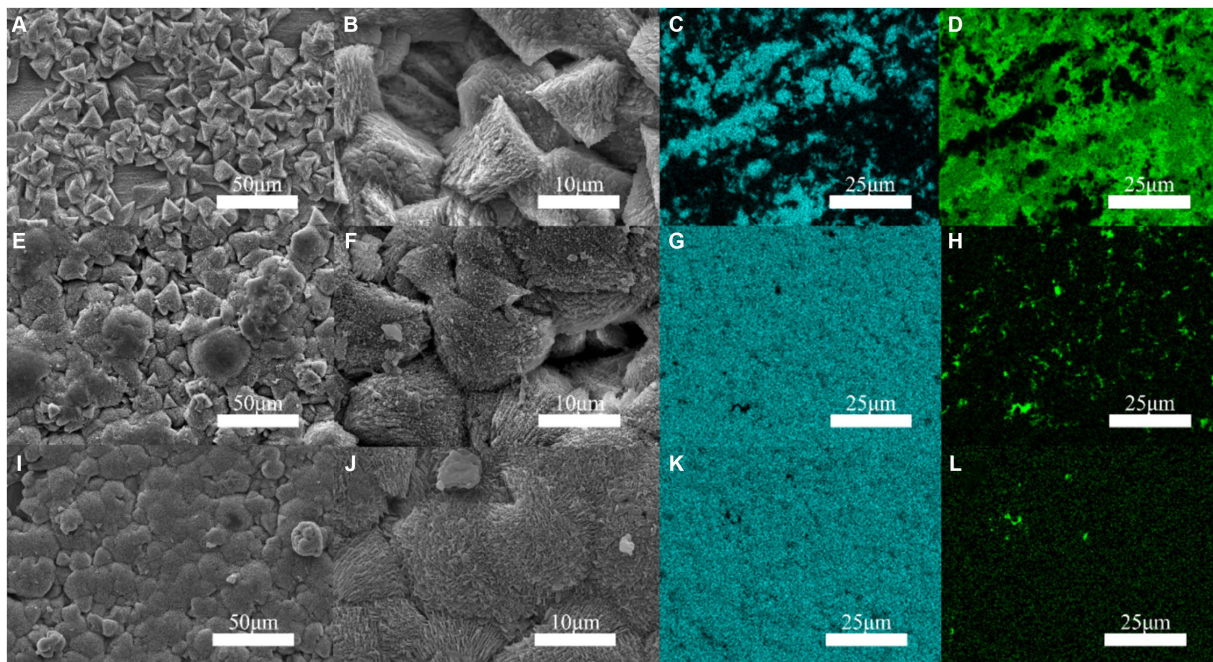
FIGURE 2
Surface mineralization of the blank steel and Mo-containing steel. **(A–D)** Blank steel, **(E–H)** 0.4 wt% Mo steel, **(I–L)** 1.0 wt% Mo steel.
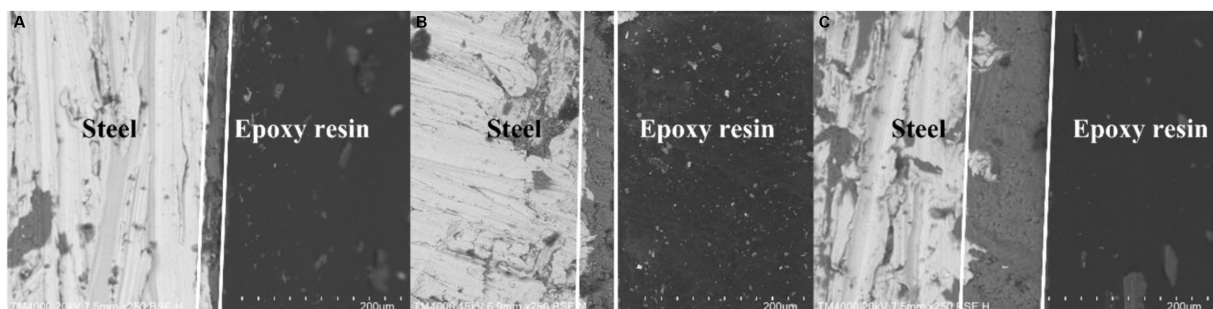

FIGURE 3
Surface mineralized thicknesses of the blank steel and steel containing Mo. **(A)** Blank steel (19μm), **(B)** 0.4wt% Mo steel (42μm), **(C)** 1.0wt% Mo steel (106μm).

the change in Ca^{2+} concentration in the solution (Figure 6C) decreased with increasing Mo content, which supported the hypothesis that the increase in Mo content increased the formation of mineralized products on the sample surface, as this process consumes Ca^{2+} in the solution.

3.5 Electrochemical impedance

Figure 7 shows the electrochemical impedance test results. As shown in the figure, the electrochemical impedance curves formed incomplete semicircles, and the radius changed with different Mo element contents. The radius of the impedance curve of the low-alloy steel without Mo elements (Figure 7A) during the immersion process was significantly smaller than that of the low-alloy steel with 0.4 wt% Mo element (Figure 7B) and low-allow steel containing 1.0 wt% Mo element (Figure 7C). Similarly, the radius of the impedance curve rose with increasing Mo content, correlating with the electrochemical impedance value. Electrochemical impedance parameters fitted from

the measured impedance plots in Figure 7 are listed in Supplementary Table S2. Thus, with rising Mo content, the impedance increases, as well as the thickness of the surface mineralized product layer, which corresponded to the results obtained from the above characteristic maps. In general, the thicker and denser mineralized layers are the more electron transfer on the material surface is hindered and conductivity lowered (Guo et al., 2019).

3.6 Transcriptome analysis results

Figure 8 summarizes the observed differences in gene expression. Based on findings of previous studies (Guo et al., 2022), we mainly focused on bacterial chemotaxis and flagellar pathways. Figure 8A shows a Venn diagram, with nine common differential genes in the experimental group. As shown in Figure 8B, *fliL*, *yvyG*, *flgK*, *hag*, *fliK*, *flgL*, *fliJ* and *ca* genes were upregulated in cells collected from the steel surface with elevated Mo content.

4 Discussion

The presented study investigated regulatory mechanisms and factors influencing biomineralization on metal material surfaces mediated by *B. subtilis*, showing an important direction for research supporting future applications of biomineralization in corrosion prevention. In our previous study, 1.0 wt% Mo content regulated the

attachment of *Pseudoalteromonas lipolytica* (Guo et al., 2019). In this work, *fliL, yvyG, flgK, hag, fliK, flgL, fliJ* and *ca* genes were upregulated by Mo in low-alloy steel, with *fliL, yvyG, flgK*, hag, *fliK, flgL*, and *fliJ* being genes involved in the assembly of bacterial flagella, and *che*V affecting the chemotaxis of bacteria. In general, adhesion of bacteria is greatly affected by the assembly of flagella and chemotaxis. Therefore, this study indicated that Mo affected flagella assembly and bacterial chemotaxis. Chemotaxis refers to the process of cells responding to a chemical gradient by the movement towards a more favorable environment (Chen et al., 2024), with methyl-accepting chemotaxis protein (Mcp) being one of key signalling molecules (Song et al., 2024). Mcps interact with other chemotactic molecules, which leads to the enhancement of phosphorylation of CheV and the charge of the Mot protein subunit, thus controlling the direction of the movement by increasing the rotation rate of the flagella. In this study, we reported that bacteria adhered more to the steel surface containing Mo, compared to Mo-free steel, by the process of flagella-assisted chemotaxis, which is consistent with our previous reports (Guo et al., 2022; Guo et al., 2019). It is noteworthy that in the transcriptome test performed in this study, the *ca* gene was also upregulated in the presence of Mo. Carbonic anhydrase is a common enzyme in bacteria, which can catalyze a series of physiological and biochemical reactions (Baidya et al., 2024). Its role involves combining carbon dioxide and water to form bicarbonate and hydrogen ions (Zheng et al., 2023):

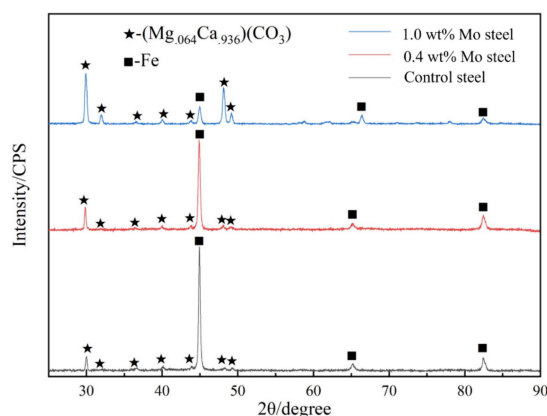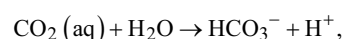$$CO_2\left(aq\right)+H_2O \rightarrow HCO_3^- + H^+,$$

FIGURE 4
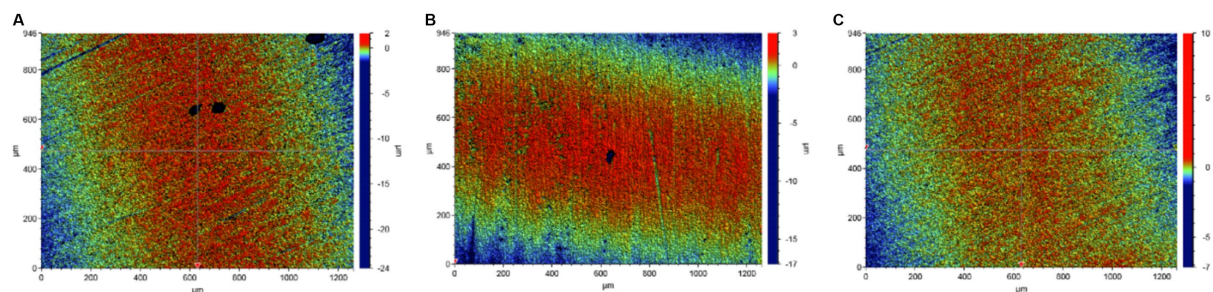XRD patterns of the surface mineralized components of the blank steel and Mo steel.

FIGURE 5
Corrosion of the blank steel and steel containing Mo in the presence of *B. subtilis*. **(A)** Blank steel, **(B)** 0.4 wt% Mo steel, **(C)** 1.0 wt% Mo steel.

FIGURE 6
Growth and physiological and biochemical analysis of *B. subtilis*. **(A)** pH, **(B)** growth curve, **(C)** Ca²⁺ content in the solution.

FIGURE 7
EIS spectra of the blank steel and steel containing Mo in the presence of *B. subtilis*. **(A)** Blank steel, **(B)** 0.4 wt% Mo steel, **(C)** 1.0 wt% Mo steel, and **(D,E)** corresponding fitting circuits.
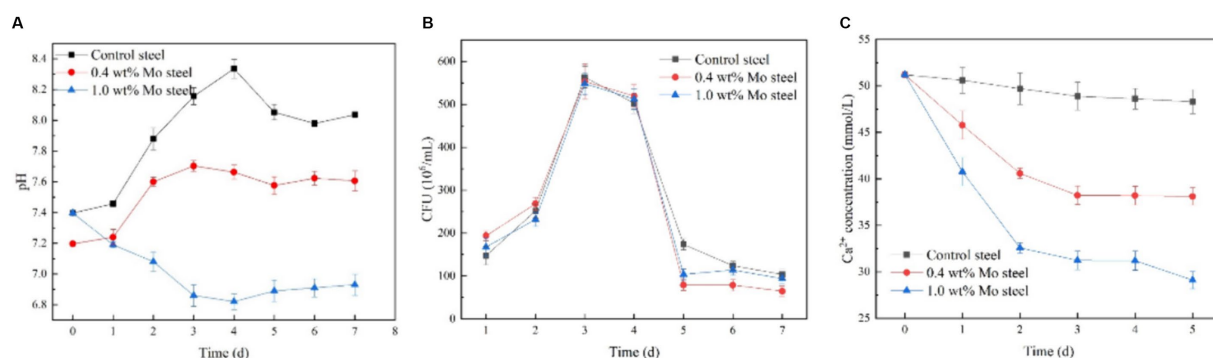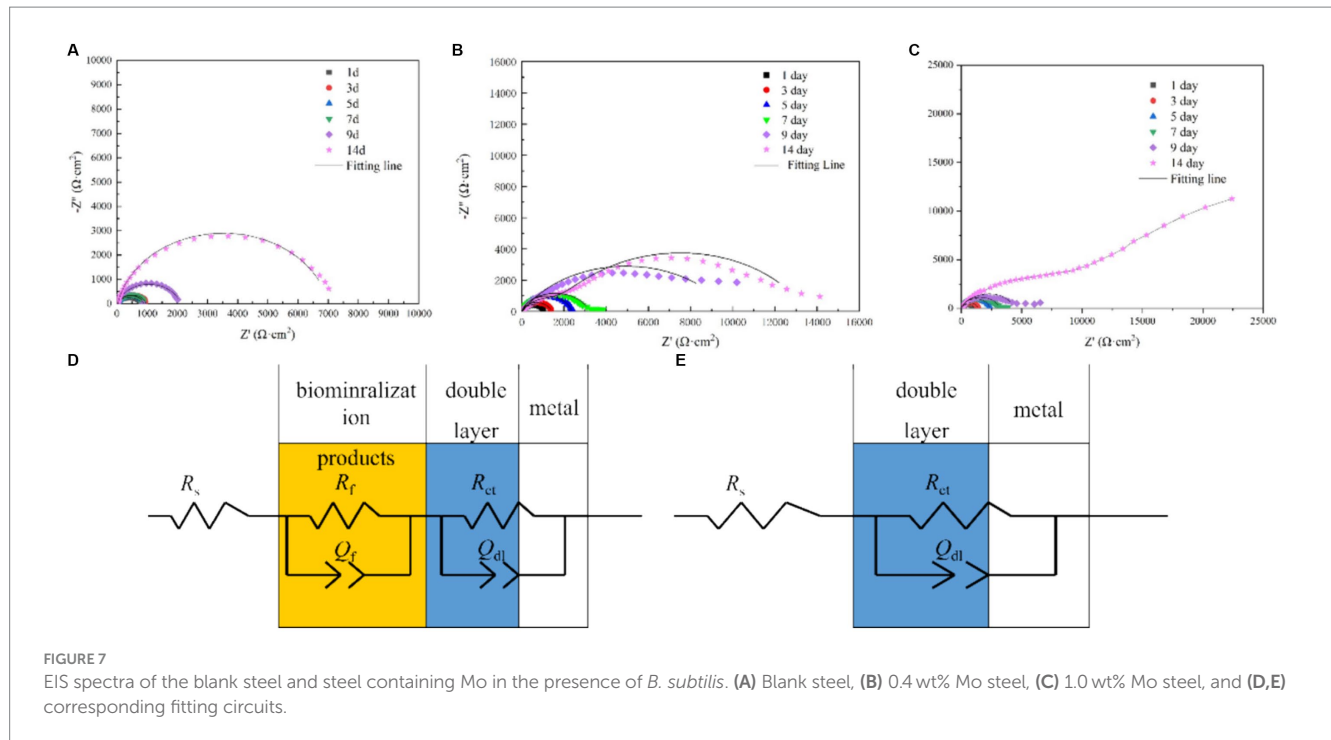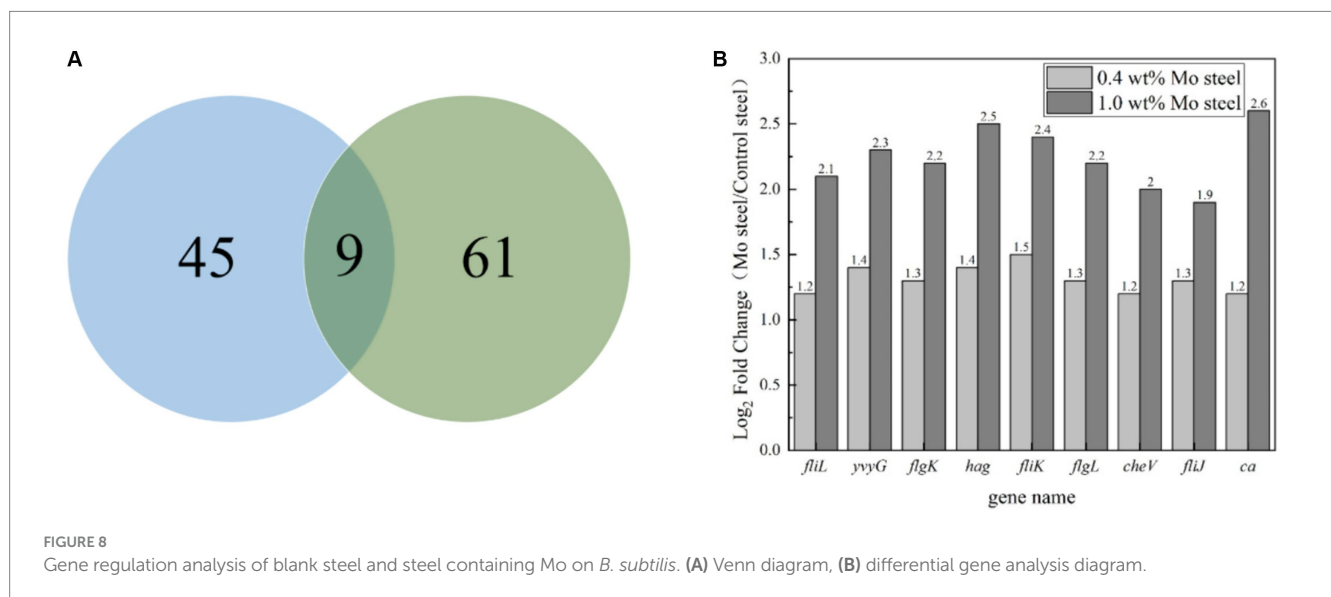

FIGURE 8
Gene regulation analysis of blank steel and steel containing Mo on *B. subtilis*. **(A)** Venn diagram, **(B)** differential gene analysis diagram.

which will reduce the pH value of the solution, which is consistent with our pH test results. At the same time, bicarbonate can form carbonate, and then combine with the Ca ions in the solution (Zheng et al., 2023):

$$HCO_3^- \rightarrow H^+ + CO_3^{2-},$$

$$Ca^{2+} + CO_3^{2-} \rightarrow CaCO_3 \downarrow,$$
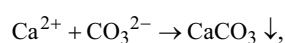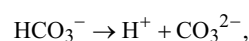
which will form a denser mineralized layer. This was evidenced by the continuous decreases in pH and Ca content in solution. The main

conclusion based on the transcriptomic analysis performed is that both chemotaxis and CA strengthened the mineralization ability of *B. subtilis* on the surface of steel with Mo content.

5 Conclusion

In this study, we report that Mo in low-alloy steel had a regulatory effect on the gram-positive bacterium *B. subtilis*. The expression of the chemotactic gene and *ca* gene in *B. subtilis* was enhanced in the presence of Mo, which improved the adhesion ability of the bacterium and enhanced the mineralization of calcium carbonate. Furthermore, mineralized products have shown to be stable and environmentally

friendly; thus, this process controlled by *ca* gene has become one of the most promising technologies for CO_2 capture. Future research should focus on the diversity of biomineralization patterns of different microbial species under specific environmental conditions, and investigate how these patterns are influenced by gene regulation and external environment.

Data availability statement

The datasets presented in this study can be found in online repositories. The names of the repository/repositories and accession number(s) can be found in the article/Supplementary material.

Author contributions

ZG: Formal analysis, Funding acquisition, Writing – review & editing. QF: Formal analysis, Funding acquisition, Writing – original draft. NG: Writing – review & editing, Formal analysis, Funding acquisition. YY: Writing – review & editing, Formal analysis, Funding acquisition. TL: Writing – review & editing, Formal analysis, Funding acquisition.

Funding

Conflict of interest

The authors declare that the research was conducted in the absence of any commercial or financial relationships that could be construed as a potential conflict of interest.

Publisher's note

All claims expressed in this article are solely those of the authors and do not necessarily represent those of their affiliated organizations, or those of the publisher, the editors and the reviewers. Any product that may be evaluated in this article, or claim that may be made by its manufacturer, is not guaranteed or endorsed by the publisher.

Supplementary material

The Supplementary material for this article can be found online at: https://www.frontiersin.org/articles/10.3389/fmicb.2024.1428286/full#supplementary-material

References

Arias, D., Rivas, M., Guiñez, R., and Cisternas, L. A. (2018). Modeling the calcium and magnesium removal from seawater by immobilized biomass of ureolytic bacteria *Bacillus subtilis* through response surface methodology and artificial neural networks, desalination. *Water Treat* 118, 294–303. doi: 10.5004/dwt.2018.22665

Arias, D., Villca, G., Pánico, A., Cisternas, L. A., Jeldres, R. I., González-Benito, G., et al. (2020). Partial desalination of seawater for mining processes through a fluidized bed bioreactor filled with immobilized cells of *Bacillus subtilis* LN8B. *Desalination* 482:114388. doi: 10.1016/j.desal.2020.114388

Baidya, P., Zhang, M., Xiao, Y., Zhang, H., Yu, L., and Li, W. (2024). Genetically engineered whole-cell biocatalyst for efficient CO_2 capture by cell surface display of carbonic anhydrase from *Bacillus cereus* GLRT202 on *Escherichia coli. Biochem. Eng. J.* 211:109446. doi: 10.1016/j.bej.2024.109446

Barabesi, C., Galizzi, A., Mastromei, G., Rossi, M., Tamburini, E., and Perito, B. (2007). *Bacillus subtilis* gene cluster involved in calcium carbonate biomineralization. *J. Bacteriol.* 189, 228–235. doi: 10.1128/JB.01450-06

Chalia, S., Baskar, S., Minakshi, P., Baskar, R., and Ranjan, K. (2017). Biomineralization abilities of *Cupriavidus* strain and *Bacillus subtilis* strains *in vitro* isolated from speleothems, Rani cave, Chhattisgarh, India. *Geomicrobiol J.* 34, 737–752. doi: 10.1080/01490451.2016.1257663

Chen, M., Trotter, V. V., Walian, P. J., Chen, Y., Lopez, R., Lui, L. M., et al. (2024). Molecular mechanisms and environmental adaptations of flagellar loss and biofilm growth of *Rhodanobacter* under environmental stress. *ISME J.* 93:e151. doi: 10.1093/ismejo/wrae151

Fein, J.B., Scott, S., and Rivera, N., The effect of Fe on Si adsorption by Bacillus subtilis cell walls: Insights into non-metabolic bacterial precipitation of silicate minerals, (2002), Available at: www.elsevier.comrlocaterchemgeo, 182, 265–273

Feng, J., Chen, B., Sun, W., and Wang, Y. (2021). Microbial induced calcium carbonate precipitation study using *Bacillus subtilis* with application to self-healing concrete preparation and characterization. *Constr. Build. Mater.* 280:122460. doi: 10.1016/j.conbuildmat.2021.122460

Guo, Z., Chai, Z., Liu, T., Gao, S., Hui, X., Zhang, C., et al. (2022). *Pseudomonas aeruginosa*-accelerated corrosion of Mo-bearing low-alloy steel through molybdenum-mediating chemotaxis and motility. *Bioelectrochemistry* 144:108047. doi: 10.1016/j.bioelechem.2021.108047

Guo, Z., Pan, S., Liu, T., Zhao, Q., Wang, Y., Guo, N., et al. (2019). *Bacillus subtilis* inhibits *Vibrio natriegens*-induced corrosion via biomineralization in seawater. *Front. Microbiol.* 10:e1111. doi: 10.3389/fmicb.2019.01111

Guo, Z., Wang, W., Guo, N., Zeng, Z., Liu, T., and Wang, X. (2019). Molybdenum-mediated chemotaxis of *Pseudoalteromonas lipolytica* enhances biofilm-induced mineralization on low alloy steel surface. *Corros. Sci.* 159:108123. doi: 10.1016/j.corsci.2019.108123

Han, Z., Wang, J., Zhao, H., Tucker, M. E., Zhao, Y., Wu, G., et al. (2019). Mechanism of biomineralization induced by *Bacillus subtilis* J2 and characteristics of the biominerals. *Fortschr. Mineral.* 9:40218. doi: 10.3390/min9040218

Huynh, N. N. T., Imamoto, K. I., and Kiyohara, C. (2019). A study on biomineralization using *Bacillus subtilis* natto for repeatability of self-healing concrete and strength improvement. *J. Adv. Concr. Technol.* 17, 700–714. doi: 10.3151/jact.17.700

Huynh, N. N. T., Imamoto, K. I., and Kiyohara, C. (2022). Biomineralization analysis and hydration acceleration effect in self-healing concrete using *Bacillus subtilis* natto. *J. Adv. Concr. Technol.* 20, 609–623. doi: 10.3151/jact.20.609

Johnson, C. R., and Fein, J. B. (2019). A mechanistic study of au(III) removal from solution by *Bacillus subtilis. Geomicrobiol J.* 36, 506–514. doi: 10.1080/01490451.2019.1573279

Kang, S. Y., Pokhrel, A., Bratsch, S., Benson, J. J., Seo, S. O., Quin, M. B., et al. (2021). Engineering *Bacillus subtilis* for the formation of a durable living biocomposite material. *Nat. Commun.* 12:7133. doi: 10.1038/s41467-021-27467-2

Keren-Paz, A., Maan, H., Karunker, I., Olender, T., Kapishnikov, S., Dersch, S., et al. (2022). The roles of intracellular and extracellular calcium in *Bacillus subtilis* biofilms. *IScience* 25:104308. doi: 10.1016/j.isci.2022.104308

Lin, W., Huang, Z., Li, X., Liu, M., and Cheng, Y. (2015). Bio-remediation of acephate–Pb(II) compound contaminants by *Bacillus subtilis* FZUL-33. *J. Environ. Sci.* 45, 94–99. doi: 10.1016/j.jes.2015.12.010

Mahmood, F., Rehman, S. K., Jameel, M., Riaz, N., Javed, M. F., Salmi, A., et al. (2022). Self-healing bio-concrete using *Bacillus subtilis* encapsulated in Iron oxide nanoparticles. *Materials* 15:7731. doi: 10.3390/ma15217731

Marvasi, M., Visscher, P. T., Perito, B., Mastromei, G., and Casillas-Martínez, L. (2010). Physiological requirements for carbonate precipitation during biofilm development of

Bacillus subtilis etfA mutant. *FEMS Microbiol. Ecol.* 71, 341–350. doi: 10.1111/j.1574-6941.2009.00805.x

Mohsin, M. Z., Omer, R., Huang, J., Mohsin, A., Guo, M., Qian, J., et al. (2021). Advances in engineered *Bacillus subtilis* biofilms and spores, and their applications in bioremediation, biocatalysis, and biomaterials. *Synth. Syst. Biotechnol.* 6, 180–191. doi: 10.1016/j.synbio.2021.07.002

Mondal, S., and Ghosh, A. (2021). Spore-forming *Bacillus subtilis* Vis-à-Vis non-spore-forming *Deinococcus radiodurans*, a novel bacterium for self-healing of concrete structures: a comparative study. *Constr. Build. Mater.* 266:121122. doi: 10.1016/j.conbuildmat.2020.121122

Mudgil, D., Baskar, S., Baskar, R., Paul, D., and Shouche, Y. S. (2018). Biomineralization potential of *Bacillus subtilis*, *Rummeliibacillus Stabekisii* and *Staphylococcus Epidermidis* strains in vitro isolated from speleothems, Khasi Hill caves, Meghalaya, India. *Geomicrobiol J.* 35, 675–694. doi: 10.1080/01490451.2018.1450461

Mukherjee, T., and Venkata Mohan, S. (2021). Metabolic flux of *Bacillus subtilis* under poised potential in electrofermentation system: gene expression vs product formation. *Bioresour. Technol.* 342:125854. doi: 10.1016/j.biortech.2021.125854

Perito, B., Casillas, L., and Marvasi, M. (2018). Factors affecting formation of large calcite crystals ($\geq$1 mm) in *Bacillus subtilis* 168 biofilm. *Geomicrobiol J.* 35, 385–391. doi: 10.1080/01490451.2017.1377788

Perito, B., Marvasi, M., Barabesi, C., Mastromei, G., Bracci, S., Vendrell, M., et al. (2014). A *Bacillus subtilis* cell fraction (BCF) inducing calcium carbonate precipitation: biotechnological perspectives for monumental stone reinforcement. *J. Cult. Herit.* 15, 345–351. doi: 10.1016/j.culher.2013.10.001

Sazanova, K. V., Frank-Kamenetskaya, O. V., Vlasov, D. Y., Zelenskaya, M. S., Vlasov, A. D., Rusakov, A. V., et al. (2020). Carbonate and oxalate crystallization by interaction of calcite marble with *Bacillus subtilis* and *Bacillus subtilis*–aspergillus Niger association. *Crystals (Basel)* 10, 1–16. doi: 10.3390/cryst10090756

Shim, H. W., Jin, Y. H., Seo, S. D., Lee, S. H., and Kim, D. W. (2011). Highly reversible lithium storage in *Bacillus subtilis*-directed porous Co_3O_4 nanostructures. *ACS Nano* 5, 443–449. doi: 10.1021/nn1021605

Song, J., Han, B., Song, H., Yang, J., Zhang, L., Ning, P., et al. (2019). Nonreductive biomineralization of uranium by *Bacillus subtilis* ATCC–6633 under aerobic conditions. *J. Environ. Radioact.* 208–209:106027. doi: 10.1016/j.jenvrad.2019.106027

Song, Q., Li, X., Hou, N., Pei, C., and Li, D. (2024). Chemotaxis-mediated degradation of PAHs and heterocyclic PAHs under low-temperature stress by *Pseudomonas fluorescens* S01: insights into the mechanisms of biodegradation and cold adaptation. *J. Hazard. Mater.* 469:133905. doi: 10.1016/j.jhazmat.2024.133905

Wightman, P. G., and Fein, J. B. (2005). Iron adsorption by *Bacillus subtilis* bacterial cell walls. *Chem. Geol.* 216, 177–189. doi: 10.1016/j.chemgeo.2004.11.008

Yan, H., Owusu, D. C., Han, Z., Zhao, H., Ji, B., Zhao, Y., et al. (2021). Extracellular, surface, and intracellular biomineralization of *Bacillus subtilis* Daniel-1 Bacteria. *Geomicrobiol J.* 38, 698–708. doi: 10.1080/01490451.2021.1937406

Yin, X., Weitzel, F., Griesshaber, E., Fernández-Díaz, L., Jimenez-Lopez, C., Ziegler, A., et al. (2020). Bacterial EPS in agarose hydrogels directs mineral Organization in Calcite Precipitates: species-specific biosignatures of *Bacillus subtilis*, *Mycobacterium phley*, *Mycobacterium smagmatis*, and *Pseudomonas putida* EPS. *Cryst. Growth Des.* 20, 4402–4417. doi: 10.1021/acs.cgd.0c00231

Zheng, T., Hou, D., Leng, W., Li, P., and Wei, W. (2023). Preparation, characterization, and formation mechanism of different biological calcium carbonate ($CaCO_3$) induced by *Bacillus mucilaginosus* and *Bacillus alcalophilus*. *J. Nanopart. Res.* 25:189. doi: 10.1007/s11051-023-05833-z

Biosurfactant-assisted bio-electrokinetic enhanced remediation of heavy metal-contaminated soil

Jayaraman Narenkumar[1]*, Bhaskar Das[1], Subramani Abilaji[2], Kuppusamy Sathishkumar[3], Mohamad S. AlSalhi[4], Sandhanasamy Devanesan[4], Aruliah Rajasekar[2] and Tabarak Malik[5,6]*

[1]Department of Environmental & Water Resources Engineering, School of Civil Engineering (SCE), Vellore Institute of Technology, Vellore, India, [2]Environmental Molecular Microbiology Research Laboratory, Department of Biotechnology, Thiruvalluvar University, Vellore, India, [3]Center for Global Health Research, Saveetha Medical College and Hospital, Saveetha Institute of Medical and Technical Sciences, Saveetha University, Chennai, India, [4]Department of Physics and Astronomy, College of Science, King Saud University, Riyadh, Saudi Arabia, [5]Department of Biomedical Sciences, Institute of Health, Jimma University, Jimma, Ethiopia, [6]Adjunct Faculty, Division of Research and Development, Lovely Professional University, Phagwara, Punjab, India

Background: Environmental soil contamination is a serious problem for humans worldwide, as it causes many diseases.

Methods: The present study focuses on utilizing biosurfactants produced by *Pseudomonas stutzeri* (*P. stutzeri*) NA3 and *Bacillus cereus* (*B. cereus*) EN6, as an electrolyte for removing chromium (Cr) from contaminated soil using the electrokinetic (EK) process.

Results: As a result, biosurfactants produced by *P. stutzeri* NA3 and *B. cereus* EN6, being lipopeptides, increase heavy metal mobility in the EK process. The Cr removal efficiency of a novel electrolyte (biosurfactants) in the EK process was compared with that of NA3 and EN6 biosurfactants. The EK results revealed a maximum Cr removal of 75 and 70% by NA3 and EN6, respectively, at the end of 7 days.

Discussion: The biosurfactant aids in the breaking down of the heavy metals that are present deeper into the soil matrix. From the metagenomics analysis, it was identified that biosurfactant changes the microbial community with an enhanced ability to remove heavy metals. The phytotoxicity assay confirms that NA3 biosurfactant solution showed 95% seed germination and can lower hazardous pollutants in the soil.

Conclusion: The application of biosurfactants as a potent electrolyte for the remediation of hazardous pollutants is an integrated process. Overall, the results of this study suggest that biosurfactants can serve as an economic and efficient electrolyte in the EK process to remove Cr from polluted soil.

KEYWORDS

Bacilluscereus EN6, biosurfactant, electrolyte, electrokinetic process, *Pseudomonas stutzeri* NA3

GRAPHICAL ABSTRACT
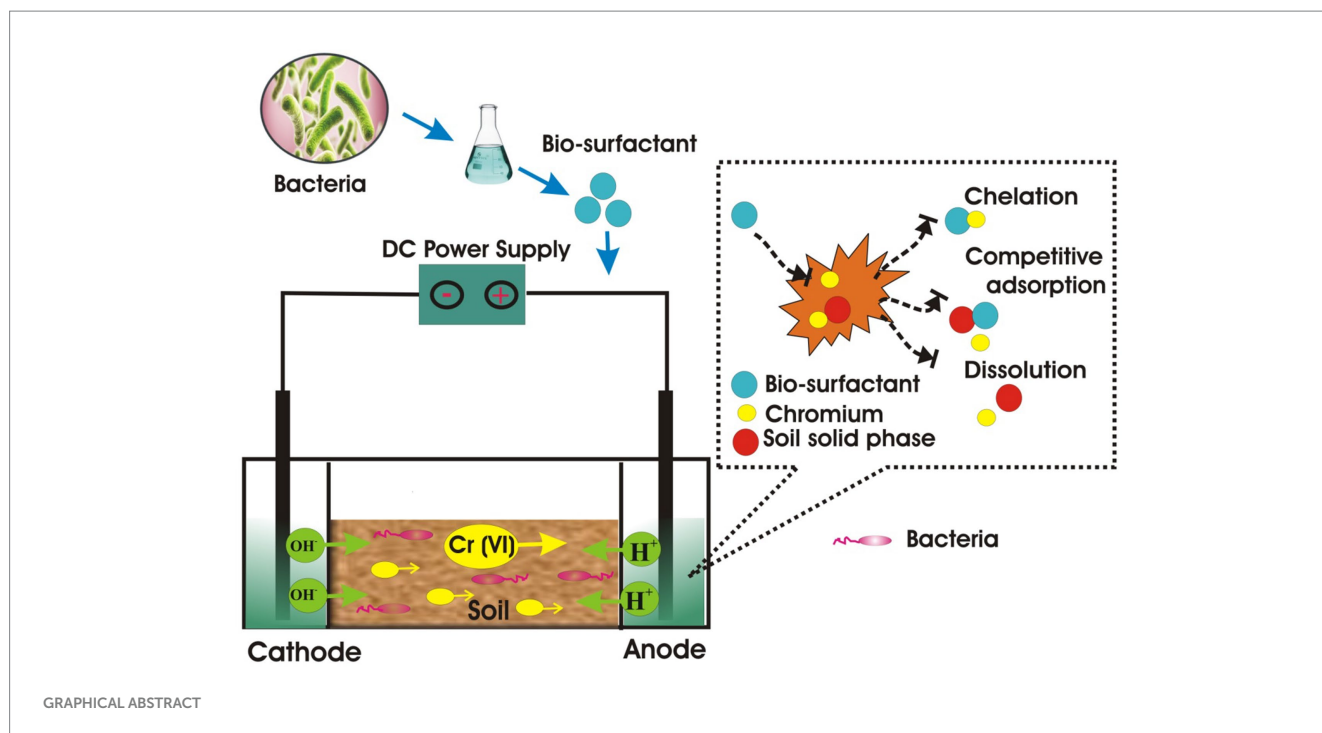
Introduction

Environmental soil pollution has become a major issue for humans across the world. The effluents from various industries have polluted the environment with various types of harmful heavy metals (Mulligan et al., 2001; Wang et al., 2023). Among various heavy metals, Cr is widely used in numerous industries, such as Cr leather tanning, ceramics, stainless steel manufacturing, pyrotechnics, electronics, and painting and textile industries (Fonseca et al., 2012; Abilaji et al., 2023a,b). Tannery wastewater has been found to have elevated levels of chemical oxygen demand (COD), total dissolved solids (TDSs), biochemical oxygen demand (BOD), total suspended solids (TSSs), phosphate, nitrogen, and heavy metals, particularly Cr (Muthukkauppan and Parthiban, 2018; Prakash et al., 2021). However, these industries fail to implement effective Cr disposal techniques, resulting in major contamination of underground water and soil. The effects of the world's expanding Cr pollution were known to cause neurological, renal, gastrointestinal, nasal bleeding, ulcers, skin rashes, allergies, and even human mortality (Thiele, 1995; Liao et al., 2014; Lewis et al., 2004; Mao et al., 2016).

Generally, many technologies have been proposed for the remediation of heavy metal-contaminated soils, including soil replacement, stabilization, chemical reduction, and acid washing (Devi et al., 2023). However, these methods are expensive and considered hazardous to the ecosystem. Therefore, it is necessary to develop an effective and economical technique to remediate heavy metal-contaminated soil (Taneja et al., 2023). EK remediation is an effective technique and a low-cost method for treating heavy metal-contaminated soil (Gu et al., 2018). According to Ren et al. (2014), the cost of the EK process (electrical energy) was approximately $83.3 per cubic meter of soil. Al-Hamdan and Reddy (2008) define EK remediation as the deployment of a low-intensity direct current

or low potential gradient to the electrodes implanted in polluted soil. Electrolysis, electroosmosis, electromigration, and electrophoresis are the primary removal processes of EK remediation (Yeung and Gu, 2011; Zhang et al., 2016; Cameselle et al., 2021; Sathish et al., 2024). During the EK process, electrolysis produces hydrogen gas and hydroxyl ions at the cathode and hydrogen ions and oxygen at the anode. The anode-produced hydrogen ions interact with the metal cations in the soil to exchange electrons. Then, by electromigration, the desorbed metal ions move toward the cathode where the heavy metals are precipitated as oxides, hydroxides, carbonates, and other compounds by the hydroxyl ions that develop at the cathode (Santhosh et al., 2024; Priyadharsan et al., 2024). Although the heavy metals are actively precipitated causing their removal, increased accumulation of those heavy metals decreases the efficacy of cleanup. To accomplish successful remediation throughout EK procedures, an EK improvement program is frequently necessary.

In the EK approach, chelating agents and inorganic/organic acids are frequently used to remove heavy metals from soil (Santhosh et al., 2024). Apart from the aforementioned removable agents, washing chemicals, such as salts and surfactants, were also utilized to reduce surface and interfacial tension and to enhance the efficiency of heavy metal removal (Guo et al., 2016; Prakash et al., 2021). Biosurfactants exhibit higher biodegradability, less toxicity, and are more eco-friendly than chemical surfactants. Accordingly, biosurfactants are more appropriate for soil remediation. Some microorganisms (bacteria, fungi, and yeast) can produce biosurfactants as a result of metabolic activities (Kumar et al., 2021; Liepins et al., 2021; Tang et al., 2018). They also produce a number of organic acids that allow it to act as a chelating agent, increasing its potential as an electrolyte for the EK process. Hence, the present investigation is attempted to demonstrate the ability of bacterial biosurfactants (*Pseudomonas stutzeri* NA3 and

Bacillus cereus EN6) to serve as a potential electrolyte for the EK process in removing Cr from contaminated soil.

Methodology

Sample collection

The heavy metal-contaminated soil sample was collected from Ranipet, Vellore, Tamil Nadu, India (latitude 12.9320°N, longitude 79.3334°E). The total Cr content of the soil was measured according to Krishna and Philip (2005) and was found to be 10.2 mg/g. This accumulation of Cr beyond the admissible limits happened during the operation of the facility, which produced sodium chromate, Cr salts, and basic chromium sulfate until 1995, and later on, the factory was closed. The samples were collected in a sterile container, transferred to the laboratory, and stored at 4°C for further studies. A physio-chemical characteristic of the soil elemental composition was analyzed using the US EPA SW 846 method 3050B. The sample was analyzed using inductively coupled plasma-mass spectrometry (ICP-MS) following acid digestion for heavy metal analysis.

Bacterial strain and culture conditions

The bacterial strains, *P. stutzeri* NA3 (KU708859), which is a Gram-negative strain, and *B. cereus* EN6 (KR183877), which is a Gram-positive strain, were used in this study. These bacterial cultures were sub-cultured on nutrient agar (NA) and incubated for 24 h at 37°C. The colonies were plated using a streak plate technique until individual cultures were obtained, after that those colonies were inoculated in nutrient broth (pH 7.0) and then incubated for 24 h at 37°C in an orbital shaker (150 rpm) (Parthipan et al., 2017; Narenkumar et al., 2018; Tang et al., 2018).

Production and extraction of biosurfactant

Bacterial cultures were centrifuged at 8,000 rpm at 4°C for 10 min. Then HCl was added to a supernatant to bring the pH level down to 2. The acidified supernatant was kept at 4°C overnight for precipitation. The precipitate was separated by centrifugation at 8,000 rpm for 10 min. This white precipitate produced by bacterial cultures was chosen and used to identify biosurfactants (Mahesh et al., 2006). After identification, the biosurfactant produced by the bacteria was extracted using a separating funnel. A total of 65 mL of chloroform, 15 mL of phenol, and 50 mL of bacterial culture were added to the separating funnel and kept at room temperature for 10 min. After separation, three layers were formed from which the bottom layer of biosurfactant was collected and further used for screening by different methods (the drop collapse method and the oil spreading method).

Characterization of biosurfactant

The extracted biosurfactant was characterized using Fourier transform infrared spectroscopy (FTIR) and gas chromatographic-mass spectroscopy (GC-MS). FTIR (PerkinElmer, Nicolet Nexus-470) was used to qualitatively characterize the functional groups of the surfactant that was extracted from *P. stutzeri* NA3 and *B. cereus* EN6. The biosurfactant (10 mg) was mixed with 5% HCl-methanol reagent for GC-MS analysis. Using a Shimadzu QP2010 Ultra Rtx-5Sil MS (30 m × 0.25 mm ID × 0.25 μm) GC-MS, 1 μL of the sample was injected after the reaction was quenched with the injection of 1 mL of sterile H_2O (Parthipan et al., 2017).

Electrokinetic remediation

The EK test setup and cell details are presented in Figure 1. The EK apparatus was composed of three chambers: a soil chamber measuring 30 × 5 × 5 cm (l×w×h) and two electrode chambers measuring 4 × 160 × 200 cm (l×w×h) (Sarankumar et al., 2020). To stop soil from seeping into the electrode chamber, two sheets of cellulose filter paper were placed between the three chambers. According to Marshall and Haverkamp (2012) and Prakash et al., 2021), a titanium-coated iridium oxide mesh measuring 10 cm in width and 10 cm in height was utilized as the anode, while stainless steel measuring the same was utilized as the cathode electrode (Prakash et al., 2021). This electrode was found to be corrosive-resistant and showed better electrocatalytic activity for chlorine estimation. Two electrolytes (biosurfactant solution) were used in the EK testing. A total of 600 g of dry soil was soaked in electrolyte solutions in the soil chamber for 3 days before each EK test, and the anode and cathode chambers were filled with the tested electrolytes. For 7 days, EK analysis was carried out at a constant direct current

FIGURE 1
FTIR spectrum of biosurfactant isolated from *P. stutzeri* NA3 and *B. cereus* EN6.
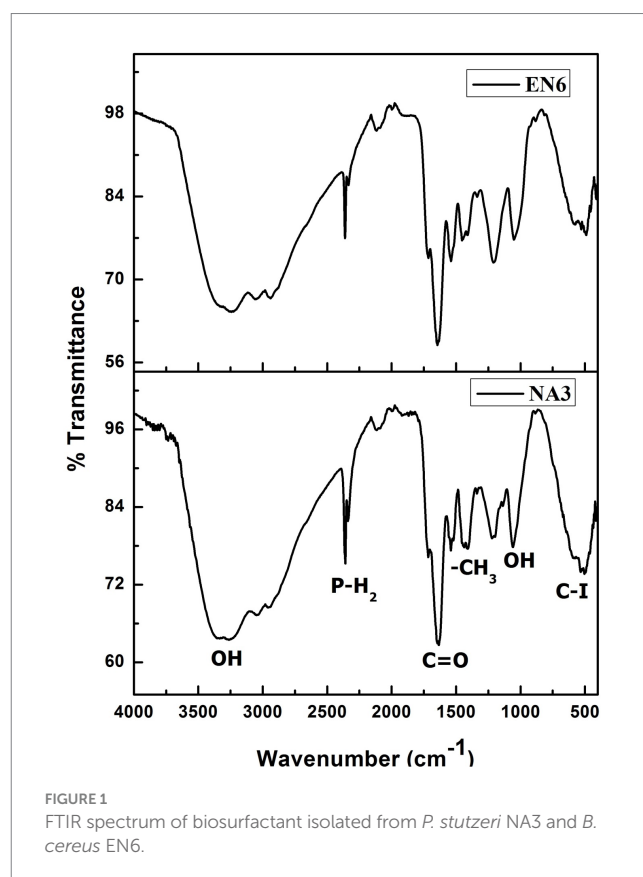
electric potential of 30 V. In order to avoid creating a hydraulic gradient in the soil column, fresh electrolyte solutions were introduced to the anode chamber every 2 days and the overflowing solution was removed from the cathode chamber during an EK procedure (Al-Hamdan and Reddy, 2008). From the anode to the cathode side, the soil chamber was divided into five slices, numbered EKS1 through EKS5. Without using a pH control, all of the trials were carried out at ambient temperature. Every day during an EK procedure, a pH electrode was inserted directly into the soil to measure the pH of the soil in each sliced segment (EKS1 to EKS5). Following the experiment, the sliced piece of soil (EKS1 to EKS5) was taken out of the EK chamber, and the soil sample was finely ground using a mortar and pestle to prepare it for X-ray diffraction (XRD) and Fourier transform infrared (FTIR) analysis (Sarankumar et al., 2020). An inductively coupled plasma mass spectrometer (ICP-MS) was used to analyze the soil sample following acid digestion. Metagenomics was used to analyze bacterial community at the end of the experiment.

Phytotoxicity assay

The phytotoxicity analysis was conducted to determine the toxicity of the treated/untreated contaminated soil on *Vigna radiata* (SathishKumar et al., 2017). A total of 10 seeds of *Vigna radiata* were planted into the EK-treated/untreated soil. The seed germination studies were conducted at room temperature, and the length of the root and shoot from the seed was tracked throughout (Sarankumar et al., 2020).

Result and discussion

Biosurfactant screening

The *P. stutzeri* NA3 and *B. cereus* EN6 were found to be good producers of biosurfactants, which were confirmed by their biosurfactant production through multiple sub-culturing and screening procedures. All biosurfactant screening techniques yielded immediate positive findings for these isolates. In particular, drops collapsing within 30 s confirmed that a higher amount of the biosurfactant was present in the solution. For initial screening, the emulsification index was 80 and 78% for *P. stutzeri* NA3 and *B. cereus* EN6, respectively. Biosurfactants generated by different microorganisms are substrate-specific, emulsifying a wide range of hydrocarbons at varying speeds (Ilori et al., 2005; Parthipan et al., 2017). In oil displacement analysis, a clear zone of 2.4 cm and 2.1 cm was observed for *P. stutzeri* NA3 and *B. cereus* EN6, respectively. These findings show that the cell-free culture contains biosurfactants.

Biosurfactant characterization

FTIR analysis was performed to determine the presence of a functional group in the biosurfactant (Figure 1). The distinctive bands at 3,309 cm^{-1} correspond to $-$OH bonds (Aparna et al., 2012). The peaks observed at 2,359 cm^{-1}, 1,631 cm^{-1}, and 1,436 cm^{-1} correspond to the P$-$H$_2$ stretch of phosphines in phosphoserine and ester carbonyl groups ($-$C=O bond in COOH) (Bayoumi et al., 2010; Parthipan et al.,
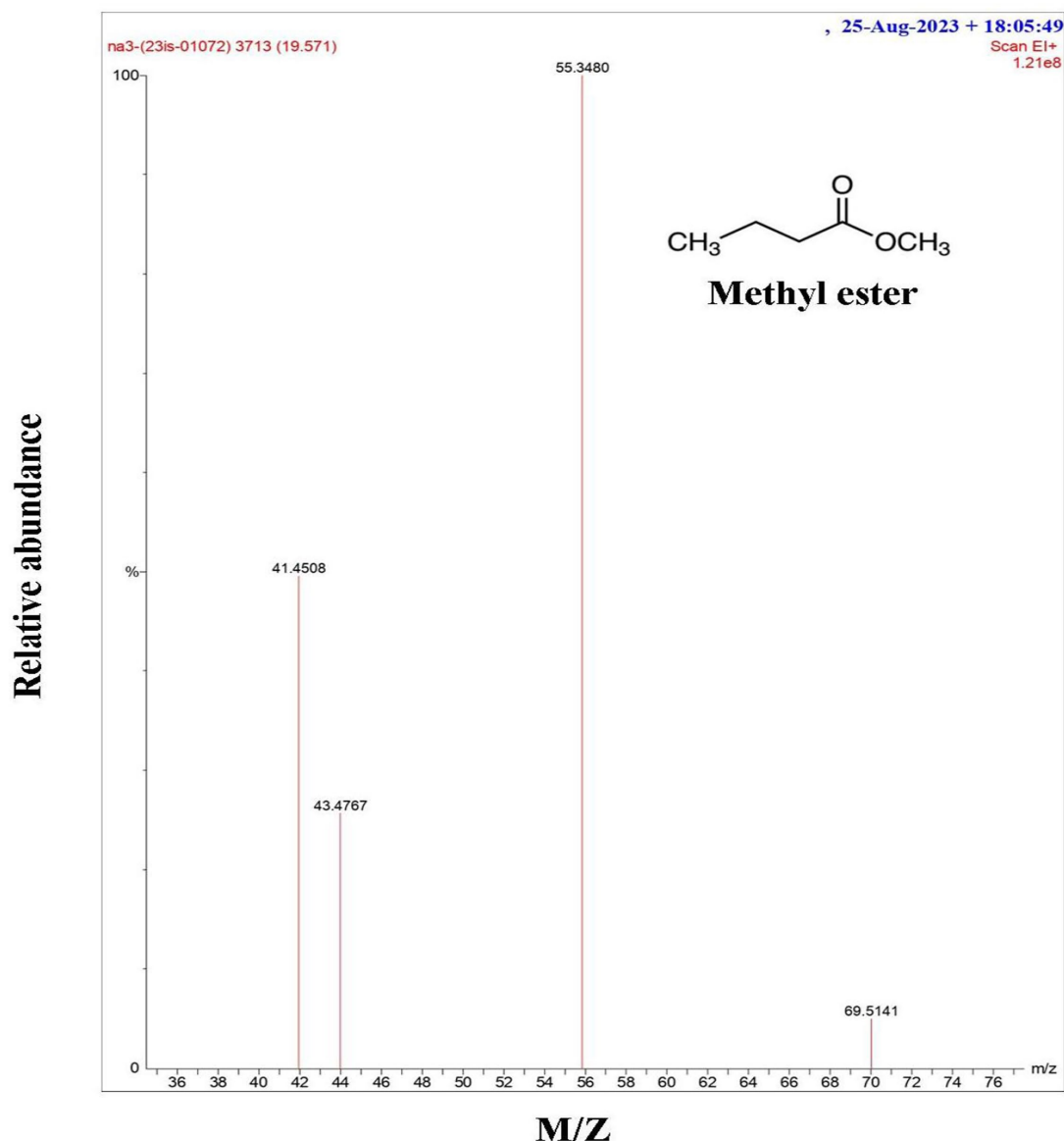

FIGURE 2 (Continued)
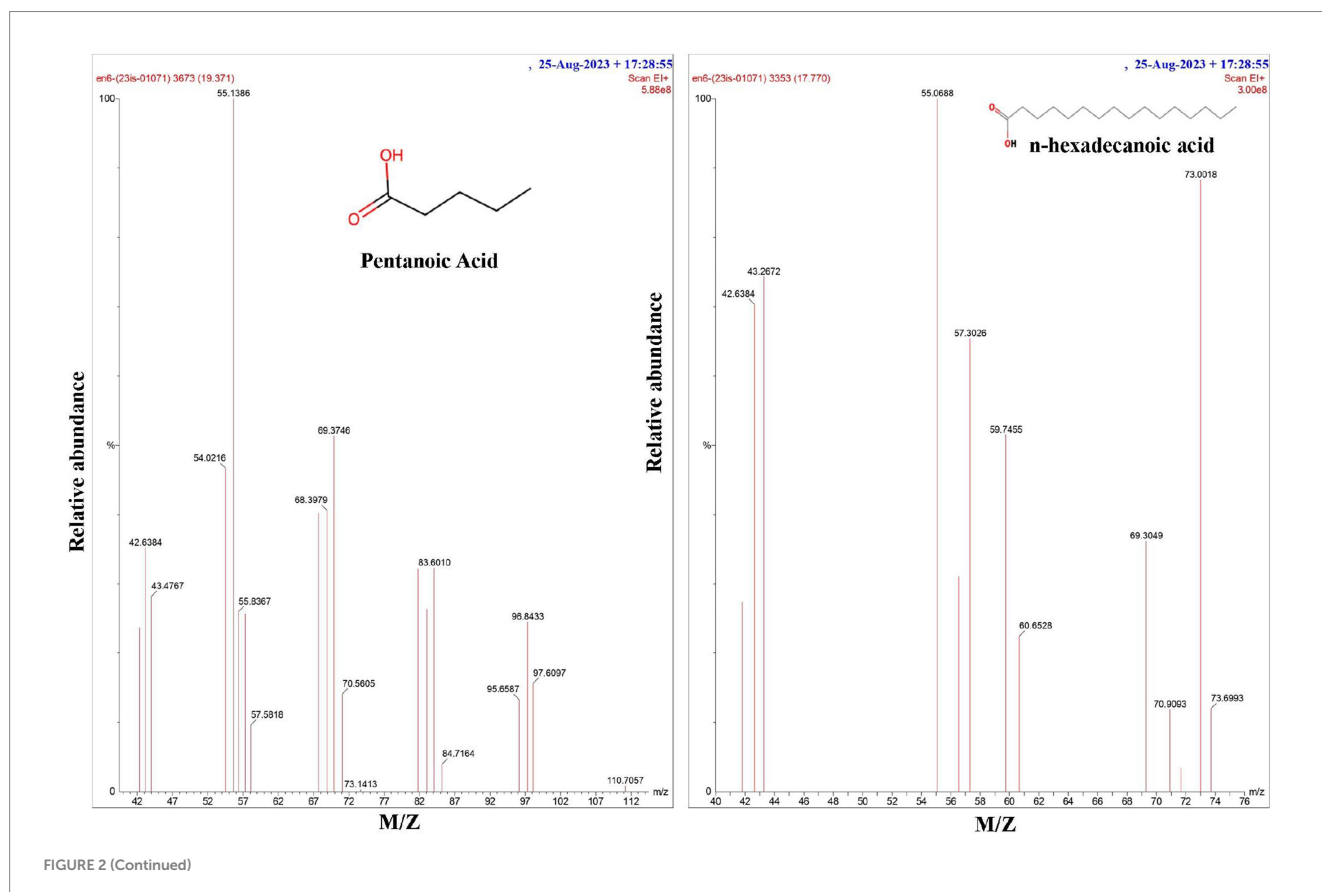
FIGURE 2
GC-MS spectrum of the biosurfactant isolated from *P. stutzeri* NA3 and *B. cereus* EN6.

2017). The absorption peaks at $1{,}057\,cm^{-1}$ and $534\,cm^{-1}$ show the presence of the O–H (carboxylic acids) and C–I (carbon-iodine) bonds, respectively. Based on this observation, *P. stutzeri* NA3 and *B. cereus* EN6 were produced as biosurfactants, which is also supported by the findings of Rodrigues et al. (2006).

GC-MS analysis

The finding from the gas chromatography study revealed (Figure 2) that the biosurfactant extracted from both bacterial strains contains hexadecanoic acid and methyl ester (a fatty acid). According to Kiran et al. (2010) and Hien et al. (2013), *P. stutzeri* NA3 and *B. cereus* EN6 included fatty acids, such as hexadecanoic acid, pentanoic acid, and methyl ester with retention times (RTs) of 17.77, 19.37, and 19.50 and

MWs of 256, 254, and 184, respectively. According to Deshmukh et al. (2012), Bacillus developed a biosurfactant that was essentially lipopeptide in nature. Tsui et al. (2022) state that many organic acids and metabolic products are produced by microorganisms; these chemicals stay in the solution (electrolyte) and contribute to its high conductivity. Because of this, microbes may effectively reduce the pH of the anode and create organic acids, which can combine with heavy metals to enhance their mobility.

Electrokinetic remediation

EK experiment for Cr (VI) remediation was conducted in the customized cell setup as mentioned above. The ICP-MS technique was used to evaluate the residual amounts of total Cr by EK. The level was
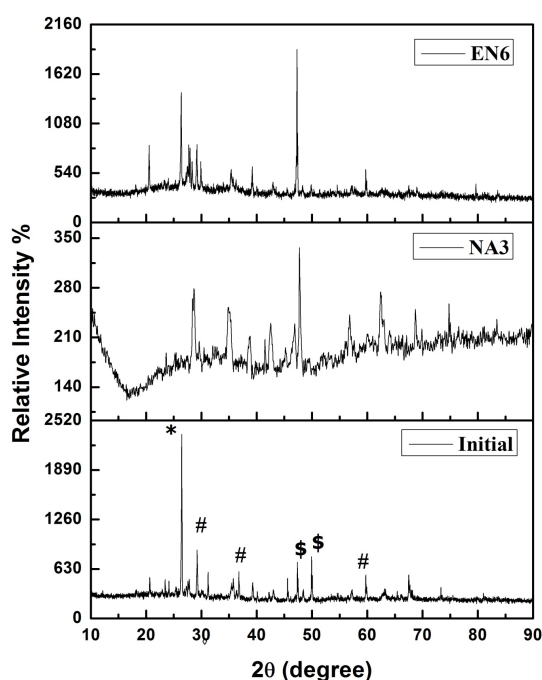
FIGURE 3
X-ray diffraction patterns of the soil before and after the EK experiment *CrOCl, #KCr$_3$O$_8$, and ^{S}C$_4$H$_{16}$Cr$_2$CuN4O$_7$.

FIGURE 4
FTIR patterns of the soil before and after the EK experiment.

found to decrease from 44,615 mg/kg to 13,523 mg/kg (70%) and 11,390 mg/kg (75%) for *P. stutzeri* NA3 and *B. cereus* EN6, respectively. As previously reported, 63.34% of Cr was removed from the soil sections by using distilled water (Yan et al., 2023). The obtained results showed that 75% was reduced by electrolytes (NA3 biosurfactant) in the approach. The results revealed that Cr removal was enhanced using biosurfactant as an electrolyte, indicating that the biosurfactant binds to Cr (chelation) to form micelles, which enhances the electromigration process to remove this heavy metal from the soil. It is important to note that synthetic surfactants may have irreversible effects on soil toward the loss of essential nutrients and organic matter. However, this biosurfactant can overcome this disadvantage and it also has an added advantage of using eco-friendly, biodegradable material for the removal of heavy metals. Researchers have identified several microorganisms as potential biosurfactants that operate extremely well in removing heavy metals (Ayangbenro and Babalola, 2020; Lopes et al., 2021; Ravindran et al., 2020). Earlier studies reported that biosurfactants contain both carboxyl and hydroxyl groups, which were able to form stable complexes with heavy metal ions, complexes such as these facilitate heavy metal mobilization and migration.

Figure 3 shows the XRD analysis of the untreated (control) and treated (*P. stutzeri* NA3 and *B. cereus* EN6) soil samples. Cr (VI) in the form of CrOCl, KCr$_3$O$_8$, and C$_4$H$_{16}$Cr$_2$CuN$_4$O$_7$ was found in the untreated sample (initial) according to the XRD pattern. In contrast, the EK-treated soil samples (*P. stutzeri* NA3) show a decreased intensity of peaks and the presence of some other additional peaks when compared to the control and *B. cereus* EN6 due to ions that may be extracted with acid and dissolved soil components (Xue et al., 2017). From this analysis, more contaminants were found to be dissolved, and electro-kinetic remediation was found to be more suitable for acid- and water-soluble ions.
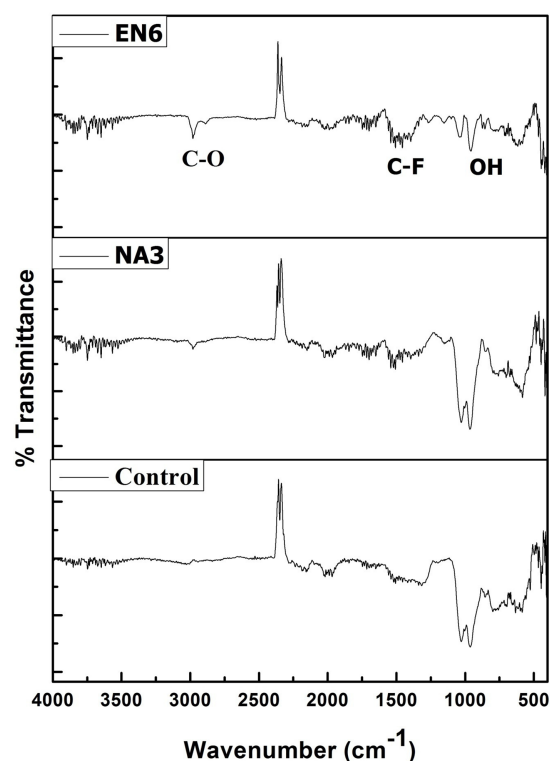
The FTIR spectrum of the before and after EK analysis (control, *P. stutzeri* NA3, and *B. cereus* EN6) of the soil is shown in Figure 4. In treated soil, the peak at 2,982 cm^{-1} corresponds to the presence of the carboxylic (C–O) group, which was due to alcohol groups being transformed into carboxylic groups during the reduction of Cr (VI) to Cr (III) (Bandara et al., 2020; Santhosh et al., 2024; Abilaji et al., 2023a,b). The peak at 1,986 cm^{-1} may be related to the soil's clay mineral composition. The C–F stretch of the alkyl halide has a peak at 1,506 cm^{-1}. A metal oxide hydroxide is indicated by narrow peaks at 964 and 599 cm^{-1} (Anandaraj et al., 2017). Conversely, the untreated control soil's absorption peaks demonstrated a significant variation in peak intensities when compared to the treated soil, indicating that the Cr remediation process facilitated by the *P. stutzeri* NA3 and *B. cereus* EN6 bacterial surfactants was successful. Functional groups of lipopeptide biosurfactant bind to the Cr heavy metal ion through chelation, complexation, and electrostatic adsorption mechanisms. First, the heavy metal gets detached from the contaminated soil, which then associates with biosurfactants to form micelles (Peng et al., 2009). As a result of their low toxicity, biodegradable nature, and low environmental footprint, biosurfactants are gaining a great deal of attention worldwide.

Bacterial diversity analysis

Figure 5 illustrates the relative abundance of different bacterial phyla in two samples, labeled as initial and sample 1 (Biosurfactant EK treatment). The plot indicates a comparison of microbial community composition before and after EK treatment. The initial sample shows the most abundant phylum as *Proteobacteria*,
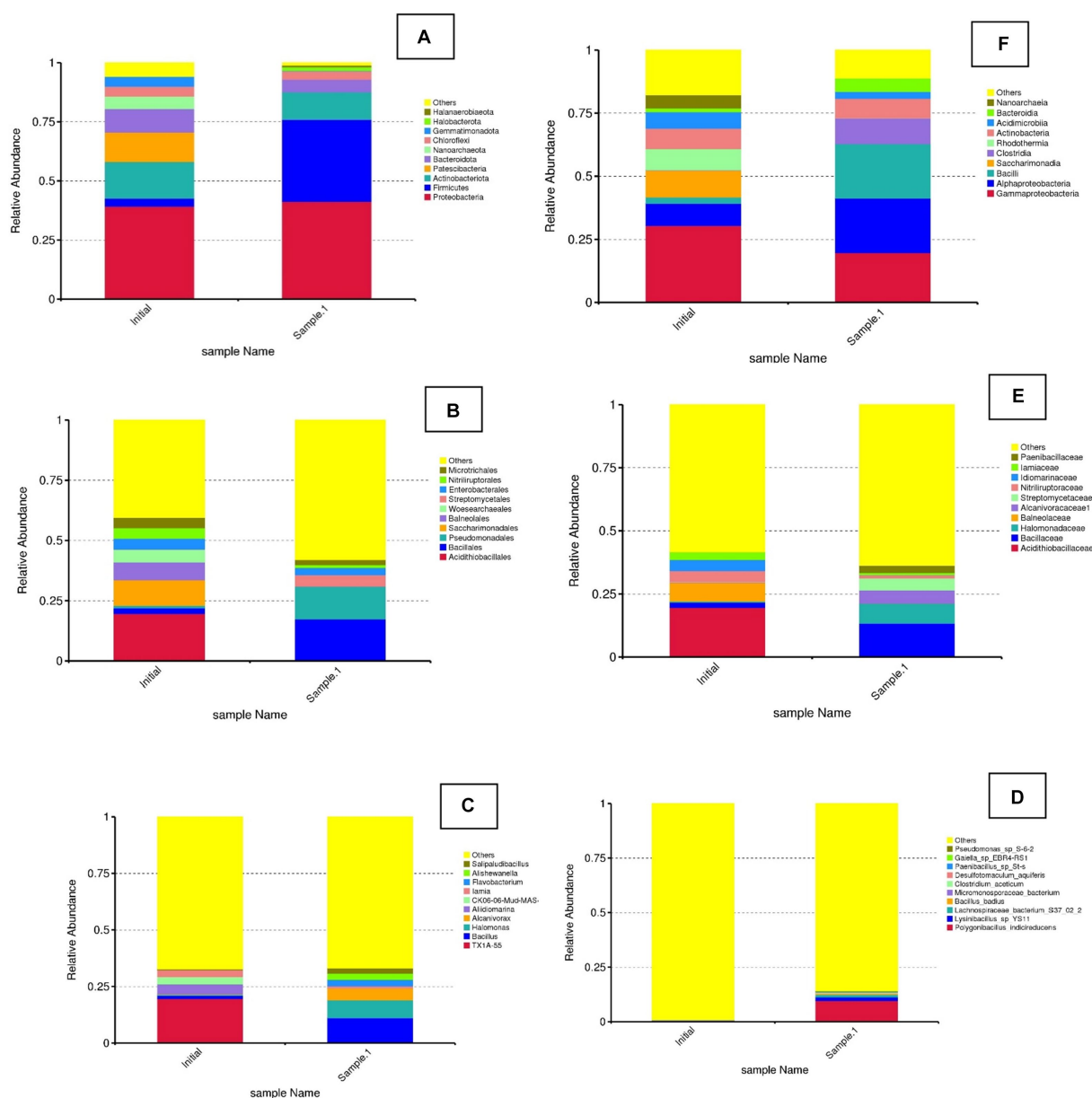
FIGURE 5
Relative abundance of bacterial diversity at phylum, class, order, family, genus, and species level in the initial and treated (EK). **(A)** Phylum. **(B)** Family. **(C)** Genus. **(D)** Species. **(E)** Order. **(F)** Class.

followed by *Actinobacteriota*, *Patescibacteria*, and others. *Firmicutes* and other phyla (*Bacteroidota*, *Nanoarchaeota*, *Chloroflexi*, etc.) were found to be present in smaller proportions. Sample 1 shows there was a noticeable shift in the microbial community composition. *Proteobacteria* and *Firmicutes* show significant changes, with *Firmicutes* becoming much more dominant in sample 1. Other phyla, such as *Actinobacteriota* and *Patescibacteria*, exhibit variations in their relative abundances. Bio-electrokinetic remediation is an emerging technology that combines bioremediation and EKs to enhance the removal of heavy metals, such as Cr, from contaminated soils. This approach leverages microbial activity and the application of electric fields to mobilize and degrade contaminants. The observed changes in

microbial community structure between the initial and BEK samples were crucial for understanding the effectiveness of bio-electrokinetic remediation. Specific bacterial phyla, such as *Proteobacteria* and *Firmicutes*, were known to play vital roles in metal reduction and detoxification processes. Studies have shown that certain strains of *Proteobacteria* can reduce Cr(VI) to the less toxic Cr(III), facilitating its removal from the soil (Zhu et al., 2017). The application of an electric field can increase the mobility of Cr ions in the soil, making them more accessible to microbial degradation. This process can also enhance the transport of nutrients and electron donors to the microbial populations, boosting their activity and efficiency (Acar and Alshawabkeh, 1993, Arulpraksh et al., 2021). The integration of bioremediation

with EK techniques can result in synergistic effects, leading to improved remediation outcomes compared to traditional methods.

In the class level of bacterial diversity, the initial sample was found to have the most abundant class as *Gammaproteobacteria*, followed by *Alphaproteobacteria*, *Bacilli*, and others. *Clostridia*, *Saccharimonadia*, and other classes (*Acidimicrobiia*, *Actinobacteria*, etc.) were present in smaller proportions. In sample 1, there was a noticeable shift in the microbial community composition. *Alphaproteobacteria* and *Bacilli* show significant changes, with *Bacilli* becoming more dominant in sample 1. Other classes, such as *Clostridia* and *Saccharimonadia*, exhibit variations in their relative abundances.

Whereas in the order level, in the initial sample, the most abundant order was "Others," followed by *Acidithiobacillales*, *Bacillales*, and *Pseudomonadales*. Other orders, such as *Saccharimonadales*, *Balneolales*, and others, were present in smaller proportions. In sample 1, there was a noticeable shift in the microbial community composition. *Pseudomonadales* and *Bacillales* show significant changes, with *Pseudomonadales* becoming much more dominant in sample 1. Other orders, such as *Acidithiobacillales* and *Saccharimonadales*, exhibit variations in their relative abundances. The observed changes in microbial community structure between the initial and EK samples are crucial for understanding the effects of specific treatments or environmental changes. This is particularly relevant in the context of bioremediation, where microbial communities play a vital role in degrading and detoxifying contaminants. The shift in microbial community composition suggests that the treatment or condition applied to sample 1 has influenced the relative abundance of different bacterial orders. *Pseudomonadales*, known for their versatile metabolic capabilities and resistance to heavy metals, have become more dominant in sample 1. This indicates their potential role in bioremediation processes (Mrozik et al., 2010). The decrease in *Acidithiobacillales*, which were typically associated with acidic environments and sulfur metabolism, might indicate a change in environmental conditions or the successful removal of specific contaminants that these bacteria thrive on Johnson and Hallberg (2009). *Pseudomonadales*: Pseudomonas species were well-known for their ability to degrade a wide range of organic pollutants and heavy metals. Their increased abundance in sample 1 suggests their active role in the bioremediation process. Recent studies have highlighted their effectiveness in Cr reduction and detoxification (Raja et al., 2020). *Bacillales*: The members of this order, including *Bacillus* species, were also important in bioremediation due to their ability to produce spores, which make them resilient in harsh conditions. They can also produce enzymes that degrade pollutants (Müller et al., 2012).

At the genus level, the results showed that in the initial sample, the most abundant group is "Others," followed by TX1A-55, *Bacillus*, and *Halomonas*. Other genera, such as *Alcanivorax*, *Aliidiomarina*, and others, were present in smaller proportions. In sample 1, there was a noticeable shift in the microbial community composition. *Bacillus* and *Halomonas* show significant changes, with *Bacillus* becoming more dominant in sample 1. Other genera, such as TX1A-55 and *Alcanivorax*, exhibited variations in their relative abundances. *Halomonas* bacteria were known for their ability to survive in high-salinity environments and their potential in bioremediation of saline and heavy metal-contaminated sites (Nieto et al., 1993).

At the species level, the most abundant group was Others, indicating a diverse set of species that were not individually listed. Specific species, such as *Pseudomonas* sp. S-6-2, *Paenibacillus* sp. and *Polygonibacillus*

indicireducens, were present in smaller proportions. In sample 1, there was a noticeable shift in the microbial community composition. The diversity seems to decrease, with specific species, such as *Polygonibacillus indicireducens*, *Pseudomonas* sp. S-6-2, and *Lysinibacillus* sp. YS11, becoming more prominent. *Lysinibacillus* spp. known for their ability to produce spores and survive in harsh environments. *Lysinibacillus* species have shown potential in heavy metal bioremediation (Raja et al., 2020). They can reduce toxic metals and facilitate their removal from contaminated environments. *Paenibacillus* spp. are known for their nitrogen-fixing abilities and production of antimicrobial compounds. They also play a crucial role in the degradation of organic pollutants and bioremediation (Grady et al., 2016).

Phytotoxicity assay

The phytotoxicity of untreated and treated plants was evaluated by *Vigna radiata*. The untreated soil showed no germination, whereas the *P. stutzeri* NA3 biosurfactant solution showed 95% germination, whereas 70% of the *B. cereus* EN6 solution did the same. This was confirmed by measuring the length of the shoot and root in the appropriate soil. It is confirmed that the treated *P. stutzeri* NA3 biosurfactant solution grows the seeds more effectively than the *B. cereus* EN6 and untreated soil because the treated soil was less hazardous. This method serves as a potential electrolyte for the EK process for the remediation of Cr from contaminated soil.

Conclusion

Biosurfactant was determined to be a novel electrolyte for removing Cr from soil through an EK process. The study's findings showed that at the end (7 days) of the EK process, *P. stutzeri* NA3 biosurfactant exhibited significantly higher Cr removal efficiency (75%) than *B. cereus* EN6 (70%). From the phytotoxicity assay, *P. stutzeri* NA3 biosurfactant solution showed 95% seed germination. Hence, it can be said that modifications to the microbial community structure result in an increase in the efficacy of heavy metal removal and that NA3 biosurfactant may be used as an electrolyte for EK applications. However, further investigation is required to determine whether biosurfactants can be used to remove other emerging pollutants.

Data availability statement

The original contributions presented in the study are included in the article/supplementary material, further inquiries can be directed to the corresponding authors.

Author contributions

JN: Project administration, Writing – review & editing, Writing – original draft. BD: Writing – review & editing, Formal analysis. SA: Writing – review & editing, Data curation. SK: Writing – review & editing, Validation, Formal analysis. MA: Writing – review & editing, Validation, Funding acquisition, Formal analysis. SD: Writing – review & editing, Validation, Investigation, Formal analysis. RA:

Conflict of interest

The authors declare that the research was conducted in the absence of any commercial or financial relationships that could be construed as a potential conflict of interest.

The reviewer VR declared a past co-authorship with the authors JN and RA to the handling editor.

Publisher's note

All claims expressed in this article are solely those of the authors and do not necessarily represent those of their affiliated organizations, or those of the publisher, the editors and the reviewers. Any product that may be evaluated in this article, or claim that may be made by its manufacturer, is not guaranteed or endorsed by the publisher.

References

Abilaji, S., Narenkumar, J., Das, B., Suresh, S., Rajakrishnan, R., Sathishkumar, K., et al. (2023a). Electrochemical oxidation of azo dyes degradation by RuO_2–IrO_2–TiO_2 electrode with biodegradation *Aeromonas hydrophila* AR1 and its degradation pathway: an integrated approach. *Chemosphere* 345:140516. doi: 10.1016/j.chemosphere.2023.140516

Abilaji, S., Sathishkumar, K., Narenkumar, J., Alsalhi, M. S., Devanesan, S., Parthipan, P., et al. (2023b). Sequential photo electro oxidation and biodegradation of textile effluent: elucidation of degradation mechanism and bacterial diversity. *Chemosphere* 331:138816. doi: 10.1016/j.chemosphere.2023.138816

Acar, Y. B., and Alshawabkeh, A. N. (1993). Principles of electrokinetic remediation. *Environ. Sci. Technol.* 27, 2638–2647. doi: 10.1021/es00049a002

Al-Hamdan, A. Z., and Reddy, K. R. (2008). Electrokinetic remediation modeling incorporating geochemical effects. *Journal of geotechnical and geoenvironmental engineering* 134, 91–105.

Anandaraj, A., Eswaramoorthi, S., Rajesh, T. P., Aravind, J., and Suresh Babu, P. (2017). Chromium (VI) adsorption by *Codium tomentosum*: evidence for adsorption by porous media from sigmoidaldose–response curve. *Int. J. Environ. Sci. Technol.* 15, 2595–2606. doi: 10.1007/s13762-017-1488-7

Aparna, A., Srinikethan, G., and Smitha, H. (2012). Production and characterization of biosurfactant produced by a novel *Pseudomonas* sp. 2B. *Colloids Surf. B* 95, 23–29. doi: 10.1016/j.colsurfb.2012.01.043

Ayangbenro, A. S., and Babalola, O. O. (2020). Genomic analysis of *Bacillus cereus* NWUAB01 and its heavy metal removal from polluted soils. *Sci. Rep.* 10:19660. doi: 10.1038/s41598-020-75170-x

Bandara, P. C., Peña-Bahamonde, J., and Rodrigues, D. F. (2020). Redox mechanisms of conversion of Cr (VI) to Cr (III) by graphene oxide-polymer composite. *Sci. Rep.* 10:9237. doi: 10.1038/s41598-020-65534-8

Bayoumi, R. A., Haroun, B. M., Ghazal, E. A., and Mahe, Y. A. (2010). Structural analysis and characterization of biosurfactants produced by some crude oil utilizing bacterial strains. *Aust. J. Basic Appl. Sci.* 4, 3484–3498.

Blue, M. Chromium (VI) Reduction, and Antibacterial Efficacy. *Water, Air, Soil Pollut.* 235:309. doi: 10.1007/s11270-024-07120-6

Cameselle, C., Gouveia, S., and Cabo, A. (2021). Enhanced electrokinetic remediation for the removal of heavy metals from contaminated soils. *Applied Sciences* 11:1799.

Deshmukh, C., Jagtap, C. B., Titus, S., and Kumar, P. (2012). Isolation and characterization of fatty acid esters and phosphatidylethanolamine surfactants from a consortium of marine bacteria. *Indian J. Geomarine sci.* 41, 398–404.

Devi, A., Verma, M., Saratale, G. D., Saratale, R. G., Ferreira, L. F. R., Mulla, S. I., et al. (2023). Microalgae: a green eco-friendly agents for bioremediation of tannery wastewater with simultaneous production of value-added products. *Chemosphere* 336:139192. doi: 10.1016/j.chemosphere.2023.139192

Fonseca, B., Pazos, M., Tavares, T., and Sanroman, M. A. (2012). Removal of hexavalent chromium of contaminated soil by coupling electrokinetic remediation and permeable reactive biobarriers. *Environ. Sci. Pollut. Res. Int.* 19, 1800–1808. doi: 10.1007/s11356-011-0694-y

Grady, E. N., Mac Donald, J., Liu, L., Richman, A., and Yuan, Z. C. (2016). Current knowledge and perspectives of *Paenibacillus*: a review. *Microb. Cell Factories* 15:203. doi: 10.1186/s12934-016-0603-7

Gu, Y., Yeung, A. T., and Li, H. (2018). Enhanced electrokinetic remediation of cadmium-contaminated natural clay using organophosphonates in comparison with EDTA. *Chin. J. Chem. Eng.* 26, 1152–1159. doi: 10.1016/j.cjche.2017.10.012

Guo, X., Wei, Z., Wu, Q., Li, C., Qian, T., and Zheng, W. (2016). Effect of soil washing with only chelators or combining with ferric chloride on soil heavy metal removal and phytoavailability: field experiments. *Chemosphere* 147, 412–419. doi: 10.1016/j.chemosphere.2015.12.087

Hien, L. T., Yen, N. T., and Nga, W. T. (2013). Biosurfactant-producing *Rhodococcus ruber* TD2 isolated from oil polluted water in Vung Tau coastal zone. *Acad. J. Biol.* 35, 454–460. doi: 10.15625/0866-7160/v35n4.3775

Ilori, M. O., Amobi, A. C., and Odocha, A. C. (2005). Factors affecting biosurfactant production by oil degrading *Aeromonas* spp. isolated from a tropical environment. *Chemosphere* 61, 985–992. doi: 10.1016/j.chemosphere.2005.03.066

Johnson, D. B., and Hallberg, K. B. (2009). Carbon, iron and sulfur metabolism in acidophilic microorganisms. *Adv. Microb. Physiol.* 54, 201–255. doi: 10.1016/S0065-2911(08)00003-9

Kiran, G. S., Thomas, T. A., Selvin, J., Sabarathnam, B., and Lipton, A. P. (2010). Optimization and characterization of a new lipopeptide biosurfactant produced by marine *Brevibacterium aureum* MSA13 in solid state culture. *Bioresour. Technol.* 101, 2389–2396. doi: 10.1016/j.biortech.2009.11.023

Krishna, K. R., and Philip, L. (2005). Bioremediation of Cr (VI) in contaminated soils. *J. Hazard. Mater.* 121, 109–117. doi: 10.1016/j.jhazmat.2005.01.018

Kumar, A., Singh, S. K., Kant, C., Verma, H., Kumar, D., Singh, P. P., et al. (2021). Microbial biosurfactant: a new frontier for sustainable agricultural and pharmaceutical industries. *Antioxidants* 10:1472. doi: 10.3390/antiox10091472

Lewis, L. K., Storici, F., Van Komen, S., Calero, S., Sung, P., and Resnick, M. A. (2004). Role of the nuclease activity of *Saccharomyces cerevisiae* Mre 11 in repair of DNA double-strand breaks in mitotic cells. *Genetics* 166, 1701–1713. doi: 10.1534/genetics.166.4.1701

Liao, Y. P., Zhang, D., Zhou, W., Meng, F. M., Bao, M. S., Xiang, P., et al. (2014). Combined folate gene MTHFD and TC polymorphisms as maternal risk factors for down syndrome in China. *Genet. Mol. Res.* 13, 1764–1773. doi: 10.4238/2014.March.17.4

Liepins, J., Balina, K., Soloha, R., Berzina, I., Lukasa, L. K., and Dace, E. (2021). Glycolipid biosurfactant production from waste cooking oils by yeast: review of substrates, producers and products. *Fermentation* 7:136. doi: 10.3390/fermentation7030136

Lopes, C. S. C., Teixeira, D. B., Braz, B. F., Santelli, R. E., de Castilho, L. V. A., Gomez, J. G. C., et al. (2021). Application of rhamnolipid surfactant for remediation of toxic metals of long and short-term contaminated sites. *Int. J. Environ. Sci. Technol.* 18, 575–588. doi: 10.1007/s13762-020-02889-5

Mahesh, N., Murugesh, S., and Mohana Srinivasan, V. (2006). Determination of presence of Biosurfactant produced by the bacteria present in the soil samples. *Research Journal of Microbiology* 1, 339–345.

Mao, X. Y., Han, F. X. X., Shao, X. H., Guo, K., McComb, J., Arslan, Z., et al. (2016). Electro-kinetic remediation coupled with phytoremediation to remove lead, arsenic and cesium from contaminated paddy soil. *Ecotoxicol. Environ. Saf.* 125, 16–24. doi: 10.1016/j.ecoenv.2015.11.021

Marshall, A. T., and Haverkamp, R. G. (2012). Nanoparticles of IrO 2 or Sb–SnO 2 increase the performance of iridium oxide DSA electrodes. *Journal of Materials Science* 47, 1135–1141.

Mrozik, A., Piotrowska-Seget, Z., and Labuzek, S. (2010). Bacterial degradation and bioremediation of polycyclic aromatic hydrocarbons. *Pol. J. Environ. Stud.* 12, 15–25.

Müller, S., Sträuber, H., and Babel, W. (2012). Fate of heavy metals in a composting process. *Ann. Microbiol.* 57, 427–433.

Mulligan, C. N., Yong, R. N., and Gibbs, B. F. (2001). An evaluation of technologies for the heavy metal remediation of dredged sediments. *J. Hazard. Mater.* 85, 145–163. doi: 10.1016/S0304-3894(01)00226-6

Muthukkauppan, M., and Parthiban, P. (2018). A study on the physicochemical characteristics of tannery effluent collected from Chennai. *Int. Res. J. Eng. Technol.* 5, 24–28.

Narenkumar, J., Ramesh, N., and Rajasekar, A. (2018). Control of corrosive bacterial community by bronopol in industrial water system. *3 Biotech* 8, 1–13.

Nieto, J. J., Fernandez-Castillo, R., Garcia, M. T., Mellado, E., and Ventosa, A. (1993). Survey of antimicrobial susceptibility of moderately halophilic eubacteria and extremely halophilic aerobic archaeobacteria: utilization of antimicrobial resistance as a genetic marker. *Systematic and applied microbiology* 16, 352–360.

Nieto, J. J., Fernández-Castillo, R., Márquez, M. C., and Ventosa, A. (2000). "Halomonadaceae" in Bergey's manual of systematics of archaea and bacteria.

Parthipan, P., Preetham, E., Machuca, L. L., Rahman, P. K., Murugan, K., and Rajasekar, A. (2017). Biosurfactant and degradative enzymes mediated crude oil degradation by bacterium *Bacillus subtilis* A1. *Front. Microbiol.* 8:193. doi: 10.3389/fmicb.2017.00193

Peng, J. F., Song, Y. H., Yuan, P., Cui, X. Y., and Qiu, G. L. (2009). The remediation of heavy metals contaminated sediment. *J. Hazard. Mater.* 161, 633–640. doi: 10.1016/j.jhazmat.2008.04.061

Prakash, A. A., Rajasekar, A., Sarankumar, R. K., AlSalhi, M. S., Devanesan, S., Aljaafreh, M. J., et al. (2021). Metagenomic analysis of microbial community and its role in bioelectrokinetic remediation of tannery contaminated soil. *J. Hazard. Mater.* 412:125133. doi: 10.1016/j.jhazmat.2021.125133

Priyadharsan, A., Ramar, K., Handayani, M., Kasilingam, T., Gnanamoorthy, G., Shaik, M. R., et al. (2024). *Hydrothermal Green Synthesis of Aloe Vera Gel-Biotemplated Iron Oxide Nanoparticles for Robust Photocatalytic Degradation of*

Raja, C. E., Anbazhagan, K., and Selvam, G. S. (2020). Bioremediation of heavy metals from contaminated soil using *Pseudomonas* species. *Indian J. Exp. Biol.* 58, 55–62.

Ravindran, A., Sajayan, A., Priyadharshini, G. B., Selvin, J., and Kiran, G. S. (2020). Revealing the efficacy of thermostable biosurfactant in heavy metal bioremediation and surface treatment in vegetables. *Front. Microbiol.* 11:222. doi: 10.3389/fmicb.2020.00222

Ren, L., Lu, H., He, L., and Zhang, Y. (2014). Enhanced electrokinetic technologies with oxidization-reduction for organically-contaminated soil remediation. *Chem. Eng. J.* 217, 111–124. doi: 10.1016/j.cej.2014.02.107

Rodrigues, L. R., Teixeira, J. A., Van Der Mei, H. C., and Oliveira, R. (2006). Isolation and partial characterization of a biosurfactant produced by *Streptococcus thermophilus* A. *Colloids Surf. B* 53, 105–112. doi: 10.1016/j.colsurfb.2006.08.009

Sathish, S., Kumar, K. S. U. S., Prabu, D., Karthikeyan, M. D. V., et al. (2024). Metal organic framework anchored onto biowaste mediated carbon material (rGO) for remediation of chromium (VI) by the photocatalytic process. *Chemosphere* 357:141963. doi: 10.1016/j.chemosphere.2024.141963

Sathishkumar, K., Sathiyaraj, S., Parthipan, P., Akhil, A., Murugan, K., and Rajasekar, A. (2017). Electrochemical decolorization of methyl red by RuO2-IrO2-TiO2 electrode and biodegradation with Pseudomonas stutzeri MN1 and Acinetobacter baumannii MN3: An integrated approach. *Chemosphere* 183, 204–211.

Santhosh, S., Abilaji, S., AlSalhi, M. S., Devanesan, S., Narenkumar, J., Rajamohan, R., et al. (2024). Remediation of azodye contaminated soil by electrokinetics. *J. Taiwan Inst. Chem. Eng.*:105262. doi: 10.1016/j.jtice.2023.105262

Sarankumar, R. K., Selvi, A., Murugan, K., and Rajasekar, A. (2020). Electrokinetic (EK) and bio-electrokinetic (BEK) remediation of hexavalent chromium in contaminated soil using alkalophilic bio-anolyte. *Indian Geotechnical Journal* 50, 330–338.

Taneja, S., Karaca, O., and Haritash, A. K. (2023). Combined effects of high voltage gradient and electrolyte conditioning on electrokinetic remediation for chromium (VI)-contaminated soils. *Rend. Fis. Acc. Lincei* 34, 635–646. doi: 10.1007/s12210-023-01159-z

Tang, J., He, J., Xin, X., Hu, H., and Liu, T. (2018). Biosurfactants enhanced heavy metals removal from sludge in the electrokinetic treatment. *Chem. Eng. J.* 334, 2579–2592. doi: 10.1016/j.cej.2017.12.010

Thiele, D. J. (1995). Metal detoxification in eukaryotic cells. Washington, DC: Crisp Data Base of National Institute of Health.

Thiripelu, P., Manjunathan, J., Revathi, M., and Ramasamy, P. (2024). Removal of hexavalent chromium from electroplating wastewater by ion-exchange in presence of Ni(II) and Zn(II) ions. *J. Water Process Eng.* 58:104815. doi: 10.1016/j.jwpe.2024.104815

Tsui, L., Paul, A., Chen, Y. T., and Tz-Chi, E. (2022). Potential mechanisms contributing to the high cadmium removal efficiency from contaminated soil by using effective microorganisms as novel electrolyte in electrokinetic remediation applications. *Environ. Res.* 215:114239. doi: 10.1016/j.envres.2022.114239

Wang, Z., He, X., Li, X., Chen, L., Tang, T., Cui, G., et al. (2023). Long-term stability and toxicity effects of three-dimensional electrokinetic remediation on chromium-contaminated soils. *Environ. Pollut.* 337:122461. doi: 10.1016/j.envpol.2023.122461

Xue, F., Yan, Y., Xia, M., Muhammad, F., Yu, L., Xu, F., et al. (2017). Electro-kinetic remediation of chromium-contaminated soil by a three-dimensional electrode coupled with a permeable reactive barrier. *RSC Adv.* 7, 54797–54805. doi: 10.1039/C7RA10913J

Yan, Y., Ling, Z., Shu, W., Huang, T., and Crane, R. (2023). Chromium removal from contaminated soil using a novel FeOx/granular activated carbon-based three-dimensional electrokinetic system. *Chem. Eng. J.* 455:140613. doi: 10.1016/j.cej.2022.140613

Yeung, A. T., and Gu, Y. Y. (2011). A review on techniques to enhance electrochemical remediation of contaminated soils. *Journal of hazardous materials* 195, 11–29.

Zhang, P., Jin, C., Sun, Z., Huang, G., and She, Z. (2016). Assessment of acid enhancement schemes for electrokinetic remediation of Cd/Pb contaminated soil. *Water, Air, & Soil Pollution* 227, 1–12.

Zhu, W., Wang, D., Li, X., and Zhao, Y. (2017). Chromium (VI) reduction by *Ochrobactrum anthropi*: mechanisms and implications for bioremediation. *Chemosphere* 173, 295–305.

Enrichment of acid-tolerant sulfide-producing microbes from an acidic pit lake

Yutong Liu[1], Jennifer L. Macalady[2], Javier Sánchez-España[3] and William D. Burgos[1]*

[1]Department of Civil and Environmental Engineering, The Pennsylvania State University, University Park, PA, United States, [2]Department of Geosciences, The Pennsylvania State University, University Park, PA, United States, [3]Department of Planetology and Habitability, Centro de Astrobiología, Spanish National Research Council (CSIC), Madrid, Spain

High concentrations of harmful metal(loid)s and extreme acidity are persistent environmental concerns in acidic pit lakes. In this study, we examine Cueva de la Mora (CM), a meromictic pit lake in the Iberian Pyrite Belt, Spain, as a model system. Our research aims to explore potential bioremediation strategies to mitigate the impacts of metal(loid)s and acidity in such environments. The major strategy applied in this research is to biologically stimulate sulfate reduction (i.e., biosulfidogenesis) in the deep layer of the lake to promote the formation of low-solubility sulfide minerals. Previous omics-based studies of CM have shown that several sulfate-reducing bacteria (SRB) taxa are present in the deep layer. However, their activities are likely limited by the availability of electron donors for sulfide production. Therefore, different amendments (glycerol, elemental sulfur, and glycerol + elemental sulfur) were tested to promote sulfide production and enrich acid-tolerant sulfide-producing microbes. Our results showed that glycerol stimulated dissimilatory sulfate reduction much faster than elemental sulfur alone, suggesting that electron donor limitations control sulfide production. Furthermore, the combined addition of glycerol and elemental sulfur (S(0)) resulted in the highest level of sulfide production. This indicates that S(0) can play a significant role as an electron acceptor in further promoting sulfide production when a suitable electron donor is present. Microbial community analysis revealed that *Desulfosporosinus acididurans*, a previously discovered acid-tolerant SRB, was enriched and became the dominant species in incubations with glycerol only (~76−96% abundance) or the combination of glycerol and S(0) (~93−99% abundance).

KEYWORDS

acidic pit lake, bioremediation, sulfate reduction, metal(loid)s removal, sulfate reducing bacteria, desulfosporosinus

Introduction

Cueva de la Mora (CM) is a meromictic (permanently stratified) acidic pit lake that originated from a mining site located in the Iberian Pyrite Belt near Huelva, Spain. Acidic pit lakes are open pits that accumulate acid mine drainage (AMD) (Geller et al., 2012). These lakes form when open-pit mining operations cease and dewatering is discontinued (Gammons et al., 2009). Oxidation of sulfide minerals, especially pyrite (FeS_2), promotes the formation of AMD such that acidic pit lakes typically contain high acidity, metal(loid)s, and sulfate (Sánchez-España et al., 2008). Environments affected by AMD often experience a decline in ecosystem value (Schippers and Sand, 1999; Olías et al., 2019). CM contains stable vertical geochemical gradients that define three distinct layers: mixolimnion, chemocline, and monimolimnion

(Sánchez-España et al., 2009). The mixolimnion (so-called *surface layer*) contains oxic water. Directly beneath this is a roughly 2-meter-thick chemocline where the oxygen concentration drops to nearly zero (Johnson and Santos, 2020). Beneath the chemocline lies the anoxic monimolimnion (referred to as the *deep layer* herafter). In terms of pH, the surface layer is approximately 2–2.5, increasing to around 3 in the chemocline, and rising to 4–4.5 in the deep layer, with minor seasonal fluctuations (Sánchez-España et al., 2009; Wendt-Potthoff et al., 2012; Ayala-Muñoz et al., 2022a; Ayala-Muñoz et al., 2022b).

The deep layer of CM poses a major environmental concern and therefore demands more focus in terms of remediation. The deep layer contains the highest concentrations of harmful metal(loid) ions, especially iron (Fe), zinc (Zn), and arsenic (As). The dominant cations and anions are Fe^{2+} and SO_4^{2-}, respectively. The concentration of Fe can reach up to 6 g/L near the pit lake bottom (with essentially no Fe(III)), while the sulfate concentration can reach 11–12 g/L (Sánchez-España et al., 2009; Falagán et al., 2015). Several other toxic metal(loid)s exceed public health standards in the deep layer. Notably, the concentration of As, a globally recognized toxic metalloid (Lindgren et al., 1984), is quite high at 15 mg/L, Zn is *ca.* 100 mg/L, and Al is *ca.* 50 mg/L (Sánchez-España et al., 2009; Ayala-Muñoz et al., 2020).

Historically, a physicochemical approach has been employed in other acidic pit lakes to remove metal ions by adding hydrated lime (Ca(OH)₂) or other alkaline solids. However, this method is costly and can generate secondary pollutants such as bulky sludge (Coulton et al., 2003; McCullough, 2008; Geller et al., 2013; Johnson and Santos, 2020). Moreover, to ensure the sustainable development of ecosystems, it is crucial to avoid alkaline chemicals like lime and sodium hydroxide (Geller et al., 2013). As an alternative, remediation through stimulating biosulfidogenesis has been considered both economical and sustainable (Geller et al., 2012; Lund and Blanchette, 2023).

Several strains of acidophilic or acid-tolerant sulfate reducers have been isolated in the past decades (Supplementary Table S1). For example, *Desulfosporosinus acididurans* was isolated from acidic sediments of the Tinto River (Sánchez-Andrea et al., 2014a), and *Desulfosporosinus acidiphilum* was isolated from a mining pond near Chessy-Les-Mines France (Alazard et al., 2010). *Desulfosporosinus metallidurans* was isolated from a tailing dam of a gold mining operation in Russia and demonstrated the ability to grow at pH as low as 4 (Panova et al., 2021). A copper-tolerant, acid-tolerant sulfate-reducing *Desulfosporosinus* species was isolated from an abandoned gold mine (Mardanov et al., 2016). The SRB genera *Desulfosporosinus* and *Desulfovibrio* were successfully enriched from Peruvian acid mine drainages with hydrogen, acetate, glycerol, or lactate as substrates (Valdez-Nuñez et al., 2022). In acidic pit lakes geographically and geologically close to CM, the SRB genus *Desulfomonile* was found to constitute more than 50% of relative abundance in the acidic pit lake located in Filón Centro (DeWeerd et al., 2015; Van der Graaf et al., 2020). Several SRB were found to be abundant in the acidic saline pit lake of Brunita Mine located at La Union (Sánchez-España et al., 2020). Additionally, *Thermodesulfobium narugense*, capable of growing at pH 4, was isolated from a hot spring in Narugo, Japan (Mori et al., 2003).

Sulfide production was rarely detected in the deep layer of CM (Diez-Ercilla et al., 2014), although sulfate reduction genes were found to be expressed in that layer (Ayala-Muñoz et al., 2022a; Ayala-Muñoz et al., 2022b). It was speculated the sulfate reduction is limited by the lack of organic matter (30 μM C as glucose) (Ayala-Muñoz et al.,

2020). While oxygen has never been detected in the deep layer of CM (10 μM detection limit), sulfide oxidases were also expressed in the deep layer (Ayala-Muñoz et al., 2022a; Ayala-Muñoz et al., 2022b), suggesting that oxygen enters the deep layer through groundwater flow and is rapidly consumed. Oxygen reduction coupled to sulfide oxidation could also help explain why sulfide minerals are rarely detected in the deep layer of CM. From a remediation perspective, promoting sulfate reduction and limiting the reoxidation of sulfide minerals should reduce risks posed by the high concentrations of metal(loid)s in the deep layer of CM. Therefore, the objectives of this research were to: (1) determine what amendments (organic C and/or elemental S) best stimulate sulfide production; and, (2) how to best overcome reoxidation of sulfide minerals.

Materials and methods

Sample collection

In October 2021, water samples were collected from a boat attached to a buoy located above the deepest part of Cueva de la Mora. A Styrofoam platform was attached to the buoy where tubing surfaced through a center hole in the platform. 34-m of 1.3-cm I.D. tubing was secured to a *ca.* 5-kg anchor to keep the tubing straight in the water column and a 1.3-cm to 1.9-cm union was used to connect the vertical tubing to the 'horizontal' tubing connected to an electric high-lift water pump and stainless-steel filter assembly. The filter assembly was 142-mm in diameter and held 0.22-μm PES filters. Photographs from the field campaign are included in Supporting Information (Supplementary Figure S1). A total of *ca.* 10 L of water was pumped through each filter before filtrate production ceased. A total of 20 biomass-laden filters were collected. After filtration, each filter was rolled and slid into a 30 mL sterile glass serum tube. Serum tubes were then filled with water from the deep layer and sealed with thick rubber stoppers and aluminum crimps. Serum tubes were purged with N_2 gas for 5 min and then over-pressurized. Serum tubes were placed in a cooler on ice and transported back to Penn State University. Upon arrival, all tubes were stored at 4°C until further use.

Media preparation and incubation setup

Media was designed to match the water chemistry of the deep layer of CM (Sánchez-España et al., 2009; Wendt-Potthoff et al., 2012; Falagán et al., 2015; Ayala-Muñoz et al., 2020). N and P were added based on cell synthesis requirements (using biomass formula of $C_5H_7O_2N_1P_{0.1}$). Media contained (per liter): 3000 mg $FeSO_4 \cdot 7H_2O$, 219 mg $CaSO_4 \cdot 2H_2O$, 202 mg $MgSO_4$, 69.5 mg NH_4Cl, 48.0 mg $ZnSO_4 \cdot 7H_2O$, 35.8 mg $MnSO_4 \cdot H_2O$, 34.0 mg $Al_2(SO_4)_3 \cdot H_2O$, 6.20 mg NaCl, 3.82 mg NaH_2AsO_4, 0.97 mg KCl, 0.82 mg $CoCl_2 \cdot 6H_2O$, 0.57 mg $NaHCO_3$, 0.43 mg $NaNO_3$, 0.37 mg $NiCl_2 \cdot 6H_2O$, 0.04 mg $CuSO_4$, 0.174 mL 1 N H_3PO_4. The medium was first prepared without the addition of $FeSO_4 \cdot 7H_2O$ and adjusted to pH 4.2. The medium was then passed through a 0.2 μm bottle-top filter to remove any undissolved solids. Subsequently, 100 mL of media was dispensed into 165 mL serum bottles (DWK Life Sciences, Millville, NJ, United States) and then purged with N_2 for 20 min using long needles submerged into the liquid. During purging, $FeSO_4 \cdot 6H_2O$

was added to the medium to avoid oxidation of Fe(II). After purging the liquid phase, the headspace was also purged for 20 min with N_2. Serum bottles containing the medium were then autoclaved at 121°C, 21 psi, for 30 min. Once cooled, the bottles were moved into an anaerobic chamber. One mL of 100x Wolfe vitamin solution (Balch and Wolfe, 1976) was added to each bottle after inoculation.

The experiment was set up with four treatments, each prepared in duplicate or quadruplicate: (1) 5 mM glycerol, (2) 5 mM glycerol combined with 5 g/L elemental sulfur, (3) 5 g/L elemental sulfur, and (4) No added substrate. Glycerol was chosen as the organic substrate and electron donor because it does not undergo deprotonation in the cells, thereby minimizing the risk of cell toxicity compared to other commonly used organic substrates, such as acetate (Pinhal et al., 2019). The glycerol stock solution (1 M) was prepared under anaerobic conditions and sterilized by autoclaving. S(0) was sterilized using a dry heat method by incubating it at 100°C in an oven for 1 h on three consecutive days. Inside the anaerobic chamber, biomass-laden filters collected at 35 m depth in CM (Ayala-Muñoz et al., 2022a; Ayala-Muñoz et al., 2022b; Falagán et al., 2015) were cut evenly into eight pie-shaped sections using sterile scissors (hereafter referred to as filter wedges). Serum bottles containing the medium were opened and the filter wedges were added as inoculum. Glycerol and/or S(0) were added to the corresponding bottles once the bottles were opened. Bottles were resealed with rubber stoppers and aluminum caps before being removed from the anaerobic chamber. Media inoculated with filter wedges are hereafter referred to as microcosms.

Microcosms were flushed with a 95:5% N_2:CO_2 mixture for 20 min to approximate dissolved inorganic concentrations in CM and vortexed for 5 min to promote the release of cells from the filter wedges into the medium. Microcosms were incubated in the dark at 18°C and shaken at 50 rpm.

Culture transfers

Microcosms were monitored regularly for changes in color and chemical composition. Microcosms were transferred to the next generation once chemical analyses confirmed substantial microbial activity. Typically, a generational transfer occurred after at least 800 µm S(-II) was measured in solution. A new generation was started by transferring 10 mL of suspension from the previous generation into 90 mL of fresh medium. Glycerol and S(0) were then added to the new microcosms as described above.

Analytical techniques

Several chemical analytes were monitored in the microcosms. Sulfide was measured using a modified Cline assay (Cline, 1969; Leavitt et al., 2016). Briefly, 0.5 mL of suspension from each microcosm was mixed with 0.5 mL of 100 mM zinc acetate. Lamotte sulfide reagents A and B (LaMotte company, Chestertown, MD) were mixed in a ratio of 80 µL to 25 µL, and then combined with the 1 mL suspension + zinc acetate for 40–60 min in the dark to digest sulfide solids. Cline-S(-II) was measured by absorbance at 670 nm using a standard curve. Sulfide standards were prepared by diluting a 1,000 ppm (31.25 µM) sodium sulfide standard solution (Aqua

Solutions Inc., TX) to concentrations of 4 µM, 1 µM, 0.5 µM, 0.25 µM, and 0.125 µM under anaerobic conditions.

Glycerol and acetate concentrations were measured using a Shimadzu HPLC model LC20-AT equipped with an HPX-87H column, a SIL 20-A autosampler, and two detectors: a Refractive Index (RI) detector (RID-20A), and a UV detector (SPD-M20A). The RI detector was used to measure glycerol and the UV detector was used to measure volatile fatty acids (VFAs) including acetate. The oven temperature was set to 65°C, with 0.005 M sulfuric acid employed as the eluent, and the column retention time was 30 min. Prior to analysis, 1 mL of suspension was filtered (0.45 µm) and acidified (5 µL 1 N H_2SO_4).

Dissolved metal(loid)s were measured using a Thermo Scientific iCAP 7,400 ICP-AES, and included Fe, Zn, Al, As, Na, Mn, Mg, and Si. Prior to analysis, 1 mL of suspension was filtered (0.45 µm) and acidified (1.5 µL 1:1 HCl:HNO_3).

The relative cell densities during the incubation were reflected by optical density at 600 nm (OD600) (Amin et al., 2017). pH was measured using a Mettler Toledo LE422 SevenExcellence micro pH electrode immersed into a plastic vial of suspension. Dissolved oxygen was measured using trace range oxygen sensor spots (FireSting TROXSP5) mounted inside the microcosms in the liquid phase with a contactless fiber optic DO detector (FireSting®-PRO) connected to PyroWorkbench software.

Thermodynamic and kinetic calculations

The maximum zero-order sulfide production rate, d[S(-II)]/dt, was used for kinetic comparisons between treatments. A zero-order rate law was used because it best fit the [S(-II)]-vs-time data and presented the simple kinetic comparison between treatments. The time period for the rate calculation started when sulfide production exceeded 0.05 mM/d and extended until production fell below 0.05 mM/d. Consequently, 2–4 time points were typically used to calculate these rates (Equation 1). The sulfide production rate was determined by:

$$\text{Sulfide production rate} \left(\mu M / d \right)$$
$$= \frac{S\left(-II\right) \text{ at the end point} - S\left(-II\right) \text{ at the starting point}}{\text{End point time} - \text{Starting point time}} \qquad (1)$$

DNA extraction and sequencing

DNA extractions were conducted in April 2022 for microcosms, and in December 2022 for filter wedges collected from CM. For microcosms, biomass was collected from 40 mL of suspension on Supor 200 Membrane Disk Filters (0.2 µm) immediately after generational transfers. DNA was also extracted directly from the circular filter collected from the field, after cutting into the same manner to produce filter wedges used to inoculate the microcosms. Quadruplicates of DNA extracts were collected and analyzed, labeled as F16_1-F16_4. Filters were added to a lysing matrix tube that underwent DNA extraction using the Qiagen DNAeasy Powerwater Kit (Qiagen, Venlo, The Netherlands) following the manufacturer's instructions. The concentration and quality of DNA extracts were measured by A260/

A280 and A260/A230, respectively (ThermoScientific NanoDrop One[C]). DNA extracts were frozen at −20°C until further use.

The V4 region of the 16S rRNA gene was amplified using 515F (5'-GTGYCAGCMGCCGCGGTAA-3′) and 806R (5'-GGACT ACNVGGGTWTCTAAT-3′) primers. PCR reactions were set up using 2 μL of extracted DNA, 11.375 μL of sterile water, 10.625 μL of Ex Taq™ master mix with 806R reverse primer and 1 μL of 515F forward barcoded primer (final concentration of 0.2 μM for each primer). The PCR thermocycler program included an initial denaturation step at 94°C for 3 min, followed by 35 cycles, each comprising 45 s at 94°C, 60 s at 50°C, and 90 s at 72°C. A final extension of amplicons was achieved by holding the reaction at 72°C for 10 min. PCR products were confirmed by analyzing the amplified products on a 2% agarose gel, with the presence of a band representing approximately 390 base pairs indicating successful amplification. The amplified region was sequenced using the Illumina MiSeq platform (250 bp paired-end with 500 bp insert) at the Wright Lab (Huntington, PA).

Bioinformatic analysis

The 16S rRNA amplicon sequences were analyzed using DADA2. Raw sequences were assembled into contigs, and unique sequences were selected after filtration. Sequences were aligned with the Silva taxonomic training data (version 132) formatted for DADA2, facilitating the classification of amplicon sequence variants (ASVs) through sequence error models (Callahan et al., 2017; Narayan et al., 2020). Relative abundances of ASVs in each microcosm were determined using rarefaction analysis at the genus level with a 0.03 cutoff. Highly abundant ASV sequences were matched against the NCBI BLAST database for species-level classification. For further analysis and visualization, output files from DADA2 and metadata files were employed in RStudio (version 4.2.2). Microbial community profiles were generated using the phyloseq package, and principal coordinate analysis (PCoA) was performed based on Bray-Curtis distances. The Shannon diversity profiles were also constructed using the phyloseq package (McMurdie and Holmes, 2013), with data visualization enhanced by the ggplot2 package.

Phylogenetic Investigation of Communities by Reconstruction of Unobserved States 2 (PICRUSt2) based on the Kyoto Encyclopedia of Genes and Genomes (KEGG) database was used to predict functional potentials of the microbial communities (Kanehisa et al., 2017; Yin and Wang, 2021). PICRUSt2 predicts the functional potential of microbial communities from 16S rRNA gene sequencing data coupled to whole genomes assumed to be representative of each taxon. PICRUSt2 uses a marker gene-based approach to infer the functional profile of a microbial community by predicting the presence of gene families and their associated functions based on the taxonomic composition of the community. PICRUSt2 calculates a dimensionless Z-score for a metabolic pathway (series of genes) or a single target gene.

Results and discussion

Sulfide production could be visually detected by noting color changes in the microcosms. High concentrations of Fe(II) (12 mM) in the medium promoted the formation of dark metal-sulfide precipitates (Supplementary Figure S2). Microcosms that contained glycerol plus elemental sulfur (Gly + S) displayed a dark color earlier than other treatments. For example, in Generation 1, the Gly + S microcosms turned dark after 8 d while the Glycerol-only (Gly) microcosms turned dark after 13 d, and only one of four replicates of the elemental sulfur-only (S(0)) microcosms turned dark after 145 d. Microcosms darkened earlier in subsequent generations suggesting enrichment and adaptation within the microbial communities. In Generations 2 and 3, the Gly + S microcosms turned dark after 3–5 d, while the Gly microcosms turned dark after 5–8 d. However, the S(0) microcosms never changed color in Generation 2 even after 180 d.

Because duplicate microcosms displayed high variability throughout all generations we present unaveraged data in Figure 1. The variability was likely caused by subtle differences in biomass quantity and/or composition of the filter wedges used as inoculum. Field collection involved rolling biomass-laden filters to fit into serum tubes for preservation and transport. We posit that biomass could have smeared onto the backside of the filters such that any 1/8th filter wedge may not have contained the same quantity of biomass. Based on 16S rRNA sequence analysis, replicate wedges from the same filter also displayed subtle differences in microbial community composition and diversity.

Sulfide production

The combination of glycerol plus S(0) best stimulated biosulfidogenesis in the microcosms (Table 1). The Gly + S microcosms had shorter lag times, produced S(-II) at faster rates, and to greater extents compared to other treatments. The Gly + S microcosms also produced more biomass (OD600) and DNA. The S(0) microcosms had the longest lag times, produced the least amount of S(-II), and grew so slowly that a third generation transfer was not completed during the experiment.

Sulfide production was accompanied by glycerol consumption, acetate accumulation, an increase in pH, and an increase in cell density (Figure 1). Changes in turbidity and color in the microcosms were typically correlated with the production of sulfide (2 μM detection limit). The zero-order rates of sulfide production were faster in the Gly + S microcosms as compared to the Gly microcosms and the S(0) microcosms. Rates of sulfide production increased in Generation 2 as compared to Generation 1, indicating enrichment and adaptation within the microbial communities. Higher sulfide concentrations were accumulated in the Gly + S microcosms (834–1,100 μM) as compared to the Gly microcosms (517–897 μM) and the S(0) microcosms (23–227 μM). Maximum sulfide concentrations also increased in Generation 2 as compared to Generation 1 (Table 1).

Based on the accumulation of acetate, glycerol was not completely mineralized in the Gly and Gly + S microcosms (Figure 1). Glycerol oxidation led to an increase in pH in Gly microcosms (from pH 4.2 up to a maximum of pH 5.83) and an increase in biomass (Table 1). The increase in pH was consistent with alkalinity production from incomplete glycerol oxidation coupled to sulfate reduction (R2 in Table 2). While even more sulfide was produced in the Gly + S microcosms, the pH did not rise as high compared to glycerol alone (from pH 4.2 up to a maximum
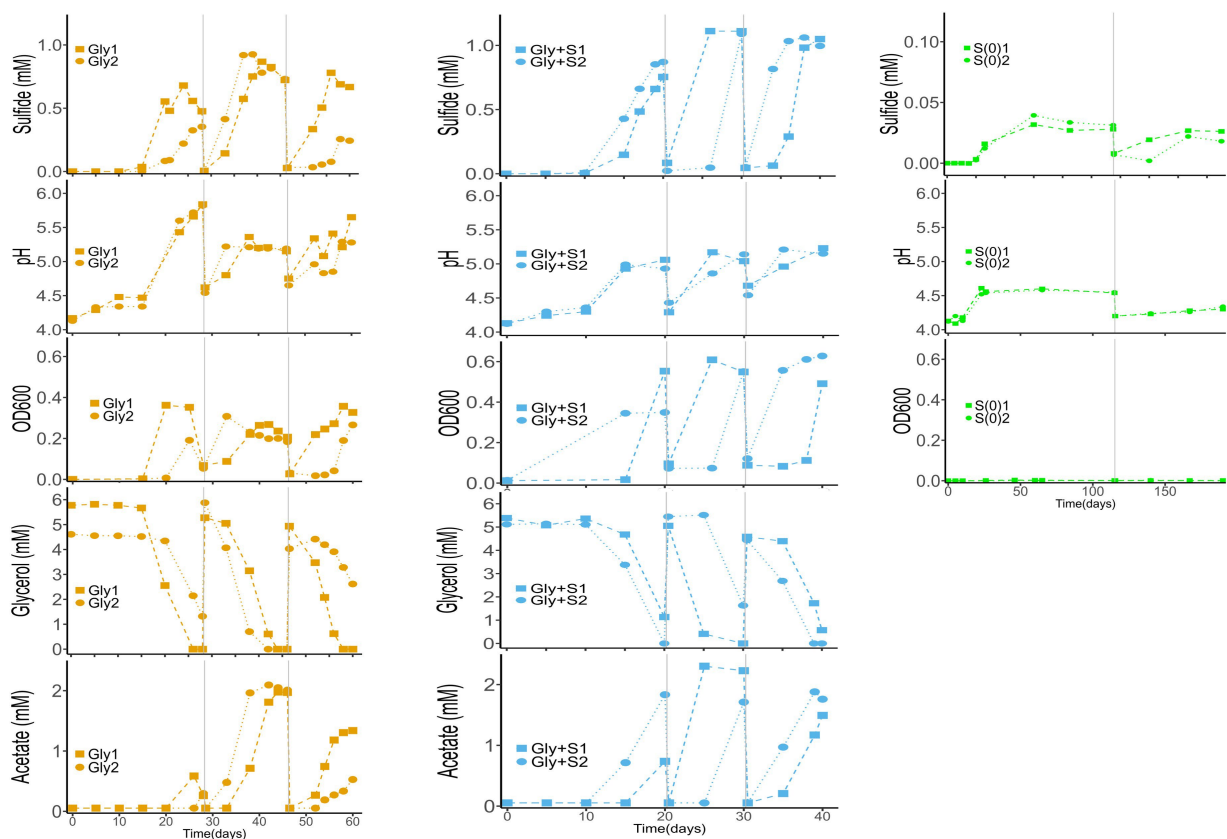
FIGURE 1
Time-course profiles of sulfide production, glycerol utilization, acetate accumulation, OD600, and pH in Gly (left), Gly + S (middle), and S(0) (right) microcosms. Vertical gray lines denote generational transfers to fresh media. In no-substrate controls, sulfide production and OD600 remained at zero, while pH remained at 4.16 ± 0.05. In uninoculated controls, sulfide production and OD600 remained at zero, pH remained at 4.20 ± 0.07, and the glycerol concentration remained at 5.00 ± 0.14 mM. Data from controls are excluded for clarity.

of pH 5.19). Because incomplete glycerol oxidation coupled to S(0) reduction (R4 in Table 2) does not produce alkalinity, measured pH changes were consistent with the utilization of both sulfate and S(0) as electron acceptors in the Gly + S microcosms. The potential toxicity of acetate (pKa = 4.76) could have been diminished by the observed increase in pH. For instance, in the Gly microcosms with a final pH of 5.5, less than 20% of ~2 mM acetate existed in the unprotonated form Pinhal et al. (2019).

Much less sulfide was produced when glycerol was absent in microcosms with added S(0) (Figure 1; Table 1), and only one out of the four S(0)-only replicates produced a substantial amount of sulfide (S-G1_4) (Supplementary Figure S3). S(0) disproportionation (R5 in Table 2) was calculated to be thermodynamically favorable at the start of the incubation (discussed in more detail below). This process produces acidity, and the pH would be expected to decrease depending on reaction extent. However, the pH increased from 4.2 up to a maximum of pH 4.88 (in S-G1_4) during incubation. This pH change could be evidence of the greater importance of endogenous decay of the biomass (i.e., oxidation of limited amount of organic carbon) as compared to S(0) disproportionation. This assumption is also supported by microbial community changes discussed below. However, this pH change does not exclude the possibility that both organic carbon oxidation and S(0) disproportionation occurred during these incubations.

Metal(loid) removal

The removal of metal(loid)s coincided with the onset of biosulfidogenesis in the microcosms (Figure 2). Arsenic, one of the most toxic elements present in the deep layer of Cueva de la Mora, was removed rapidly in microcosms provided with glycerol. Zinc was removed from solution before the removal of Fe(II), consistent with the lower solubility of ZnS (log K_{sp} = −24.7) as compared to FeS (log K_{sp} = −17.3). The As-sulfide mineral, As_2S_3 (log K_{sp} = −71.8) (Monhemius, 1977), also has a lower solubility than FeS (Diez-Ercilla et al., 2019; Diez-Ercilla et al., 2014; Kousi et al., 2011; Johnson and Sánchez-Andrea, 2019). Compared to As, less Al was removed in microcosms supplied with glycerol and considerably less Al was removed in Generations 2 and 3. The removal of Al was likely due to a slight increase in pH as the incubations progressed, leading to formation of Al-hydroxide or Al-hydroxide-sulfate minerals (Bigham and Nordstrom, 2000; Sánchez-España et al., 2016). Microcosms with only elemental sulfur (S(0)) exhibited minimal removal of metal(loid)s, consistent with their lower production of sulfide.

While mineral products were not examined in this lab study, suspended particulate matter collected from the deep layer of Cueva de la Mora during the field sampling campaign was characterized by X-ray diffraction and electron microscopy (SEM, TEM, and STEM-EDX) (Ilin, 2024). These analyses confirmed the presence of Zn, Cu,

TABLE 1 Rate and extent of sulfide generation with different treatments and through multiple generations.

Treatment	Parameter	G1	G2	G3
Gly	Lag time (days)	15, 15	4, 4	5, 6
	Maximum d[S(-II)]/dt (μM/d)	71.5, 47.1	90.5, 108	111, 50.2
	Maximum S(-II) as AVS (μM)	679, 354	867, 814	780, 256
	Max pH	5.84, 5.82	5.36, 5.21	5.65, 5.28
	DNA concentration (ng/μL)	21.4, 45.4	55.2 25.2	61.4, 104
	final OD600	0.352, 0.191	0.268, 0.231	0.357, 0.266
Gly + S	Lag time (days)	10, 10	5, 3	5, 3
	Maximum d[S(-II)]/dt (μM/d)	75.0, 93.8	171, 260	230, 164
	Maximum S(-II) as AVS (μM)	797, 871	1,100, 1,090	1,060, 1,060
	Max pH	5.06, 4.93	5.04, 5.14	5.23, 5.15
	DNA concentration (ng/μL)	53.8, 50.0	26.1, 128	102, 58.7
	final OD600	0.553, 0.349	0.549, 0.551	0.491, 0.628
S(0)	Lag time (days)	18[1], 18[2]	34[1]	
	Maximum d[S(-II)]/dt (μM/d)	0.266[1], 7.23[2]	0.314[1]	
	Maximum S(-II) as AVS (μM)	22.7[1], 276[2]	22.6[1]	
	Max pH	4.59[1], 4.88[2]	4.34[1]	
	DNA concentration (ng/μL)	3.3[1], 6.8[2]	NA[3]	
	final OD600	0.003[1], 0.133[2]	0.003[1]	

[1]The data for S(0) amended microcosms, except for S(0)-G1_4, are presented as the average of replicates in each generation. This presentation is used because the sulfide production efficiencies are consistently low among the replicates under such amendments. [2]S(0)_4 was a notable outlier among the four S(0) replicates with a greater sulfide production, higher DNA concentration, and distinct microbial community. [3]DNA extraction was not conducted for S(0)-G2, because no significant sulfide production and pH change were observed. Data for individual replicates are presented.

TABLE 2 Standard Gibbs free energy (ΔG_r^0) and Gibbs free energy under starting conditions ($\Delta G_r'$) (kJ/mol substrate) calculated for possible reactions in these experiments.

Rxn#		ΔG_r^0 (298 K)	$\Delta G_r'$ (291 K)	
R1	$C_3H_8O_3 + 1.75SO_4^{2-} + 3.5H^+ \rightarrow 1.75H_2S + 3CO_2 + 4H_2O$	−439	−408	kJ/mol glycerol
R2	$C_3H_8O_3 + 0.25SO_4^{2-} + 0.5H^+ \rightarrow 1.5CH_3COOH + 0.25H_2S + H_2O$	−214	−231	kJ/mol glycerol
R3	$C_3H_8O_3 + 7S(0) + 3H_2O \rightarrow 3CO_2 + 7H_2S$	−228	−464	kJ/mol glycerol
R4	$C_3H_8O_3 + S(0) \rightarrow 1.5CH_3COOH + H_2S$	−184	−239	kJ/mol glycerol
R5	$S(0) + H_2O \rightarrow 0.25SO_4^{2-} + 0.5H^+ + H_2S$	29.8	−7.69	kJ/mol S(0)

$\Delta G_r'$ refers to pH = 4.2; {glycerol} = $5*10^{-3}$ M, {acetate} = $5*10^{-5}$ M, {$CO_2(g)$} = 0.05 atm, {SO_4^{2-}} = 0.14 M, {$H_2S(aq)$} = 10^{-6} M, T = 18°C.

Fe, As and Pb sulfides in the water column of CM (Supplementary Figure S4). These sulfides included FeS, As₂S₃, CuS, ZnS, and a mixture interpreted as Zn(As)S. Arsenic has previously been suggested to co-precipitate with ZnS (Monte et al., 2015) such that the formation of Zn(As)S is plausible based on the timing of As and Zn loss from solution (Figure 2). The lab media used to match the water chemistry of the deep layer of CM included As, Fe, and Zn but not Cu and Pb. The removal of metal(loid)s in this lab study was consistent with field observations and confirms that microbial sulfate reduction promoted the precipitation of As, Fe, and Zn sulfides.

Stoichiometric relationships between the production of S(-II) and acetate, the consumption of glycerol and H⁺ (Figure 1), and the removal of divalent metals (Figure 2) as metal sulfides were compared to reactions proposed to occur in the microcosms (Table 2). For example, the incomplete oxidation of glycerol coupled with sulfate reduction (R2) should produce 1.5 moles of acetate and

0.5 mole of sulfide per mole of glycerol. In comparison, the incomplete oxidation of glycerol coupled with S(0) reduction (R4) should produce 1.5 moles of acetate and 1.0 mole of sulfide per mole of glycerol. Correlations between reaction products and reactants were consistent with the incomplete oxidation of glycerol in the Gly and Gly + S microcosms (Supplementary Figure S5). The potential toxicity of sulfide was likely mitigated by its removal in metal-sulfide precipitates.

Nevertheless, the Gly + S microcosms did not produce four times the amount of sulfide compared to the Gly-only microcosms, as stoichiometrically anticipated when elemental sulfur is the sole electron acceptor. This discrepancy suggests that both sulfate and elemental sulfur act as electron acceptors, with sulfate likely serving as the predominant electron acceptor.

Stoichiometric relationships between the production of S(-II) and the removal of divalent metals [i.e., $\Delta(Fe^{2+}) + \Delta(Zn^{2+})$] were consistent
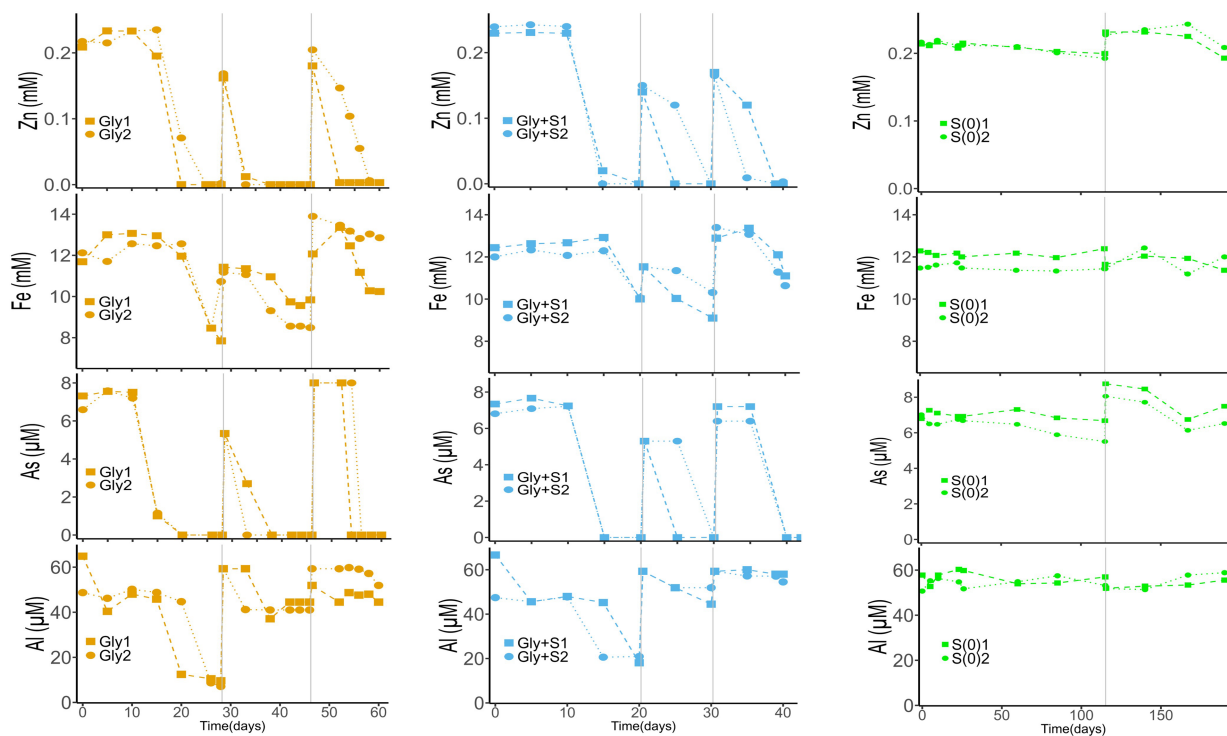
FIGURE 2
Time-course profiles of dissolved metal(loid)s in Gly (left), Gly + S (middle), and S(0) (right) microcosms. Vertical gray lines denote generational transfers to fresh media. In no-substrate controls and uninoculated controls, all metal(loid) concentrations remained unchanged. Data from controls are excluded for clarity.

with the formation of metal sulfides (1 mol S(-II)/1 mol Me^{2+}) at the start of biosulfidogenesis. However, as the incubations proceeded, sulfide continued to be produced but with little further removal of dissolved metal(loid)s (Supplementary Figure S5). Several potential explanations could account for this discrepancy between S(-II) production and Me(II) removal at later times in the incubations. First, sulfur existing in the form of S(-II) might have been transformed into S(-I) via the Berzelius reaction (Berzelius, 1814), leading to the formation of pyrite (FeS$_2$) which cannot be detected by the Cline assay. Second, sulfate may have not been fully reduced to S(-II) such that electrons donated by glycerol were coupled, e.g., only to the reduction of sulfate to sulfite. Third, the formation of greigite (Fe$_3$S$_4$) instead of mackinawite (FeS) would decrease measured S(-II) by the Cline assay because greigite is less soluble in acidic solution (Rickard and Morse, 2005). Finally, if sulfide minerals adhered to the microcosm walls, less would have been removed in suspension samples.

Bioenergetics

Gibbs free energies were calculated for the non-standard state conditions ($\Delta G_r'$) at the start of the incubations for metabolisms proposed to occur in these microcosms (Table 2). For these calculations, product and reactant concentrations and activities were based on experimental conditions used to prepare the media ({H$^+$} = 10$^{-4.2}$, [SO$_4{}^{2-}$] = 0.14 M, {S(0) (s)} = 1, [glycerol] = 5*10^{-3} M, [CO$_2$(g)] = 0.05 bar) and informed assumptions ([H$_2$S(aq)] = 10^{-6} M, [acetate] = 5*10^{-6} M). The standard state Gibbs free energy (ΔG_r^0) for incomplete glycerol oxidation coupled to

sulfate reduction (−214 kJ/mol) is more negative (i.e., more favorable) than incomplete glycerol oxidation coupled to S(0) reduction (−184 kJ/mol). However, this relationship changes mainly due to the difference in concentrations from the standard state at the start of the incubations, where $\Delta G_r'$ for incomplete glycerol oxidation coupled to S(0) reduction becomes slightly more negative (−239 kJ/mol), compared to $\Delta G_r'$ for incomplete glycerol oxidation coupled to sulfate reduction (−231 kJ/mol).

The bioenergetics of glycerol oxidation presents the simplest explanation for why sulfide was produced more rapidly, with a shorter lag time, and to a greater extent in microcosms provided with both glycerol and S(0) as compared to glycerol alone. In the Gly + S incubation, an additional electron acceptor, i.e., S(0), that provided a large free energy allowed for a second pathway for sulfide production. A slower sulfide production rate and lower sulfide production were anticipated based on the bioenergetics of S(0) disproportionation. While S(0) disproportionation is thermodynamically unfavorable under standard conditions ($\Delta_r G^0$ = +29.8 kJ/mol), this process was slightly favorable ($\Delta_r G^0$ = −7.69 kJ/mol) at the start of these incubations.

Microbial communities

Based on OD600 values and DNA concentrations (Table 2; Supplementary Table S2), the greatest amounts of biomass were produced in the Gly + S microcosms, followed by the Gly microcosms. Little biomass was produced in the S(0) microcosms but there was enough to extract sufficient amounts of DNA for sequencing the 16S rRNA gene. Biomass production followed the same trend as sulfide
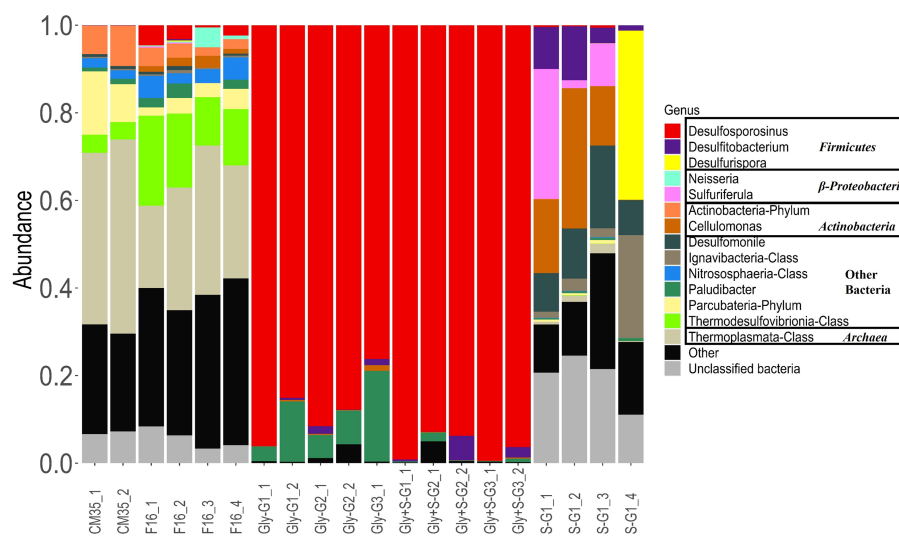
FIGURE 3
Microbial diversity at the genus-level based on 16S rRNA amplicon sequencing of microbial communities from Cueva de la Mora in May 2018(CM35) and October 2021 (F16), and from enrichment experiments with glycerol (Gly), glycerol plus elemental sulfur (Gly + S), and elemental sulfur (S). Labels _# designate replicate number, and G# designate generation number.

production. The bioenergetic-based explanation for greater sulfide production in the Gly + S microcosms is consistent with their greater biomass production.

Based on current and prior work, both the microbial community in the deep layer of CM and the microbial community on the filter wedges stored at 4°C has remained relatively stable over time. Microbial community structures in the microcosms were compared to the microbial community recovered on the filters from October 2021 and to previous samples (CM35_1 and CM35_2 in Figure 3) collected in May 2018 (Ayala-Muñoz et al., 2020). Inoculum for the microcosms in the current study were collected in October 2021 and stored at 4°C until April 2022.

In May 2018, the acidophilic archaeal order *Thermoplasmatales* (Arce-Rodríguez et al., 2019), was the most abundant, representing 39 to 44% of the community. The fermentative bacterial phylum *Parcubacteria* (Nelson and Stegen, 2015) was the most abundant bacterial group, with an abundance ranging from 8.6 to 14%. In October 2021, the relative abundance of *Thermoplasmatales* decreased to between 18 and 34%, while *Parcubacteria* decreased to between 2 and 5%. The thermophilic sulfate-reducing bacterial class *Thermodesulfovibrionia* (Willis et al., 2019) had a relative abundance of 3.9 to 4.1% in May 2018, which increased to 11 to 21% by October 2021. The relative abundance of *Desulfosporosinus* was 0.01 to 0.05% in May 2018 and 0.3 to 4.6% in October 2021. The genus *Desulfomonile* was found to be the most abundant mesophilic SRB in the deep layer in May 2018, comprising approximately 0.7% of the microbial community. In October 2021 samples, it was outcompeted by *Desulfosporosinus* in the microbial communities. This shift in dominance may have been influenced by the long-term storage at 4°C before DNA was extracted, allowing the spore-forming genus *Desulfosporosinus* to better adapt to the cold environment (Campbell and Postgate, 1965).

Based on a PCoA of the Bray Curtis pairwise dissimilarity metric of the sample ASVs, the samples from May 2018 and October 2021

clustered closely together, suggesting high similarity (Figure 4). Although we suspect that the increase in the relative abundances of certain taxa, such as *Desulfosporosinus*, was due to physiological capabilities that helped them better survive storage at 4°C, natural variability in the physico-chemical conditions over the years and even the different DNA extraction methods may also contribute to the differences among the microbial communities.

In comparison, in a study conducted at the Brunita Mine in La Unión, SE Spain, the 16S microbial community was analyzed at a relatively deep layer (17 m). Typical sulfate-reducing bacteria such as *Desulfomonile*, *Desulfosporosinus*, and *Desulfobacca* were detected exclusively at the deepest depth. The relative abundance of these bacteria was found to be similar to that observed in deep layers of CM site at 35 m. For instance, *Desulfomonile* was the most abundant SRB in both the 17 m depth at Brunita Mine and the 35 m depth at CM. *Desulfosporosinus*, although present in both the deep CM layer and the 17 m layer at Brunita Mine, had a relatively low abundance (0.05% at CM and 0.5% at Brunita). We also note that *Paludibacteraceae* and *Ignavibacteria*, though their roles remain uncertain, were found exclusively in both the 17 m depthin the deep layers at Brunita Mine and CM (Sánchez-España et al., 2020).

Filón Centro (FC), also located in the Huelva province of Spain in the southern Iberian Peninsula, was mined for copper and pyrite. Typical mesophilic SRB in acidic pit lakes, such as *Desulfomonile* and *Desulfosporosinus*, were predominantly found in the deep layer (45 m) of FC. Notably, *Desulfomonile* was still highly abundant in this deep layer, with a relative abundance of approximately 50%. Similar to the 17 m depth at Brunita Mine and the 35 m depth at CM, *Desulfosporosinus* was most abundant in the deep layer of FC, though with a low relative abundance. Additionally, *Paludibacteraceae* were detected exclusively in anoxic, sulfate-reducing conditions at FC (Van der Graaf et al., 2020).
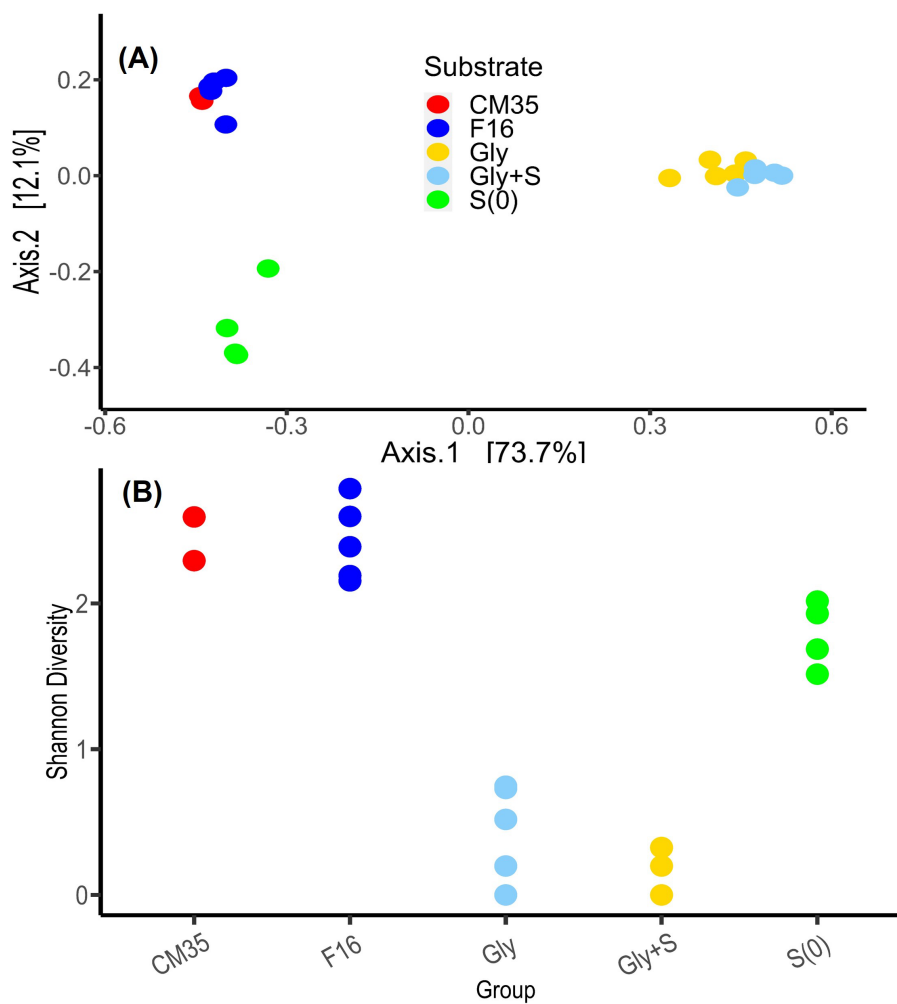
FIGURE 4
(A) Principal coordinate analysis (PCoA) of the Bray Curtis pairwise dissimilatory metric based on the ASVs from field samples and enrichment experiments. Field samples were collected from Cueva de la Mora in May 2018 (CM35) and October 2021 (F16). Enrichment experiments were conducted with glycerol (Gly), glycerol plus elemental sulfur (Gly + S), and elemental sulfur (S(0)). Each dot represents a single sample. Enrichment samples include all generations. **(B)** A comparison of the Shannon Diversity index for these same samples.

Desulfosporosinus quickly dominated all microcosms provided with glycerol (Figure 3). In these microcosms, the predominant genus was identified as *Desulfosporosinus acididurans* based on 100% similarity of 16S rRNA sequences in the V4 region to an isolate obtained from sediments in Tinto River (Sánchez-Andrea et al., 2014a). The relative abundance of *Desulfosporosinus* was 76 to 96% in the Gly microcosms and 93 to 99% in the Gly+S microcosms. *D. acididurans* is known to reduce both sulfate and S(0), and this likely explains why its relative abundance was even greater in the Gly+S microcosms. The sulfide produced was in agreement with the removal of metal(loid)s facilitated by *D. acididurans*. Rod-shaped microorganisms encrusted with metal-sulfide minerals were observed under SEM-EDS analysis (Supplementary Figure S6). *D. acididurans* is known to incompletely oxidize glycerol to acetate, consistent with chemical measurements from these incubations (Figure 1).

Desulfosporosinus is one of the few genera of SRB capable of growing under acidic conditions. Although *Desulfosporosinus* exhibited only ~0.5% relative abundance *in situ* in the deep layer of Brunita Mine, it is typically enriched once suitable organic substrates

are supplied under acidic conditions (Ilin, 2024). Among the mesophilic SRB present in the deep layers or sediments of acidic pit lakes worldwide, *Desulfosporosinus* is often predominant. For instance, in the sediment of an acidic pit lake in the Lusatian lignite mining district in Germany, *Desulfosporosinus* is significantly present and subject to enrichment (Meier et al., 2012). Similarly, in Ulan-Bulak, an acidic natural spring, *Desulfosporosinus* is found exclusively within its sediment (Gavrilov et al., 2019). Lastly, the sediment of Penn Mine, California, which produced nearly 900,000 metric tons of ore, also contains *Desulfosporosinus* exclusively in its sediment (Church et al., 2007).

Other species were also enriched in microcosms provided with glycerol. The relative abundance of the family *Paludibacteraceae* ranged from 0.8 to 3.3% in the inoculum, and increased up to 20% in the Gly microcosms, and decreased to 0.1% in the Gly+S microcosms. *Paludibacteraceae* were not detected at all in the uninoculated control (data not shown), suggesting that *Paludibacteraceae* must have come from the deep layer of CM. This phenomenon aligns with previous findings that *Paludibacteraceae* are
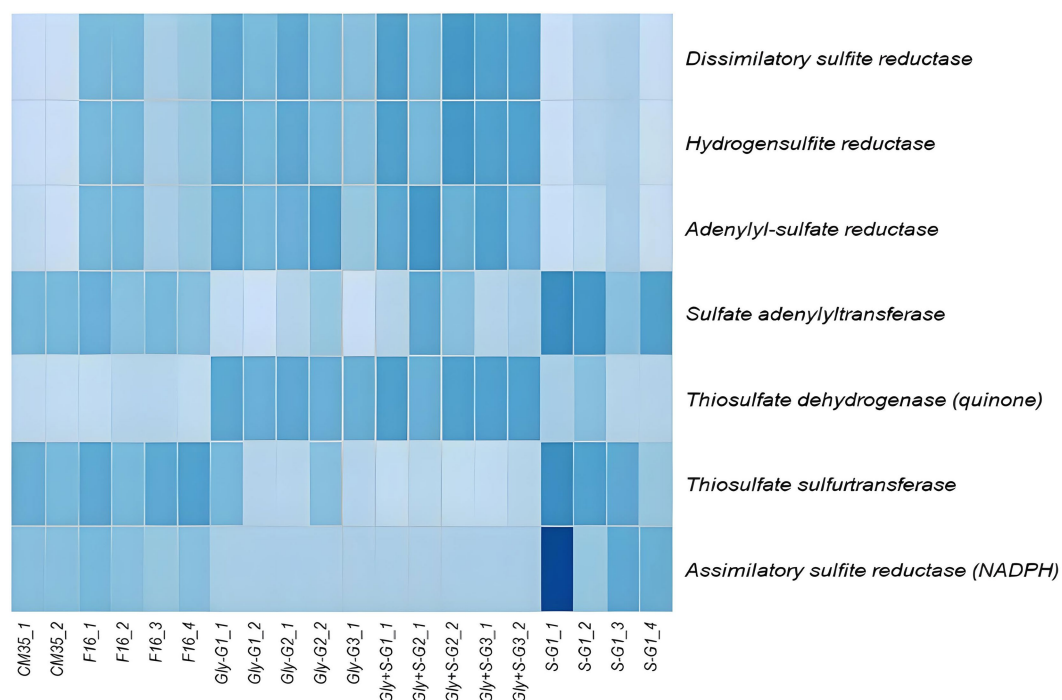
FIGURE 5
Relative abundances of genes associated with dissimilatory and assimilatory sulfate reduction, and sulfur transfer in each sample. Gene abundances were inferred using PiCRUST2 based on the 16S rRNA sequences. Darker colors represent higher relative abundance (normalized as Z-scores). As shown, darkest blue = 1.5 Z-score and lightest blue = −2 Z-score. White box for S-G1_1 for *asr* = 2.2. The darkest box for S-G1_1 for *asr* = 2.2.

consistently enriched in sulfate-reducing reactors under acidic conditions, around pH 4.5 (Liang et al., 2013; Vasquez et al., 2016; Xue et al., 2023). Further investigation revealed that the *Paludibacteraceae* identified in the microcosms are closely related to a recently isolated species, *Microbacter margulisiae,* from the sediment in the Tinto River, Spain, which is also the isolation site of *D. acididurans*. However, there is no evidence to suggest that *M. margulisiae* is directly involved in sulfate reduction (Sánchez-Andrea et al., 2014b). Moreover, the absence of significant growth of *M. margulisiae* in the Gly + S microcosms supported these findings, as elemental sulfur (S(0)), in addition to sulfate, served as the electron acceptor in these microcosms. The relative abundance of *Desulfitobacterium* was 0 to 0.3% in the inoculum, increased up to 1.3% in the Gly microcosms and up to 5.6% in the Gly + S microcosms. Despite its inability to reduce sulfate, *Desulfitobacterium* can reduce sulfite and S(0) (Villemur et al., 2006) and this could explain its greater abundance in the Gly + S microcosms. Considering *Desulfosporosinus* could produce sulfite via incomplete sulfate reduction, the increase in the relative abundance of *Desulfitobacterium* could also represent a synergistic relationship between these microbes.

The microbial communities in the Gly and Gly + S microcosms were similar to one another (Figure 4A) and both treatments yielded low Shannon Diversity indices (Figure 4B). Both results reflected the dominant enrichment of *Desulfosporosinus* when the community was provided with glycerol. This is in good agreement with recent studies which have shown conspicuous growth and clear dominance of *Desulfosporosinus* over other sulfate-reducing bacterial groups in

glycerol-amended incubation columns built with sediments of other acidic pit lakes (Ilin et al., 2022). Microcosms provided with only S(0) resulted in distinctly different microbial communities (Figure 4A) and higher Shannon Diversity indices compared to glycerol treatments (Figure 4B). Because sulfur disproportionation is almost a thermodynamically unfavorable reaction under the given conditions, and no other thermodynamically favorable substrates are available, there may be no dominant metabolism in the microcosms, leading to greater microbial diversity. In three of the four S(0)-only microcosms, prevalent species included *Cellulomonas*, *Desulfitobacterium*, *Desulfomonile*, and *Sulfuriferula*. In the one S(0)-only microcosm that produced the most sulfide, S-G1_4, *Desulfurispora* and *Ignavibacteria* were the most abundant species. *Desulfurispora* (38.6% relative abundance) was a unique species, detected at a maximum relative abundance of 0.003% in field samples (F16_2). *Desulfurispora* has been shown to reduce sulfate and S(0) although it has not been demonstrated to carry out sulfur disproportionation (Kaksonen et al., 2007). Considering that the pH increased in the S(0)-only microcosms (Figure 1), while pH should decrease during sulfur disproportionation (Table 1), sulfide production in this S(0)-only microcosm, plausibly by *Desulfurispora*, was likely coupled to the endogenous decay of cells in the inoculum.

The metabolic potential of each sample with respect to sulfur cycling were predicted from the 16S rRNA gene sequences using PICRUSt2 (Figure 5). Specifically, we queried for dissimilatory sulfur reduction genes: dissimilatory sulfite reductase (*Dsr*), hydrogen sulfite reductase (*Hsr*), adenylyl-sulfate reductase (*Apr*), sulfate adenylyltransferase (*Sad*), thiosulfate dehydrogenase (*Tsd*),

thiosulfate sulfurtransferase (*Tst*), and assimilatory sulfite reductase (*Asr*). We found that genes associated with dissimilatory sulfate reduction, including *Dsr*, *Apr*, *Hsr*, and *Tsd*, had higher inferred abundance in the Gly and Gly + S microcosms. In contrast, we found that genes associated with assimilatory sulfate reduction, including *Asr*, had higher inferred abundance in the S(0)-only microcosms. Gene communities observed *in situ* were generally more similar to those in the microcosms amended with S(0), as compared to microcosms provided with glycerol. This greater similarity likely reflected the impact of oligotrophic conditions on the *in situ* community. However, genes associated with dissimilatory sulfate reduction showed more similarity among the inoculum and the Gly and Gly + S amended microcosms, whereas genes encoding sulfur transferases (e.g., *Sad* and *Tst*) were more similarly distributed in the S(0)-amended microcosms. Genes linked to sulfur oxidation, such as sulfur oxygenase/reductase (*Sox*), were not inferred to be present in any of the samples (data not shown).

Conclusion

The removal of harmful metal(loid)s through the formation of insoluble metal-sulfide minerals by stimulating the biosulfidogenesis potential of the microbial community in the deep layer of CM has been proven feasible in small-scale lab research. Based on this study and on prior work, the activity of dissimilatory sulfate reduction in the deep layer of CM is limited by the low organic carbon concentration in the lake. Thus, supplying suitable electron donors enhances biosulfidogenesis, neutralizes the acidity by stimulating sulfate reduction, and may counteract the effects of sulfide re-oxidation by stimulating aerobic organotrophy. In this research, glycerol successfully stimulated sulfate reduction in the microcosm community. The combination of glycerol and elemental sulfur further enhanced biosulfidogenesis suggesting that S(0) is an alternative and feasible electron acceptor for sulfide-producing microbes in the deep layer of CM. However, S(0) alone was not a favorable substrate for sulfide production in the microcosms. We successfully enriched the acidophilic sulfate-reducing bacterium, *Desulfosporosinus acididurans*, from the deep layer of CM using glycerol. A greater enrichment of *D. acididurans* was achieved by providing both glycerol and S(0), consistent with the capability of *D. acididurans* to reduce both sulfate and S(0) and coincident with increased sulfide production. Because high concentrations of metal(loid)s in the deep layer of meromictic acidic pit lakes represent a great risk to surrounding environments, a targeted approach to first remediate the deep layer before attempting to remediate the whole lake could be attempted. This study demonstrates that such an approach could readily leverage the *in-situ* microbial community to achieve remediation.

Data availability statement

The data were deposited at the National Center for Biotechnology Information and can be found under the BioProject accession numbers PRJNA1141620. These BioProjects contain the raw sequences of 16S rRNA gene amplicons (SRX25540343–SRX25540362).

Author contributions

Funding

Acknowledgments

Conflict of interest

The authors declare that the research was conducted in the absence of any commercial or financial relationships that could be construed as a potential conflict of interest.

Publisher's note

All claims expressed in this article are solely those of the authors and do not necessarily represent those of their affiliated organizations, or those of the publisher, the editors and the reviewers. Any product that may be evaluated in this article, or claim that may be made by its manufacturer, is not guaranteed or endorsed by the publisher.

Supplementary material

The Supplementary material for this article can be found online at: https://www.frontiersin.org/articles/10.3389/fmicb.2024.1475137/full#supplementary-material

References

Alazard, D., Joseph, M., Battaglia-Brunet, F., Cayol, J.-L., and Ollivier, B. (2010). *Desulfosporosinus acidiphilus* sp. nov.: a moderately acidophilic sulfate-reducing bacterium isolated from acid mining drainage sediments. *Extremophiles* 14, 305–312. doi: 10.1007/s00792-010-0309-4

Amin, M., Zomorodian, S. M. A., and O'Kelly, B. C. (2017). Reducing the hydraulic erosion of sand using microbial-induced carbonate precipitation. *Proc. Inst. Civil Eng.* 170, 112–122. doi: 10.1680/jgrim.16.00028

Arce-Rodríguez, A., Puente-Sánchez, F., Avendaño, R., Martínez-Cruz, M., de Moor, J. M., Pieper, D. H., et al. (2019). Thermoplasmatales and sulfur-oxidizing bacteria dominate the microbial community at the surface water of a CO 2-rich hydrothermal spring located in Tenorio volcano National Park, Costa Rica. *Extremophiles* 23, 177–187. doi: 10.1007/s00792-018-01072-6

Ayala-Muñoz, D., Burgos, W. D., Sánchez-España, J., Couradeau, E., Falagán, C., and Macalady, J. L. (2020). Metagenomic and metatranscriptomic study of microbial metal resistance in an acidic pit lake. *Microorganisms* 8:1350. doi: 10.3390/microorganisms8091350

Ayala-Muñoz, D., Burgos, W. D., Sánchez-España, J., Falagán, C., Couradeau, E., and Macalady, J. L. (2022a). Novel microorganisms contribute to biosulfidogenesis in the deep layer of an acidic pit lake. *Front. Bioeng. Biotechnol.* 10. doi: 10.3389/fbioe.2022.867321

Ayala-Muñoz, D., Macalady, J. L., Sánchez-España, J., Falagán, C., Couradeau, E., and Burgos, W. D. (2022b). Microbial carbon, sulfur, iron, and nitrogen cycling linked to the potential remediation of a meromictic acidic pit lake. *ISME J.* 16, 2666–2679. doi: 10.1038/s41396-022-01320-w

Balch, W. E., and Wolfe, R. (1976). New approach to the cultivation of methanogenic bacteria: 2-mercaptoethanesulfonic acid (HS-CoM)-dependent growth of *Methanobacterium ruminantium* in a pressureized atmosphere. *Appl. Environ. Microbiol.* 32, 781–791. doi: 10.1128/aem.32.6.781-791.1976

Berzelius, J. J. (1814). An attempt to establish a pure scientific system of mineralogy: By the application of the electro-chemical theory and the chemical proportions. Sacramento, CA: Creative Media Partners, LLC.

Bigham, J., and Nordstrom, D. K. (2000). Iron and aluminum hydroxysulfates from acid sulfate waters. *Rev. Mineral. Geochem.* 40, 351–403. doi: 10.2138/rmg.2000.40.7

Campbell, L. L., and Postgate, J. R. (1965). Classification of the spore-forming sulfate-reducing bacteria. *Bacteriol. Rev* 29, 359–363.

Callahan, B. J., McMurdie, P. J., and Holmes, S. P. (2017). Exact sequence variants should replace operational taxonomic units in marker-gene data analysis. *ISME J.* 11, 2639–2643. doi: 10.1038/ismej.2017.119

Church, C. D., Wilkin, R. T., Alpers, C. N., Rye, R. O., and McCleskey, R. B. (2007). Microbial sulfate reduction and metal attenuation in pH 4 acid mine water. *Geochem. Trans.* 8, 1–14. doi: 10.1186/1467-4866-8-10

Cline, J. D. (1969). Spectrophotometric determination of hydrogen sulfide in natural waters 1. *Limnol. Oceanogr.* 14, 454–458. doi: 10.4319/lo.1969.14.3.0454

Coulton, R., Bullen, C., Dolan, J., Hallett, C., Wright, J., and Marsden, C. (2003). Wheal Jane mine water active treatment plant-design, construction and operation. *Land Contam. Reclam.* 11, 245–252. doi: 10.2462/09670513.821

DeWeerd, K. A., Todd Townsend, G., and Suflita, J. M. (2015). "Desulfomonile" in Bergey's Manual Systematics of Archaea and Bacteria. ed. K. A. DeWeerd (Hoboken, NJ: Wiley), 1–5.

Diez-Ercilla, M., Falagán, C., Yusta, I., and Sánchez-España, J. (2019). Metal mobility and mineral transformations driven by bacterial activity in acidic pit lake sediments: evidence from column experiments and sequential extraction. *J. Soils Sediments* 19, 1527–1542. doi: 10.1007/s11368-018-2112-2

Diez-Ercilla, M., Sánchez-España, J., Yusta, I., Wendt-Potthoff, K., and Koschorreck, M. (2014). Formation of biogenic sulphides in the water column of an acidic pit lake: biogeochemical controls and effects on trace metal dynamics. *Biogeochemistry* 121, 519–536. doi: 10.1007/s10533-014-0020-0

Falagán, C., Sánchez-España, F., Yusta, I., and Johnson, D. B. (2015). Microbial communities in sediments in acidic, metal-rich mine lakes: results from a study in south-West Spain. *Adv. Mater. Res.* 1130, 7–10. doi: 10.4028/www.scientific.net/AMR.1130.7

Gammons, C. H., Harris, L. N., Castro, J. M., Cott, P. A., and Hanna, B. W. (2009). *Creating lakes from open pit mines: Processes and considerations, emphasis on northern environments.*

Gavrilov, S. N., Korzhenkov, A. A., Kublanov, I. V., Bargiela, R., Zamana, L. V., Popova, A. A., et al. (2019). Microbial communities of polymetallic deposits' acidic ecosystems of continental climatic zone with high temperature contrasts. *Front. Microbiol.* 10:462219. doi: 10.3389/fmicb.2019.01573

Geller, W., Schultze, M., Kleinmann, B., and Wolkersdorfer, C. (2013). Acidic pit lakes: The legacy of coal and metal surface mines. Berlin: Springer Science and Business Media.

Geller, W., Schultze, M., and Wisotzky, F. (2012). "Remediation and management of acidified pit lakes and outflowing waters" in Acidic pit lakes: the legacy of coal and metal surface mines. eds. W. Geller, M. Schultze, B. Kleinmann and C. Wolkersdorfer (Berlin: Springer Science and Business Media), 225–264.

Ilin, A. M. (2024). *Microbially-mediated mineralization processes in acid mine drainage systems: Influence on metal removal* [Unpublished doctoral dissertation]. University of the Basque Country.

Ilin, A. M., Van der Graaf, C. M., Yusta, I., Sorrentino, A., Sánchez-Andrea, I., and Sánchez-España, J. (2022). Glycerol amendment enhances biosulfidogenesis in acid mine drainage-affected areas: an incubation column experiment. *Front. Bioeng. Biotechnol.* 10:728. doi: 10.3389/fbioe.2022.978728

Johnson, D. B., and Sánchez-Andrea, I. (2019). Dissimilatory reduction of sulfate and zero-valent sulfur at low pH and its significance for bioremediation and metal recovery. *Adv. Microb. Physiol.* 75, 205–231. doi: 10.1016/bs.ampbs.2019.07.002

Johnson, B., and Santos, A. L. (2020). "Biological removal of sulfurous compounds and metals from inorganic wastewaters" in Environmental technologies to treat sulfur pollution: Principles and engineering. ed. B. Johnson (London: IWA Publishing), 215–246.

Kaksonen, A. H., Spring, S., Schumann, P., Kroppenstedt, R. M., and Puhakka, J. A. (2007). *Desulfurispora thermophila* gen. Nov., sp. nov., a thermophilic, spore-forming sulfate-reducer isolated from a sulfidogenic fluidized-bed reactor. *Int. J. Syst. Evol. Microbiol.* 57, 1089–1094. doi: 10.1099/ijs.0.64593-0

Kanehisa, M., Furumichi, M., Tanabe, M., Sato, Y., and Morishima, K. (2017). KEGG: new perspectives on genomes, pathways, diseases and drugs. *Nucleic Acids Res.* 45, D353–D361. doi: 10.1093/nar/gkw1092

Kousi, P., Remoundaki, E., Hatzikioseyian, A., Battaglia-Brunet, F., Joulian, C., Kousteni, V., et al. (2011). Metal precipitation in an ethanol-fed, fixed-bed sulphate-reducing bioreactor. *J. Hazard. Mater.* 189, 677–684. doi: 10.1016/j.jhazmat.2011.01.083

Leavitt, W. D., Venceslau, S. S., Pereira, I. A., Johnston, D. T., and Bradley, A. S. (2016). Fractionation of sulfur and hydrogen isotopes in *Desulfovibrio vulgaris* with perturbed DsrC expression. *FEMS Microbiol. Lett.* 363:fnw226. doi: 10.1093/femsle/fnw226

Liang, F., Xiao, Y., and Zhao, F. (2013). Effect of pH on sulfate removal from wastewater using a bioelectrochemical system. *Chem. Eng. J.* 218, 147–153. doi: 10.1016/j.cej.2012.12.021

Lindgren, A., Danielsson, B. R., Dencker, L., and Vahter, M. (1984). Embryotoxicity of arsenite and arsenate: distribution in pregnant mice and monkeys and effects on embryonic cells in vitro. *Acta Pharmacol. Toxicol.* 54, 311–320. doi: 10.1111/j.1600-0773.1984.tb01936.x

Lund, M. A., and Blanchette, M. L. (2023). Closing pit lakes as aquatic ecosystems: risk, reality, and future uses. *Wiley Interdisc. Rev. Water* 10:e1648. doi: 10.1002/wat2.1648

Mardanov, A. V., Panova, I. A., Beletsky, A. V., Avakyan, M. R., Kadnikov, V. V., Antsiferov, D. V., et al. (2016). Genomic insights into a new acidophilic, copper-resistant Desulfosporosinus isolate from the oxidized tailings area of an abandoned gold mine. *FEMS Microbiol. Ecol.* 92:111. doi: 10.1093/femsec/fiw111

McCullough, C. D. (2008). Approaches to remediation of acid mine drainage water in pit lakes. *Int. J. Min. Reclam. Environ.* 22, 105–119. doi: 10.1080/17480930701350127

McMurdie, P. J., and Holmes, S. (2013). Phyloseq: an R package for reproducible interactive analysis and graphics of microbiome census data. *PLoS One* 8:e61217. doi: 10.1371/journal.pone.0061217

Meier, J., Piva, A., and Fortin, D. (2012). Enrichment of sulfate-reducing bacteria and resulting mineral formation in media mimicking pore water metal ion concentrations and pH conditions of acidic pit lakes. *FEMS Microbiol. Ecol.* 79, 69–84. doi: 10.1111/j.1574-6941.2011.01199.x

Monhemius, A. (1977). *Precipitation diagrams for metal hydroxides, sulphides, arsenates and phosphates.*

Monte, C. N., Rodrigues, A. P., Cordeiro, R. C., Freire, A. S., Santelli, R. E., and Machado, W. (2015). Changes in cd and Zn bioavailability upon an experimental resuspension of highly contaminated coastal sediments from a tropical estuary. *Sustain. Water Resour. Manag.* 1, 335–342. doi: 10.1007/s40899-015-0034-3

Mori, K., Kim, H., Kakegawa, T., and Hanada, S. (2003). A novel lineage of sulfate-reducing microorganisms: Thermodesulfobiaceae fam. Nov., *Thermodesulfobium narugense*, gen. Nov., sp. nov., a new thermophilic isolate from a hot spring. *Extremophiles* 7, 283–290. doi: 10.1007/s00792-003-0320-0

Narayan, N. R., Weinmaier, T., Laserna-Mendieta, E. J., Claesson, M. J., Shanahan, F., Dabbagh, K., et al. (2020). Piphillin predicts metagenomic composition and dynamics from DADA2-corrected 16S rDNA sequences. *BMC Genomics* 21, 1–12. doi: 10.1186/s12864-019-6427-1

Nelson, W. C., and Stegen, J. C. (2015). The reduced genomes of Parcubacteria (OD1) contain signatures of a symbiotic lifestyle. *Front. Microbiol.* 6:144940. doi: 10.3389/fmicb.2015.00713

Olías, M., Cánovas, C., Basallote, M., Macías, F., Pérez-López, R., González, R. M., et al. (2019). Causes and impacts of a mine water spill from an acidic pit lake (Iberian Pyrite Belt). *Environ. Pollut.* 250, 127–136. doi: 10.1016/j.envpol.2019.04.011

Panova, I. A., Ikkert, O., Avakyan, M. R., Kopitsyn, D. S., Mardanov, A. V., Pimenov, N. V., et al. (2021). *Desulfosporosinus metallidurans* sp. nov., an acidophilic, metal-resistant sulfate-reducing bacterium from acid mine drainage. *Int. J. Syst. Evol. Microbiol.* 71:4876. doi: 10.1099/ijsem.0.004876

Pinhal, S., Ropers, D., Geiselmann, J., and De Jong, H. (2019). Acetate metabolism and the inhibition of bacterial growth by acetate. *J. Bacteriol.* 201, e00147–e00119. doi: 10.1128/JB.00147-19

Rickard, D., and Morse, J. W. (2005). Acid volatile sulfide (AVS). *Mar. Chem.* 97, 141–197. doi: 10.1016/j.marchem.2005.08.004

Sánchez-Andrea, I., Sanz, J. L., Bijmans, M. F., and Stams, A. J. (2014a). Sulfate reduction at low pH to remediate acid mine drainage. *J. Hazard. Mater.* 269, 98–109. doi: 10.1016/j.jhazmat.2013.12.032

Sánchez-Andrea, I., Sanz, J. L., and Stams, A. J. (2014b). *Microbacter margulisiae* gen. Nov., sp. nov., a propionigenic bacterium isolated from sediments of an acid rock drainage pond. *Int. J. Syst. Evol. Microbiol.* 64, 3936–3942. doi: 10.1099/ijs.0.066241-0

Sánchez-España, J., Pamo, E. L., Diez, M., and Santofimia, E. (2009). Physico-chemical gradients and meromictic stratification in Cueva de la Mora and other acidic pit lakes of the Iberian Pyrite Belt. *Mine Water Environ.* 28, 15–29. doi: 10.1007/s10230-008-0059-z

Sánchez-España, J., Pamo, E. L., Pastor, E. S., and Ercilla, M. D. (2008). The acidic mine pit lakes of the Iberian Pyrite Belt: an approach to their physical limnology and hydrogeochemistry. *Appl. Geochem.* 23, 1260–1287. doi: 10.1016/j.apgeochem.2007.12.036

Sánchez-España, J., Yusta, I., and Burgos, W. D. (2016). Geochemistry of dissolved aluminum at low pH: Hydrobasaluminite formation and interaction with trace metals, silica and microbial cells under anoxic conditions. *Chem. Geol.* 441, 124–137. doi: 10.1016/j.chemgeo.2016.08.004

Sánchez-España, J., Yusta, I., Ilin, A., van der Graaf, C., and Sánchez-Andrea, I. (2020). Microbial geochemistry of the acidic saline pit lake of Brunita mine (La Unión, SE Spain). *Mine Water Environ.* 39, 535–555. doi: 10.1007/s10230-020-00655-0

Schippers, A., and Sand, W. (1999). Bacterial leaching of metal sulfides proceeds by two indirect mechanisms via thiosulfate or via polysulfides and sulfur. *Appl. Environ. Microbiol.* 65, 319–321. doi: 10.1128/AEM.65.1.319-321.1999

Valdez-Nuñez, L. F., Ayala-Muñoz, D., Sánchez-España, J., and Sánchez-Andrea, I. (2022). Microbial communities in Peruvian acid mine drainages: low-abundance sulfate-reducing Bacteria with high metabolic activity. *Geomicrobiol J.* 39, 867–883. doi: 10.1080/01490451.2022.2087808

Van der Graaf, C. M., Sánchez-España, J., Yusta, I., Ilin, A., Shetty, S. A., Bale, N. J., et al. (2020). Biosulfidogenesis mediates natural attenuation in acidic mine pit lakes. *Microorganisms* 8:1275. doi: 10.3390/microorganisms8091275

Vasquez, Y., Escobar, M. C., Neculita, C. M., Arbeli, Z., and Roldan, F. (2016). *Microbial community dynamics during the biochemical treatment of acid mine drainage under three different hydraulic retention times.*

Villemur, R., Lanthier, M., Beaudet, R., and Lépine, F. (2006). The desulfitobacterium genus. *FEMS Microbiol. Rev.* 30, 706–733. doi: 10.1111/j.1574-6976.2006.00029.x

Wendt-Potthoff, K., Koschorreck, M., Ercilla, M. D., and España, J. S. (2012). Microbial activity and biogeochemical cycling in a nutrient-rich meromictic acid pit lake. *Limnologica* 42, 175–188. doi: 10.1016/j.limno.2011.10.004

Willis, G., Nancucheo, I., Hedrich, S., Giaveno, A., Donati, E., and Johnson, D. B. (2019). Enrichment and isolation of acid-tolerant sulfate-reducing microorganisms in the anoxic, acidic hot spring sediments from Copahue volcano, Argentina. *FEMS Microbiol. Ecol.* 95:fiz175. doi: 10.1093/femsec/fiz175

Xue, J., Yao, Y., Li, W., Shi, K., Ma, G., Qiao, Y., et al. (2023). Insights into the effects of operating parameters on sulfate reduction performance and microbial pathways in the anaerobic sequencing batch reactor. *Chemosphere* 311:137134. doi: 10.1016/j.chemosphere.2022.137134

Yin, Y., and Wang, J. (2021). Predictive functional profiling of microbial communities in fermentative hydrogen production system using PICRUSt. *Int. J. Hydrog. Energy* 46, 3716–3725. doi: 10.1016/j.ijhydene.2020.10.246

Bioleaching of lithium from jadarite, spodumene, and lepidolite using *Acidiothiobacillus ferrooxidans*

Rebecca D. Kirk[1]*, Laura Newsome[1], Carmen Falagan[1,2] and Karen A. Hudson-Edwards[1]

[1]Environment and Sustainability Institute and Camborne School of Mines University of Exeter, Cornwall, United Kingdom, [2]School of Environment and Life Sciences, University of Portsmouth, Portsmouth, United Kingdom

Lithium (Li) is becoming increasingly important due to its use in clean technologies that are required for the transition to net zero. Although acidophilic bioleaching has been used to recover metals from a wide range of deposits, its potential to recover Li has not yet been fully explored. In this study, we used a model Fe(II)- and S-oxidising bacterium, *Acidiothiobacillus ferrooxidans* (At. Ferrooxidans), to extract Li from three different minerals and kinetic modelling to predict the dominant reaction pathways for Li release. Bioleaching of Li from the aluminosilicate minerals lepidolite (K(Li,Al)$_3$(Al,Si,Rb)$_4$O$_{10}$(F,OH)$_2$) and spodumene (LiAl(Si$_2$O$_6$)) was slow, with only up to 14% (approximately 12 mg/L) of Li released over 30 days. By contrast, *At. ferrooxidans* accelerated Li leaching from a Li-bearing borosilicate clay (jadarite, LiNaB$_3$SiO$_7$OH) by over 50% (over 120mg/L) in 21days of leaching, and consistently enhanced Li release throughout the experiment compared to the uninoculated control. Biofilm formation and flocculation of sediment occurred exclusively in the experiments with *At. ferrooxidans* and jadarite. Fe(II) present in the jadarite-bearing clay acted as an electron donor. Chemical leaching of Li from jadarite using H2SO4 was most effective, releasing approximately 75% (180 mg/L) of Li, but required more acid than bioleaching for pH control. Kinetic modelling was unable to replicate the data for jadarite bioleaching after primary abiotic leaching stages, suggesting additional processes beyond chemical leaching were responsible for the release of Li. A new crystalline phase, tentatively identified as boric acid, was observed to form after acid leaching of jadarite. Overall, the results demonstrate the potential for acidophilic bioleaching to recover Li from jadarite, with relevance for other Li-bearing deposits.

1 Introduction

Lithium (Li) is the lightest alkali metal in group one of the periodic table and has a wide range of applications from metallurgy and electrochemistry to medicine (Talens Peiró et al., 2013). It was added to the EU Critical Raw Materials list in 2017 (European Commission, 2017), and its demand increased by over 60% between 2019 and 2024 due to its use in technologies to aid in the energy transition to net zero, such as Li-ion batteries for vehicles (Greim et al., 2020; European Commission, 2017). The global maximum annual extraction demand for Li has been projected to increase to approximately 12 times the current demand by 2050 (Junne et al., 2020).

Li is found in a range of geological deposits, with closed-basin brines such as salars, estimated to represent 50–60% of the current estimated global resources. Pegmatites and Li enriched

GRAPHICAL ABSTRACT
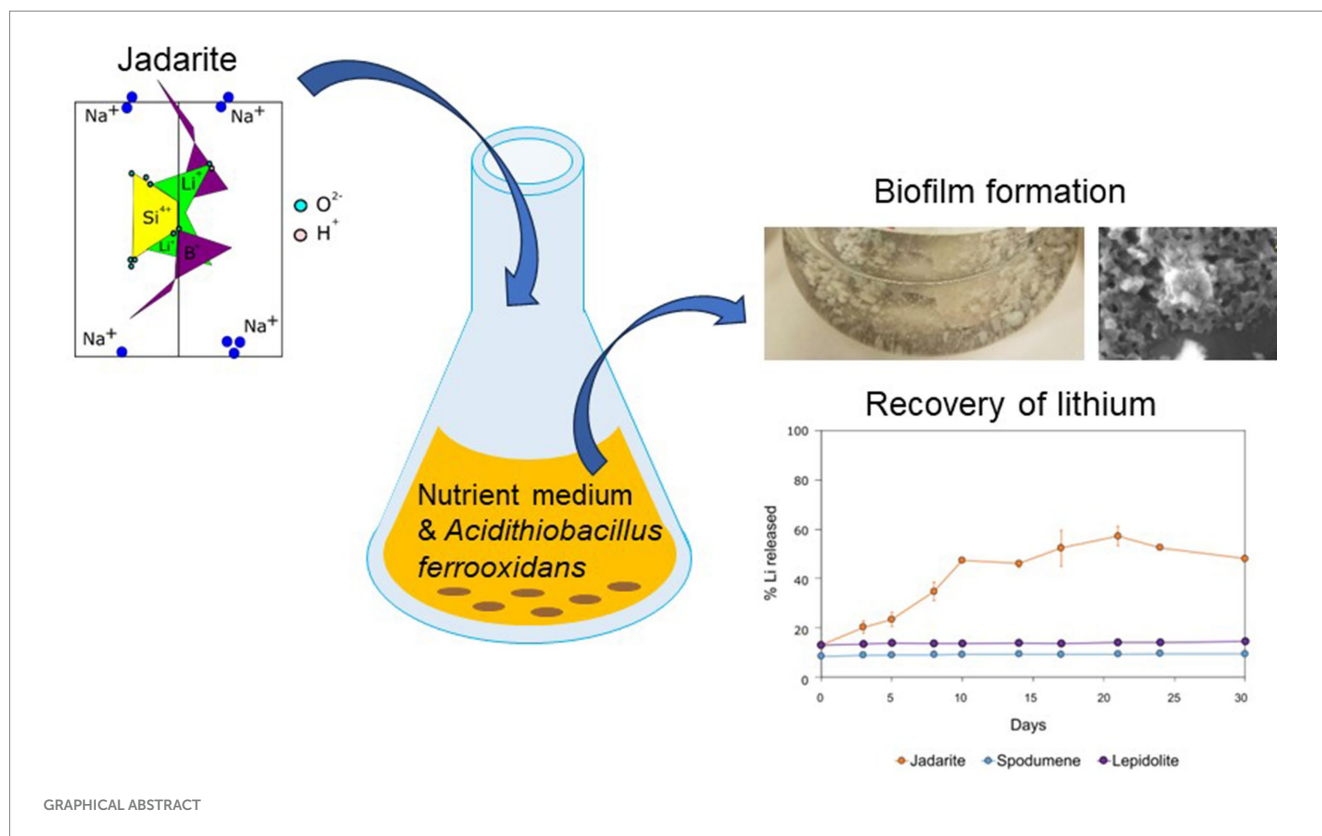
granites provide approximately 26%, Li clays 7% and Li-zeolites such as jadarite ($LiNaB_3SiO_7$) account for 3% (Jaskula, 2023; USGS Commodity Statistics, 2014). While Li concentrations in most terrestrial rocks are up to 60 mg/kg, high-concentration ore deposits such as pegmatites contain up to 8,000 mg/kg (Bradley et al., 2017; Cipollina et al., 2022) The highest concentrations of Li are seen in LCT-pegmatites (lithium, caesium, and tantalum); these deposits are a subset of granitic pegmatites containing spodumene ($LiAl(Si_2O_6)$) and/or lepidolite ($K(Li,Al)_3(Al,Si,Rb)_4O_{10}(F,OH)_2$) (Bradley et al., 2010). Jadarite may also become a significant source of Li; it is expected that from the Jadar deposit alone [Li-B deposit located in the Jadar Valley, Serbia (Stanley et al., 2007)], up to 1.6 million tons of Li could be extracted (Siljkovic et al., 2017). However, concerns with spatial planning, environmental impacts, and local politics are affecting project progression (Stefanović et al., 2023).

The main techniques used for Li recovery of spodumene and lepidolite are froth flotation and acid leaching. The flotation method involves preparing mineral pulps by adding deionised water adjusted to low pH with fatty acid collectors and flotation reagents such as $CaCl_2$ that separate the minerals of interest (Xie et al., 2021), with Li_2O yields of approximately 7.25% (Cerny et al., 1996). The acid leaching method uses high temperature, high-pressure roasting, and sulfuric acid (H_2SO_4) to recover Li from ores. This method can extract over 90% of the total Li from ores (Gao et al., 2020). These are energy-intensive processes with negative environmental consequences such as carbon emissions, water loss, ground destabilisation, ecosystem degradation, biodiversity loss, contaminated soil, and toxic waste. With the demand for Li increasing, the need to maximise each resource is paramount (Siezen and Wilson, 2009; Vera et al., 2022). Extraction techniques for materials such as jadarite are poorly documented in the literature, but low-temperature acid leaching methods may be suitable for Li release, depending on the chemical structure of the mineral.

Bioleaching involves using microorganisms to recover metals from minerals and rocks (Cerny et al., 1996). Chemolithoautotrophic organisms that can oxidise ferrous iron (Fe) or reduced inorganic sulphur compounds (RISCs), such as $S°$, $S_2O_3^{2-}$, and $S_4O_6^{2-}$, as electron donors (Siezen and Wilson, 2009) are used to generate acidity, which causes the release of metals within the mineral into solution or causes the metals to become fixed onto produced biomass or extracellular polymers in the system (Vera et al., 2022). These reactions are normally carried out at low pH (1–3) and have been highly successful in the bioleaching of sulphides for the extraction of copper (Cu) (Ristović et al., 2022). In materials containing low concentrations of reduced S and Fe(II), other microbes such as heterotrophs can be used for bioleaching. This involves the formation of organic acids and complexes that enhance metal release (Rezza et al., 2001); this process can be carried out over a wider pH range and can be manipulated for more alkali-rich materials such as battery wastes (Bahaloo-Horeh et al., 2018).

Leaching of Li from spodumene and lepidolite by fungi and heterotrophic bacteria has been investigated, with limited success. The results of these studies suggest that aluminosilicate structure may be a key control on the extent of leaching, and that biomechanical activity can play an important role (Rezza et al., 2001; Marcinčáková et al., 2015). Lepidolite bioleaching experiments caused the loss of muscovite, and fungal bioleaching led to the formation of a new silicate (quartz (SiO_2)) phase identified through X-ray diffraction (Sedlakova-Kadukova et al., 2020; Liu et al., 2019). The biomechanical activity of microorganisms may be significant, as observed from fungal hyphae penetration of lepidolite colonised by *Aspergillus niger* (Rezza et al., 2001). Up to 95% of Li was recovered when bioleaching spent Li-ion batteries with *A. niger* (Horeh et al., 2016).

Acidophilic bioleaching by chemolithoautotrophs has previously been investigated for the recovery of Li from spodumene and

lepidolite, as well as e-wastes and spent batteries (Roy et al., 2021). Up to 10% of the total Li was recovered when *At. ferrooxidans* was used to bioleach spent Li-ion batteries with data suggesting indirect bioleaching through acid generation as the predominant mechanism of metal release (Mishra et al., 2008; Moazzam et al., 2021). However, lepidolite bioleaching has been shown to be slow, and H_2SO_4 leaching has been proposed to be more effective (Liu et al., 2019). The first reported application of autotrophic bacteria (a mixed culture of mesophilic S-oxidising bacteria including high concentrations of *Acidiothiobacilli*) used in bioleaching was for zinnwaldite $(KLiFeAl(AlSi_3)O_{10}(F,OH)_2)$. In these experiments, 11 and 26% Li recovery was reported for batch and bioreactor experiments, respectively (Rezza et al., 2001). Bioleaching of Li from jadarite, mine waste, and mixed sediments is yet to be investigated.

A study comparing the bioleaching of Li by acidophiles and fungi reported up to $11\,mg\,l^{-1}$ Li dissolved from lepidolite using a consortium of *At. ferrooxidans* and *Acidothiobacillus thiooxidans* equating to up to 8.8% recovery, with limited intracellular accumulation or extracellular fixation of Li observed. The *At. ferrooxidans* and *At. thiooxidans* consortium was more effective than *R. mucilaginosa* or *A. niger* for which only 1.1% of Li and 0.2% of Li were recovered, respectively. (Sedlakova-Kadukova et al., 2020; Roy et al., 2021).

The effectiveness of bioleaching by heterotrophic organisms, including bacteria and fungi such as *A. niger* is believed to depend on the presence of organic acids, which solubilise the minerals (Müller et al., 1995; Vandevivere et al., 1994). The results of spodumene leaching by *A. niger, R. rubra,* and *Penicillium purporogenum* showed adaptation of *R. rubra* and *P. purporogemum* to extreme, low nutrient environments that also contributed to Li release (Rezza et al., 1997).

The effects of deposit type and mineral structure on Li release through bioleaching are poorly understood, but identifying these may aid optimisation and choice of Li extraction method based on the chemical structure of the Li mineral. There are few data available on Li extraction from jadarite using conventional or bioleaching methods. In this study, a simple bioleaching mechanism containing *At. ferrooxidans* was used to investigate Li bioleaching from three deposit types via the oxidation of natural Fe presence within the minerals, compared to uninoculated controls. Through comparison with H_2SO_4 leaching, this study aims to outline the feasibility of bioleaching compared to conventional well-optimised leaching methods. Similarly, this study provides the initial data to understand Li leaching from jadarite through acid leaching and bioleaching methods. By adaptation of the shrinking core kinetic model, the results can be modelled to confirm the influence of bacteria in each reactive system compared to abiotic and acidic counterparts and therefore confirm whether the presence of *At. ferrooxidans* is necessary in leaching experiments. These data can be used to determine Li deposit types where exploration of bioleaching is worthwhile and to provide initial data on Li release from jadarite through both acid chemical leaching and bioleaching (Liddell, 2005).

2 Materials and methods

2.1 Minerals

The bioleaching of spodumene, lepidolite, and jadarite was investigated in this study. Samples of spodumene and lepidolite were

collected from the Bikita mine (Zimbabwe) and donated by the British Geological Survey for the purpose of this study. Jadarite concentrate was collected from Jadar Valley (Serbia) and donated by the Natural History Museum, London. Spodumene makes up approximately 25% of the global Li resource, occurs in economically viable deposit grades (Swain, 2017), and is the most abundant and frequently mined Li-bearing mineral. Lepidolite also occurs in concentrations economically viable for extraction and hence has an established industry associated with it (Gao et al., 2023). The chemical structure of lepidolite is much more complex than that of spodumene (Lin et al., 2024). Jadarite is a less well-understood Li-bearing mineral that is not currently mined nor has an established extraction method. Jadarite has a very different chemical structure from spodumene and lepidolite, meaning that by comparing the three mineral types, the effect of chemical structure can be assessed. This provides a contrast between traditionally mined Li minerals and the novel jadarite borosilicate mineral to compare the effectiveness of bioleaching on these ore types.

Samples were acquired as dry consolidated rocks and sediments. They were characterised by grinding to approximately $0.5\,\mu m$ using a Siebtechnik grinding mill, then analysed using X-ray diffraction (Siemens D5000 XRD) with the EVA identification software and database for spodumene and lepidolite, and against a reference jadarite spectra for the jadarite sediment. For bulk chemistry, $0.1\,g$ of the samples were digested in an $HF/HCl/HNO_3/HClO_4$ mix (4-acid digest) at $180°C$ (Garbe-Schonberg, 1993), made up to $50\,mL$ using Milli Q DI water [resistivity $18.2\,M\Omega \cdot cm$ @ $25°C$; total organic carbon (TOC) $\leq 5\,ppb$ (Merck, 2023)] and analysed using an ICP-OES (Agilent 5110 VDV Inductively Coupled Plasma—Optical Emission Spectrometer). A ferrozine assay was used to estimate the proportion of bioavailable Fe(II) and Fe(III) in the materials using HCl-extractable Fe (Lovley and Phillips, 1986).

2.2 Microorganisms

The bacterium *At. ferrooxidans* was used in the experiments due to its documented success in Li bioleaching compared to other microorganisms (Sedlakova-Kadukova et al., 2020). This was obtained from an in-lab culture obtained from a mined ore (H2020-Nemo, n.d.). Cultures were maintained in a basal salt containing $7.5\,g\,L^{-1}$ $(NH_4)_2SO_4$, $7.5\,g\,L^{-1}$ $Na_2SO_4.10H_2O$, $2.5\,g\,L^{-1}$ KCl, $25\,g\,L^{-1}$ $MgSO_4$, $2.5\,g\,L^{-1}$ KH_2PO_4, and $0.7\,g\,L^{-1}$ $Ca(NO_3)_2$ and a trace element solution (Ñancucheo et al., 2016) supplemented with $25\,mM$ $FeSO_4$ solution, adjusted to pH 1.8 using $5.5\,M$ H_2SO_4. Cultures were grown in $50\,mL$ of media at $28°C$ and $180\,rpm$. Cultures were maintained by subculturing in fresh media supplemented with $25\,mM$ $FeSO_4$ biweekly.

2.3 Bioleaching experiments and geochemical monitoring

Powdered mineral $(2\,g)$ was added to $190\,mL$ of basal medium at pH 1.8 (adjusted with $5.5\,M$ H_2SO_4) at 2% w/v concentration in sterile $250\,mL$ conical flasks. These 'bioleaching (biotic)' experiments were inoculated with $10\,mL$ of *At. ferrooxidans* (from stock grown for 14 days prior to inoculation), sealed with a foam stopper and foil cap

to allow only airflow. These were left static to mimic heap leaching conditions at 23°C in a Thermo Scientific Heratherm incubator. All biotic experiments were conducted in triplicate. To quantify the role of microorganisms in metal leaching, 'negative (uninoculated)' controls consisting of 2 g of mineral were added to the basal medium without bacterial inoculation. To compare the results to a standard 'chemical leaching' system, 2 g of mineral was added to 8 mM H_2SO_4 (pH 1.8) solution. No Fe(II) was added to these to test the ability of *At. ferrooxidans* to oxidise Fe(II) present within the mineral.

All experiments were acidified to a final H_2SO_4 concentration of 8 mM equivalent to pH 1.8. For the bioleaching, uninoculated, and chemical leaching experiments 0.29 mL of 5.5 M H_2SO_4 was added to produce this pH at a final volume of 200 mL. Rewrite as Subsequent H_2SO_4 additions of 0.1–0.6 mL were needed predominantly at day 0 and between day 13 to keep the pH at 1.8 in the jadarite bioleaching, uninoculated, and sulphuric acid experiments.

To monitor changes in geochemistry, 1 mL aliquots from each replicate were taken from the bioleaching experiments on days 0, 3, 5, 8, 10, 14, 17, 21, 24, and 30 and from the chemical leaching experiments on days 0, 2, 6, 8, 13, 16, 22, 27, and 30. The samples were then centrifuged at 10,000 g for 60 s, diluted with deionised water, acidified to 2% HNO_3, and stored at 3°C. To determine the amount of Li leached and to monitor the release of other metals from the minerals, concentrations of Al, B, Ca, Fe, K, Mg, Mn Li, S, P, Pb, and Zn in solution were measured using the ICP-OES (Aligent 5,110 series). pH was measured using a HANNA pH meter (calibrated with HANNA pH 1.68, 4.01, 7.01, and 10.01 standards). Following the bioleaching experiments, 1 mL aliquots were used to inoculate fresh media containing Fe(II) to test the viability of *At. ferrooxidans* by observing Fe(III) oxidation.

2.4 SEM imaging

A Thermo Fisher FEI Quanta 650F FEG-SEM was used to observe samples of jadarite taken before and after bioleaching to identify any structural changes and biofilm formation on the mineral surface. Samples were fixed with increasing concentrations of glutaraldehyde (0.75–2.5%) in phosphate-buffered saline solution and then dehydrated in increasing concentrations of ethanol (25–100%). The samples were subsequently deposited onto a silicon wafer, fixed to a pin stub with carbon tape (Newsome et al., 2018), coated using an Agar automatic carbon coater to approximately 25 nm in thickness, and analysed under high vacuum with secondary electron mode at 10.00 kV.

2.5 X-ray diffraction (XRD) analysis of bioleaching residues

After leaching, solid jadarite residues were washed in 15 mL MilliQ water to remove salts and allow drying, centrifuged at 2500 g for 10 min (Thermo Fisher Megafuge 40R), and left to dry for at least 24 h in a fume cabinet. These residues were powdered in an agate mortar and pestle and analysed using a powder XRD to determine changes in major mineral phases (Siemens D5000 XRD) and compared to similar spectra in the literature to find peaks not available in the EVA (Diffrac) database. Analysis of spodumene and lepidolite was not undertaken due to the lack of leaching observed based on no metal release or change to media composition through bioleaching.

2.6 Kinetic analysis

The shrinking core kinetic model was used to model the reaction kinetics for each system to predict whether acid leaching acted as a driver within the kinetic system (Fogler, 2020). The model was chosen based on the assumption that the conditions of the experiment were similar to that of acid leaching and previous successful use of the model to predict Li release from lepidolite in H_2SO_4 (Olaoluwa et al., 2023). This model describes experiments in which solid particles are consumed by reactions and are therefore described as 'shrinking'. Reaction kinetics for heterogenous non-catalytically driven reactions can also be developed (Velardo et al., 2002). The shrinking core kinetic model has been used previously in predicting zinc oxide leaching from zinc-containing ore in high concentration H_2SO_4 and in lepidolite bioleaching using an *At. ferrooxidans* and *At. thiooxidans* consortium (Sedlakova-Kadukova et al., 2020).

The main assumptions for the model are as follows particles are spherical, shrinkage is uniform across the particles, the main reaction is the shrinking of the Li-containing minerals in the presence of the acidic media, other substances present in the ore (e.g., quartz, dolomite ($MgCO_3$. $CaCO_3$), and other non-Li bearing minerals) do not have any significant effect on the reaction or kinetics, the solids involved are non-porous and the reaction is dominated by outer diffusion, as in other lepidolite bioleaching experiments (Fogler, 2020; Didyk-Mucha et al., 2016). These assumptions are appropriate for the outlined experiments providing acid leaching is the predominant contributor to Li release.

The shrinking core model can be used to model chemical and diffusion-driven reactions, by using the relationship of these functions on reaction time (Equation 1).

$$t = \frac{\rho_{Li-mineral}}{bM_{Li-mineral}c}\left\{\frac{r_L}{k_0}\left[\left(1 - 1 - x\right)^{\frac{1}{3}}\right] + \frac{r_L^2}{6D_c}\left[1 - \frac{2}{3}x - \left(1 - x\right)^{\frac{2}{3}}\right]\right\} \quad (1)$$

where t is reaction time, ρ is the density of the mineral particles, b is the molar ratio of reactants, M is the relative molar mass of the Li mineral, c is the concentration of acid in media, r_L is the radius of the mineral particles, and D_C is the diffusion coefficient in the porous product layer.

Using the generalised equation for the shrinking core model, (Equation 2) the rate constant can be shown as k_r when assuming that the reaction is chemically controlled, and the reaction rate is much greater than the diffusion coefficient for the system:
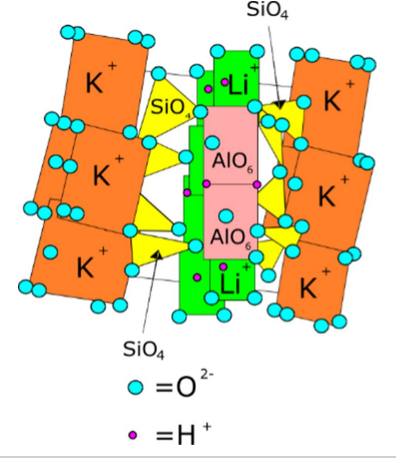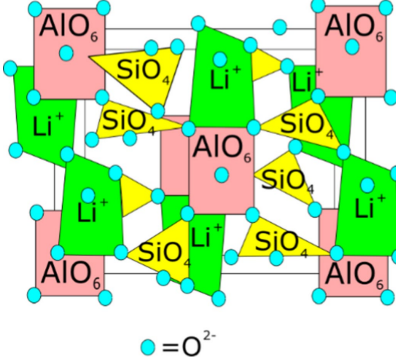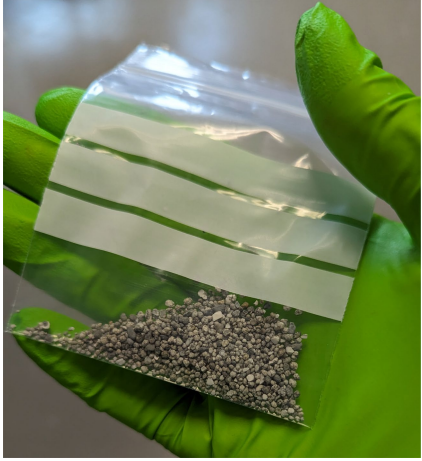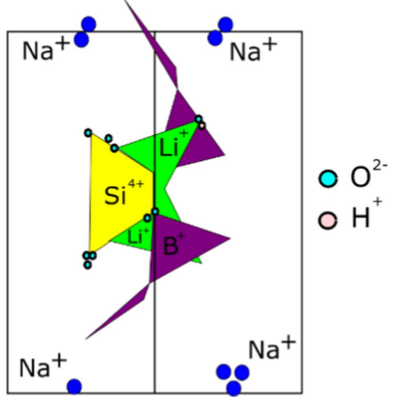
$$1 - \left(1 - x\right)^{\frac{1}{3}} = k_r t \quad (2)$$

where x is the Li leaching rate (determined by considering the amount of the total Li released by dividing Li released by total Li available from added mineral), k_r is the apparent rate constant and t is the leaching time (Equation 3).

$$k_r = \frac{kM_{Li-mineral}}{a\rho_{Li-mineral}r_0}C_A \quad (3)$$

where k is the kinetic constant, $M_{Li-mineral}$ is the relative molecular mass of the mineral, $\rho_{Li-mineral}$ is the density of the mineral, a is a

TABLE 1 Minerals present in lepidolite, spodumene, and jadarite samples identified using XRD, with photographs of the samples as supplied and simplified 2D diagrams of the predicted Li-bearing mineral phases.

Ore type	Mineral	Formula(s)	Sample diagram	2D crystal structure
Lepidolite	Lepidolite Quartz	$K(Li,Al)_3(Si,Al)_4O_{10}(F, OH)_2$ Syn-SiO_2		
Spodumene	Spodumene Quartz	Alpha-$LiAl(Si_2O_6)$ Syn-SiO_2		
Jadarite	Jadarite Dolomite Probertite	$LiNaB_3SiO_7$ (Stanley et al., 2007) $MgCO_3.CaCO_3$ $CaNa(B_5O_7(OH)_4).3H_2O$ (Gatta et al., 2022)		

The crystal structures for lepidolite and spodumene were adapted from Su et al. (2019) and the single unit cell bonding structure for jadarite was adapted from Stanley et al. (2007).
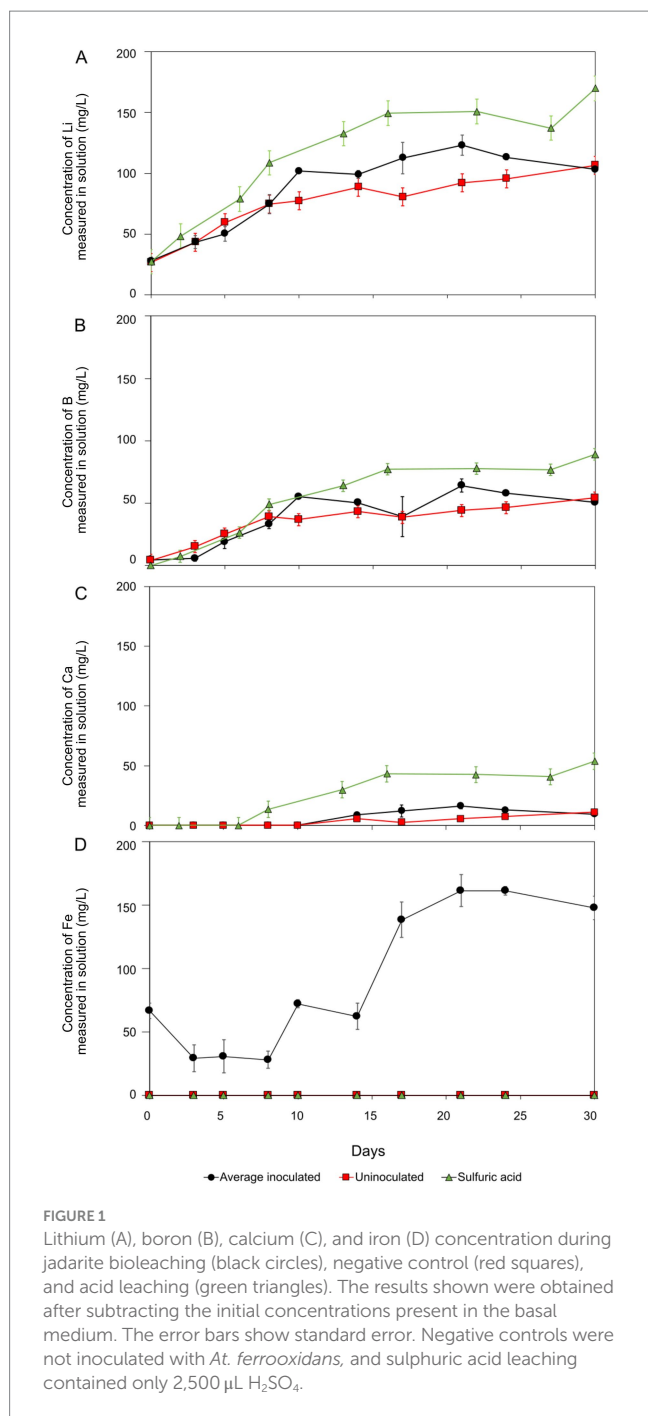
stoichiometric coefficient of reaction reagents, r_0 is the initial radius of the mineral particle, and C_A is the concentration of acid.

3 Results and discussion

3.1 Material characterisation

The three samples contained Li-bearing phases and accessory minerals including quartz in the lepidolite and spodumene samples, and dolomite and probertite ($NaCaB_5O_7(OH)_4 3(H_2O)$) in the jadarite sample

(Table 1). The jadarite sample had the highest concentration of Li (2.2 wt.%), followed by spodumene (1.2 wt.%) and lepidolite (0.66 wt.%). Iron concentration was highest in jadarite (0.40 wt.%), followed by lepidolite (0.033 wt.%), and spodumene (<0.001 wt.%). The ferrozine assay indicated that bioavailable Fe(II) was present at concentrations of 0.020 mM in jadarite, 0.031 mM in lepidolite, and 0.023 mM in spodumene (Supplementary Table S2). Magnesium content was higher in jadarite (0.73 wt.%) when compared to lepidolite and spodumene in which Magnesium was <0.001 wt.% (Supplementary Table S1). The stoichiometry of Li, B, Fe, Ca, and Mg in jadarite could not be balanced solely by the presence of jadarite, dolomite, and probertite, suggesting

Lithium (A), boron (B), calcium (C), and iron (D) concentration during jadarite bioleaching (black circles), negative control (red squares), and acid leaching (green triangles). The results shown were obtained after subtracting the initial concentrations present in the basal medium. The error bars show standard error. Negative controls were not inoculated with *At. ferrooxidans,* and sulphuric acid leaching contained only 2,500 μL H_2SO_4.

the sample likely contained other poorly crystalline or amorphous minerals that were not identifiable using XRD.

3.2 Jadarite bioleaching

The rate of jadarite bioleaching with *At. ferrooxidans* was highest in the initial stage of the reaction, from day 0 to day 10, after which the Li, B, and Ca concentrations plateaued (Figure 1A). A maximum concentration of 120 mg/L Li was recorded for the bioleaching experiments, representing approximately 57% of the Li within the mineral. This was approximately 24 mg/L higher than concentrations

measured in the uninoculated control at this time point, demonstrating that *At. ferrooxidans* contributed to the leaching of Li from jadarite. The initial day 0 concentrations of approximately 30 mg/L Li in solution for all experiments may have been caused by surface Li release or release from exchangeable phases. By day 30, the Li concentration in the uninoculated negative control was similar to those in the biotic experiments, likely due to the decomposition of jadarite in the presence of $H_2SO_4.$ Between days 10 to 25, the rate of Li release was more than 10% higher than in the uninoculated control. After this, the rate of Li release declined, possibly due to the loss of functionality of the bacteria due to the consumption of available Fe(II) from the mineral or to the Li being 'armoured' by secondary minerals or biofilms preventing surficial release. The H_2SO_4 chemical leaching released more Li than the inoculated and uninoculated acidic media leaches consistently throughout the experiment, with a final concentration measuring around 180 mg/L. The rate of Li release was comparable for both the bioleaching and acid leaching experiments. There are no available studies on Li release from jadarite by bioleaching, but the high concentration of Li released from H_2SO_4 leaching may indicate acid leaching contributing to some Li release from the inoculated bioleaching system. The 17 mM maximum Li concentration did not affect the functionality of the *At. ferrooxidans* once it had been inoculated into fresh media with 25 mM Fe(II) present for oxidation.

Boron (B) release was similar to that of Li for the biotic, uninoculated, and acid leaching experiments (Figure 1B). Approximately 64 mg/L B bioleached. Approximately 20 mg/L more B was released by bioleaching in the first 28 days than in the uninoculated control, suggesting the accelerated breakdown of Li–B bonds in jadarite in the bioleaching system. Boron release from the acid leaching was approximately 25 mg/L higher than the bioleaching system at the end of the 30-day experiment.

Controlling the pH was challenging within the jadarite system, possibly due to the presence of dolomite ($MgCO_3.CaCO_3$), which is known to buffer acidity (Roberts, 2016). Up to 20 mg/L in Ca and little change in Mg concentrations were documented (Figure 1C). The differences in the rates of Mg and Ca release suggest, that along with the dissolution of dolomite, other potentially non-crystalline Ca and Mg-bearing phases were also present and dissolved during the experiment. The final concentration of Ca in the acid-leaching system was more than double that of the bioleaching (53 mg/L) system and higher amounts of Ca were released in the bioleaching experiments compared to the uninoculated control experiments. The pH of the experiments increased from 1.8 to 7.0 immediately after the addition of jadarite, with the need for continuous adjustment of pH for the first 17 days to ensure the experiments remained in the pH 1–2 range required for bioleaching. The acid-leaching system required 31 and 18% more H_2SO_4 to maintain the pH range required for comparison with the bioleaching and uninoculated experiments, respectively (Supplementary Figure S1).

Soluble and therefore bioavailable Fe was present throughout the experiment (from the mineral) to support bacterial metabolism (Figure 1D), with a maximum of 47% of total Fe released in the biotic system and no release in the uninoculated control. The viability of the cells was confirmed at the end of the experiment by adding 1 mL aliquots to a basal medium containing $FeSO_4$. Microbial Fe(II) oxidation was confirmed by the generation of Fe(III), which produced an orange colour in the medium.
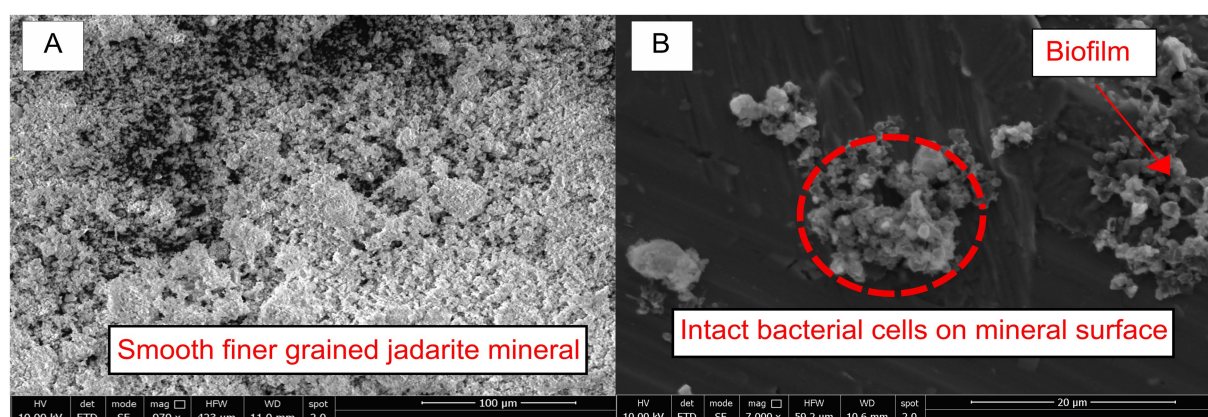
FIGURE 2
(A) Untreated ground jadarite sediment before exposure to the acidic basal medium and bacteria. (B) Jadarite sediment after bioleaching with flocculation, intact bacterial cells, and biofilm are indicated by the red arrow and label.

Before bioleaching, the mineral surfaces were intact, and many showed regular crystal shapes (Figure 2A). After the experiments containing *At. ferrooxidans,* a shiny biofilm sheet was observed on the mineral surfaces, with some flocculation and clumping of the mineral also occurring (Figure 2B). Biofilm formation was identified by predominantly structural and morphological components observed through SEM analysis. The texture of the mineral surface in the biological systems varied greatly compared to that in the non-inoculated acidic system, and it had surface characteristics of bacterial biofilms seen in previous SEM studies of *Acidiothiobacillus* species (García-Meza et al., 2013). By contrast, no visible changes to the media or mineral were observed in the uninoculated control. Cells were present on many of the clumped mineral surfaces (Figure 2B), while some smoother surfaces appeared not to have cells present. The precipitation of new minerals through bioleaching was confirmed by XRD (Figure 3); therefore, variations in the mineral surface and biofilm presence may be due to the presence of the newly formed minerals. Since Li and B are undetectable by EDS spectra, characterising and observing variations in the minerals present after bioleaching is challenging.
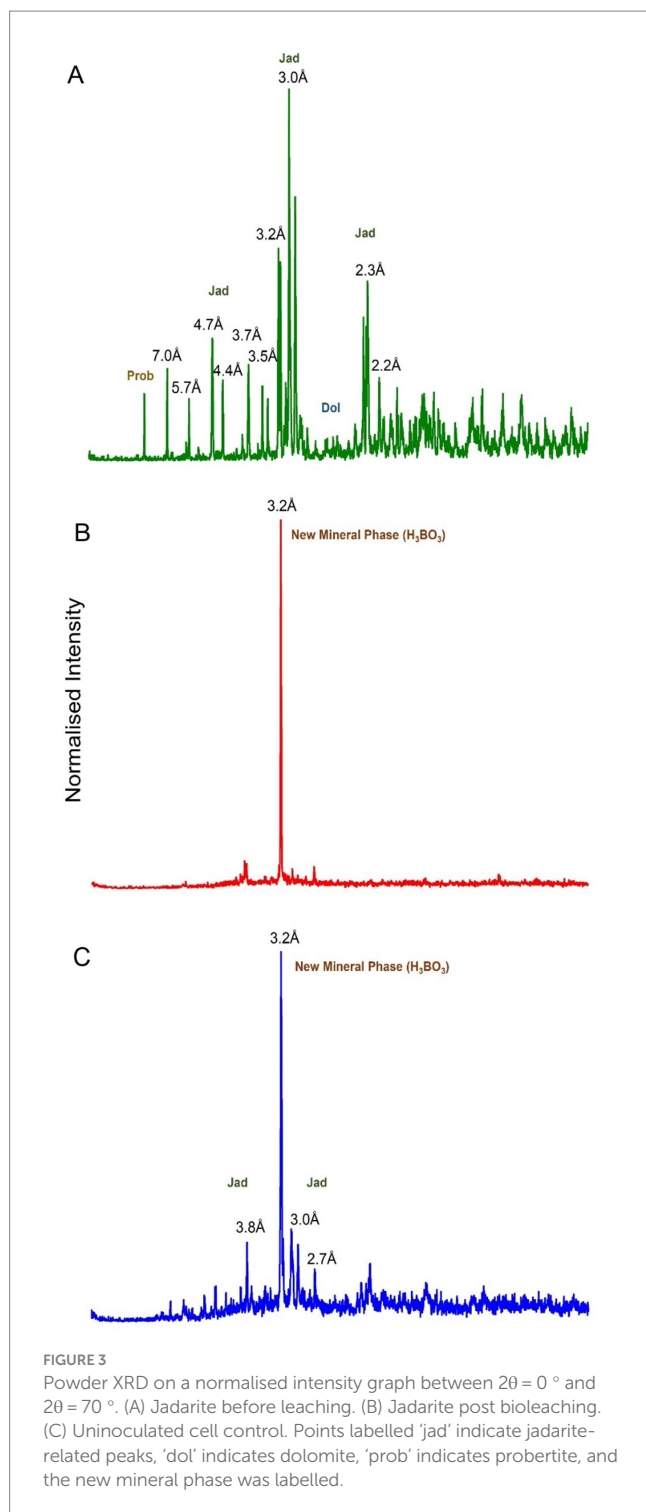
The XRD analysis of samples from before and after bioleaching, as well as from the uninoculated control, revealed significant changes in the minerals present (Figure 3). The peaks for jadarite, dolomite, and probertite were no longer present in the bioleached sample, indicating their dissolution during the bioleaching experiment. The amount of Li dissolved, however, stoichiometrically exceeded that provided by the B in jadarite, suggesting that other unidentified poorly crystalline Li minerals were likely present in the sample. At the end of the experiment, a single new peak was present at $2\theta = 27.9°$, suggesting formation of a new solid phase. The same phase formed in the uninoculated control, which also retained some of the jadarite peaks with lower intensity, while no significant dolomite or probertite peaks were identified. The new solid phase material had a single peak that was fine and symmetrical indicating the presence of a highly crystalline phase (Jian and Hejing, 2003). The $2\theta = 27.9°$ value may be indicative of boric acid (H_3BO_3) crystals precipitating

from a boron-saturated solution in this acidic system (Figure 3B; XRD) (Sheikh et al., 2017; Ata et al., 2000). Boric acid has a triclinic structure when formed at 23°C, with 4 symmetric units of $B(OH)_3$ providing the highly symmetrical crystalline structure for the sharp XRD peak (Alavia et al., 2023). Therefore, the reported XRD spectra directly indicated H_3BO_3 formation in the outlined conditions and are comparable to previously reported XRD spectra of crystalline H_3BO_3 (Mergen et al., 2004). Boric acid is categorised as a human reproductive toxicant, therefore the formation of a solid that contains boric acid would have serious implications for the industrial application of acid (bio) leaching of jadarite and warrants further investigation.
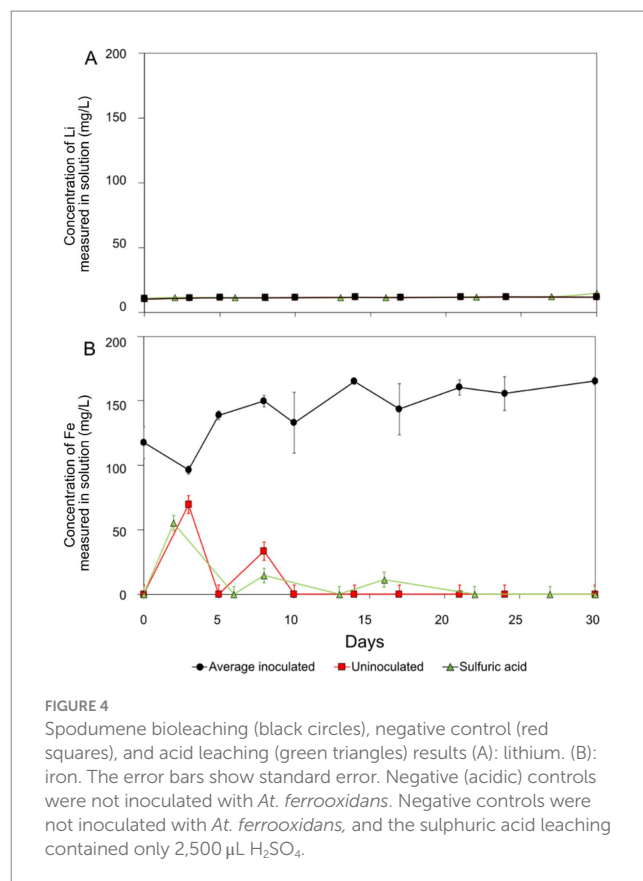
Overall, the experiments showed that jadarite was amenable to acid leaching and that the presence of *At. ferrooxidans* increased the rate of leaching and resulted in the formation of a biofilm that may have contributed to the dissolution of the mineral surface (Han et al., 2024). However, substantial quantities of acid were required to maintain the pH levels required for the bioleaching, uninoculated acidic media leaching, and H_2SO_4 leaching reaction to occur, likely due to the presence of dolomite, which may influence the potential of bioleaching to be applied on an industrial scale.

3.3 Spodumene bioleaching

After 30 days, 12 mg/L of Li was released into the solution from spodumene, equating to approximately 9% of the total Li content of the mineral (Figure 4A). The pH remained constant at 1.8 for the whole experiment with no requirement for H_2SO_4 addition. Minimal changes to the appearance of the mineral were noted. The uninoculated negative control behaved similarly to those containing *At. ferrooxidans* throughout the experiment, with a maximum of 11 mg/L of Li measured in the solution. Only a small proportion of the Li in spodumene was susceptible to acid leaching, and bacteria did not enhance the rate or extent of leaching most likely due to Fe(II) oxidation not influencing the release of Li into the system due to the chemical structure of the mineral.

FIGURE 3
Powder XRD on a normalised intensity graph between 2θ = 0 ° and 2θ = 70 °. (A) Jadarite before leaching. (B) Jadarite post bioleaching. (C) Uninoculated cell control. Points labelled 'jad' indicate jadarite-related peaks, 'dol' indicates dolomite, 'prob' indicates probertite, and the new mineral phase was labelled.

FIGURE 4
Spodumene bioleaching (black circles), negative control (red squares), and acid leaching (green triangles) results (A): lithium. (B): iron. The error bars show standard error. Negative (acidic) controls were not inoculated with *At. ferrooxidans*. Negative controls were not inoculated with *At. ferrooxidans,* and the sulphuric acid leaching contained only 2,500 μL H_2SO_4.

More Fe was solubilised from spodumene in the biotic system compared to the controls (uninoculated and acid leaching), demonstrating microbial cycling of Fe(II)/Fe(III) in this system (Figure 4B). The fluctuations in the negative control may have been due to heterogeneity in the system, for example, the release of exchangeable phases and precipitation. The initial concentrations in the biotic system (44% of to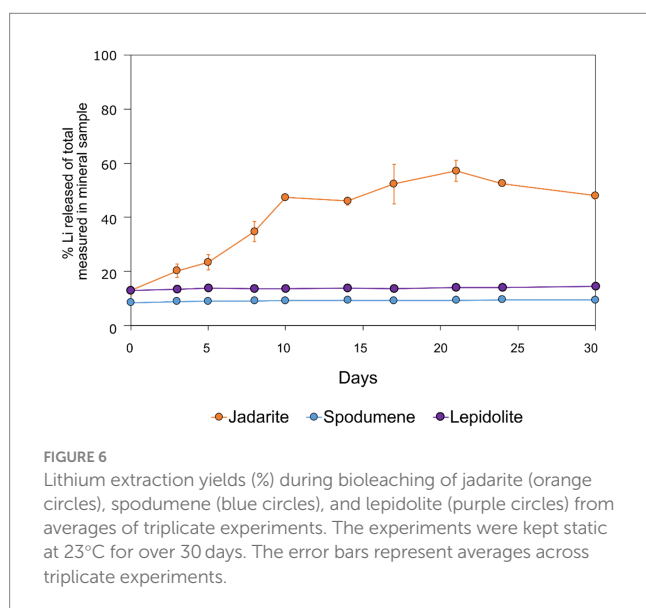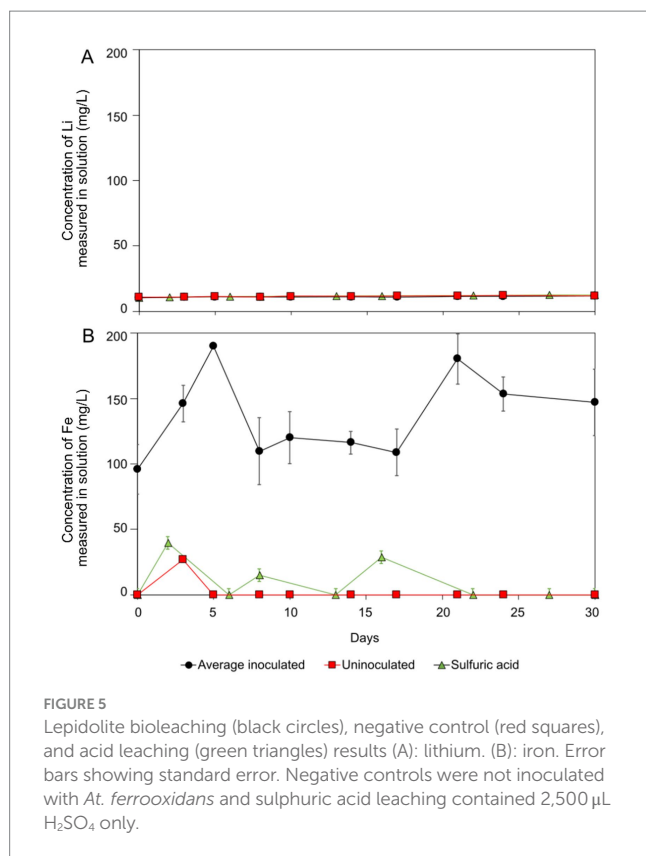tal Fe present in solution) were much higher than the uninoculated control, indicating some carryover of Fe from the growth medium (Figure 4B).

3.4 Lepidolite bioleaching

Lithium release from lepidolite was similar to that from spodumene, with the maximum Li concentrations in solution measuring at approximately 12 mg/L, equating to approximately 14% of the total Li concentration. This was similar to the negative control which yielded 12 mg/L Li over 30 days (Figure 5A). The pH remained constant at 1.8 with no H_2SO_4 additions, and there were no visible changes in the appearance of the mineral or solution throughout the experiment. In a previous study, a bacterial consortium yielded approximately 8% Li recovery from lepidolite (Horeh et al., 2016). Comparable with spodumene, the similarity of the experiments with *At. ferrooxidans* and compared to the uninoculated control suggests the bacteria had minimal impact on the leaching of Li, with abiotic acid leaching responsible for the small proportion of Li leaching that occurred.

Fe concentrations were elevated in the biotic experiments because of release from the mineral. The maximum concentration seen in the biotic system was 180 mg/L Fe, compared to no release in the uninoculated control (Figure 5B). Fluctuation in the aqueous concentration measurements implies changes in the proportion of aqueous and precipitated Fe by Fe(II) bio-oxidation by *At. ferrooxidans* during the reaction time. The trend was not observed in the uninoculated control (see Figure 5).

FIGURE 5
Lepidolite bioleaching (black circles), negative control (red squares), and acid leaching (green triangles) results (A): lithium. (B): iron. Error bars showing standard error. Negative controls were not inoculated with *At. ferrooxidans* and sulphuric acid leaching contained 2,500 μL H$_2$SO$_4$ only.

FIGURE 6
Lithium extraction yields (%) during bioleaching of jadarite (orange circles), spodumene (blue circles), and lepidolite (purple circles) from averages of triplicate experiments. The experiments were kept static at 23°C for over 30 days. The error bars represent averages across triplicate experiments.
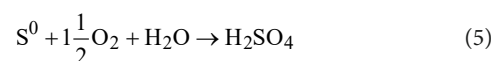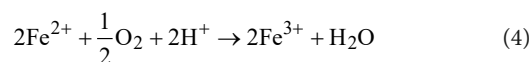
3.5 Comparison of the bioleaching experiments

The bioleaching and acid leaching of jadarite resulted in much higher concentrations and proportions of Li released into the solution than for of spodumene and lepidolite (Figure 6). The yield of Li release from jadarite was considerably higher in the presence of bacteria, whereas the role of the bacteria in the spodumene and lepidolite bioleaching experiments was insignificant due to their similarity to the

uninoculated and acid controls (Jian and Hejing, 2003; Sheikh et al., 2017).

Iron release to the solution was enhanced in the biotic reactions for all ore types, indicating biomechanisms involved in solubilising Fe from Fe(II)-bearing minerals. *At. ferrooxidans* can oxidise Fe(II) to Fe(III) (Equation 4) or oxidise RISCs (Equation 5). However, it was difficult to determine if the bacterium was using only Fe(II) or both Fe(II) and RISCs as electron donors (Zhan et al., 2019; Harahuc et al., 2000). The Fe content of jadarite exceeded that of spodumene and lepidolite (Supplementary Table S1). Similar amounts of bioavailable Fe (approximately 0.02 mM of 0.5 N HCl-extractable Fe) were present in each of the three ore types. However, the changes in Fe concentrations observed in these experiments allude to the contribution of the Fe(II) bio-oxidation mechanism. Following Fe(II) oxidation, the formed Fe(III) can act as an oxidant that leaches the mineral and can be reduced back to Fe(II) for further oxidation by *At. ferrooxidans* (Equation 6) (Brock and Gustafson, 1976). The S concentrations were low in all samples (Supplementary Table S1) and no elemental S was added to the system, further indicating Fe oxidation mechanisms to be the main contributor to metal release. This cycling can further enhance the release of Li from the jadarite, as well as affect the concentration of solubilised Fe over time. Acidity was not produced during these experiments, with the pH remaining around 1.8 (spodumene and lepidolite) and increasing likely due to dolomite consumption (jadarite). This may suggest that *At. ferrooxidans* was predominantly metabolising via Fe(II) oxidation and Fe(II)/Fe(III) cycling.

$$2Fe^{2+} + \frac{1}{2}O_2 + 2H^+ \rightarrow 2Fe^{3+} + H_2O \quad (4)$$

$$S^0 + 1\frac{1}{2}O_2 + H_2O \rightarrow H_2SO_4 \quad (5)$$

$$Fe^{2+} \rightleftharpoons Fe^{3+} \quad (6)$$

The enhanced leaching of Li from jadarite is likely to be due to the mineral structure and bonding of Li, which is different from Li in spodumene and lepidolite. The Li in jadarite is bound in a tetrahedral borosilicate structure with Na$^+$ ions situated between the layers (Table 1). Li appears in 'triangular'-like bonding to B^{3+} and Si^{4+} in a lattice with O2-ions within the Li–B–Si bond space and Na$^+$ in the free space (Table 1) (Whitfield et al., 2007). In contrast, it is theorised that the Li in spodumene is present within a tetrahedral 4-fold or 6-fold tetrahedral structure bound to O within the aluminosilicate structure, where Al forms octahedral bonds in the bonding chain. The cavities in the polyhedral host Li act as a high-energy bonding environment, which is difficult to overcome in low-energy reaction conditions (Li and Peacor, 1968; Quezada and Toledo, 2020). In lepidolite, it is predicted that the Li is bound between layers of AlO$_6$ in an octahedral structure and SiO$_4$ in a tetrahedral structure acting as predominantly charge supplementing ions. Therefore, the dominating bonding force is predicted to be highly ionic in these crystal structures (Su et al., 2019; Franco et al., 1973). As such, releasing Li from spodumene and lepidolite requires breaking high-energy aluminosilicate bonds. In jadarite, only lower energy Li–B bonds are required to be broken to release Li to the solution. Similarly, the bonding is described as low
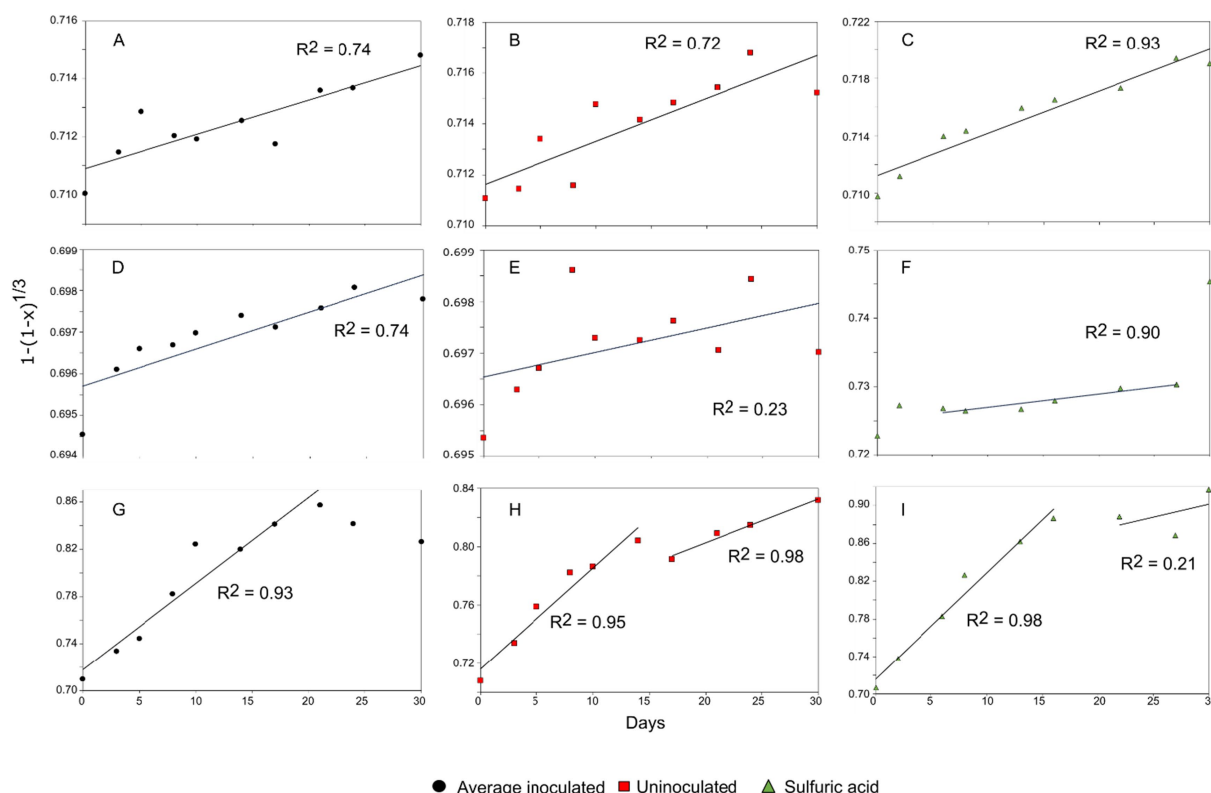
FIGURE 7

Linear regression of the chemical shrinking core model for the leaching of Li from lepidolite via (A) bioleaching $R^2 = 0.74$, (B) uninoculated control $R^2 = 0.72$ and (C) sulphuric acid leaching $R^2 = 0.93$. Linear regression of the chemical shrinking core model for the leaching of Li from spodumene via (D) bioleaching $R^2 = 0.74$, (E) uninoculated control $R^2 = 0.23$, and (F) sulphuric acid leaching $R^2 = 0.90$. Linear regression of the chemical shrinking core model for the leaching of Li from jadarite via (G) bioleaching $R^2 = 0.93$, (H) uninoculated control $R^2 = 0.95$, $R^2 = 0.98$ and (I) sulphuric acid leaching $R^2 = 0.98$, $R^2 = 0.21$. The black circles represent bioleaching reactions, the red squares represent uninoculated controls, and the green triangles represent acid leaching.

energy within the jadarite structure (Whitfield et al., 2007), indicating that it may be easier to release metals at ambient temperature in acidic conditions than the Li mineral types, as seen in both the bioleaching experiments and the uninoculated control (Ñancucheo et al., 2016). Abiotic leaching caused the decomposition of a significant proportion of jadarite to produce aqueous Li. This is further evidence of the lower stability of the mineral in acidic conditions due to lower activation pathways to bond-breaking reactions resulting in Li release.

3.6 Kinetic analysis

The shrinking core kinetic model was used to model the reaction kinetics for each system. This model predicts whether acid leaching is the predominant mechanism of release for a given element but will not conform in the presence of catalysts such as biological mechanisms. This is useful for understanding the influence of bacteria in the bioleaching process compared to the acid leaching, as well as for understanding the extent of the reactions taking place. For both lepidolite and spodumene, the collected data does not adjust to the shrinking core model as denoted by the low R^2 ($R^2 = 0.74$), (Figures 7A,D). A multiphase reaction was difficult to predict, and the model further confirmed little to no reaction

progression over 30 days, as indicated by shallow the gradients of the plotted results. The slopes of the plotted data were small for both lepidolite and spodumene (1×10^{-4} and 9×10^{-5}, respectively), indicating low rate constants (gradient) and hence slow reaction times. The model showed good agreement for acid leaching of both minerals, with R^2 values exceeding 0.9 in both cases, proving validity in the model for mineral–acid interactions. The contribution of the bacteria was probably very limited based on these values and helps to explain the lack of difference in aqueous Li concentration between the biotic experiments and the uninoculated controls.

Jadarite showed a poor fit to the chemically driven shrinking core model after the first 15 days of reaction, with no established rate constant and low correlation ($R^2 = 0.67$) when plotted against the established model (Figure 7G). The contrasts in gradient between the two reaction phases indicated a much larger gradient and hence a greater reaction rate during the first stages of the model. There is a difference in gradient during the initial reaction stages and later days, with a more positive gradient in the linear regression in the second stage of the reaction. This implies that the quasi-steady state may have been reached from at least day 20 of the reaction, with a positive rate constant (gradient) and agreement with the model (Figures 7G–I). This is shown in the release of Li at

a greater rate in the earlier stage of the reaction. The later reaction stages did not fit the model ($R^2 = 0.42$), likely due to the contribution of the bacterial activity and formation of secondary products as well as the chemical leaching due to the nature of the kinetic model. There would be a poor fit when there is the contribution of the biological catalyst to the reaction rate. This is further emphasised by the elevated concentrations of Li recorded in the jadarite bioleaching from day 10 compared to the negative control (Figure 1) (Fogler, 2020). The model showed a good fit for the acid leaching of jadarite in the first reaction stages, which followed a similar trend to that of bioleaching. However, the Li concentration continued to increase slowly rather than plateauing as with the bioleaching system, indicated by the more positive gradient on the second stage of the acidic kinetic plot.

3.7 Scale-up of jadarite bioleaching

The feasibility of scale-up of the jadarite experiment was considered and deemed to have many barriers. The first is the volume of acid required to produce and maintain the pH 1–2 conditions needed for successful bioleaching. For this, a minimum of 0.9% of the total volume of the system needs to be $5.5\,M\ H_2SO_4$. A volume of 1,000 L would require 9 L of $5.5\,M\ H_2SO_4$ to initiate leaching and additional amounts throughout the process to neutralise components whose dissolution buffers the pH (e.g., the dolomite within the jadarite used in this study). This is less than the 1.3% required volume for acid leaching with H_2SO_4, which equates to 13 L per 1,000 L volume. While the Li release from bioleaching was lower than with H_2SO_4, the requirement for less acid would reduce the costs associated with the reaction. The rate of Li release by *At. ferrooxidans* was comparable to that of the acid leaching over 30 days. Typically, bioleaching can have slow reaction rates. For example, bioleaching of chalcopyrite ($CuFeS_2$) by *At. ferrooxidans* can take up to 80 days to release 60–70% of available Cu (Zhao et al., 2013). Therefore, Li release is considerably fast through these experiments in comparison to other bioleaching processes. Another consideration is the formation of H_3BO_3, which poses additional hazards and its disposal would add cost and risk to the scale-up (likely to occur in all jadarite acid leaching experiments). Therefore, while Li release was enhanced by the presence of *At. ferrooxidans*, its scale-up would need careful consideration of environmental impact and waste management prior to use.

4 Conclusion

Bioleaching released up to 57% of Li from jadarite, but this required substantial additions of H_2SO_4 to maintain the pH below 2. The presence of the model Fe(II)/S-oxidising bacterium *A. ferroxidans* increased the rate of bioleaching of jadarite in early reaction stages, but the overall extent of Li leaching from jadarite, spodumene, and lepidolite was not significantly greater than abiotic acid leaching. The conformity of the spodumene and lepidolite data to the shrinking core model indicates a heterogenous, non-catalytically driven reaction where chemistry is the predominant driver. This supports previous findings that showed lepidolite to follow the same leaching trends as chemical leaching (Olaoluwa et al., 2023). The jadarite system did not conform to the chemical model for the kinetics in later reaction stages, indicating catalytic and biological contributions to the reaction. In conclusion, these results give preliminary evidence of the suitability of a (bio)leaching system for Li extraction from jadarite-containing minerals containing dolomite as a buffering contaminant and other competing metals in different mineral phases, with reaction times like that of chemical leaching methods. Bioleaching released 18% less Li than sulphuric acid leaching but showed increased selectivity with lower concentrations of B and Ca measured in solution. The lower concentration of B may be due to the formation of crystalline structures during the bioleaching. This could be beneficial when optimised to make further processing and concentrating of Li more effective. However, further studies on the extent of the formation of crystalline H_3BO_3 in the jadarite system should be considered prior to scale-up, as environmental implications and health effects of H_3BO_3 may be significant (Hadrup et al., 2021).

Data availability statement

The datasets presented in this study can be found in online repositories. The names of the repository/repositories and accession number(s) can be found at: Kirk, Rebecca (2024), "Bioleaching lithium from jadarite, spodumene and lepidolite using Acidiothiobacillus ferrooxidans", Mendeley Data, V1, doi: 10.17632/djkf7tkm8d.1.

Author contributions

RK: Writing – original draft, Writing – review & editing. LN: Writing – review & editing. Funding acquisition, Supervision. CF: Writing – review & editing. KH-E: Writing – review & editing, Supervision.

Conflict of interest

The authors declare that the research was conducted in the absence of any commercial or financial relationships that could be construed as a potential conflict of interest.

The author(s) declared that they were an editorial board member of Frontiers, at the time of submission. This had no impact on the peer review process and the final decision.

Publisher's note

All claims expressed in this article are solely those of the authors and do not necessarily represent those of their affiliated organizations, or those of the publisher, the editors and the reviewers. Any product that may be evaluated in this article, or claim that may be made by its manufacturer, is not guaranteed or endorsed by the publisher.

Supplementary material

The Supplementary material for this article can be found online at: https://www.frontiersin.org/articles/10.3389/fmicb.2024.1467408/full#supplementary-material

References

Alavia, W., Seidel-Morgenstern, A., Hermsdorf, D., Lorenz, H., and Graber, T. A. (2023). Real-time crystal growth monitoring of boric acid from sodium or Lithium sulfate containing aqueous solutions by atomic force microscopy. *ACS Omega* 8, 10822–10835. doi: 10.1021/acsomega.2c06953

Ata, O., Çolak, S., Çopur, M., and Çelik, C. (2000). Determination of the optimum conditions for boric acid extraction with carbon dioxide gas in Aqueous Media from Colemanite Containing Arsenic. *Ind. Eng. Chem. Res.* 39, 488–493. doi: 10.1021/ie990314z

Bahaloo-Horeh, N., Mousavi, S. M., and Baniasadi, M. (2018). Use of adapted metal tolerant aspergillus Niger to enhance bioleaching efficiency of valuable metals from spent lithium-ion mobile phone batteries. *J. Clean. Prod.* 197, 1546–1557. doi: 10.1016/j.jclepro.2018.06.299

Bradley, D. C., McCauley, A. D., and Stillings, L. M. (2010). Mineral-deposit model for lithium-cesium-tantalum pegmatites: U.S. Geological Survey Scientific Investigations Report 2010–5070–O, 48. doi: 10.3133/sir20105070O

Bradley, D., Stillings, L. L., Jaskula, B. W., Munk, L. A., and McCauley, A. D. (2017). Lithium, Eds. K. Chap, K. J. Schulz, J. H. DeYoung, Jr., R. R. Seal, II, and D. C. Bradley. Critical mineral resources of the United States—Economic and environmental geology and prospects for future supply: U.S. Geological Survey professional paper 1802.

Brock, T. D., and Gustafson, J. (1976). Ferric iron reduction by sulfur-and iron-oxidizing bacteria. *Appl. Environ. Microbiol.* 32, 567–571. doi: 10.1128/aem.32.4.567-571.1976

Cerny, P., Ercit, T. S., and Vanstone, P. T. (1996). "Petrology and mineralization of the Tanco rare-element pegmatite, southeastern Manitoba" in Geological Association of Canada—Mineralogical Association of Canada, field trip guidebook, Geological Society of Canada/Mineralogical Association of Canada Annual Meeting, Winnipeg, Manitoba.

Cipollina, A., Battaglia, G., Berkemeyer, L., Cortina, J. L., Fernandez de Labastida, M., Lopez Rodriguez, J., et al. (2022). Recovery of Lithium carbonate from dilute Li-rich brine via homogenous and heterogeneous precipitation. *Ind. Eng. Chem. Res.* 61, 13589–13602. doi: 10.1021/acs.iecr.2c01397

Didyk-Mucha, A., Pawlowska, A., and Sadowski, Z., (2016) Application of the shrinking core model for dissolution of serpentinite in an acid solution. E3S Web Conf., 8. doi: 10.1051/e3sconf/20160801035

European Commission (2017) Communication From The Commission To The European Parliament, The Council, The European Economic And Social Committee And The Committee Of The Regions Critical Raw Materials Resilience: Charting a Path towards greater Security and Sustainability COM/2020/474. Available at: https://eur-lex.europa.eu/legal-content/EN/TXT/?uri=CELEX:52020DC0474&print=true (Accessed June 27, 2023).

Fogler, S. (2020). *Elements of Chemical Reaction Engineering - Chapter 14 Mass Transfer Limitations in Reacting Systems: Vol. 6th Edition.* 6th ed. International Series in the Physical and Chemical Engineering Sciences.

Franco, S., Marco, F., and Stefano, M. (1973). Crystal structure of a 2M2 lepidolite. *Acta Cryst* 29, 573–578. doi: 10.1107/S0567740873002931

Gao, T., Fan, N., Chen, W., and Dai, T. (2023). Lithium extraction from hard rock lithium ores (spodumene, lepidolite, zinnwaldite, petalite): technology, resources, environment and cost. *China Geol.* 6, 137–153. doi: 10.31035/cg2022088

Gao, L., Wang, H., Li, J., and Wang, M. (2020). Recovery of Lithium from Lepidolite by sulfuric acid and separation of Al/Li by Nanofiltration. *Fortschr. Mineral.* 10:981. doi: 10.3390/min10110981

Garbe-Schonberg, C. D. (1993). Simultaneous determination of thirty-seven trace elements in twenty-eight international rock standards by ICP-MS. *Geostandards Geoanalyt. Res.* 17, 81–97. doi: 10.1111/j.1751-908X.1993.tb00122.x

García-Meza, J. V., Fernández, J. J., Lara, R. H., and González, I. (2013). Changes in biofilm structure during the colonization of chalcopyrite by *Acidithiobacillus thiooxidans.* *Appl. Microbiol. Biotechnol.* 97, 6065–6075. doi: 10.1007/s00253-012-4420-6

Gatta, G. D., Cannaò, E., Gagliardi, V., and Fabelo, O. (2022). Crystal-chemical reinvestigation of probertite, CaNa[B5O7(OH)4]·3H2O, a mineral commodity of boron. *Am. Mineral.* 107, 1378–1384. doi: 10.2138/am-2022-8086

Greim, P., Solomon, A. A., and Breyer, C. (2020). Assessment of lithium criticality in the global energy transition and addressing policy gaps in transportation. *Nat. Commun.* 11:4570. doi: 10.1038/s41467-020-18402-y

H2020-Nemo Near-Zero-Waste Recycling of Low-Grade Sulphidic Mining Waste. Available at: https://h2020-nemo.eu/project-2/nemo-pilots/ (Accessed July 06 2023).

Hadrup, N., Frederiksen, M., and Sharma, A. K. (2021). Toxicity of boric acid, borax and other boron containing compounds: a review. *Regul. Toxicol. Pharmacol.* 121:104873. doi: 10.1016/j.yrtph.2021.104873

Han, M., Zhu, X., Ruan, C., Wu, H., Chen, G., Zhu, K., et al. (2024). Micro-biophysical interactions at bacterium-mineral interfaces determine potassium dissolution. *Environ. Technol. Innov.* 33:103524. doi: 10.1016/j.eti.2023.103524

Harahuc, L., Lizama, H. M., and Suzuki, I. (2000). Selective inhibition of the oxidation of ferrous Iron or sulfur in *Thiobacillus ferrooxidans.* *Appl. Environ. Microbiol.* 66, 1031–1037. doi: 10.1128/AEM.66.3.1031-1037.2000

Horeh, N. B., Mousavi, S. M., and Shojaosadati, S. A. (2016). Bioleaching of valuable metals from spent lithium-ion mobile phone batteries using aspergillus Niger. *J. Power Sources* 320, 257–266. doi: 10.1016/j.jpowsour.2016.04.104

Jaskula, B. (2023) USGS Lithium commodity summary 2023, U.S. Geological Survey Annual Publications.

Jian, Z., and Hejing, W. (2003). The physical meanings of 5 basic parameters for an X-ray diffraction peak and their application. *Chin. J. Geochem.* 22, 38–44. doi: 10.1007/BF02831544

Junne, T., Wulff, N., Breyer, C., and Naegler, T. (2020). Critical materials in global low-carbon energy scenarios: the case for neodymium, dysprosium, lithium, and cobalt. *Energy* 211:118532. doi: 10.1016/j.energy.2020.118532

Li, C.-T., and Peacor, D. R. (1968) The crystal structure of LiAlSi2O6-II ("β spodumene"). Zeitschrift für Kristallographie - Crystalline Materials. 126, 46–65. doi: 10.1524/zkri.1968.126.16.46

Liddell, K. N. C. (2005). Shrinking core models in hydrometallurgy: what students are not being told about the pseudo-steady approximation. *Hydrometallurgy* 79, 62–68. doi: 10.1016/j.hydromet.2003.07.011

Lin, X., Zhang, Z., Jiao, F., and Wei, Q. (2024). Process and mechanism of recovery of lepidolite and spodumene by flotation with synergistic action of alkali corrosion and mg(II). *Powder Technol.* 443:119962. doi: 10.1016/j.powtec.2024.119962

Liu, J., Yin, Z., Li, X., Hu, Q., and Liu, W. (2019). Recovery of valuable metals from lepidolite by atmosphere leaching and kinetics on dissolution of lithium. *Trans. Nonferrous Metals Soc. China* 29, 641–649. doi: 10.1016/S1003-6326(19)64974-5

Lovley, D. R., and Phillips, E. J. (1986). Availability of ferric Iron for microbial reduction in bottom sediments of the freshwater tidal Potomac River. *Appl. Environ. Microbiol.* 52, 751–757. doi: 10.1128/aem.52.4.751-757.1986

Marcinčáková, R., Kaduková, J., Mražíková, A., Velgosová, O., and Vojtko, M., (2015) Lithium bioleaching from Lepidolite using the yeast *Rhodotorula Rubra.* J Pol Miner Eng Soc.

Merck. (2023) Milli-Q-EQ-7000-Ultrapure-Water-Purification-System. Available at: https://www.merckmillipore.com/GB/en/product/Milli-Q-EQ-7000-Ultrapure-Water-Purification-System,MM_NF-C228480 (Accessed October 04 2023).

Mergen, A., Demirhan, M., and Bilen, M. (2004). "Fabrication of boric acid and sodium sulfate from borax." *Ceramic Forum Int.* 81, E37–E42.

Mishra, D., Kim, D.-J., Ralph, D. E., Ahn, J.-G., and Rhee, Y.-H. (2008). Bioleaching of metals from spent lithium ion secondary batteries using *Acidithiobacillus ferrooxidans.* *Waste Manag.* 28, 333–338. doi: 10.1016/j.wasman.2007.01.010

Moazzam, P., Boroumand, Y., Rabiei, P., Baghbaderani, S. S., Mokarian, P., Mohagheghian, F., et al. (2021). Lithium bioleaching: an emerging approach for the recovery of Li from spent lithium ion batteries. *Chemosphere* 277:130196. doi: 10.1016/j.chemosphere.2021.130196

Müller, B., Burgstaller, W., Strasser, H., Zanella, A., and Schinner, F. (1995). Leaching of zinc from an industrial filter dust with Penicillium, Pseudomonas and Corynebacterium: citric acid is the leaching agent rather than amino acids. *J. Ind. Microbiol.* 14, 208–212. doi: 10.1007/BF01569929

Ñancucheo, I., Rowe, O. F., Hedrich, S., and Johnson, D. B. (2016). Solid and liquid media for isolating and cultivating acidophilic and acid-tolerant sulfate-reducing bacteria. *FEMS Microbiol. Lett.* 363:fnw083. doi: 10.1093/femsle/fnw083

Newsome, L., Adams, R. L., Downie, H. F., Moore, K. L., and Lloyd, J. R. (2018). NanoSIMS imaging of extracellular electron transport processes during microbial iron(III) reduction. *FEMS Microbiol. Ecol.* 94:fiy104. doi: 10.1093/femsec/fiy104

Olaoluwa, D. T., Baba, A. A., and Oyewole, A. L. (2023). Beneficiation of a Nigerian lepidolite ore by sulfuric acid leaching. *Miner. Process. Extract. Metallurgy* 132, 134–140. doi: 10.1080/25726641.2023.2216612

Quezada, G. R., and Toledo, P. G. (2020). Structure of the Interface between Lithium-rich Spodumene and saltwater by density functional theory calculations and molecular dynamics simulations. *J. Phys. Chem. C* 124, 1446–1457. doi: 10.1021/acs.jpcc.9b10074

Rezza, I., Salinas, E., Calvente, V., Benuzzi, D., and de Tosetti, M. I. S. (1997). Extraction of lithium from spodumene by bioleaching. *Lett. Appl. Microbiol.* 25, 172–176. doi: 10.1046/j.1472-765X.1997.00199.x

Rezza, I., Salinas, E., Elorza, M., Sanz de Tosetti, M., and Donati, E. (2001). Mechanisms involved in bioleaching of an aluminosilicate by heterotrophic microorganisms. *Process Biochem.* 36, 495–500. doi: 10.1016/S0032-9592(00)00164-3

Ristović, I., Štyriaková, D., Štyriaková, I., Šuba, J., and Širadović, E. (2022). Bioleaching process for copper extraction from waste in alkaline and acid medium. *Fortschr. Mineral.* 12:100. doi: 10.3390/min12010100

Roberts, J. A. (2016). "Dolomite and Dolomitization" in Encyclopedia of geochemistry: A comprehensive reference source on the chemistry of the earth. ed. W. M. White (Cham: Springer International Publishing), 1–4.

Roy, J. J., Madhavi, S., and Cao, B. (2021). Metal extraction from spent lithium-ion batteries (LIBs) at high pulp density by environmentally friendly bioleaching process. *J. Clean. Prod.* 280:124242. doi: 10.1016/j.jclepro.2020.124242

Sedlakova-Kadukova, J., Marcincakova, R., Luptakova, A., Vojtko, M., Fujda, M., and Pristas, P. (2020). Comparison of three different bioleaching systems for Li recovery from lepidolite. *Sci. Rep.* 10:14594. doi: 10.1038/s41598-020-71596-5

Sheikh, E., El Aassy, I. E., Abdel-Rahman, A. A. H., Ayad, M. I., Fathy, W. M., Taha, M. N., et al. (2017). Recovery of uranium and associated elements from Ferruginous Gibbsite-Bearing Shale of Dabbet Abu Thor Locality, Sw Sinai, Egypt. *Int. J. Adv. Res.* 5, 1445–1459. doi: 10.21474/IJAR01/6105

Siezen, R. J., and Wilson, G. (2009). Bioleaching genomics. *Microb. Biotechnol.* 2, 297–303. doi: 10.1111/j.1751-7915.2009.00108.x

Siljkovic, B., Denic, N., and Rakic, G. (2017). Environmental and economic assessments the effect of critical mineral of green revolution: Lithium. *Mining Metallurgy Eng. Bor.* 2, 103–114. doi: 10.5937/mmeb1702103s

Stanley, C. J., Jones, G. C., Rumsey, M. S., Blake, C., Roberts, A. C., Stirling, J. A. R., et al. (2007). Jadarite, LiNaSiB3O7(OH), a new mineral species from the Jadar Basin, Serbia. *Eur. J. Mineral.* 19, 575–580. doi: 10.1127/0935-1221/2007/0019-1741

Stefanović, N., Danilović Hristić, N., and Petrić, J. (2023). Spatial planning, environmental activism, and politics—case study of the Jadar project for Lithium exploitation in Serbia. *Sustain. For.* 15:1736. doi: 10.3390/su15021736

Su, H., Zhu, Z., Wang, L., and Qi, T. (2019). Research progress in extraction and recovery of lithium from hard-rock ores. *CIESC J.* 70, 10–23. doi: 10.11949/j.issn.0438-1157.20180465

Swain, B. (2017). Recovery and recycling of lithium: a review. *Sep. Purif. Technol.* 172, 388–403. doi: 10.1016/j.seppur.2016.08.031

Talens Peiró, L., Villalba Méndez, G., and Ayres, R. U. (2013). Lithium: sources, production, uses, and recovery outlook. *JOM* 65, 986–996. doi: 10.1007/s11837-013-0666-4

USGS Commodity Statistics (2014) How Do We Use Lithium? Where Does Lithium Come From? USGS Mineral Resources Program Lithium-For Harnessing Renewable Energy.

Vandevivere, P., Welch, S. A., Ullman, W. J., and Kirchman, D. L. (1994). Enhanced dissolution of silicate minerals by bacteria at near-neutral pH. *Microb. Ecol.* 27, 241–251. doi: 10.1007/BF00182408

Velardo, A., Giona, M., Adrover, A., Pagnanelli, F., and Toro, L. (2002). Two-layer shrinking-core model: parameter estimation for the reaction order in leaching processes. *Chem. Eng. J.* 90, 231–240. doi: 10.1016/S1385-8947(02)00038-4

Vera, M., Schippers, A., Hedrich, S., and Sand, W. (2022). Progress in bioleaching: fundamentals and mechanisms of microbial metal sulfide oxidation – part A. *Sci. Bus. Media Deutsc. GmbH.* 106, 6933–6952. doi: 10.1007/s00253-022-12168-7

Whitfield, P. S., le Page, Y., Grice, J. D., Stanley, C. J., Jones, G. C., Rumsey, M. S., et al. (2007). LiNaSiB3O7(OH) - novel structure of the new borosilicate mineral jadarite determined from laboratory powder diffraction data. *Acta Crystallogr. B* 63, 396–401. doi: 10.1107/S0108768107010130

Xie, R., Zhu, Y., Liu, J., and Li, Y. (2021). The flotation behavior and adsorption mechanism of a new cationic collector on the separation of spodumene from feldspar and quartz. *Sep. Purif. Technol.* 264:118445. doi: 10.1016/j.seppur.2021.118445

Zhan, Y., Yang, M., Zhang, S., Zhao, D., Duan, J., Wang, W., et al. (2019). Iron and sulfur oxidation pathways of *Acidithiobacillus ferrooxidans*. *Springer* 35:2632. doi: 10.1007/s11274-019-2632-y

Zhao, X., Wang, R., Lu, X., Lu, J., Li, C., and Li, J. (2013). Bioleaching of chalcopyrite by *Acidithiobacillus ferrooxidans*. *Miner. Eng.* 53, 184–192. doi: 10.1016/j.mineng.2013.08.008

The promotion effect of FeS$_2$ on Sb$_2$S$_3$ bioleaching and Sb speciation transformation

Xing-fu Zheng[1,2,3], Jin-lan Xia[1,3]*, Zhen-yuan Nie[1,3], Hong-peng Cao[1,3], Rui-Jia Hu[2], Yu-ting Liang[1] and Hong-chang Liu[1,3]*

[1]School of Minerals Processing and Bioengineering, Central South University, Changsha, China, [2]Guangxi Academy of Sciences, Nanning, China, [3]Key Lab of Biometallurgy of Ministry of Education of China, Central South University, Changsha, China

Stibnite (Sb$_2$S$_3$) is an important but difficult to biologically leach mineral, so it is important to find a potential scheme for improving the bioleaching rate of Sb$_2$S$_3$. In this study, by combining experiments and first-principles density functional theory (DFT) calculations, the impact and related mechanisms of pyrite (FeS$_2$) on stibnite (Sb$_2$S$_3$) bioleaching were studied for the first time. The bioleaching results revealed that FeS$_2$ obviously improved the Sb$_2$S$_3$ bioleaching rate, and in the 0.5FeS$_2$:0.5CuFeS$_2$ system, the bioleaching rate of Sb$_2$S$_3$ increased from 2.23 to 24.6%, which was the best mass mixing ratio. The XPS and XANES results revealed that during the bioleaching process, Sb$_2$S$_3$ was transformed to Sb$_2$O$_3$ and Sb$_2$O$_5$. The electrochemical results revealed that after FeS$_2$ was mixed, a FeS$_2$-Sb$_2$S$_3$ galvanic cell formed, which promoted the electron transfer efficiency and redox reaction of Sb$_2$S$_3$. The DFT results show that between the Sb$_2$S$_3$ (0 1 0) and FeS$_2$ (1 0 0) surfaces, S-Fe, S-S, S-Sb, and Sb-Fe bonds are formed, and the direction of electron transfer is from Sb$_2$S$_3$ to FeS$_2$; the work functions for Sb$_2$S$_3$ after addition of FeS$_2$ decrease, implying that faster electron transfer occurs; Fe(III)-6H$_2$O derived from FeS$_2$ adsorbs on the surface more easily than does glucose, which is the major component of the extracellular polymeric substances in bacteria, indicating that during the bioleaching process, Fe(III)-6H$_2$O plays an important role; after mixing, both Fe(III)-6H$_2$O and glucose adsorb on the Sb$_2$S$_3$ (0 1 0) surface more easily, with stronger bonds and larger adsorption energies, which are in good agreement with the experimental results.
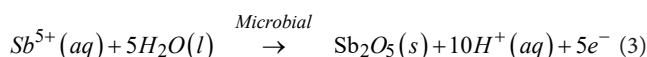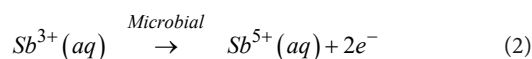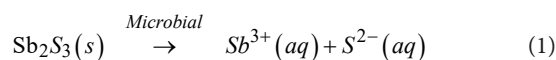
KEYWORDS

Sb$_2$S$_3$, FeS$_2$, bioleaching, XANES spectroscopy, electrochemistry, DFT calculations

1 Introduction

Antimony (Sb) plays an important role in social development and is used in storage batteries, printing industries, semiconductors, and pharmaceuticals (Awe and Sandström, 2013; Zhang et al., 2019) and is an important strategic material. Currently, via the pyrometallurgical route, Sb can be extracted from stibnite (Sb$_2$S$_3$), which is the most important and ubiquitous antimony ore (Biver and Shotyk, 2012; Multani et al., 2016), but such a method results in high-energy consumption and environmental pollution. In addition, with the mining of antimony ore and the decrease in high-grade antimony ores, there is a need to develop new methods to extract Sb from low-grade ores or tailings.

Bioleaching is a green, low-cost, and low-emission technology used to extract metal ions from ores (Hong et al., 2023; Zhao et al., 2020), and plenty of bioleaching research has been carried out on sulfide ore. For Sb$_2$S$_3$, several researchers have explored the dissolution process

of Sb_2S_3 and reported that microorganisms play important roles in the release, migration, and transformation processes of Sb_2S_3 (Bagherifam et al., 2021; Loni et al., 2020), as well as the environmental processes and relevant molecular mechanisms of antimony in mining areas (Wang et al., 2020; Yang and He, 2015; Ye et al., 2020). These studies have focused mainly on the environmental effects of environmental microorganisms. The use of acidophiles to extract Au from refractory gold ores containing abundant stibnite and gudmundite has also been studied (de Carvalho et al., 2019); recently, we studied the dissolution of stibnite mediated by *Acidithiobacillus ferrooxidans* (*A. ferrooxidans*) and relevant Sb and S speciation transformations and reported that *A. ferrooxidans* can enhance the leaching process of stibnite in comparison with sterile control experiments (Wang et al., 2022). During the bioleaching process, microorganisms convert antimony through direct oxidation or indirect reduction, that is, Sb(III) is oxidized as an energy metabolism substrate to Sb(V), as shown in Equations (1)–(3), obtaining the energy required for its growth (Loni et al., 2020; Lu et al., 2018). However, the bioleaching rate is not high because of the toxicity and insolubility of Sb_2S_3. Therefore, it is necessary to study methods to improve the antimony leaching rate. The associated minerals significantly impact on mineral dissolution (Multani et al., 2016; Wilson et al., 2004); however, few studies have investigated about how pyrite (FeS_2), a common natural mineral associated with Sb_2S_3, affects the bioleaching rate of Sb_2S_3 (Yan et al., 2020) and the transformation process of Sb during the bioleaching process, and the related mechanisms are still unclear.

$$Sb_2S_3(s) \xrightarrow{Microbial} Sb^{3+}(aq) + S^{2-}(aq) \qquad (1)$$

$$Sb^{3+}(aq) \xrightarrow{Microbial} Sb^{5+}(aq) + 2e^- \qquad (2)$$

$$Sb^{5+}(aq) + 5H_2O(l) \xrightarrow{Microbial} Sb_2O_5(s) + 10H^+(aq) + 5e^- \quad (3)$$

In the present study, the effects of FeS_2 on the fate and speciation transformation of Sb during the bioleaching of stibnite were studied via synchrotron radiation-based Sb X-ray near-edge structure (XANES) spectroscopy, and X-ray photoelectron spectroscopy (XPS) analyses, combined with density functional theory (DFT) calculations. In bioleaching bacterial strains, e.g., *Sulfobacillus thermosulfidooxidans* (Liu et al., 2024; Li, 2017), extracellular polymeric substances (EPS) are important components that are beneficial for bacterial adhesion processes (Wang et al., 2010), and glucose is the major sugar component in EPS (Gehrke et al., 1998); thus, in DFT calculations, glucose is utilized to simulate the interactions between bacteria and minerals (Zheng et al., 2020), and the Fe(III)-6H$_2$O that is oxidized from FeS_2 is also considered to simulate indirect effects during the bioleaching process (Zheng et al., 2019; Magini, 1979; Magini and Radnai, 1979). This study aims to understand the element migration mechanism in the Sb mining area, thus further identifying a potential scheme for improving the bioleaching rate of Sb_2S_3. To our knowledge, reports exploring the interfacial interactions for the FeS_2-Sb_2S_3 bioleaching system by combining experiments and DFT calculations are rare.

2 Materials and methods

2.1 Minerals

The minerals Sb_2S_3 and FeS_2 were provided by the School of Minerals Processing and Bioengineering, Central South University, Changsha, China. The XRD (X-ray diffraction patterns) results in Figure 1 revealed that the pyrite is pure, and the stibnite is mainly composed of Sb_2S_3 and quartz. Furthermore, the composition of stibnite was determined by XRF (X-ray fluorescence), and the results (Supplementary Table S1) show that Sb, S, and Si are the main components, with a small amount of Al. The ICP (inductively coupled plasma-optical emission spectroscopy) results revealed that the contents of Sb, S, and Fe were 2:3:0. Before the bioleaching tests, the mineral samples were crushed and milled to 37–74 µm particle sizes.
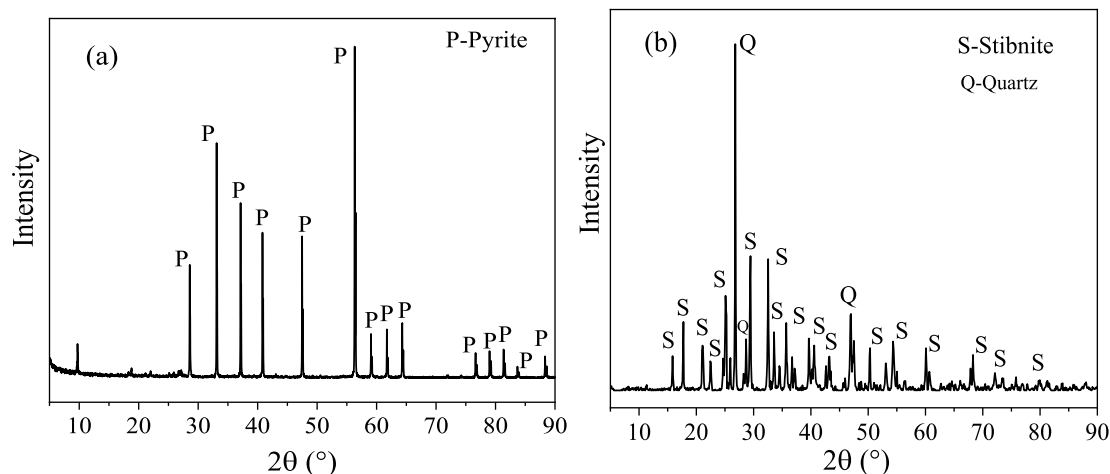

FIGURE 1
XRD results for FeS_2 **(A)** and Sb_2S_3 **(B)**.

FeS$_2$ and Sb$_2$S$_3$ were mixed well at weight ratios of 0:1, 0.1:0.9, 0.2:0.8, 0.3:0.7, 0.5:0.5, and 0.8:0.2.

2.2 Bioleaching experiments

For the bioleaching experiments, the mixed samples were used as energy substrates, and the pulp density was 1% (w/v). The bacterium, *Sulfobacillus thermosulfidooxidans* YN22 (*S. thermosulfidooxidans*), provided by the School of Minerals Processing and Bioengineering, was used; the inoculation concentration was 4×10^7 cells/mL in 100 mL 9 K medium, and the pH was adjusted to 2.0. Then, the flasks were placed in a rotary shaker at 180 rpm and 45°C. The pH and ORP during the bioleaching process were determined by a pH meter (PHS-3C) and Pt electrode using a calomel electrode (Ag/AgCl) as the reference, respectively; the concentrations of Sb and Fe were determined by ICP (SPECTROBLUE FMX26, Philadelphia, PA, United States), and the concentration of [Fe^{3+}] was determined by the sulfosalicylic acid method. In detail, for [Sb] and [TFe], 1 mL of solution was collected, diluted with 10% nitric acid, and preserved at −80°C until analysis; for [Fe^{3+}], 1 mL of solution was collected in the anaerobic chamber and diluted with prepared anaerobic water; then, 300 μL of 10% sulfosalicylic acid solution and 300 μL of diluted solution were added into a colorimetric tube, quantified to 10 mL with distilled water, shaken well, and then the mixed solution was measured using a microplate spectrophotometer at a wavelength of 500 nm. All the experiments were conducted in triplicate.

2.3 Residues composition analysis

The solid leaching residues were collected after leaching for 0, 5, and 10 days, washed three times with diluted sulfuric acid (pH 2.0) and hydrochloric acid (pH 2.0), and stored at −70°C. The surface morphologies of the residues were determined by scanning electron microscopy (SEM, Nano230, FEI) coupled with energy dispersive spectroscopy (EDS). In detail, the samples were prefixed with 25% formaldehyde, dehydrated via a graded ethanol series, coated with gold nanoparticles, and introduced into the SEM chamber for observation.

The residues phase compositions were analyzed by XRD in the range of 10–90° on a Bruker D8 instrument (BrukerAXS) with Cu Kα radiation The Sb speciation of the solid residue was analyzed by X-ray photoelectron spectroscopy (XPS). Briefly, XPS spectra were collected by an X-ray photoelectron spectrometer (Thermo Scientific K-Alpha+, United Kingdom) with a voltage and current of 12 kV and 6 mA, respectively. The obtained XPS data were analyzed in CasaXPS software, and all photoelectron binding energies were referenced to the C1s adventitious contamination peak set at 284.5 eV BE. Furthermore, Sb L-edge XANES spectroscopy was performed at beamline 4B7A in the Beijing Synchrotron Radiation Facility, Beijing, China. The Sb L-edge XANES spectra were recorded in total electron yield (TEY) mode with a step size of 0.1 eV and a dwell time of 2 s at each energy at 25°C from 4.60 to 4.80 keV across the Sb L-edge. Owing to the easy oxidization of the sample surfaces, all samples and tests were performed under strict anaerobic conditions with high-purity nitrogen gas (Goh et al., 2006), and were detected under the same conditions and parameter settings. The XANES spectra were normalized to the maximum of the absorption spectrum using reference spectra with the IFEFFIT program (Ide-Ektessabi et al., 2004; Prange, 2008; Ravel and Newville, 2005).

2.4 Electrochemical experiments

Electrochemical measurements were performed in 9 K medium (pH 2.0) via an electrochemical working station (INTERFACE 1010E, GAMRY, America). A conventional three-electrode system was used, including a counter electrode (carbon rods), a reference electrode (Ag/AgCl), and a working electrode (mineral electrode). The working electrodes were prepared by mixing 0.3 g graphite, 1.05 g minerals, and 0.15 g solid paraffin, and then the mixture was compressed at 120 KPa for 10 min. The Tafel curves were tested from −200 to +750 mV (vs open circuit potential, OCP) with a scan rate of 1 mV/s; the EIS (electrochemical impedance spectroscopy) curves were tested in the frequency range of 10^{-1} to 10^{-5} Hz, and fitted by Gamry Echem Analyst; the forward CV (cyclic voltammetry) was scanned from −1.0 to +1.0 V, while the reversed CV from +1.0 to −1.0 V. To explore the role of bacteria, *S. thermosulfidooxidans* was added to the medium with an inoculation amount of $2*10^8$ cells/mL during the CV test. In this study, all the potentials reported were expressed vs. Ag/AgCl.

2.5 Computational details

The DFT calculations were performed via CASTEP (Cambridge Sequential Total Energy Package) (Segall et al., 2002) and GGA-PBE (Generalized gradient approximation-Perdew-Burke-Ernzerhof functional) (Perdew et al., 1996; Segall et al., 2002), in which only the valence electrons were considered explicitly using ultrashort pseudopotentials (Vanderbilt, 1990). Sb$_2$S$_3$ belongs to the space group Pmn21 (Park et al., 2010), and FeS$_2$ belongs to the space group Th^6-Pa3 (Qiu et al., 2004). After obtaining the Sb$_2$S$_3$ (0 1 0) surface and the FeS$_2$ (1 0 0) surface, which are the most stable surfaces of the two sulfide ores (Blanchard et al., 2007; Cao et al., 2018; de Lima et al., 2011; de Oliveira et al., 2012), the supercells were built with a vacuum slab of 15 Å to avoid adjacent interlayer interactions (Fan et al., 2017). The FeS$_2$-Sb$_2$S$_3$ interaction model was built by using building layer tools, and the calculation was performed after constraining the model size. A $3 \times 3 \times 1$ k-point and 500 eV cutoff energy were used for the calculations. Glucose and Fe(III)-6H$_2$O were optimized in a $15 \times 15 \times 15$ Å slab. The convergence tolerances were set to a maximum displacement of 0.002 Å, a maximum force of 0.05 eV/Å, a maximum energy change of 2.0×10^{-5} eV/atom, and a maximum stress of 0.1 GPa, while the SCF convergence tolerance was set to 2.0×10^{-6} eV/atom. For all the calculations, spin polarization, dipole correction, and DFT-D correction were considered. The frontier orbitals, HOMO-LUMO, were calculated in DMol^3. According to previous work, the calculation method above can provide reliable results for Sb$_2$S$_3$ and FeS$_2$ (Cao et al., 2018; Cao et al., 2020; Zheng et al., 2018).

The glucose or Fe(III)-6H$_2$O adsorption energies (E$_{ads}$) can be calculated using equation 4:

$$E_{ads} = E_{(FeS2-Sb2S3-adsorbate)} - \left(E_{FeS2-Sb2S3} + E_{adsorbate} \right) \quad (4)$$

where $E_{FeS2-CuFeS2}$, $E_{adsorbate}$, and $E_{(FeS2-CuFeS2 - adsorbate)}$ represent the total energies for the clean FeS_2-Sb_2S_3 surface, the free glucose/Fe(III)-$6H_2O$, and the FeS_2-Sb_2S_3–adsorbate system, respectively.

3 Results and discussion

3.1 Leaching parameters

The results (Figure 2) show that by adding FeS_2, the pH decreases faster while the ORP increases faster, implying that the dissolution process of Sb_2S_3 may be accelerated. After leaching for 5 days, the extraction rates of Sb were approximately 2.22% (Sb_2S_3), 3.15% (0.1 FeS_2: 0.9 Sb_2S_3), 4.1% (0.2 FeS_2: 0.8 Sb_2S_3), 5.7% (0.3 FeS_2: 0.7 Sb_2S_3), 24.6% (0.5 FeS_2: 0.5 Sb_2S_3), and 18.7% (0.8 FeS_2: 0.2 Sb_2S_3), where in the sterile control results (Supplementary Figure S1), the extraction rates of Sb were lower than 0.7%. After 10 days of leaching, the extraction rates of Sb decreased, and the reason may be the formation of secondary products that were found by the further results. In the

0.5 FeS_2: 0.5 Sb_2S_3 system, the Sb dissolution rate was almost 11 times higher than that of pure Sb_2S_3, indicating that such a mixing ratio is the best leaching group. In addition, Figure 2D shows that Fe^{3+} occurs after the addition of FeS_2 because FeS_2 is oxidized by *S. thermosulfidooxidans*. In addition, Fe^{3+} attacks minerals (Jiang et al., 2019), which is called indirect action, thereby accelerating the dissolution of minerals. Notably, the concentration of Fe^{3+} is lower than that of the total Fe (Supplementary Figure S2A), which is probably because of formation of Fe^{2+} (Ubaldini et al., 2000; Zhang et al., 2019), as shown in Supplementary Figure S2B. In the next section, the 0.5 FeS_2: 0.5 Sb_2S_3 mixture is analyzed further.

The XRD results (Figure 3) revealed that after 5 and 10 days of bioleaching, the peaks of FeS_2 at 47.5° weakened, implying the dissolution of FeS_2; the peak at 27° associated with Sb_2O_3 became stronger, and the peaks at 15.7° and 17.6° associated with Sb_2S_3 became weaker, indicating that Sb_2S_3 was transformed to Sb_2O_3 during bioleaching (Wang et al., 2022). Notably, in the sterile control sample, the peaks presented little or no change after 10 days of leaching. The SEM results (Figure 4; Supplementary Figure S3) show that by adding FeS_2, the Sb_2S_3 surface obviously changed after 5 days of leaching with obvious secondary products, whereas the changes in pure Sb_2S_3 (Supplementary Figure S4) were negligible, confirming the promoting
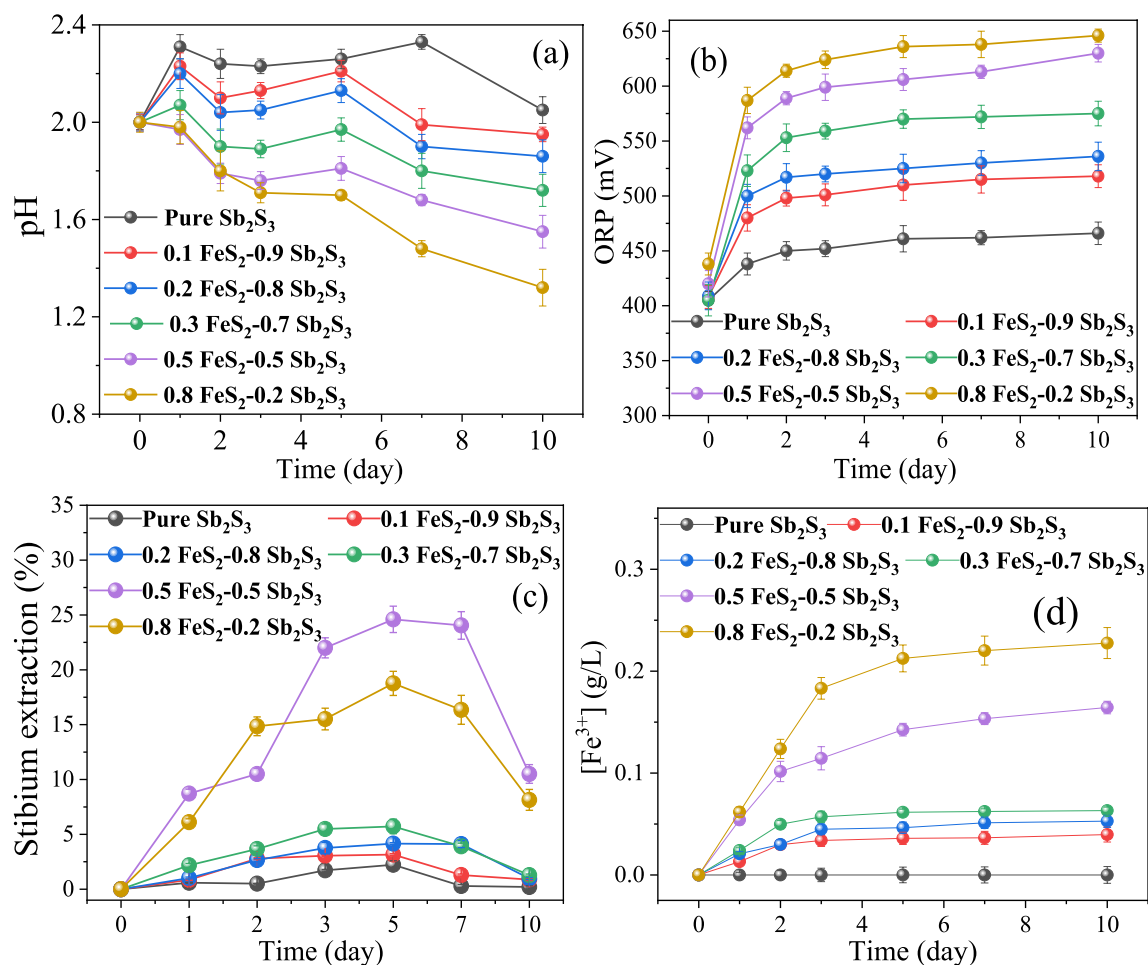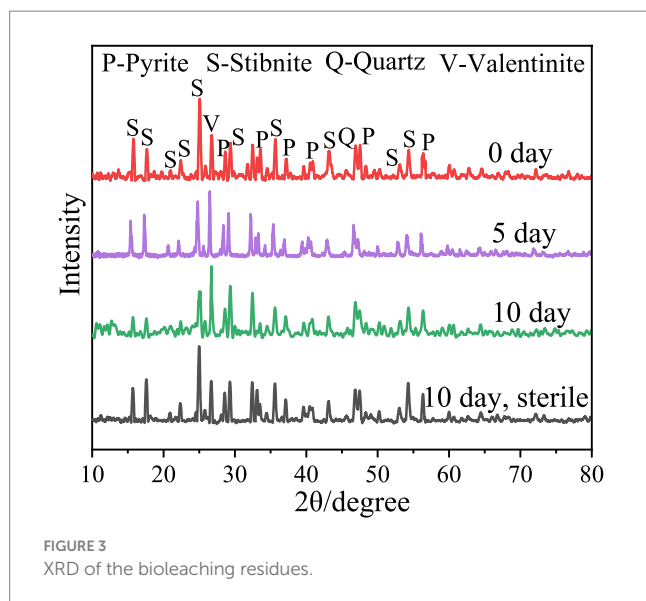

FIGURE 2
Curves for the pH **(A)**, ORP **(B)**, Sb extraction rate **(C)**, and Fe^{3+} concentration for the bioleaching of Sb_2S_3 in the presence of varying concentrations of FeS_2.

FIGURE 3
XRD of the bioleaching residues.

effect of FeS_2, and the source of secondary minerals was the dissolution of some FeS_2 (Yang et al., 2016). In addition, in the sterile control sample (Figures 4D,E), the mineral surface changed little, indicating that bacteria play an important role in the oxidation of minerals.

The XPS results (Figure 5) show that after 5 days of bioleaching, part of Sb_2S_3 (529.5 eV) (Morgan et al., 1973) was transformed to Sb_2O_3 (530.5 eV, 48.7%) and Sb_2O_5 (532.1 eV, 9%), and the proportion of Sb_2S_3 decreased from 74.6 to 42.3%; as the leaching time increased to 10 days, the proportion of Sb_2O_3 increased to 66%, and that of Sb_2O_5 increased to 9.4%, whereas the proportion of Sb_2S_3 decreased to 24.5%; in the sterile controlled experiment (Figure 5D), the proportion of Sb_2S_3 decreased to 62.4% after 10 days of leaching, which was much slower.

The Sb L-edge XANES spectra (Figure 6) show that after 5 and 10 days of bioleaching, the peak shifts from 4.7062 to 4.707 keV, indicating the conversion of Sb_2S_3 to Sb_2O_3, and the peak at 4.711 keV increases with increasing bioleaching time, which indicates the conversion of Sb(III) to Sb(V), similar to the XPS results. In addition, in the sterile controlled experiment, after 10 days, no or little Sb(III) was converted to Sb(V), confirming the important role of bacteria.

3.2 Electrochemical analyses

For mineral-mineral interactions, a galvanic effect may occur when two minerals have different corrosion potentials; however, minerals with higher potentials can act as cathodes and the other minerals with lower potential can act as anodes electrode (Ekmekqi and Demirel, 1997). The lower the value of the corrosion potential is, the easier it is for the mineral to corrode. Tafel tests were performed to analyze the mineral corrosion kinetics. The Tafel results (Figure 7A) show that the corrosion potentials (vs. Ag/AgCl) for FeS_2 and Sb_2S_3 are 428 mV and 327 mV, respectively; thus in a FeS_2-Sb_2S_3 system, the galvanic effect occurs, and Sb_2S_3 is the anode electrode, implying that the leaching rate of Sb_2S_3 is promoted (Zheng et al., 2021).

Among electrochemical methods, CV is widely used due to its simple operation and effective results for the interpretation of electrochemical reactions. The results in Figure 7 show that the

oxidation peaks of Sb_2S_3 and the corresponding reduction peaks are not symmetrical, indicating that the redox reaction on the Sb_2S_3 surface is an irreversible process (Córdoba et al., 2009). Figures 7B,C shows that the CV peaks of FeS_2-Sb_2S_3 are similar to those of Sb_2S_3 (A1, B1, and C1), implying that Sb_2S_3 reacts preferentially during the electrochemical process. The current density is greater after addition of FeS_2, indicating an increase in the Sb_2S_3 reaction.

To investigate the effects of bacteria on the dissolution of Sb_2S_3, the effects of CV with *S. thermosulfidooxidans* were analyzed. Supplementary Figure S5 shows that after adding bacteria ($2*10^8$ cells/ml), the current density increased further, confirming that the bacteria can obviously enhance the leaching rate of Sb_2S_3. During the bioleaching process, some of the FeS_2 is oxidized by bacteria to produce Fe^{3+} (Yang et al., 2016), so the effect of Fe^{3+} was also studied, and the results (Supplementary Figure S6) revealed that after adding Fe^{3+} (0.15 g/L), the current density also increased, indicating that Fe^{3+} can also enhance the leaching rate of Sb_2S_3.

The electron transfer efficiency of minerals was analyzed via EIS. The data obtained were analyzed by fitting the impedance data to an appropriate equivalent circuit as Rs(Q1(R1Q2)) (Bevilaqua et al., 2009; Supplementary Figure S7). In the equivalent circuit, Rs, R1, and Q1 represent the solution resistance, ion exchange impedance, and constant phase element, respectively. Q1 is connected to the electrode interface. Q2 represents a Warburg element, and is related to the electrode/electrolyte interface diffusion process (Zeng et al., 2020). Figure 8 shows that after adding FeS_2, the curve radius decreases; the results in Table 1 show that R1 for FeS_2-Sb_2S_3 (30.71 $\Omega\cdot cm^{-2}$) is much smaller than that for Sb_2S_3 (24,300 $\Omega\cdot cm^{-2}$). Both results indicate that after mixing, the ion exchange resistance on the mineral surface decreases; in other words, after Sb_2S_3 mixed with FeS_2, the leaching system has a relatively high electron transfer efficiency, which significantly promotes the bioleaching rate.

3.3 Computational results

3.3.1 Electronic structure

The models of Sb_2S_3 and FeS_2-Sb_2S_3 are shown in Figure 9, and the corresponding atomic numbers used are shown in Supplementary Figure S8. The results in Figure 9 show that after adding FeS_2, the surface structure of Sb_2S_3 gradually became disordered, which was conducive to the dissolution of Sb_2S_3. Table 2 shows that after adding FeS_2, the Hirshfeld charge value of FeS_2 decreases from 0 to −0.77, whereas the charge value of Sb_2S_3 increases from 0 to 0.77, indicating that the direction of electron transfer is from Sb_2S_3 to FeS_2.

The bond lengths between FeS_2 and Sb_2S_3 are shown in Table 3. In the FeS_2-Sb_2S_3 galvanic cell, S-Fe, S-S, Sb-Fe, and S-Sb bonds formed at the interface, and the number of S-Fe bonds was greater than that of the other materials. S3-S23 is the shortest bond (2.128 Å), whereas Sb12-S48 is the longest bond (2.619 Å). The Mulliken bond population results show that the S2-Fe2 bond has stronger covalent interactions, and that the Sb5-S32 bond has stronger ionic interactions.

The PDOS of the S3-S23, S6-Fe5, Sb4-Fe8, and Sb6-S32 bonds were analyzed further. Figure 10 shows that in the S3-S23 bond, from −20 eV to 10 eV, the main peaks belong to $\sigma(2s)$, $\sigma^\star(2s)$, $\sigma(2p)$, $\pi(2p)$, $\pi^\star(2p)$, and $\sigma^\star(2p)$ bonds, and the maximum overlap area between S 3p ranges from −10 eV to 5 eV, implying that $\sigma(2p)$ and $\pi(2p)$ are the
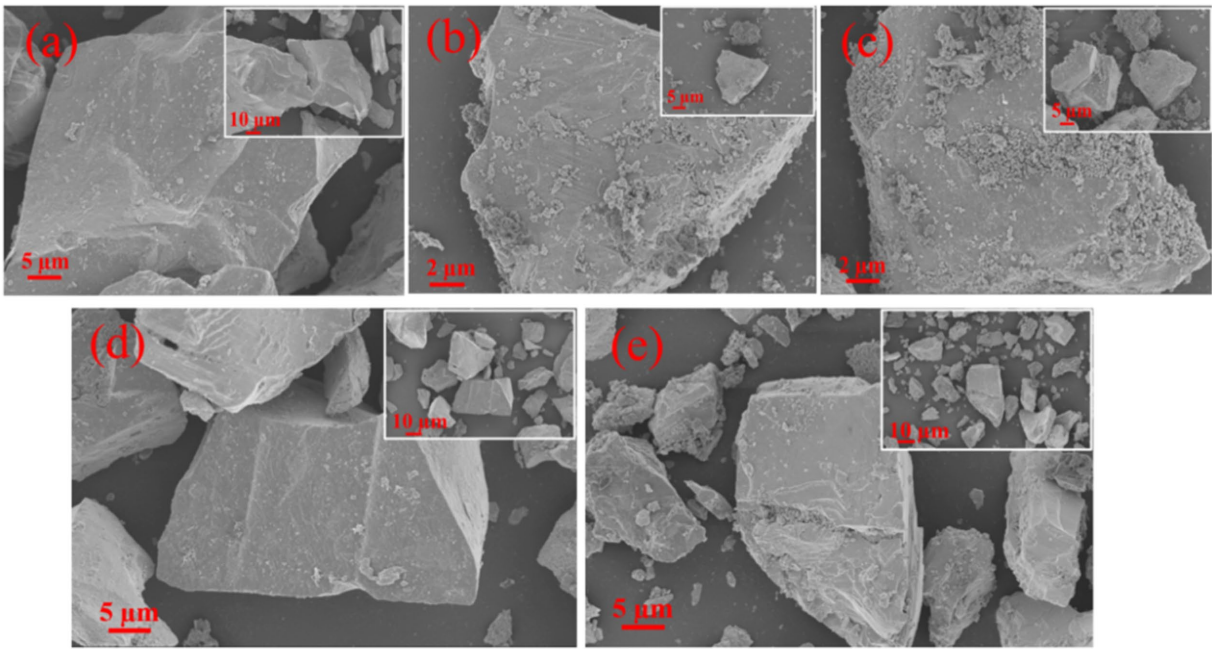
FIGURE 4
(A–C) SEM images of the bioleaching residues after 0, 5, and 10 days with the addition of FeS$_2$; **(D,E)** SEM images of the residues after 0 and 10 days in the sterile control.
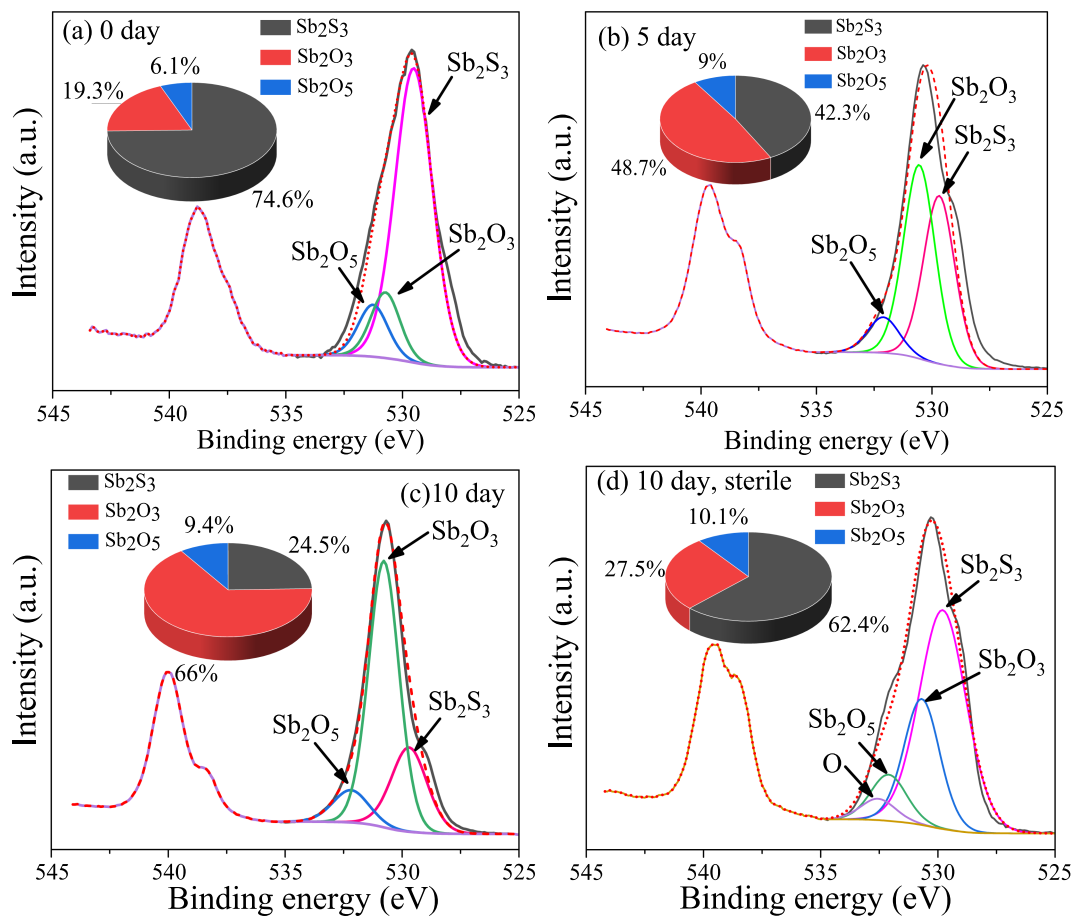

FIGURE 5
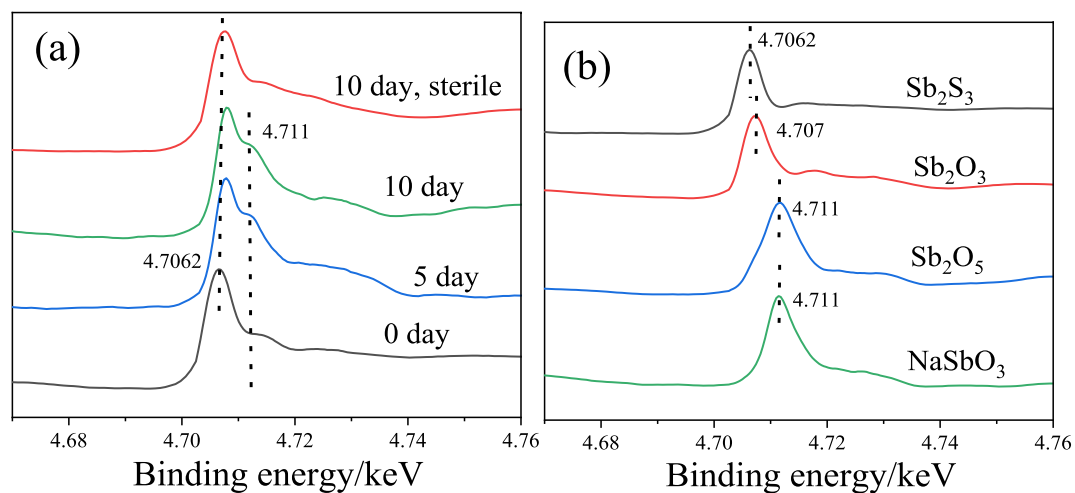XPS spectra of Sb on the surface of the bioleaching residues.

FIGURE 6
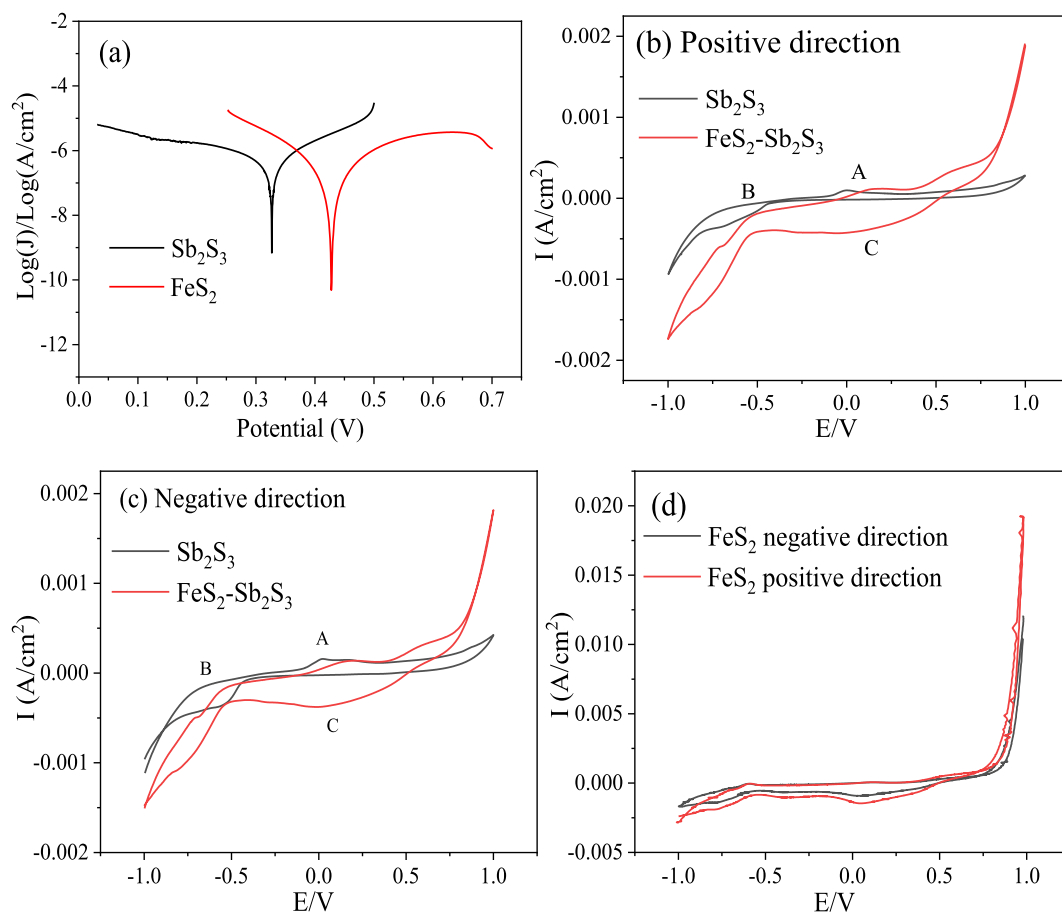Sb L-edge XANES spectra of the residues during bioleaching **(A)** and the reference materials **(B)**.

FIGURE 7
Tafel and CV curves for FeS$_2$, Sb$_2$S$_3$ and FeS$_2$-Sb$_2$S$_3$.

main covalent interactions; in the S6-Fe5 bond, from −15 eV to 5 eV, the main peaks belong to σ(s-d), σ*(s-d), π(p-d), and π*(p-d) bonds, and the maximum overlap area between S 3p and Fe 3d ranges from −10 eV to 5 eV, implying that π(p-d) are the main covalent interactions, and the same result can also be obtained in the Sb4-Fe8 bond; in the Sb6-S32 bond, the antibonding function from 0 eV to 15 eV is strong, implying weak covalent interactions, similar to the population results.
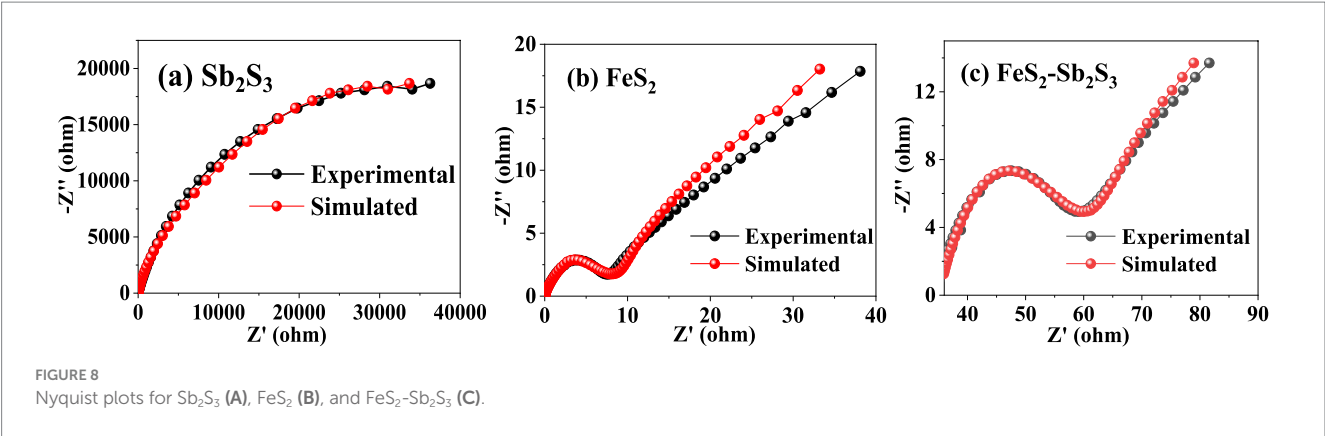
FIGURE 8
Nyquist plots for Sb_2S_3 **(A)**, FeS_2 **(B)**, and FeS_2-Sb_2S_3 **(C)**.

TABLE 1 Fitting results obtained via the circuit Rs(Q1(R1Q2)) for Sb_2S_3, FeS_2, and FeS_2-Sb_2S_3.

	Rs $\Omega \cdot cm^{-2}$	R1 $\Omega \cdot cm^{-2}$	Q1-T $S \cdot s^a \cdot cm^{-2}$	Q1-P $S \cdot s^a \cdot cm^{-2}$	Q2 $S \cdot s^{1/2} \cdot cm^{-2}$
Sb_2S_3	16.73	24,300	1.781×10^{-5}	0.817	6.820×10^{-5}
FeS_2	16.73	10	9.25×10^{-4}	0.753	9.027×10^{-2}
FeS_2-Sb_2S_3	16.73	30.71	8.59×10^{-4}	0.631	7.872×10^{-2}

FIGURE 9
Optimized configurations of Sb_2S_3 **(A)**, and FeS_2-Sb_2S_3 **(B)**.
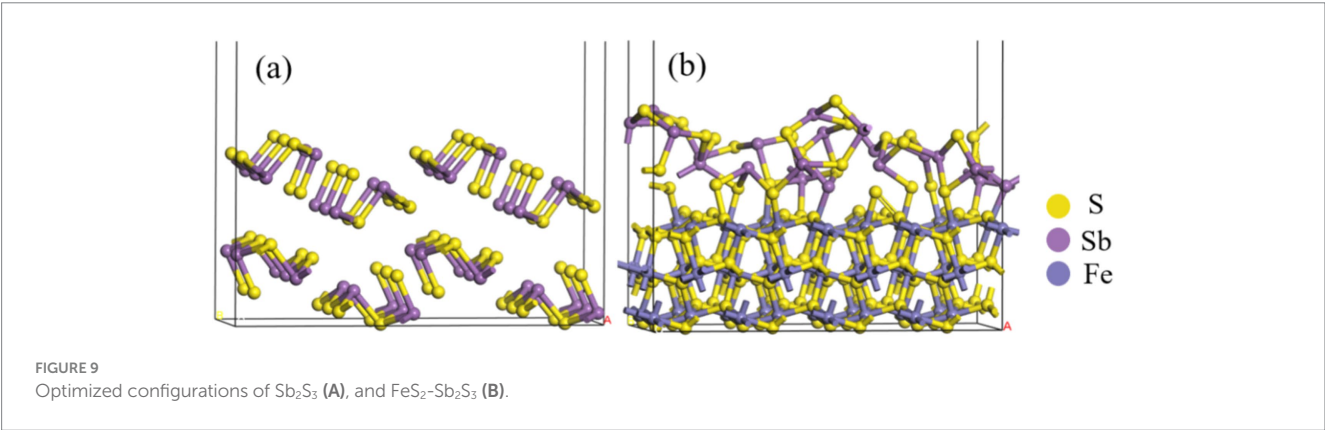
TABLE 2 Hirshfeld charge analysis of FeS_2-Sb_2S_3.

	Charge/e Before optimization	Charge/e After optimization
FeS_2	0	-0.77
Sb_2S_3	0	0.77

The work functions (Figure 11) for Sb_2S_3 and FeS_2-Sb_2S_3 were calculated to be 5.17 eV, and 4.59 eV, respectively, implying that the electron transfer efficiency becomes faster after mixing, which agrees with the EIS results above.

3.3.2 Adsorption configurations and energies

In the theory of frontier orbitals, HOMO (highest occupied molecular orbital) can donate electrons, and LUMO (lowest unoccupied molecular orbital) can accept electrons (Sauer and Sustmann, 1980). According to previous studies (Sauer and Sustmann, 1980; Zheng et al., 2018), a smaller HOMO-LUMO energy difference absolute value implies a more beneficial interaction. The results in Table 4 shows that

TABLE 3 Mulliken bond population analysis of FeS_2-Sb_2S_3.

Bond	Bond Lengths (Å)	Populations
S2-Fe2	2.354	0.44
S3-S23	2.128	0.25
S4-Fe4	2.307	0.44
S6-Fe5	2.267	0.42
S7-Fe6	2.491	0.32
Sb4-Fe8	2.546	0.14
Sb5-S32	2.606	0.10
S12-Fe11	2.306	0.26
S13-Fe12	2.334	0.41
S15-Fe13	2.323	0.42
S16-Fe14	2.306	0.26
Sb11-Fe16	2.547	0.21
Sb12-S48	2.619	0.20

FIGURE 10
PDOS of the bonds between the FeS_2 and Sb_2S_3 surfaces.

FIGURE 11
Work functions of Sb_2S_3 **(A)**, and FeS_2-Sb_2S_3 **(B)**.
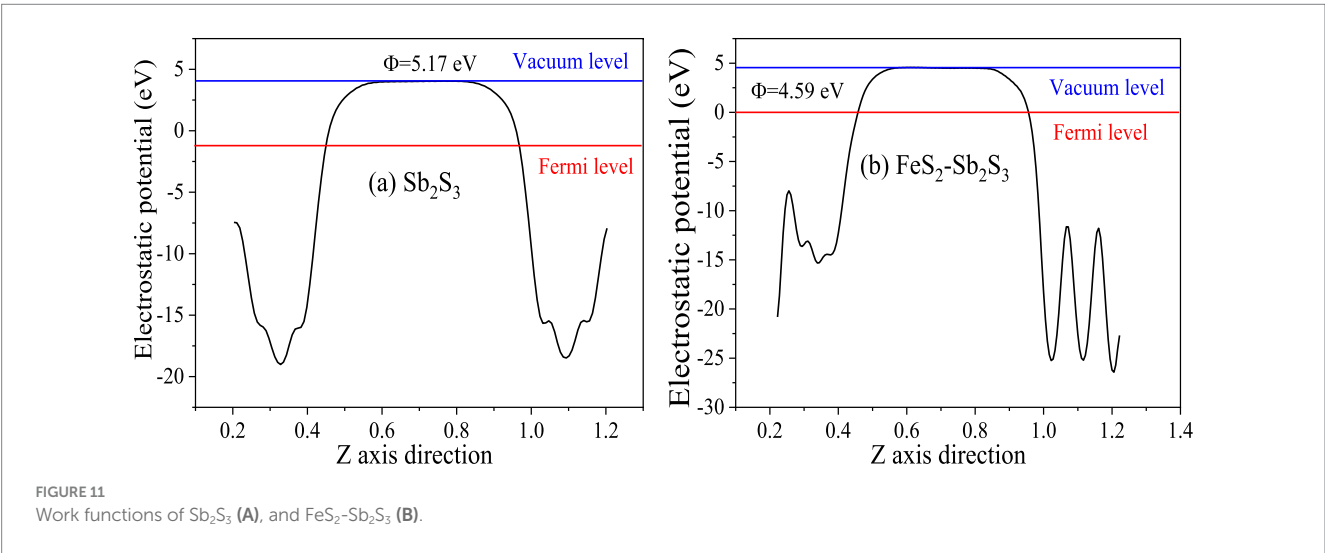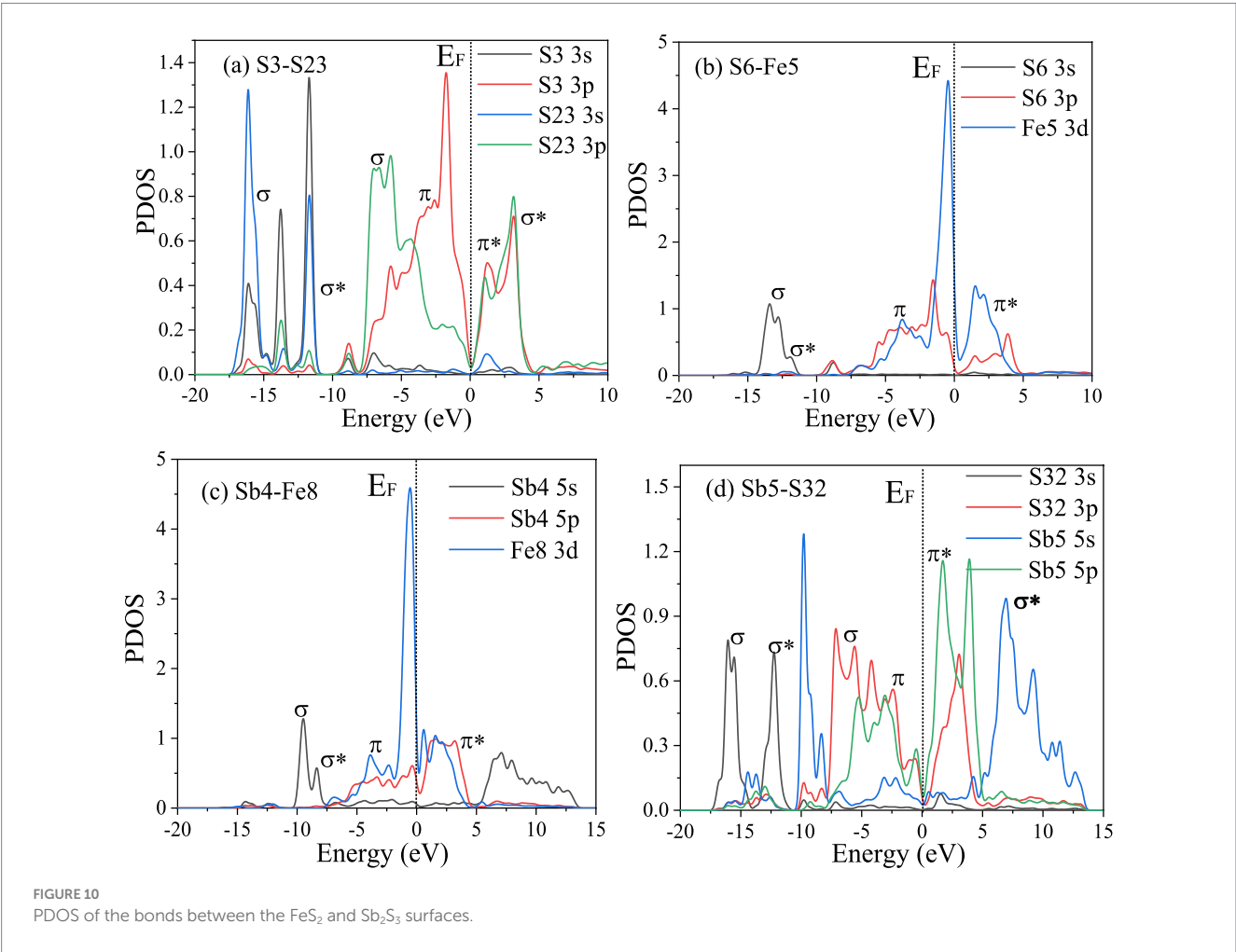
TABLE 4 Frontier orbital energies of FeS_2-$CuFeS_2$ and glucose/Fe(III)-$6H_2O$.

	HOMO	LUMO	ΔE1	ΔE2	ΔE3	ΔE4
0.1496	0.1496	0.1496	0.1496	0.1496	0.1496	0.1496
0.1496	0.1496	0.1496	0.1496	0.1496	0.1496	0.1496
0.1496	0.1496	0.1496	0.1496	0.1496	0.1496	0.1496

$\Delta E_1 = |E (HOMO_{FeS2\text{-}Sb2S3})\text{-}E (LUMO_{glucose})|$; $\Delta E_2 = |E (HOMO_{glucose})\text{-}E (LUMO_{FeS2\text{-}Sb2S3})|$; $\Delta E_3 = |E (HOMO_{FeS2\text{-}Sb2S3})\text{-}E (LUMO_{Fe(III)\text{-}6H2O})|$; $\Delta E_4 = |E (HOMO_{Fe(III)\text{-}6H2O})\text{-}E (LUMO_{FeS2\text{-}Sb2S3})|$.

FIGURE 12
Optimized configurations of glucose **(A,B)** or Fe(III)-6H$_2$O **(C,D)** adsorbed on Sb$_2$S$_3$, FeS$_2$-Sb$_2$S$_3$.
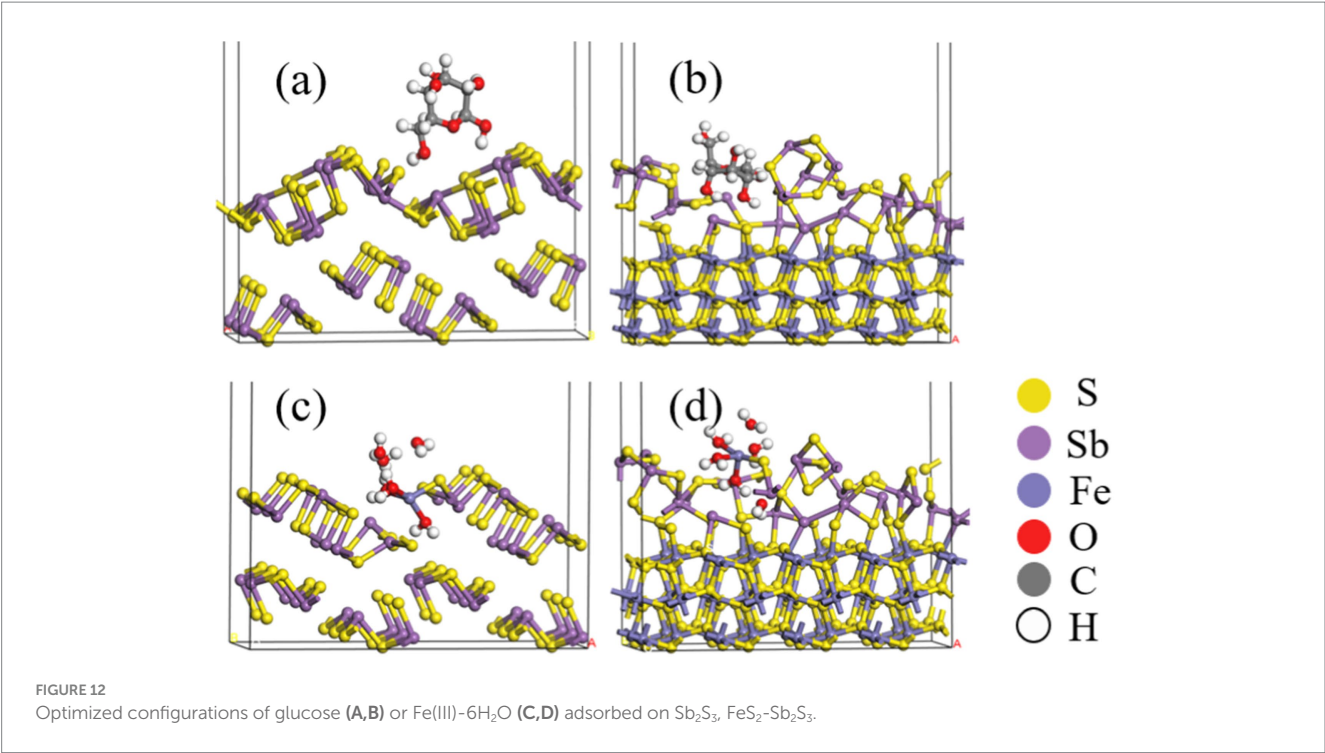
TABLE 5 Mulliken bond population analysis of FeS$_2$-Sb$_2$S$_3$.

	Bond (shorter one)	Bond lengths (Å)	Populations	Adsorption energies (eV)
Glucose-Sb$_2$S$_3$	O-Sb	3.093	–	0.35
Glucose-FeS$_2$-Sb$_2$S$_3$	O-Sb	2.907	–	0.16
Fe^{3+}-6H$_2$O- Sb$_2$S$_3$	Fe-S	2.276	0.49	−0.18
Fe^{3+}-6H$_2$O-FeS$_2$-Sb$_2$S$_3$	Fe-S	2.271	0.48	−0.21

TABLE 6 Hirshfeld charge analysis of Sb in Sb$_2$S$_3$.

Atom	Charge/e Before adsorption	Charge/e Glucose adsorption	Charge/e Fe^{3+}-6H$_2$O adsorption
Sb	5.64	5.61	5.43

ΔE_2 is lower than ΔE_1, indicating that the interaction mainly occurs between the HOMO of glucose and LUMO of FeS$_2$-Sb$_2$S$_3$ rather than the HOMO of FeS$_2$-Sb$_2$S$_3$ and the LUMO of glucose; the results also show that ΔE_4 is lower than ΔE_3, implying a beneficial interaction between the HOMO of Fe(III)-6H$_2$O and LUMO of FeS$_2$-Sb$_2$S$_3$.

Figures 12A,B and Table 5 show that after adding FeS$_2$, the bond length (Å) between glucose and the Sb$_2$S$_3$ surface becomes shorter, from 3.093 Å to 2.907 Å, and the adsorption energy decreases from 0.35 eV to 0.16 eV, indicating that FeS$_2$ can promote the adsorption of bacteria on the Sb$_2$S$_3$ surface, thereby enhancing bioleaching. Figures 12C,D and Table 5 show that Fe(III)-6H$_2$O can adsorb on the Sb$_2$S$_3$ surface and has a shorter bond length and lower adsorption energy than glucose. Table 6 shows that after Fe(III)-6H$_2$O adsorption, the charge change is more greater (−0.21) than that of glucose (−0.03). The EDD (Electron density difference) result (Figure 13) shows that there is more electron transfer between Fe(III)-6H$_2$O and Sb$_2$S$_3$,

implying stronger adsorption. Notably, the results also show that FeS$_2$ can promote the adsorption of Fe(III)-6H$_2$O on the Sb$_2$S$_3$ surface, possibly because adding FeS$_2$ makes the Sb$_2$S$_3$ surface disordered, which is beneficial for Fe(III)-6H$_2$O adsorption. In general, trivalent iron derived from FeS$_2$ has a stronger oxidation effect on Sb$_2$S$_3$ during the bioleaching process.

4 Conclusion

In this work, the effects of FeS$_2$ on the bioleaching of Sb$_2$S$_3$ were investigated by combining experiments and DFT calculations, and the results can be summarized as follows: (1) After adding FeS$_2$, the bioleaching rate of Sb$_2$S$_3$ increased significantly, from 2.23 to 24.6% after 5 days of bioleaching, and the best mass mixing ratio was 0.5:0.5; (2) During the bioleaching process, Sb$_2$S$_3$ was gradually transformed
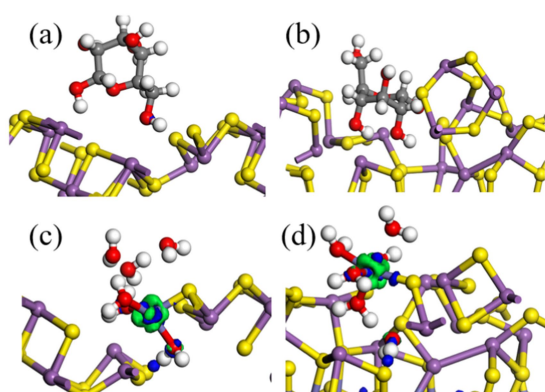
FIGURE 13
(A,B) Electron density difference for the interaction between glucose and the Sb_2S_3, FeS_2-Sb_2S_3 surface; **(C,D)** electron density difference for the interaction between Fe(III)-$6H_2O$ and the Sb_2S_3, or FeS_2-Sb_2S_3 surface. The green area represents electron loss, and the blue contours indicate an increase in the electron density.

to Sb_2O_3 and Sb_2O_5; (3) Adding FeS_2 can form a FeS_2-Sb_2S_3 galvanic cell, which has a greater redox reaction current density, and faster electronic delivery efficiency; and (4) The DFT results indicated that after mixing, both Fe(III)-$6H_2O$ and glucose could adsorb onto the Sb_2S_3 (0 1 0) surface more easily, and Fe(III)-$6H_2O$ may play a major role in Sb_2S_3 bioleaching.

Data availability statement

The original contributions presented in the study are included in the article/Supplementary material, further inquiries can be directed to the corresponding authors.

Author contributions

X-fZ: Methodology, Resources, Software, Validation, Visualization, Writing – original draft, Writing – review & editing. J-lX: Funding acquisition, Resources, Supervision, Visualization, Writing – original draft, Writing – review & editing. Z-yN: Formal analysis, Methodology, Resources, Supervision, Writing – review & editing. H-pC: Investigation, Methodology, Resources,

Writing – review & editing. R-JH: Formal analysis, Supervision, Writing – review & editing. Y-tL: Data curation, Methodology, Supervision, Writing – review & editing. H-cL: Funding acquisition, Methodology, Visualization, Writing – original draft, Writing – review & editing.

Funding

Acknowledgments

Conflict of interest

The authors declare that the research was conducted in the absence of any commercial or financial relationships that could be construed as a potential conflict of interest.

Publisher's note

Supplementary material

The Supplementary material for this article can be found online at: https://www.frontiersin.org/articles/10.3389/fmicb.2025.1475572/full#supplementary-material

References

Awe, S. A., and Sandström, Å. (2013). Electrowinning of antimony from model sulphide alkaline solutions. *Hydrometallurgy* 137, 60–67. doi: 10.1016/j.hydromet.2013.04.006

Bagherifam, S., Brown, T. C., Wijayawardena, A., and Naidu, R. (2021). The influence of different antimony (Sb) compounds and ageing on bioavailability and fractionation of antimony in two dissimilar soils. *Environ. Pollut.* 270:116270. doi: 10.1016/j.envpol.2020.116270

Bevilaqua, D., Acciari, H. A., Arena, F. A., Benedetti, A. V., Fugivara, C. S., Filho, G. T., et al. (2009). Utilization of electrochemical impedance spectroscopy for monitoring bornite (Cu_5FeS_4) oxidation by *Acidithiobacillus ferrooxidans*. *Miner. Eng.* 22, 254–262. doi: 10.1016/j.mineng.2008.07.010

Biver, M., and Shotyk, W. (2012). Stibnite (Sb_2S_3) oxidative dissolution kinetics from pH 1 to 11. *Geochim. Cosmochim. Acta* 79, 127–139. doi: 10.1016/j.gca.2011.11.033

Blanchard, M., Wrigh, K., Gale, J. D., and Catlow, C. R. A. (2007). Adsorption of as(OH)$_3$ on the (0 0 1) surface of FeS_2 pyrite: a quantum-mechanical DFT study. *J. Phys. Chem. C* 111, 11390–11396. doi: 10.1021/jp072468v

Cao, Q., Chen, X., Feng, Q., and Wen, S. (2018). Activation mechanism of lead ion in the flotation of stibnite. *Miner. Eng.* 119, 173–182. doi: 10.1016/j.mineng.2018.01.039

Cao, S., Zheng, X., Nie, Z., Zhou, Y., Liu, H., Chen, J., et al. (2020). Mechanical activation on bioleaching of chalcopyrite: a new insight. *Fortschr. Mineral.* 10:788. doi: 10.3390/MIN10090788

Córdoba, E. M., Muñoz, J. A., Blázquez, M. L., González, F., and Ballester, A. (2009). Passivation of chalcopyrite during its chemical leaching with ferric ion at 68°C. *Miner. Eng.* 22, 229–235. doi: 10.1016/j.mineng.2008.07.004

de Carvalho, L. C., da Silva, S. R., Giardini, R. M. N., de Souza, L. F. C., and Leão, V. A. (2019). Bio-oxidation of refractory gold ores containing stibnite and gudmundite. *Environ. Technol. Innov.* 15:100390. doi: 10.1016/j.eti.2019.100390

de Lima, G. F., de Oliveira, C., de Abreu, H. A., and Duarte, H. A. (2011). Water adsorption on the reconstructed (001) chalcopyrite surfaces. *J. Phys. Chem. C* 115, 10709–10717. doi: 10.1021/jp201106e

de Oliveira, C., de Lima, G. F., de Abreu, H. A., and Duarte, H. A. (2012). Reconstruction of the chalcopyrite surfaces—a DFT study. *J. Phys. Chem. C* 116, 6357–6366. doi: 10.1021/jp300713z

Ekmekqi, Z., and Demirel, H. (1997). Effects of galvanic interaction on collectorless flotation behaviour of chalcopyrite and pyrite. *Int. J. Miner. Process.* 52, 31–48. doi: 10.1016/S0301-7516(97)00050-1

Fan, Y., Zhang, J., Qiu, Y., Zhu, J., Zhang, Y., and Hu, G. (2017). A DFT study of transition metal (Fe, co, Ni, cu, ag, au, Rh, Pd, Pt and Ir)-embedded monolayer MoS$_2$ for gas adsorption. *Comput. Mater. Sci.* 138, 255–266. doi: 10.1016/j.commatsci.2017.06.029

Gehrke, T., Telegdi, J., Thierry, D., and Sand, W. (1998). Importance of extracellular polymeric substances from *Thiobacillus ferrooxidans* for bioleaching. *Appl. Environ. Microb.* 64, 2743–2747. doi: 10.1128/AEM.64.7.2743-2747.1998

Goh, S. W., Buckley, A. N., Lamb, R. N., Rosenberg, R. A., and Moran, D. (2006). The oxidation states of copper and iron in mineral sulfides, and the oxides formed on initial exposure of chalcopyrite and bornite to air. *Geochim. Cosmochim. Acta* 70, 2210–2228. doi: 10.1016/j.gca.2006.02.007

Hong, M., Lin, M., Yang, B., Xiao, J., Liao, R., and Yu, S. (2023). Evolution of passivating species on bornite surface during microbial dissolution. *Trans. Nonferr. Metal. Soc.* 33, 1906–1918. doi: 10.1016/s1003-6326(23)66231-4

Ide-Ektessabi, A., Kawakami, T., and Watt, F. (2004). Distribution and chemical state analysis of iron in the parkinsonian substantia nigra using synchrotron radiation micro beams. *Nucl. Instrum. Meth. B* 213, 590–594. doi: 10.1016/S0168-583X(03)01755-5

Jiang, L., Wei, D., Liu, W., Liu, K., and Zhang, H. (2019). Effects of Fe^{3+} and ag$^+$ on column bioleaching of a low-grade sulfide copper ore. *Int. J. Electrochem. Sci.* 14, 6303–6314. doi: 10.20964/2019.07.43

Li, Q. (2017). Extracellular polymeric substances involved in adhesion and biofilm formation by *Sulfobacillus thermosulfidooxidans*. Germany: Universität Duisburg-Essen Durchgeführt.

Liu, A., Yu, R., Qiu, G., and Zeng, W. (2024). Insights into the EPS production and distribution of planktonic and attached *Sulfobacillus thermosulfidooxidans* cells during bioleaching. *Miner. Eng.* 205:108494. doi: 10.1016/j.mineng.2023.108494

Loni, P., Wu, M., Wang, W., Wang, H., and Tuovonen, O. (2020). Mechanism of microbial dissolution and oxidation of antimony in stibnite under ambient conditions. *J. Hazard. Mater.* 385:121561. doi: 10.1016/j.jhazmat.2019.121561

Lu, X., Zhang, Y., Liu, C., Wu, M., and Wang, H. (2018). Characterization of the antimonite.and arsenite-oxidizing bacterium Bosea sp, AS-1 and its potential application in ar-senic removal. *J. Hazard. Mater.* 359, 527–534. doi: 10.1016/j.jhazmat.2018.07.112

Magini, M. (1979). Solute structuring in aqueous iron(III) sulphate solutions. Evidence for the formation of iron (III)-sulphate complexes. *J. Chem. Phys.* 70, 317–324. doi: 10.1063/1.437193

Magini, M., and Radnai, T. (1979). X-ray diffraction study of ferric chloride solutions and hydrated melt. Analysis of the iron(III)-chioride complexes formation. *J. Chem. Phys.* 71, 4255–4262. doi: 10.1063/1.438233

Morgan, W., Stec, W., and Wazer, J. (1973). Inner-orbital binding-energy shifts of antimony and bismuth compounds. *Inorg. Chem.* 12, 953–955. doi: 10.1021/ic50122a054

Multani, R. S., Feldmann, T., and Demopoulos, G. P. (2016). Antimony in the metallurgical industry: a review of its chemistry and environmental stabilization options. *Hydrometallurgy* 164, 141–153. doi: 10.1016/j.hydromet.2016.06.014

Park, C. M., Hwa, Y., Sung, N. E., and Sohn, H. J. (2010). Stibnite (Sb$_2$S$_3$) and its amorphous composite as dual electrodes for rechargeable lithium batteries. *J. Mater. Chem.* 20, 1097–1102. doi: 10.1039/B918220A

Perdew, J. P., Burke, K., and Ernzerhof, M. (1996). Generalized gradient approximation made simple. *Phy. Rev. Lett.* 77, 3865–3868. doi: 10.1103/PhysRevLett.77.3865

Prange, A. (2008). "Speciation analysis of microbiologically produced sulfur by X-ray absorption near edge structure spectroscopy," in *Microbial sulfur metabolism*. (Heidelberg, Berlin: Springer Berlin Heidelberg Press). 259–272.

Qiu, G., Xiao, Q., Hu, Y., Qin, W., and Wang, D. (2004). Theoretical study of the surface energy and electronic structure of pyrite FeS$_2$ (100) using a total-energy pseudopotential method, CASTEP. *J. Colloid Interf. Sci.* 270, 127–132. doi: 10.1016/j.jcis.2003.08.028

Ravel, B., and Newville, M. (2005). HEPHAESTUS: data analysis for X-ray absorption spectroscopy using IFEFFIT. *Synchrotron. Radiat.* 12, 537–541. doi: 10.1107/s0909049505012719

Sauer, J., and Sustmann, R. (1980). Mechanistic aspects of Diels-Alder reactions a critical survey. *Angew. Chem. Inr. Ed. Engl.* 19, 779–807. doi: 10.1002/anie.198007791

Segall, M. D., Lindan, P. J. D., Probert, M. J., Pickard, C. J., Hasnip, P. J., Clark, S. J., et al. (2002). First-principles simulation-ideas, illustrations and the CASTEP code. *J. Phys. Cond. Matt.* 14, 2717–2744. doi: 10.1088/0953-8984/14/11/301

Ubaldini, S., Veglio, F., Toro, L., and Abbruzzese, C. (2000). Technical note combined bio-hydrometallurgical process for gold recovery from refractory stibnite. *Miner. Eng.* 13, 1641–1646. doi: 10.1016/S0892-6875(00)00148-5

Vanderbilt, D. (1990). Soft self-consistent pseudopotentials in a generalized eigenvalue formalism. *Phys. Rev. B* 41, 7892–7895. doi: 10.1103/physrevb.41.7892

Wang, C., Xia, J., Liu, H., Zhou, Y., and Nie, Z. (2022). Enhancement mechanism of stibnite dissolution mediated by *Acidithiobacillus ferrooxidans* under extremely acidic condition. *Int. J. Mol. Sci.* 23:3580. doi: 10.3390/ijms23073580

Wang, Z., Xie, X., Xiao, S., and Liu, J. (2010). Adsorption behavior of glucose on pyrite surface investigated by TG, FTIR and XRD analyses. *Hydrometallurgy* 102, 87–90. doi: 10.1016/j.hydromet.2010.01.004

Wang, L., Ye, L., and Jing, C. (2020). Genetic identification of Antimonate respiratory reductase in Shewanella sp. ANA-3. *Environ. Sci. Technol.* 54, 14107–14113. doi: 10.1021/acs.est.0c03875

Wilson, N. J., Craw, D., and Hunter, K. (2004). Antimony distribution and environmental mobility at an historic antimony smelter site, New Zealand. *Environ. Pollut.* 129, 257–266. doi: 10.1016/j.envpol.2003.10.014

Yan, L., Chan, T., and Jing, C. (2020). Mechanistic study for stibnite oxidative dissolution and sequestration on pyrite. *Environ. Pollut.* 262:114309. doi: 10.1016/j.envpol.2020.114309

Yang, H., and He, M. (2015). Speciation of antimony in soils and sediments by liquid chromatography–hydride generation–atomic fluorescence spectrometry. *Anal. Lett.* 48, 1941–1953. doi: 10.1080/00032719.2015.1004077

Yang, Y., Liu, W., Bhargava, S. K., Zeng, W., and Chen, M. (2016). A XANES and XRD study of chalcopyrite bioleaching with pyrite. *Miner. Eng.* 89, 157–162. doi: 10.1016/j.mineng.2016.01.019

Ye, L., Meng, X., and Jing, C. (2020). Influence of sulfur on the mobility of arsenic and antimony during oxic-anoxic cycles: differences and competition. *Geochim. Cosmochim. Acta* 288, 51–67. doi: 10.1016/j.gca.2020.08.007

Zeng, W., Peng, Y., Nan, M., and Shen, L. (2020). Electrochemical studies on dissolution and passivation behavior of low temperature bioleaching of chalcopyrite by *Acidithiobacillus ferrivorans* YL15. *Miner. Eng.* 155:106416. doi: 10.1016/j.mineng.2020.106416

Zhang, Y., Wang, C., Ma, B., Jie, X., and Xing, P. (2019). Extracting antimony from high arsenic and gold-containing stibnite ore using slurry electrolysis. *Hydrometallurgy* 186, 284–291. doi: 10.1016/j.hydromet.2019.04.026

Zhao, C., Yang, B., Wang, X., Zhao, H., Gan, M., and Qiu, G. (2020). Catalytic effect of visible light and Cd^{2+} on chalcopyrite bioleaching. *Trans. Nonferr. Metal. Soc. China* 30, 1078–1090. doi: 10.1016/s1003-6326(20)65279-7

Zheng, X., Cao, S., Nie, Z., Chen, J., and Ling, W. (2020). Impact of mechanical activation on bioleaching of pyrite: a DFT study. *Miner. Eng.* 148:106209. doi: 10.1016/j.mineng.2020.106209

Zheng, X., Liu, L., Nie, Z., Yang, Y., Chen, J., Yang, H., et al. (2019). The differential adsorption mechanism of hexahydrated iron and hydroxyl irons on a pyrite (10 0) surface: a DFT study and XPS characterization. *Miner. Eng.* 138, 215–225. doi: 10.1016/j.mineng.2019.05.006

Zheng, X., Nie, Z., Jiang, Q., Yao, X., Chen, J., Liu, H., et al. (2021). The mechanism by which FeS$_2$ promotes the bioleaching of CuFeS$_2$: an electrochemical and DFT study. *Miner. Eng.* 173:107233. doi: 10.1016/j.mineng.2021.107233

Zheng, X., Pan, X., Nie, Z., Yang, Y., Liu, L., Yang, H., et al. (2018). Combined DFT and XPS investigation of cysteine adsorption on the pyrite (1 0 0) surface. *Fortschr. Mineral.* 8:366. doi: 10.3390/min8090366

Check for updates

Microbial proliferation deteriorates the corrosion inhibition capability, lubricity, and stability of cutting fluid

Yuanyuan Shen[1]*, Wenkai Zhang[1], Lili Wu[2], Yaohua Dong[1]*, Guoqiang Guo[2], Lihua Dong[1] and Zhangwei Guo[1]

[1]Institute of Marine Materials Science and Engineering, College of Ocean Science and Engineering, Shanghai Maritime University, Shanghai, China, [2]Shanghai Spaceflight Precision Machinery Institute, Shanghai, China

Cutting fluid is a type of fluid used in the metal-cutting process. It is prone to microbial growth during use, which can lead to the deterioration of its various useful properties; however, the mechanism underlying this deterioration remains unclear. This study analyzed the microbial diversity of field-sampled cutting fluids, and those with higher levels of diversity were used to inoculate other fluid samples in order to further study the effects of microbial growth on the properties of cutting fluids. The results show that the surface of cutting fluid sampled from the tank of a machining tool tank contained predominantly aerobic bacteria, while the bottom mainly harbored anaerobic and facultative microorganisms, with *Yarrowia lipolytica* representing the dominant fungus. Some obligate anaerobic bacteria were also present in the cutting fluid. Organic acids secreted by anaerobic microbial activity reduced the pH of the cutting fluid, as well as its resistance to corrosion. The metabolic activity of the aerobic microorganisms also consumed certain key components of the cutting fluid, which ultimately further lowered its pH and resistance to corrosion. Moreover, the number of fungi increased significantly during the later stages of the experiment. The rolling and bridging action of the resulting fungal mycelium caused flocculation of the effective components in the cutting fluid, resulting in reduced lubricity and poor stability. This study provides a theoretical basis for developing more effective measures to inhibit microbial growth and delay the deterioration of cutting fluid, thereby helping to improve the technical quality of the metal-cutting industry.

KEYWORDS

microbial reproduction, deterioration of cutting fluid performance, corrosion inhibition capability, lubricity, stability, microbial metabolism

1 Introduction

Cutting fluid (i.e., coolant) is a type of industrial liquid used for cooling, lubricating, cleaning, and preventing corrosion during the metal-cutting process. It comprises and is synthesized using a variety of functional chemical additives (Osama et al., 2017; Choudhury and Muaz, 2020; Chen et al., 2024). In recent years, as cutting speeds have increased in this industry, greater requirements are being placed concerning the safety and cooling properties of cutting fluid, leading to the gradual replacement of traditional oil-based cutting fluids with water-based ones. These water-based cutting fluids mainly contain water and mineral oil, along with anti-corrosion agents, defoamers, lubricants, and other additives with different chemical structures that ensure their performance and stability (Simpson et al., 2000; Lillienberg et al.,

2008; Lillienberg et al., 2010). These additives are organic, and thus can represent nutritional sources for certain microorganisms (Trafny, 2013).

Microorganisms can enter cutting fluids in various ways. For example, tap water—which is often used to dilute concentrated cutting fluid—can represent a significant source of microbial contamination. Residues from used cutting fluids often remain even after pipelines or the dead spaces of machines have been cleaned, thus representing another source of microbial contamination when new fluids are added to such cutting systems. Microorganisms also enter cutting fluids through the equipment, or be inoculated by the equipment operators. Fresh cutting fluids are also susceptible to contamination by microorganisms from dust particles or aerosols. Such microorganisms not only threaten the health of workers in the industry, but also lead to spoiling of the cutting fluid, which can produce foul odors and affect its physicochemical properties (Liu et al., 2010; Schwarz et al., 2015). This, in turn, can lead to deterioration of the quality of the workpiece and reduce the lifespan of the tool (Rakić and Rakić, 2002).

Studies have shown that microorganisms are highly capable of growth in water-based cutting fluids from machining plants, leading to environmental malodor, fluid discoloration, and increased acidity (Gast et al., 2001; Grijalbo et al., 2015). After isolating fungi and bacteria from cutting fluids, Elansky et al. investigated their growth in cutting fluid, and hypothesized that microorganisms could be used to treat metal-working fluid waste through biodegradation (Elansky et al., 2022). Hill found that microbial growth consumes certain components of cutting fluid and increases the diameter of the droplets formed by its dispersion, which in turn leads to decreased performance that affects the machining accuracy of workpiece surfaces (Hill, 1992). Rabenstein et al. studied the microbial community in water-based metal-working fluids and the microbial degradation of their active ingredients, ultimately demonstrating that the active ingredients were not consumed simultaneously, but rather in a sequential order (Rabenstein et al., 2009). Zhang et al. investigated the effect of corrosion caused by microorganisms on cemented carbide (WC-30Co) cutting tools in an oil–water emulsion (Zhang et al., 2015). They found that preferential cobalt loss determined the corrosion failure in biodegraded emulsions, and that the sulfate-reducing bacterium *Citrobacter* sp. made the emulsion even more corrosive to the hard metal. To date, the safety hazards and economic losses caused by microorganisms have attracted significant attention in the fields of marine engineering, pipeline transportation, construction engineering, and nuclear power (Yazdi et al., 2022; Lu et al., 2023; Sun et al., 2023; Li et al., 2024). Conversely, microbial growth in cutting fluid, and the related deterioration of its performance, as well as the environmental pollution caused by the resultant waste (Sankaranarayanan et al., 2021; Korkmaz et al., 2023), has not yet attracted sufficient attention. This has resulted in a scarcity of research concerning the underlying mechanisms of its degradation.

The main objectives of this study were to: (1) examine the diversity and characteristics of the microbial communities in industrial cutting fluid; (2) study the effects of microbial growth and metabolism on the performance of industrial cutting fluid, based on parameters such as pH, anticorrosion, lubrication, and stability, under laboratory conditions; and (3) analyze the mechanism underlying the microbially-induced deterioration of industrial cutting fluid. The theoretical data provided herein will hopefully be of great significance to preventing microbial corrosion in industrial cutting fluid, as well as

for maintaining and extending the life of cutting fluids used in metal-processing operations.

2 Materials and methods

2.1 Microbial sampling

Cutting fluid samples (labeled "CF"), were collected from the surface and bottom of four equally-sized machine tool tanks (labeled 1, 2, 3, and 4), that had been filled with the same cutting fluid, used to cut the same metal, and received equal use at a research institute for aerospace materials in Shanghai, China. All of the cutting fluids had been in use for 4 months prior to the study, during which they had blackened and begun emitting a foul odor. Samples (50 mL) of each fluid were centrifuged in a high-speed refrigerated centrifuge (Multifuge X1R, Thermo Fisher Scientific, Waltham, MA, United States) at 44,720 × g and 4°C for 10 min. The supernatants were discarded, and the pellets were resuspended and diluted in physiological buffered saline (PBS), after which the resultant solutions were centrifuged again under the same conditions. The final pellets were then analyzed for biodiversity via high-throughput sequencing.

2.2 Microbial community analysis

2.2.1 DNA extraction and quality assessment

Microbial DNA from the cutting fluid samples was extracted using a FastDNA Spin Kit for Soil (MP Biomedicals LLC, Irvine, SC, United States), after which the concentration and purity of the extracted DNA were measured using a NanoDrop 2000 fluorometer (Thermo Fisher Scientific, Waltham, MA, United States).

2.2.2 Polymerase chain reaction amplification

The V3–V4 hypervariable region of the bacterial 16S rRNA gene was amplified using the universal primers 338F (5′-ACTCCTACGG GAGGCAGCAG-3′) and 806R (5′-GGACTACNNGGGTATCTAA T-3′). The fungal ITS2 region was amplified using the universal primer sets ITS1 (5′-CTTGGTCATTTAGAGGAAGTAA-3′) and ITS2 (5′-TGCGTTCTTCATCGATGC-3′) (Abarenkov et al., 2010). Both the 16S rRNA and ITS rRNA amplicons were generated using the same protocol. The PCR mixtures comprised 5× buffer (10 µL), forward primer (1 µL), reverse primer (1 µL), deoxy-ribonucleoside triphosphates (dNTPs) (10 µL), double-distilled water (ddH2O), Phusion high-fidelity DNA polymerase (0.5 µL, New England Biolabs, Inc., Ipswich, MA, United States), and template DNA (30 ng), with total reaction volumes of 50 µL. The cycling parameters were: 94°C for 2 min; followed by 24 cycles of 94°C for 30 s, 55°C for 30 s, and 72°C for 30 s; before a final extension at 72°C for 5 min (Rognes et al., 2016). The generated PCR products were recovered via 2% agarose gel electrophoresis before being purified using an AxyPrep DNA Gel Extraction Kit (Axygen Biosciences, Silicon Valley, CA, United States). A Quantus™ fluorometer (Promega Corporation, Madison, WI, United States) was used for nucleic acid quantification of purified PCR products. Sequencing was then performed on an Illumina MiSeq PE3000 platform (Illumina, Inc., San Diego, CA, United States) at Shanghai Meiji Biomedical Technology Co., Ltd., China (Zhang et al., 2014). The data presented in the study are deposited in the National

Center for Biotechnology Information (NCBI) repository, accession number SRP554559: PRJNA1204126.

2.2.3 Bioinformatic analysis

The raw fastq files were demultiplexed based on the barcode. PE reads for all samples were run through Trimmomatic (version 0.35) to remove low quality base pairs using these parameters (SLIDINGWINDOW: 50:20; MINLEN: 50) (Pruesse et al., 2007). Trimmed reads were then cut primer and adaptors using cutadapt (version:1.16). And then further merged using FLASH program (version 1.2.11) with default parameters. The low quality contigs were removed based on screen.seqs command using the following filtering parameters, maxambig = 0, minlength = 200, maxlength =485, maxhomop = 8.

The 16S sequences were analyzed using a combination of software mothur (version 1.33.3),UPARSE (version v8.1.1756), and R (version 3.6.3). The demultiplexed reads were clustered at 97% sequence identity into operational taxonomic units (OTUs) and the chimera was removed and the singleton OTUs were deleted using the UPARSE pipeline (Edgar et al., 2011; Edgar, 2013). The OTU representative sequences were assignment for taxonomy against Silva 128 database with confidence score ≥ 0.6 by the classify.seqs command in mothur. As for the ITS taxonomic analysis, the UNITE database was used.

For the alpha-diversity analysis, Shannon, simpson, Chao1, ACE index and rarefaction curves were calculated and plotted by R. For the beta-diversity metrics, the weighted and unweighted UniFrac distance matrix were calculated and visualized with Principal Coordinate Analysis (PCoA) by ape package in R, NMDS by vegan package in R and tree by dendextend package in R (Harmon-Smith et al., 2010). The bray curits and jaccard metrics were calculated by vegan package in R and visualized also by R the same as Unifrac analysis.

2.3 Experimental solutions

In order to better analyze the effects of microorganisms on cutting fluid performance, the cutting fluid formulation was simplified and its fungicide was removed for this experiment. The fluid's composition therefore comprised: 4.9% nonylphenol polyoxyethylene ether, 7.8% triethanolamine, 9.6% fatty alcohol polyoxyethylene ether, 9.6% dehydrated sorbitol fatty acid ester (i.e., Span), 9.6% polyethylene glycol dioleate, 50.3% mineral oil, 6% tall oil, 0.2% organic silicon, and 2% organic phosphate ester (all proportions in w/w). Before the formal experiments, the simplified cutting fluid was diluted to a volume fraction of 5% wt (the concentration recommended by the supplier) with deionized water, and dubbed "SCF." This fluid contained sufficient organic components to supply ample nutrients for microbial growth, so it was not further supplemented with any additional nutrients. The total volume of this solution was 1 L.

2.4 Microbial growth curve

To ensure high microbial diversity, CF samples with higher levels of biodiversity were selected as sources of the microbial strains. Appropriate amounts of spoiled CF were inoculated into 100 mL aliquots of sterilized SCF solution, to initial bacterial concentrations of ~10^6 CFU/mL. Since the cutting fluid was milky-white, it was

difficult to accurately determine its microbial concentration using the absorbance method. Therefore, to plot the growth curve of the microorganisms in the fluid, microbial concentrations at different incubation times were quantified via the plate-count method. Three replicate solutions were prepared to increase the experiment's accuracy. The main components of the solid medium used in the plates were: beef extract (5 g/L), peptone (5 g/L), triethanolamine borate and its derivatives (100 g/L), oleic acid (5 g/L), methanol (3 g/L), organophosphate ester and its derivatives (3 g/L), and agar (15 g/L) (Yin et al., 2019). The bacterial solution was appropriately diluted via step-wise dilution. Aliquots of the diluted microbial suspension (1 mL) were taken using sterile pipettes and inoculated onto the solid medium in Petri dishes, before being evenly spread using a sterilized glass scraper. The plates were then left face-up on the sterile experimental benchtop for 30 min to allow the solution to penetrate the medium, before being inverted for culturing in a controlled-temperature incubator at 37°C. The plates were removed at different time points, and Scan 300 colony-counters (Interscience, Puy Capel, Cantal Province, France) were used to count the resultant colonies.

2.5 Testing of physical and chemical properties

The SCF solution was packed in two 1 L conical flasks that were plugged with cotton plugs, sterilized in an autoclave at 121°C for 20 min, then air-cooled in a biosafety cabinet. One of the conical flasks was inoculated with 200 µL of a CF sample with high microbial diversity, which was dubbed "Test-SCF." The other conical flask was not inoculated, to serve as a control, and dubbed "Control-SCF." These two conical bottles were incubated at 38°C for static culturing. After 1 month, samples from the middle regions of the solutions within the flasks were taken so that the compositions of their bacterial and fungal communities could be analyzed.

2.5.1 Cutting fluid pH and redox potential

To study the effect of microbial growth on pH, he pH levels of the two SCF solutions were measured at 7, 14, 21, and 28 days using an FE20 pH meter (Mettler-Toledo International Inc., Zurich, Switzerland). The redox potential (ORP) of two solutions was measured at various stages throughout the experiment using an SX712 ORP meter (Shanghai San-Xin Instrumentation, Inc., Shanghai, China).

2.5.2 Cutting fluid corrosion-inhibiting properties

The corrosion inhibition ability of the cutting fluid was evaluated using the iron filings method. A section of qualitative filter paper was placed into a Petri dish, after which 2 g of iron filings were uniformly spread over its surface, with the weight confirmed using a precision balance. A 1 mL sample of SCF was then added to saturate the iron filings, and the dish was sealed using its lid. After incubating at room temperature for 2 h, the filter paper was removed and the iron filings were washed with running water. The number of rust spots was then counted, once the filter paper had dried completely.

Given the use of both onsite-sampled CF and the laboratory-prepared SCF, both needed to be analyzed regarding the impact of microbial contamination on their abilities to inhibit corrosion. Electrochemical

analyses, including measurements of open circuit potential (OCP) and polarization curves, were conducted using samples of 7,050 aluminum alloy (Shanghai Hanglv Aviation Materials Co., Ltd., Shanghai, China) that were exposed to spoiled cutting fluids for varying periods. The aluminum alloy, sourced from an aerospace materials research institute in Shanghai, comprised 0.04% Cr, 0.12% Zr, 6.2% Zn, 0.11% Si, 0.08% Fe, 0.06% Mn, 2.3% Mg, 0.05% Ti, and 0.04% Cu, with the remaining composition being aluminum. Prior to testing, the alloy was sectioned into $10 \times 10 \times 2$ mm samples that were sequentially polished under wet conditions with 800 grit silicon carbide paper, ultrasonically cleaned in anhydrous ethanol for 10 min, and air-dried. Lengths of copper wire were then soldered to the reverse sides of each sample. The soldered faces and remaining samples were encapsulated in epoxy resin, leaving only 10×10 mm working surfaces exposed on each. These working surfaces were further polished using 800 grit water-resistant sandpaper, sequentially cleaned with anhydrous ethanol and deionized water, and dried before being used for electrochemical evaluation.

Electrochemical evaluation was performed using a CHI 660 electrochemical workstation (Shanghai Chenhua Instrument Co., Ltd., Shanghai, China). The experimental configuration used a three-electrode system comprising a saturated calomel electrode (SCE) as the reference, a platinum plate (10×10 mm) as the counter electrode, and aluminum alloy samples immersed in experimental cutting fluid samples as the working electrodes. The sterilized SCF comprised the electrolyte used to assess the electrochemical behavior of the working electrode. After being immersed for varying lengths of time, samples were extracted from the conical flasks and tested in an electrochemical testing system. To ensure the system's stability prior to the measurements, all of the samples were equilibrated at OCP for 30 min in a sterile environment at ambient temperature.

Polarization curve tests were carried out at a scan rate of 5 mV/s and range of -1 to $+1$ V relative to the stabilized OCP. The resultant polarization curve data were analyzed and fitted using the electrochemical workstation's integrated analysis software.

2.5.3 Cutting fluid lubricity

Lubricity is commonly quantified by measuring tapping torque, with higher values signifying better lubricity. As the experiment progressed, the effects of microbial activity on the tapping torque values of the cutting fluid samples were quantified using a Labtap G8 threading torque meter (Microtap, Taufkirchen, BY, Germany). These measurements used aluminum alloy 7,075 for the standard extruded-hole test block, with a hole diameter and depth of 3.7 mm and 20 mm, respectively. A syringe was used to inject the solutions into the holes until they were fully filled. The tap used for extrusion molding had a diameter of 3.64 mm. The tests were conducted at a set rotational speed of 1,500 rpm, an applied torque of 400 N·cm, and a tapping depth of 12 cm.

2.5.4 Cutting fluid stability

The stability of industrial cutting fluid is primarily assessed via two methods: oil droplet morphology analysis and zeta potential measurement. In general, smaller molecules or dispersed particles within the fluid correspond to greater absolute zeta potential values (positive or negative), signifying higher stability.

The methodology used to assess the oil droplet morphology in the cutting fluid samples involved staining with Oil Red O. A 1 g aliquot of Oil Red O was dissolved in 2 mL of anhydrous ethanol and mixed

thoroughly to prepare the dye solution. A 100 µL aliquot of this dye was then added to 1 mL of the fluid being analyzed, followed by vigorous shaking to achieve uniform staining. The morphologies of the resultant oil droplets were then examined using a DM500 optical microscope (Leica, Wetzlar, HE, Germany).

Zeta potential was measured using a Litesizer 500 nanoscale particle analyzer (Anton Paar GmbH, Graz, ST, Austria) at various time points over the course of the experiment. Measurements were performed in an omega-shaped sample cell maintained at a target temperature of 25°C, with an equilibration time of 1 min. The Smoluchowski approximation was used, with Henry's function set at 1.5. The adjustment mode was automatic, the running mode was manual (100 runs), and water was used as the solvent.

2.6 Microbial degradation of primary cutting fluid constituents

To examine the microbial degradation of the cutting fluid, 100 mg samples of three of its primary active ingredients—triethanolamine, tall oil, and organophosphate esters—were added separately to 150 mL aliquots of mineral medium without additional carbon sources. Nine such replicate samples were prepared for each ingredient. The composition of the mineral medium was 1.0 g/L K_2HPO_4, 1.0 g/L $NaNO_3$, 0.5 g/L $MgCl_2$ and 1.0 g/L $MgSO_4 \cdot 7H_2O$ in deionized water. The pH was adjusted to 8.5–9.0 using a 0.1 mol/L NaOH solution to mimic that of the cutting fluid used on-site. Samples of spoiled and sterile cutting fluid samples (2 mL each) were then inoculated into the test media and incubated at 25°C. The total organic carbon levels of each of these mixtures were tested after 0, 5, and 9 days of incubation, with three 10 mL samples tested from each mixture on a Multi N/C 3100 total organic carbon analyzer (Analytik Jena GmbH+Co., Jena, JN, Germany). The total volume was maintained at 150 mL with mineral medium. This approach facilitated precise quantification of which cutting fluid components were being actively metabolized by microorganisms.

3 Results and discussion

3.1 Microbial diversity in cutting fluid

Genus-level microbial community analysis revealed significant differences in the composition and relative abundances of the microorganisms retrieved from the surfaces and bottoms of the four machine tool tanks (Figure 1). The biodiversity was high in the B1 and B3 samples, and the relative abundances of the different microorganisms were relatively consistent. The microbial communities in the surface samples from the tanks of machines 1 and 4 were similar, being predominantly composed of *Pseudomonas.* Similarly, the microbial communities in the surface samples from the surface samples of machines 2 and 3 were also consistent, being predominantly composed of *Pseudomonas*, *Acinetobacter*, and *Ochrobactrum*. The bottom samples from all four machines mainly contained *Brachymonas*, *Sebaldella*, *Corynebacterium*, and *Comamonas*. Notably, the microbial communities in the surface samples had a high relative abundance of *Pseudomonas*, with percentages of 90.7, 57.5, 55.4, and 95.6% in samples 1–4, respectively. *Pseudomonas* is a facultative Gram-negative bacterium that thrives in aerobic conditions and can

FIGURE 1
Combined analysis chart of genus-level sample clustering tree and bar chart.
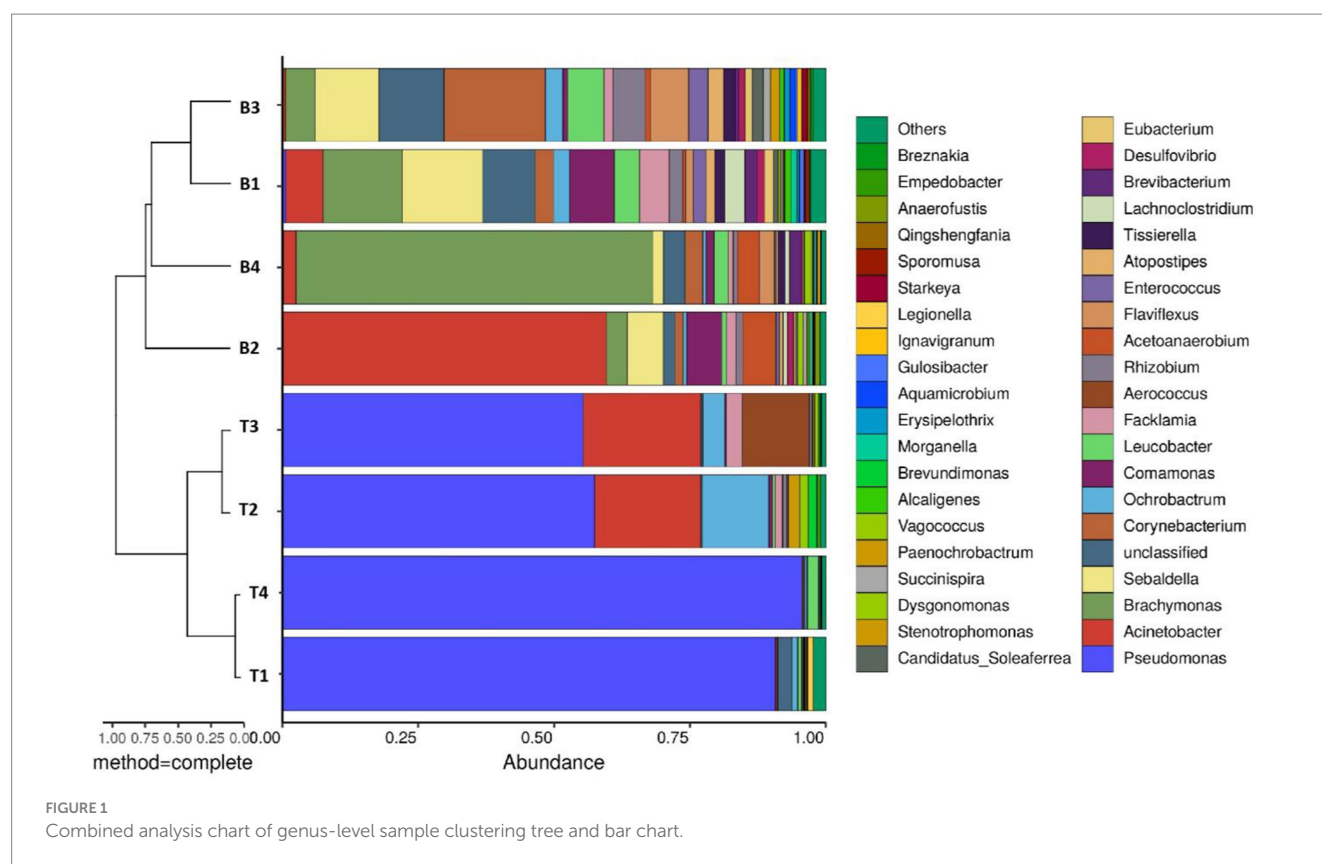
metabolize various carbon-, nitrogen-, and sulfur-containing compounds (Daniels et al., 2010; Babaei et al., 2014), thus facilitating the full degradation of various organic components (Caballero et al., 2005; Roca et al., 2009) and often leading to the deterioration of cutting fluid. The effective components in the cutting fluid were reduced by evaporation and splashing during the actual operational use of the cutting fluids. Microbial degradation represents a major factor that reduces the functional ingredients in cutting fluid (Rabenstein et al., 2009). Furthermore, the lower oxygen level at the bottom of the machine tool tank provides a favorable environment for the proliferation of anaerobic and facultative bacteria.

The Shannon index is used to measure the biodiversity of species. The higher the Shannon value is, the higher the microbial diversity will be (Lopes et al., 2024). The α-diversity of microbial communities in the four machine tool tanks were shown in Figure 2. The results showed that samples located bottom presented higher diversity and species richness in comparison with the samples located surface. The surface of the cutting fluid is usually in contact with air, and the oxygen content is relatively high. This oxygen-rich environment is conducive to the growth of aerobic microorganisms. For example, some bacteria of the genus *Pseudomonas* can utilize oxygen for respiration and decompose the organic components in the cutting fluid. However, at the bottom of the cutting fluid, oxygen diffuses relatively slowly, and it is easy to form an anoxic or even anaerobic environment. This provides living space for anaerobic microorganisms. These anaerobic microorganisms have unique metabolic pathways. As a result, aerobic, anaerobic and facultative anaerobic microorganisms coexist at the bottom, which increases the biodiversity. Based on the above results, it could be seen that sample B3 had a relatively high biodiversity and the relative abundances of each microorganism were relatively even.

Therefore, sample B3 would be used as the source of strains and inoculated into the cutting fluid for experiments in the follow-up.

3.2 Microcosm experiment of cutting fluid microbial community

The microbial community structure in the cutting fluid from the Test-SCF sample is shown in Figure 3. The microbial communities were predominantly composed of *Acinetobacter*, *Comamonas*, and *Pseudomonas* at percentages of 60.0, 18.0, and 2.7%, respectively in Sample A; and 49.9, 6.9, and 9.0%, respectively, in Sample B.

Genus- and species-level analyses of the fungal communities showed that, although there were fewer types of fungi than bacteria in the Test-SCF sample, their relative abundances were higher (Figure 4).

The experiment identified 85.4% *Yarrowia lipolytica* in sample A, and 98.9% in sample B, with 13.9% unclassified fungi in sample A, and < 1% each of *Wallemia_tropicalis*, *Candida_tropicalis*, *Cryptococcus*, *pseudolongus*, and *Candida_glaebosa*. *Yarrowia lipolytica* exhibited the highest relative abundance, indicating its dominance in the cutting fluid. This yeast is characterized by rapid reproduction, a robust colonization capability, a high survival rate, and resilience in low pH environments.

3.3 Microbial growth curve determination

The growth of microorganisms in the configured cutting fluid is presented in Figure 5. The graph indicates a slow microbial growth rate between 0 and 24 h, representing the lag phase. There
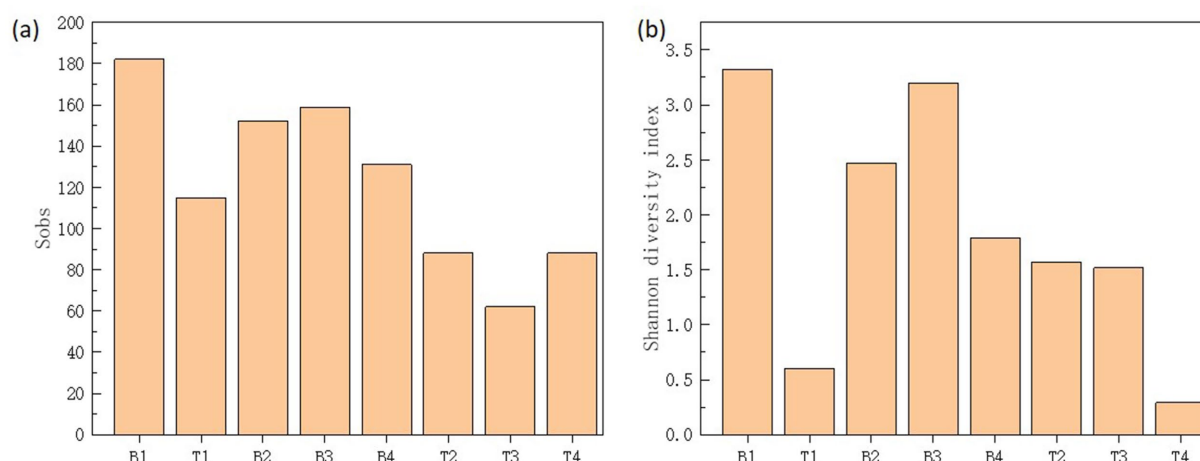
FIGURE 2
Sobs **(a)** and Shannon diversity index **(b)** of microbial communities in top (T1-4) and bottom (B1-4) cutting fluid samples taken from the four (1-4) machine tool tanks.
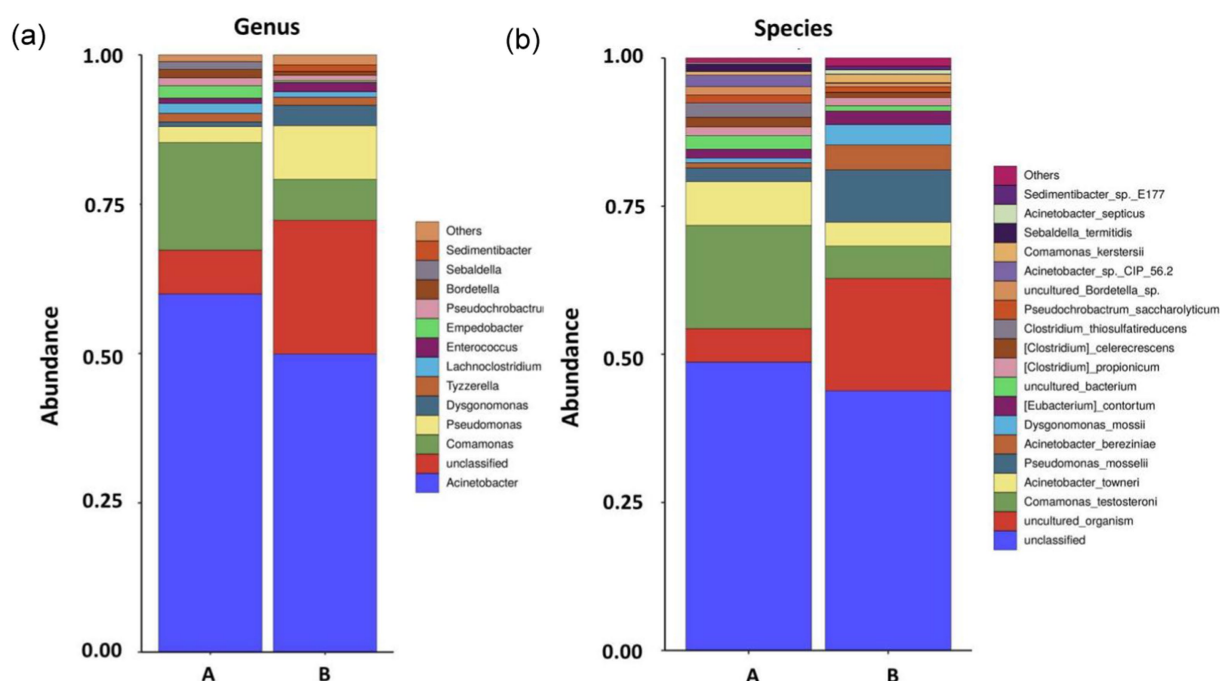

FIGURE 3
Microbial community structures and relative abundances at the conclusion of the enrichment cutting fluid culturing experiment at the genus **(A)** and species **(B)** levels (samples A and B are parallel samples).

was an exponential increase in biomass between 24 and 96 h, denoting rapid growth during the log phase. The biomass reached its peak at ~108 h, corresponding to the highest observed microbial concentration. After this point the biomass underwent a slight decline followed by a steady downward trend until 168 h, marking the onset of the death phase. Because of the high organic content in the cutting fluid that continuously supplied the necessary nutrients for microbial growth, the growth and death of the microorganisms eventually reached an equilibrium at a total count of ~10^{11} CFU/mL.

3.4 Impact of microorganisms on cutting fluid pH

The stability and corrosion-preventing physicochemical properties of cutting fluid are highly dependent on its pH, which is frequently used as a performance indicator in industrial testing. Cutting fluid pH should typically be maintained between 8.5–9.2 to ensure optimal performance.

Figure 6 displays the pH of cutting fluids over various time points, clearly showing that the pH of the cutting fluid sample that was
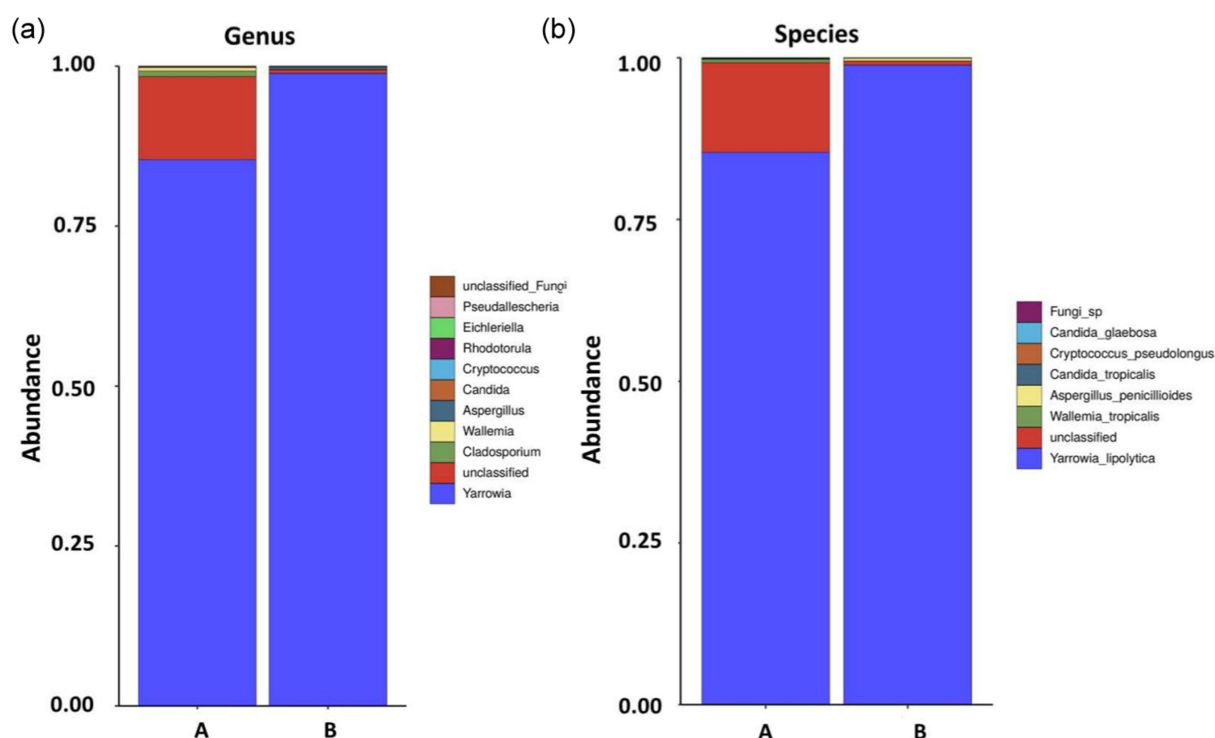
FIGURE 4

Fungal community structures and relative abundances in expanded experimental cutting fluids at the genus (A) and species (B) levels (samples A and B are parallel samples).
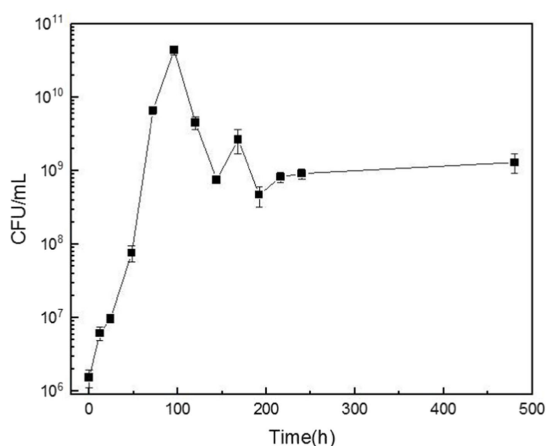

FIGURE 5

The variation curve of bacterial colony-forming units (CFU) per milliliter of cutting fluid over time.
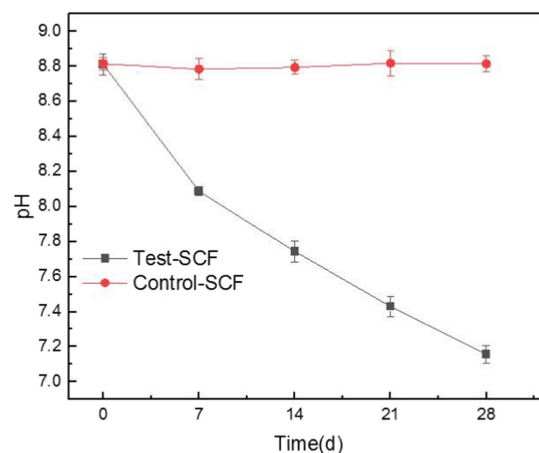

FIGURE 6

Trends in the pH values of the cutting fluids inoculated with bacteria (Test-SCF) and without bacteria (Control-SCF) over time.

inoculated with microorganisms decreased from an initial value of 8.81 to a final one of 7.15, whereas the pH of the uninoculated fluid did not change significantly. These results indicate that the presence of microorganisms significantly lowered the pH of the cutting fluid as the experiment progressed. The microbial growth curve indicates that microorganisms proliferate rapidly over time, which significantly impacts the pH of the cutting fluid. The microbial community analysis revealed the presence of various anaerobic bacteria, including the *Sebaldella* genus, at the bottom of the tool's tank. These bacteria

produce a range of organic acids such as acetic, lactic, and occasionally formic acid that reduce the pH of the cutting fluid (Li et al., 2023).

After being used for extended periods, cutting fluid harbors aerobic, facultative, and anaerobic bacteria. Aerobic bacteria can degrade the active ingredients of the fluid, leading to decreased performance. The metabolism of facultative and anaerobic bacteria produces organic acids, resulting in a lower pH (Ma et al., 2018). Moreover, *Y. lipolytica* produces significant quantities of citric acid that accumulate over time (Ledesma-Amaro et al., 2016). This
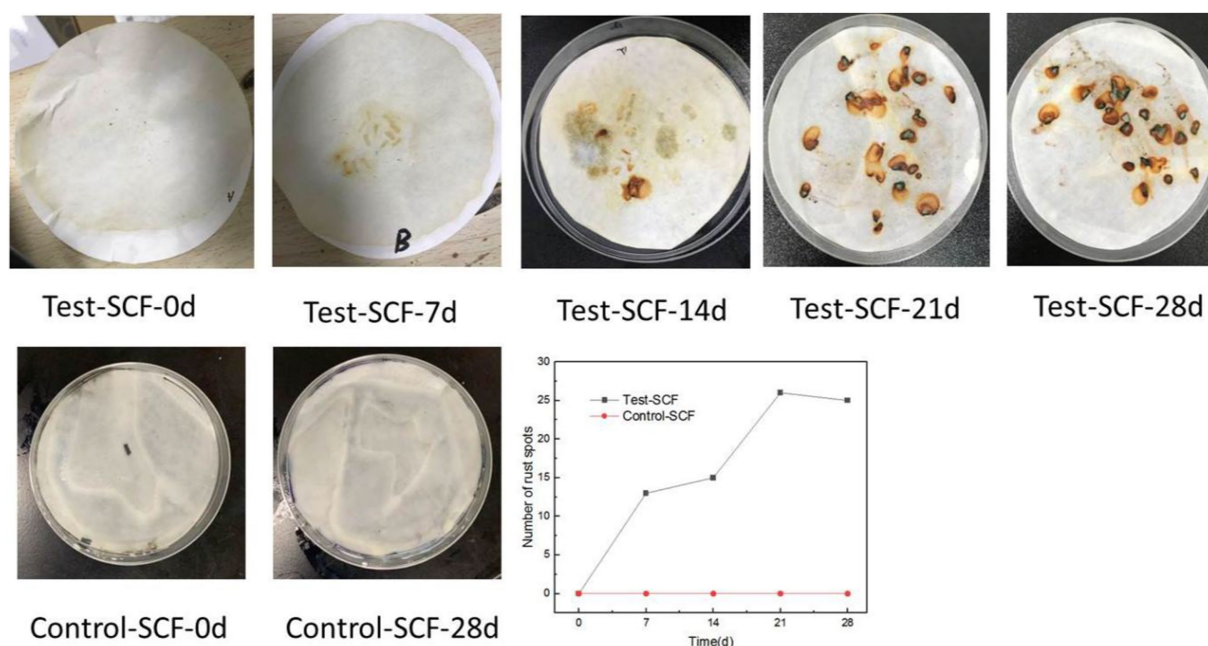
FIGURE 7
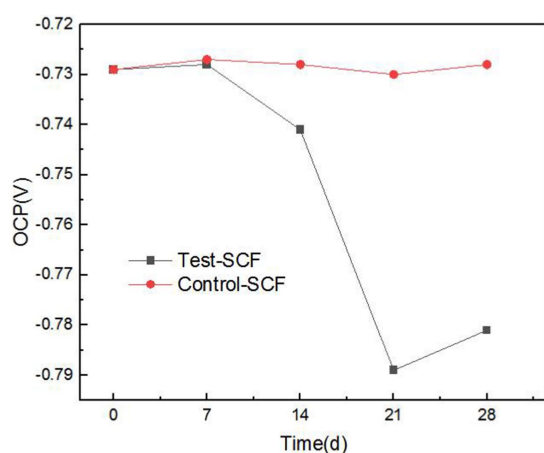Iron filings experiment results and statistical map of the numbers of rust spots.

FIGURE 8
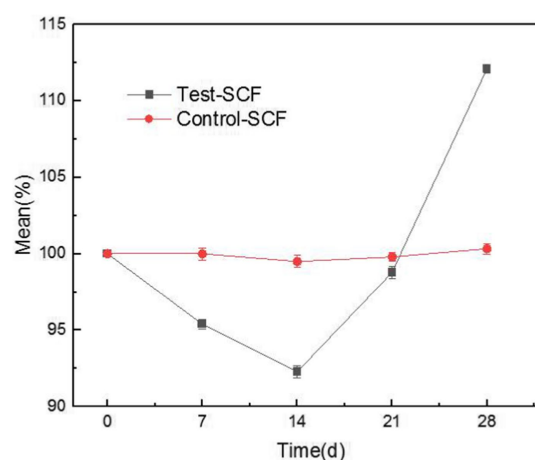Open-circuit potential (OCP) trend in two cutting fluid samples over time.

FIGURE 9
Trends in the tapping efficiency of two cutting fluid samples over time.

bacterium also produces other acidic substances such as alpha-ketoglutaric acid and unsaturated fatty acids (Guo et al., 2016).

3.5 Impact of microorganisms on the corrosion-inhibiting properties of cutting fluid

The iron filings experimental results are shown in Figure 7. No rust spots were observed in the Control-SCF sample after 28 days, indicating no impact on the corrosion inhibition properties of the

sterile SCF. Similarly, no rust spots were observed when iron filings were added to the fresh Test-SCF sample, indicating that the newly-prepared fluid effectively inhibited their corrosion. However, as the experiment progressed, more rust spots appeared on the filter paper, indicating a decrease in the corrosion-inhibiting properties of the fluid. This deterioration is likely attributable to a rapid increase in the microbial population and a corresponding intensification in their metabolic activity that significantly reduced the corrosion-inhibiting properties of the fluid.

As cutting fluid is primarily used to process aluminum alloys, this iron filings method does not comprehensively assess the impact of

cutting fluid deterioration on its properties related to inhibiting the corrosion of aluminum alloy workpieces. Consequently, the effects of microbes on the ability of cutting fluid to inhibit corrosion were further investigated through electrochemical testing. Electrochemical tests were conducted using aluminum alloy samples that had been immersed in microorganism-inoculated cutting fluid for durations of 1, 7, 14, 21, and 28 days. Figure 8 presents the OCP of the aluminum alloy in the cutting fluid at various time points. Generally, a more negative OCP indicates that the alloy has a higher sensitivity to corrosion. The data revealed a noticeable downward trend in OCP, thereby suggesting that the sensitivity to corrosion of the aluminum alloy in the cutting fluid increased progressively. Cutting fluid includes corrosion inhibitors that are adsorbed onto metallic surfaces, exerting protective effects on the metal. Nevertheless, as the experiment progressed, the OCP of the aluminum alloy in the cutting fluid with microorganisms gradually declined. This was primarily attributed to

the failure of the corrosion inhibitor to be adsorbed onto the surface of the aluminum alloy (Alobaid et al., 2024).

3.6 Impact of microorganisms on the lubricity of cutting fluid

Figure 9 illustrates the tapping efficiency of the cutting fluid at different time points over the experiment. The results showed that the tapping torque value initially decreased gradually over time, before increasing again after 14 days. This suggests that in the early stage of the experiment, the presence of microorganisms slightly enhanced the lubricity of the cutting fluid (D'Addona et al., 2020). However, a biofilm was observed to have formed on the fluid's surface. After stirring, clumpy substances appeared that resembled undissolved milk powder
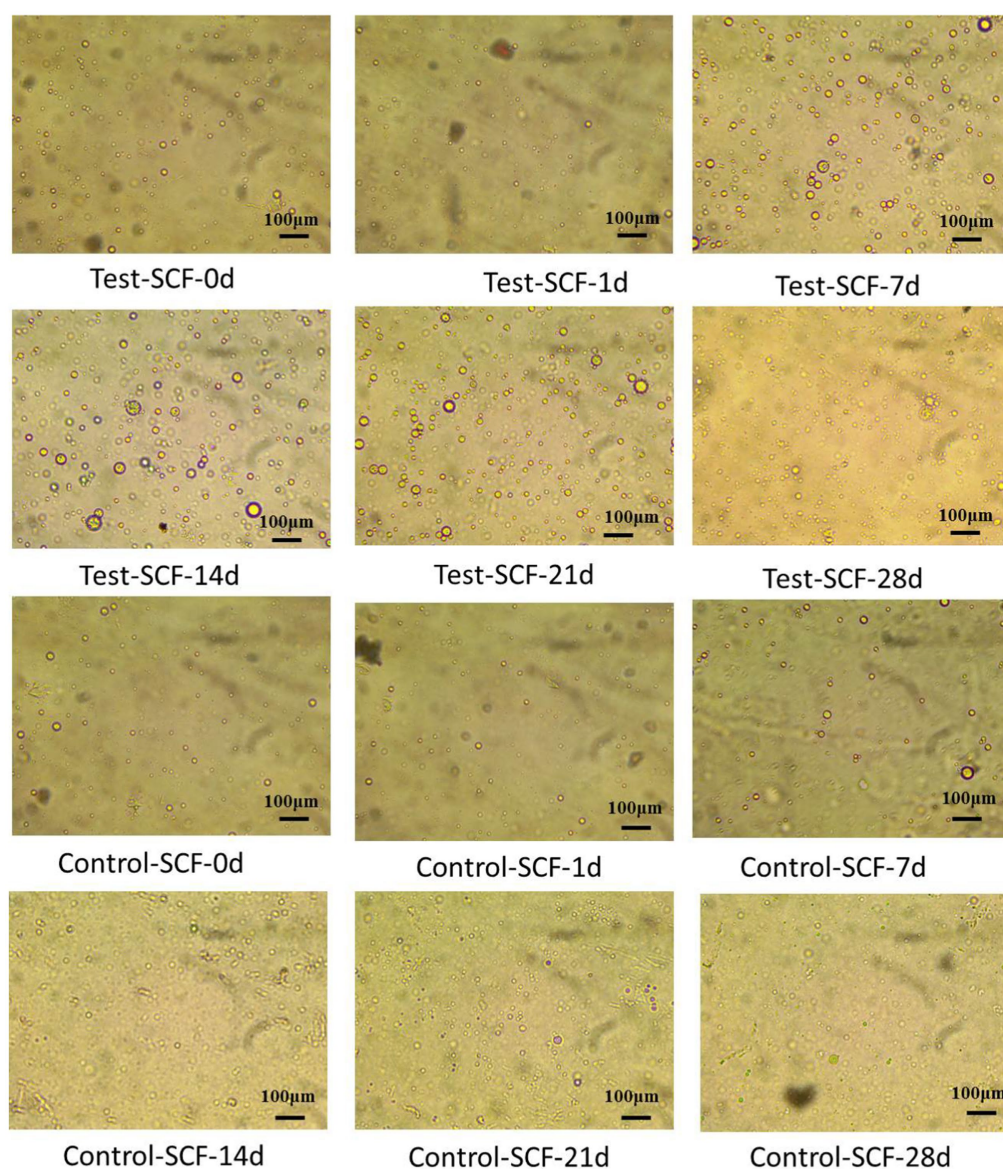

FIGURE 10
Droplet morphologies in two cutting fluid samples at various time points.

(Supplementary Figure S1). This observation was consistent with the characteristics of fungal growth, indicating that the number of fungi increased significantly. Fungal activity therefore likely became the determining factor, with *Y. lipolytica* representing the dominant fungus (Figure 4). In the cutting fluid environment with a high mineral oil content, *Y. lipolytica* follows a filamentous growth pattern (Ermakova and Morgunov, 1988). The growth and movement of fungal hyphae make the cutting fluid unable to form an effective lubricating film between the tool, chip, and machining surface (Elansky et al., 2022), resulting in reduced lubricity. Moreover, fungi produce various enzymes that can disrupt the active ingredients of cutting fluid, resulting in reduced lubricity (Buarque et al., 2023).
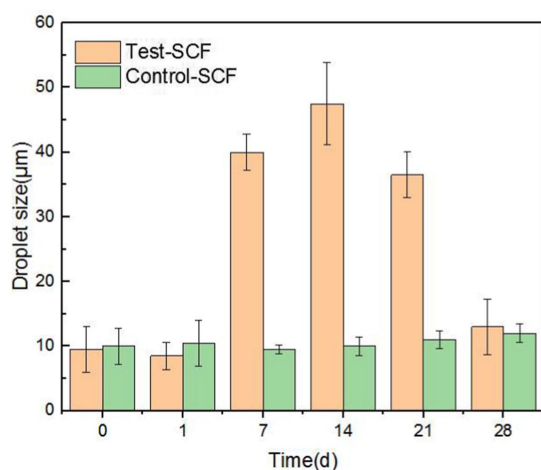

FIGURE 11
Diameters of randomly extracted droplets in two cutting fluid samples over time.
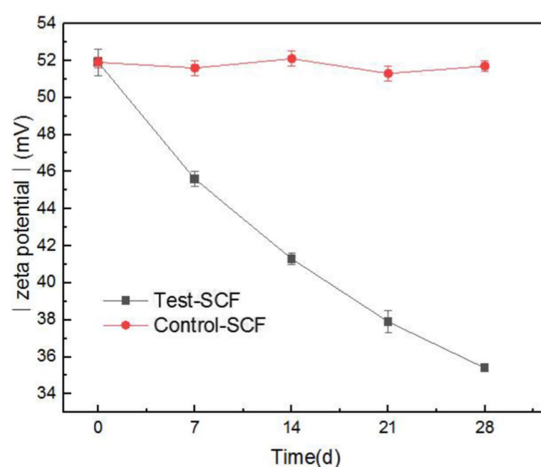

FIGURE 12
Absolute value of Zeta potential of two cutting fluid samples over time.

3.7 Impact of microorganisms on cutting fluid stability

The impact of microorganisms on the stability of cutting fluid was assessed through droplet morphology and zeta potential. Figures 10, 11 show the morphology and diameter statistics of droplets in the cutting fluid at different time points over the experiment. The size of the oil droplets in the Test-SCF sample initially increased before increasing gradually after 14 days and stabilizing. Conversely, in the Control-SCF sample, the particle sizes of the oil droplets did not change appreciably, remaining stable at ~10 μm.

Zeta potential was used to show the stability of the cutting fluid system, with larger absolute values indicating a more stable system. Figure 12 shows the absolute value of the zeta potential of the freshly-prepared cutting fluid compared to the fluid that had progressed through 28 days of experimentation. The results indicated that the absolute zeta potential value decreased from 51.9 to 35.4 mV after 28 days. The significant reduction in the absolute value indicates a deterioration in the stability of the cutting fluid system.

This was primarily caused by the increased number of fungi after day 14 playing a dominant role. Fungal mycelia grew continuously in the cutting fluid, intertwining to form a network structure (Hotz et al., 2023). This led to the flocculation of oil droplets in the cutting fluid system, thereby reducing its stability. The effective components that provide lubrication also flocculated concurrently, resulting in the reduced lubricity observed in the tapping torque experiment results.

3.8 Impact of microorganisms on the reduction−oxidation potential of cutting fluid

ORP has rarely been used to assess the performance of cutting fluid, but our study innovatively used this property to analyze the cutting fluid samples. In most biological systems, aerobic cells exhibit high cell potentials, whereas anaerobic ones have low potentials. Enzymatic activity, cellular assimilation capabilities, and microbial growth are also influenced by ORP. The ORP of the cutting fluid gradually decreased over the test month and eventually stabilized at a relatively low value (Figure 13). This indicated that the number of anaerobic bacteria in the cutting fluid increased as the experiment progressed. For example, there was a significant presence of bacteria such as *S. termitidis* and *C. lubricantis*, and even the obligate anaerobe *C. celerecrescens* was detected. This demonstrated a clear correlation between ORP and the dominant microorganisms in the cutting fluid.

3.9 Mechanism analysis of the microbial effect on cutting fluid properties

In general, the growth and reproduction of microorganisms impacted the pH and corrosion inhibition capability of the cutting fluid in two ways. First, the microbial metabolic byproducts affected the pH and corrosion inhibition capability of the fluid. Second, the metabolic activity of the microorganisms themselves may have degraded the active ingredients of the cutting fluid.

Total organic carbon content was tested to investigate how microbial degradation affected the various components of industrial cutting fluid. Triethanolamine, which regulates pH, can cause pH imbalances in cutting fluid emulsions when degraded, thereby reducing performance (Pimenov et al., 2024). Tall oil, known for its excellent properties related to emulsification, lubrication, and corrosion inhibition, serves as a crucial emulsifying agent in cutting fluid (Kazeem et al., 2020). Organic phosphates, commonly added as corrosion inhibitors in cutting fluids for aluminum, help prevent corrosion during the machining process. These three substances were therefore selected to assess the effects of microbial degradation.

Figure 14 shows the effects of microbial degradation on these different components. Initially, the degradation rate of all three components was slow, owing to the lower microbial content and slower metabolism, thus resulting in a slower aerobic degradation rate. On day 5, during the logarithmic growth phase, the microbial population and metabolic activity increased substantially,

FIGURE 13
Redox potential (ORP) values of two cutting fluid samples over time.

accelerating the degradation of the organic components. By day 9, the degradation rates reached 26.82% for triethanolamine, 34.15% for tall oil, and 11.04% for organophosphate esters. The highest microbial degradation rates were observed for triethanolamine, followed by tall oil, with the organophosphate esters showing the lowest rates. Although their rate of microbial degradation was relatively slow, the organophosphate esters were nevertheless degraded. This indicates that, during metabolism, microorganisms can use corrosion-inhibiting organophosphate esters as a nutrient source, thus reducing the corrosion-inhibition properties of cutting fluid. Microorganisms also degraded triethanolamine, a pH regulator, ultimately leading to lowered pH in the cutting fluid.

4 Conclusion

The microbial compositions of the spoiled cutting fluid samples varied significantly between those taken from the surface and the bottom of the onsite instrument's liquid tank. The surface layer predominantly contained aerobic bacteria such as *Pseudomonas*, *Acinetobacter*, and *Ochrobactrum*. Conversely, the bottom layer was primarily composed of anaerobic and facultative bacteria such as *Brachymonas*, *Sebaldella*, *Corynebacterium*, and *Comamonas*. The results of laboratory microbial culturing experiments showed that the fungal communities in these samples mainly consisted of the yeast *Yarrowia lipolytica*. Microbial metabolic activity inhibited the formation of passivation films on the aluminum alloys, through the secretion of various organic acids. These activities also consumed the primary active ingredients of the cutting fluid, leading to a significant decrease in its pH and ability to inhibit corrosion. The presence of microorganisms slightly enhanced the lubricity of the cutting fluid; however, in the later stages of the experiment, an increase in fungi, as well as the corresponding sweeping and bridging actions of the fungal hyphae, caused the active ingredients in the cutting fluid system to flocculate, reducing both its lubricity and stability. The results of this study showed that microorganisms impact all properties of industrial cutting fluid, with the most pronounced effects being related to corrosion inhibition,
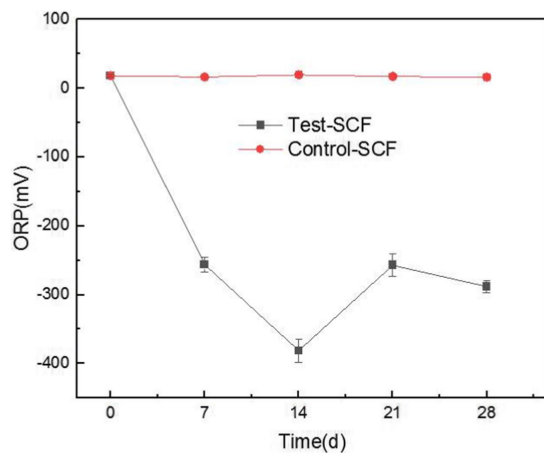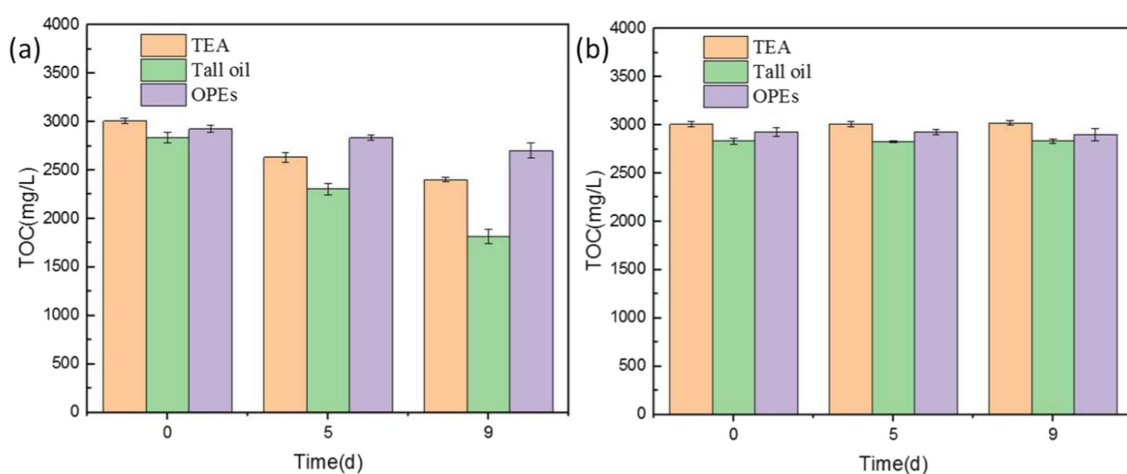

FIGURE 14
Total organic carbon (TOC) values of cutting fluid samples with **(A)** and without **(B)** microbial growth.

pH, and stability. The experimental conditions were restricted to a laboratory environment, so there may be many other potential microbial species and influencing factors related to this phenomenon that have remained unexplored. A deeper understanding of the impact of microorganisms on the deterioration of cutting fluid performance plays a key role in improving the quality, efficiency, and sustainability of the cutting process. It will also hopefully lay a theoretical foundation for the future development and application of new cutting fluids.

Data availability statement

The data presented in the study are deposited in the National Center for Biotechnology Information (NCBI) repository, accession numbers SRP554559 and PRJNA1204126.

Author contributions

YS: Formal analysis, Project administration, Writing – original draft. WZ: Data curation, Formal analysis, Investigation, Writing – original draft. LW: Writing – review & editing, Supervision, Visualization. YD: Conceptualization, Data curation, Methodology, Writing – review & editing. GG: Writing – review & editing, Supervision, Methodology. LD: Conceptualization, Funding acquisition, Methodology, Writing – review & editing. ZG: Conceptualization, Formal analysis, Writing – review & editing.

Funding

Conflict of interest

The authors declare that the research was conducted in the absence of any commercial or financial relationships that could be construed as a potential conflict of interest.

Generative AI statement

The author(s) declare that no Gen AI was used in the creation of this manuscript.

Publisher's note

All claims expressed in this article are solely those of the authors and do not necessarily represent those of their affiliated organizations, or those of the publisher, the editors and the reviewers. Any product that may be evaluated in this article, or claim that may be made by its manufacturer, is not guaranteed or endorsed by the publisher.

Supplementary material

The Supplementary material for this article can be found online at: https://www.frontiersin.org/articles/10.3389/fmicb.2025.1522265/full#supplementary-material

References

Abarenkov, K., Nilsson, R. H., Larsson, K. H., Alexander, I. J., Eberhardt, U., Erland, S., et al. (2010). The UNITE database for molecular identification of fungi-recent updates and future perspectives. *New Phytol.* 186, 281–285. doi: 10.1111/j.1469-8137.2009.03160.x

Alobaid, A. A., Allah, A., El, M. A., Dahmani, K., Aribou, Z., Kharbouch, O., et al. (2024). Comprehensive investigation of novel synthesized Thiophenytoin derivative (antiepileptic drug) as an environmentally friendly corrosion inhibitor for mild steel in 1 M HCl: theoretical, electrochemical, and surface analysis perspectives. *Mater. Today Commun.* 41:110698. doi: 10.1016/j.mtcomm.2024.110698

Babaei, P., Ghasemi-Kahrizsangi, T., and Marashi, S. A. (2014). Modeling the differences in biochemical capabilities of pseudomonas species by flux balance analysis: how good are genome-scale metabolic networks at predicting the differences? *The Scientific World J.* 2014:289. doi: 10.1155/2014/416289

Buarque, F. S., Carniel, A., Ribeiro, B. D., and Coelho, M. A. Z. (2023). Selective enzymes separation from the fermentation broth of Yarrowia lipolytica using aqueous two-phase system based on quaternary ammonium compounds. *Sep. Purif. Technol.* 324:124539. doi: 10.1016/j.seppur.2023.124539

Caballero, A., Esteve-Núñez, A., Zylstra, G. J., and Ramos, J. L. (2005). Assimilation of nitrogen from nitrite and trinitrotoluene in *Pseudomonas putida* JLR11. *J. Bacteriol.* 187, 396–399. doi: 10.1128/JB.187.1.396-399.2005

Chen, H. M., Liu, N. C., Lu, H., Li, X. F., and Zheng, Y. Y. (2024). Evaluation of new nano-cutting fluids for the processing of carbon fiber-reinforced composite materials. *J. Clean. Prod.* 437:140771. doi: 10.1016/j.jclepro.2024.140771

Choudhury, S. K., and Muaz, M. (2020). Renewable metal working fluids for aluminum and heavy duty machining. *Encycl. Renew. Sustain. Mater.* 5, 242–248. doi: 10.1016/B978-0-12-803581-8.11546-2

D'Addona, D. M., Conte, S., Teti, R., Marzocchella, A., and Raganati, F. (2020). Feasibility study of using microorganisms as lubricant component in cutting fluids. *Proc. CIRP* 88, 606–611. doi: 10.1016/j.procir.2020.05.106

Daniels, C., Godoy, P., Duque, E., Molina-Henares, M. A., de la Torre, J., del Arco, J. M., et al. (2010). Global regulation of food supply by *Pseudomonas putida* DOT-T1E. *J. Bacteriol.* 192, 2169–2181. doi: 10.1128/JB.01129-09

Edgar, R. C. (2013). UPARSE: highly accurate OTU sequences from microbial amplicon reads. *Nat. Methods* 10, 996–998. doi: 10.1038/nmeth.2604

Edgar, R. C., Haas, B. J., Clemente, J. C., Quince, C., and Knight, R. (2011). UCHIME improves sensitivity and speed of chimera detection. *Bioinformatics* 27, 2194–2200. doi: 10.1093/bioinformatics/btr381

Elansky, S. N., Chudinova, E. M., Elansky, A. S., Kah, M. O., Sandzhieva, D. A., Mukabenova, B. A., et al. (2022). Microorganisms in spent water-miscible metalworking fluids as a resource of strains for their disposal. *J. Clean. Prod.* 350:131438. doi: 10.1016/j.jclepro.2022.131438

Ermakova, I. T., and Morgunov, I. G. (1988). Pathways of metabolism in Yarrowia (candida) Lipolytica yeasts. *Microbiology* 57, 429–432.

Gast, C. J. V. D., Knowles, C. J., Wright, M. A., and Thompson, I. P. (2001). Identification and characterisation of bacterial populations of an in-use metal-working fluid by phenotypic and genotypic methodology. *Int. Biodeterior. Biodegradation* 47, 113–123. doi: 10.1016/S0964-8305(01)00036-1

Grijalbo, L., Garbisu, C., Martin, I., Etxebarria, J., Gutierrez-Mañero, F. J., and Garcia, J. A. L. (2015). Functional diversity and dynamics of bacterial communities in a membrane bioreactor for the treatment of metal-working fluid wastewater. *J. Water Health* 13, 1006–1019. doi: 10.2166/wh.2015.079

Guo, H. W., Su, S. J., Madzak, C., Zhou, J. W., Chen, H. W., and Chen, G. (2016). Applying pathway engineering to enhance production of alpha-ketoglutarate in

Yarrowia lipolytica. Appl. Microbiol. Biot. 100, 9875–9884. doi: 10.1007/s00253-016-7913-x

Harmon-Smith, M., Celia, L., Chertkov, O., Lapidus, A., Copeland, A., Del Rio, T. G., et al. (2010). Complete genome sequence of *Sebaldella termitidis* type strain (NCTC 11300T). *Stand. Genomic Sci.* 2, 220–227. doi: 10.4056/sigs.811799

Hill, E. C. (1992). COSHH regulations and microbial hazards associated with metalworking fluids. *Tribol. Int.* 25, 141–143. doi: 10.1016/0301-679X(92)90091-Z

Hotz, E. C., Bradshaw, A. J., Elliott, C., Carlson, K., Dentinger, B. T. M., and Naleway, S. E. (2023). Effect of agar concentration on structure and physiology of fungal hyphal systems. *J. Mater. Res. Technol.* 24, 7614–7623. doi: 10.1016/j.jmrt.2023.05.013

Kazeem, R. A., Fadare, D. A., Abutu, J., Lawal, S. A., and Adesina, O. S. (2020). Performance evaluation of jatropha oil-based cutting fluid in turning AISI 1525 steel alloy. *CIRP J. Manuf. Sci. Technol.* 31, 418–430. doi: 10.1016/j.cirpj.2020.07.004

Korkmaz, M. E., Gupta, M. K., Ross, N. S., and Sivalingam, V. (2023). Implementation of green cooling/lubrication strategies in metal cutting industries: a state of the art towards sustainable future and challenges. *Sustain. Mater. Technol.* 36:e00641. doi: 10.1016/j.susmat.2023.e00641

Ledesma-Amaro, R., Lazar, Z., Rakicka, M., Guo, Z. P., Fouchard, F., Crutz-Le, C. A. M., et al. (2016). Metabolic engineering of Yarrowia lipolytica to produce chemicals and fuels from xylose. *Metab. Eng.* 38, 115–124. doi: 10.1016/j.ymben.2016.07.001

Li, J. L., Chen, L. J., Wei, B., Xu, J., Wei, B. X., and Sun, C. (2024). Microbiologically influenced corrosion of circulating cooling systems in power plants – a review. *Arab. J. Chem.* 17:105529. doi: 10.1016/j.arabjc.2023.105529

Li, B. H., Huang, J. H., Li, X. L., Ma, Q., Zhao, P. F., and Huang, W. (2023). The microbial degradation of AAOO based cutting fluid wastewater. *J. Water Process Eng.* 55:104167. doi: 10.1016/j.jwpe.2023.104167

Lillienberg, L., Andersson, E. M., Jarvholm, B., and Torén, K. (2010). Respiratory symptoms and exposure-response relations in workers exposed to metalworking fluid aerosols. *Ann. Occup. Hyg.* 54, 403–411. doi: 10.1093/annhyg/meq009

Lillienberg, L., Burdorf, A., Mathiasson, L., and Thorneby, L. (2008). Exposure to metalworking fluid aerosols and determinants of exposure. *Ann. Occup. Hyg.* 52, 597–605. doi: 10.1093/annhyg/men043

Liu, H. M., Lin, Y. H., Tsai, M. Y., and Lin, W. H. (2010). Occurrence and characterization of culturable bacteria and fungi in metalworking environments. *Aerobiologia* 26, 339–350. doi: 10.1007/s10453-010-9169-8

Lopes, E. L., Semedo, M., Tomasino, M. P., Mendes, R., Sousa, J. B., and Magalhães, C. (2024). Horizontal distribution of marine microbial communities in the North Pacific subtropical front. *Front. Microbiol.* 15:1455196. doi: 10.3389/fmicb.2024.1455196

Lu, S. H., He, Y., Xu, R. C., Wang, N. X., Chen, S. Q., Dou, W. W., et al. (2023). Inhibition of microbial extracellular electron transfer corrosion of marine structural steel with multiple alloy elements. *Bioelectrochemistry* 151:108377. doi: 10.1016/j.bioelechem.2023.108377

Ma, S., Kim, K., Huh, J., Kim, D. E., Lee, S., and Hong, Y. (2018). Regeneration and purification of water-soluble cutting fluid through ozone treatment using an air dielectric barrier discharge. *Sep. Purif. Technol.* 199, 289–297. doi: 10.1016/j.seppur.2018.02.005

Osama, M., Singh, A., Walvekar, R., Khalid, M., Gupta, T. C., and Yin, W. W. (2017). Recent developments and performance review of metal working fluids. *Tribol. Int.* 114, 389–401. doi: 10.1016/j.triboint.2017.04.050

Pimenov, D. Y., Silva, L. R. R., Machado, A. R., França, P. H. P., Pintaude, G., Unune, D. R., et al. (2024). A comprehensive review of machinability of difficult-to-machine alloys with advanced lubricating and cooling techniques. *Tribol. Int.* 196:109677. doi: 10.1016/j.triboint.2024.109677

Pruesse, E., Quast, C., Knittel, K., Fuchs, B. M., Ludwig, W., and Peplies, J. (2007). SILVA: a comprehensive online resource for quality checked and aligned ribosomal RNA sequence data compatible with ARB. *Nucleic Acids Res.* 35, 7188–7196. doi: 10.1093/nar/gkm864

Rabenstein, A., Koch, T., Remesch, M., Brinksmeier, E., and Kuever, J. (2009). Microbial degradation of water miscible metal working fluids. *Int. Biodeterior. Biodegradation* 63, 1023–1029. doi: 10.1016/j.ibiod.2009.07.005

Rakić, R., and Rakić, Z. (2002). The influence of the metal working fluids on machine tool failures. *Wear* 252, 438–444. doi: 10.1016/S0043-1648(01)00890-0

Roca, A., Rodriguez-Herva, J. J., and Ramos, J. L. (2009). Redundancy of enzymes for formaldehyde detoxification in *Pseudomonas putida. J. Bacteriol.* 191, 3367–3374. doi: 10.1128/JB.00076-09

Rognes, T., Flouri, T., Nichols, B., Quince, C., and Mahe, F. (2016). VSEARCH: a versatile open source tool for metagenomics. *Peer J* 4:e2584. doi: 10.7717/peerj.2584

Sankaranarayanan, R., Hynes, N. R. J., Kumar, J. S., and Krolczyk, G. M. (2021). A comprehensive review on research developments of vegetable-oil based cutting fluids for sustainable machining challenges. *J. Manuf. Process.* 67, 286–313. doi: 10.1016/j.jmapro.2021.05.002

Schwarz, M., Dado, M., Hnilica, R., and Veverková, D. (2015). Environmental and health aspects of metalworking fluid use. *Pol. J. Environ. Stud.* 24, 37–45.

Simpson, A. T., Groves, J. A., Unwin, J., and Piney, M. (2000). Mineral oil metal working fluids (MWFs)-development of practical criteria for mist sampling. *Ann. Occup. Hyg.* 44, 165–172. doi: 10.1016/S0003-4878(99)00085-X

Sun, M., Xu, W. W., Rong, H., Chen, J. T., and Yu, C. L. (2023). Effects of dissolved oxygen (DO) in seawater on microbial corrosion of concrete: morphology, composition, compression analysis and transportation evaluation. *Constr. Build. Mater.* 367:130290. doi: 10.1016/j.conbuildmat.2023.130290

Trafny, E. A. (2013). Microorganisms in metalworking fluids: current issues in research and management. *Int. J. Occup. Med. Environ. Health* 26, 4–15. doi: 10.2478/S13382-013-0075-5

Yazdi, M., Khan, F., Abbassi, R., Quddus, N., and Castaneda-Lopez, H. (2022). A review of risk-based decision-making models for microbiologically influenced corrosion (MIC) in offshore pipelines. *Reliab. Eng. Syst. Safe.* 223:108474. doi: 10.1016/j.ress.2022.108474

Yin, Y. S., Guo, Z. W., Liu, T., Guo, N., and Shen, Y. Y. (2019). *A culture medium used for culturing and isolating microorganisms in cutting fluid, as well as its preparation method and application. CN 110846247 a [patent].* China: State Intellectual Property Office of the People's Republic of China. Available at: https://www.iprdb.com.

Zhang, Q. K., He, Y. H., Wang, W., Lin, N., Wu, C. H., and Li, N. F. (2015). Corrosion behavior of WC–co hardmetals in the oil-in-water emulsions containing sulfate reducing Citrobacter sp. *Corros. Sci.* 94, 48–60. doi: 10.1016/j.corsci.2015.01.036

Zhang, J. J., Kobert, K., Flouri, T., and Stamatakis, A. (2014). PEAR: a fast and accurate Illumina paired-end reAd mergeR. *Bioinformatics* 30, 614–620. doi: 10.1093/bioinformatics/btt593

Frontiers in Microbiology

Explores the habitable world and the potential of microbial life

The largest and most cited microbiology journal which advances our understanding of the role microbes play in addressing global challenges such as healthcare, food security, and climate change.

Discover the latest Research Topics

See more →

frontiers | Research Topics